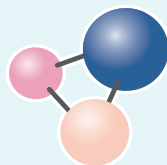


ИЗВЕСТИЯ ВУЗОВ



**ПОРОШКОВАЯ МЕТАЛЛУРГИЯ
И ФУНКЦИОНАЛЬНЫЕ ПОКРЫТИЯ**

**POWDER
METALLURGY
AND FUNCTIONAL
COATINGS**

2025

Том 19 № 4
Vol. No.

powder.misis.ru

**К 100-летию
Олега Владиславовича Романа**

ISSN 1997-308X
eISSN 2412-8767

POWDER METALLURGY AND FUNCTIONAL COATINGS

Scientific and Technical Journal
Founded in 2007
Six issues per year

2025

Том 19 № 4
Vol. 19 No. 4

ИЗВЕСТИЯ ВУЗОВ ПОРОШКОВАЯ МЕТАЛЛУРГИЯ И ФУНКЦИОНАЛЬНЫЕ ПОКРЫТИЯ

Научно-технический журнал
Основан в 2007 г.
Выходит 6 раз в год

POWDER METALLURGY AND FUNCTIONAL COATINGS

SCIENTIFIC AND TECHNICAL JOURNAL
FOUNDED IN 2007
SIX ISSUES PER YEAR

<http://powder.misis.ru>

ISSN 1997-308X
eISSN 2412-8767



Founder:

National University of Science
and Technology "MISIS"

Address: 1 Bld, 4 Leninskiy Prosp., Moscow 119049, Russian Federation

<http://www.misis.ru>

Editor-in-Chief

Evgeny A. Levashov

Dr. Sci. (Eng.), Corr. Mem. of the RAS, Prof., NUST MISIS, Moscow, Russian Federation

Journal is included into the List of peer-reviewed scientific publications recommended by the Highest Attestation Commission of the Ministry of Education and Science of the Russian Federation for publishing the results of doctoral and candidate dissertations. Abstracting/Indexing: Scopus, Russian Science Citation Index (RSCI), Ulrich's Periodicals Directory, VINITI Database (Abstract Journal).

Editorial Board

M. I. Alymov – Dr. Sci. (Eng.), Corresponding Member of the RAS, Merzhanov Institute of Structural Macrokinetics and Materials Sciences of the RAS, Chernogolovka, Russia
A. P. Amosov – Prof., Dr. Sci. (Phys.-Math.), Samara State Technical University, Samara, Russia
I. V. Blinkov – Prof., Dr. Sci. (Eng.), NUST MISIS, Moscow, Russia
M. V. Chukin – Prof., Dr. Sci. (Eng.), Magnitogorsk State Technical University, Magnitogorsk, Russia
H. Danning – Prof., Dr. Sci., Vienna University of Technology, Vienna, Austria
B. Derin – Assoc. Prof., Dr. Sci. (Phil.), Istanbul Technical University, Maslak, Istanbul, Turkey
V. Yu. Dorofeyev – Prof., Dr. Sci. (Eng.), South-Russian State Polytechnical University (NPI), Novocherkassk, Russia
A. Ph. Ilyushchanka – Prof., Dr. Sci. (Eng.), Acad. of the NAS of Belarus, State Research and Production Powder Metallurgy Association, Minsk, Belarus
Yu. R. Kolobov – Prof., Dr. Sci. (Phys.-Math.), Federal Research Center of Problems of Chemical Physics and Medicinal Chemistry of the RAS, Chernogolovka, Russia
V. S. Komlev – Prof., Dr. Sci. (Eng.), Corresponding Member of the RAS, Institute of Metallurgy of the RAS, Moscow, Russia
I. Konyashin – Prof., Dr. Sci. (Econ.), Element Six GmbH, Burghaun, Germany
Yu. M. Korolyov – Prof., Dr. Sci. (Eng.), Scientific and Technical Association "Powder Metallurgy", Moscow, Russia
D. Yu. Kovalev – Dr. Sci. (Phys.-Math.), Merzhanov Institute of Structural Macrokinetics and Materials Sciences of the RAS, Chernogolovka, Russia
S. A. Kulinich – Assoc. Prof., PhD (Chem.), Tokai University, Hiratsuka, Kanagawa, Japan
S. V. Kuzmin – Prof., Dr. Sci. (Eng.), Corresponding Member of the RAS, Volgograd State Technical University, Volgograd, Russia
V. P. Kuznetsov – Prof., Dr. Sci. (Eng.), Ural Federal University, Ekaterinburg, Russia
Yu. V. Levinsky – Prof., Dr. Sci. (Eng.), Merzhanov Institute of Structural Macrokinetics and Materials Sciences of the RAS, Chernogolovka, Russia
A. E. Ligachyov – Prof., Dr. Sci. (Phys.-Math.), Prokhorov General Physics Institute of the RAS, Moscow, Russia
V. Yu. Lopatin – Cand. Sci., NUST MISIS, Moscow, Russia
A. A. Lozovan – Prof., Dr. Sci. (Eng.), Moscow Aviation Institute (NRU), Moscow, Russia

V. I. Lysak – Prof., Dr. Sci. (Eng.), Acad. of the RAS, Volgograd State Technical University, Volgograd, Russia
A. V. Makarov – Dr. Sci. (Eng.), Acad. of the RAS, M.N. Mikheev Institute of Metal Physics of the Ural Branch of the RAS, Ural Federal University, Ekaterinburg, Russia
L. L. Mishnaevsky – Dr. Habil. (Eng.), Technical University of Denmark, Roskilde, Denmark
A. S. Mukasyan – Prof., Dr. Sci. (Phys.-Math.), University of Notre Dame, Notre Dame, USA
S. A. Oglezneva – Prof., Dr. Sci. (Eng.), Perm National Research Polytechnical University, Perm, Russia
R. Orrù – Prof., Dr. Sci. (Eng.), University of Cagliari, Cagliari, Italy
I. B. Panteleev – Prof., Dr. Sci. (Eng.), St. Petersburg State Technological Institute (Technical University), St. Petersburg, Russia
F. Peizhong – Prof., Dr. Sci., China University of Mining and Technology, Xuzhou, P.R. China
C. Pengwan – Prof., Dr. Sci., Beijing Institute of Technology, Beijing, P.R. China
M. I. Petrzhik – Dr. Sci. (Eng.), NUST MISIS, Moscow, Russia
Yu. S. Pogozhev – Assoc. Prof., Cand. Sci. (Eng.), NUST MISIS, Moscow, Russia
V. V. Polyakov – Prof., Dr. Sci. (Phys.-Math.), Altai State University, Barnaul, Russia
A. A. Popovich – Prof., Dr. Sci. (Eng.), Corresp. Member of the RAS, St. Petersburg State Polytechnical University (National Research University), St. Petersburg, Russia
S. E. Porozova – Dr. Sci. (Eng.), Perm National Research Polytechnical University, Perm, Russia
A. A. Rempel – Prof., Dr. Sci. (Phys.-Math.), Acad. of the RAS, Institute of Metallurgy of the Ural Branch of the RAS, Ekaterinburg, Russia
F. Rusticelli – Prof., Dr. Sci. (Phys.), University of Marches, Ancona, Italy
S. D. Shlyapin – Prof., Dr. Sci. (Eng.), Moscow Aviation Institute (NRU), Moscow, Russia
D. V. Shtansky – Prof., Dr. Sci. (Phys.-Math.), NUST MISIS, Moscow, Russia
A. N. Timofeev – Dr. Sci. (Eng.), JSC "Komposite", Korolev, Russia
P. A. Vityaz – Prof., Dr. Sci. (Eng.), Acad. of the NAS of Belarus, Minsk, Belarus
A. A. Zaitsev – Assoc. Prof., Cand. Sci. (Eng.), NUST MISIS, Moscow, Russia
Zheng YongTing – Prof., Dr. Sci., Harbin Institute of Technology, Harbin, P.R. China
F. Zhengyi – Prof., Dr. Sci., Wuhan University of Technology, Wuhan, P.R. China

Editorial Staff

Address: NUST MISIS,
1 Bld, 4 Leninskiy Prosp., Moscow 119049, Russian Federation

Phone: +7 (495) 638-45-35. E-mail: izv.vuz@misis.ru

Certificate of registration No. FS77-27955 (12.04.2007)

Re-registration PI No. FS77-79230 (25.09.2020)



PM & FC © NUST MISIS, Moscow, 2025

Articles are available under Creative Commons
Attribution Non-Commercial No Derivatives

Leading Editor: O.V. Sosnina
Executive Editor: A.A. Kudinova
Layout Designer: V.V. Rasenets

Signed print 20.08.2025. Format 60×90 1/8
Offset paper No. 1. Digital printing. Quires 12.5

Order 22789. Free price

Printed in the printing house of the MISIS Publish House
1 Bld, 4 Leninskiy Prosp., Moscow 119049, Russian Federation
Phone/fax: +7 (499) 236-76-17

ИЗВЕСТИЯ ВУЗОВ ПОРОШКОВАЯ МЕТАЛЛУРГИЯ И ФУНКЦИОНАЛЬНЫЕ ПОКРЫТИЯ

ISSN 1997-308X
eISSN 2412-8767



Учредитель:

ФГАОУ ВО Национальный исследовательский
технологический университет «МИСИС»

Адрес: 119049, Москва, Ленинский пр-т, 4, стр. 1

<https://www.misis.ru>

Главный редактор

Евгений Александрович Левашов

д.т.н., чл.-корр. РАН, профессор, НИТУ МИСИС, г. Москва

НАУЧНО-ТЕХНИЧЕСКИЙ ЖУРНАЛ

ОСНОВАН В 2007 Г.

ВЫХОДИТ 6 РАЗ В ГОД

<http://powder.misis.ru>

Журнал включен в Перечень рецензируемых научных изданий, рекомендованных ВАК Минобрнауки РФ
для публикации результатов диссертаций на соискание ученых степеней.

Журнал включен в базы данных: Scopus, Russian Science Citation Index (RSCI), Ulrich's Periodicals Directory, РИНЦ, БД/РЖ ВИНТИ.

Редакционная коллегия

М. И. Алымов – д.т.н., чл.-корр. РАН, проф., ИСМАН, г. Черноголовка
А. П. Амосов – д.ф.-м.н., проф., СамГТУ, г. Самара
И. В. Блинков – д.т.н., проф., НИТУ МИСИС, г. Москва
П. А. Витязь – д.т.н., проф., акад. НАН Беларуси, г. Минск
В. Ю. Дорофеев – д.т.н., проф., ЮРГПУ (НПИ), г. Новочеркасск
А. А. Зайцев – к.т.н., доц., НИТУ МИСИС, г. Москва
А. Ф. Ильющенко – д.т.н., акад. НАН Беларуси, проф.,
ГНПО ПМ НАН Беларуси, г. Минск
Д. Ю. Ковалев – д.ф.-м.н., ИСМАН, г. Черноголовка
Ю. Р. Колобов – д.ф.-м.н., проф., ФИЦ ПХФ и МХ РАН, г. Черноголовка
В. С. Комлев – д.т.н., чл.-корр. РАН, проф., ИМЕТ РАН, г. Москва
Ю. М. Королёв – д.т.н., проф., НТА «Порошковая металлургия»,
г. Москва
В. П. Кузнецов – д.т.н., проф., УрФУ, г. Екатеринбург
С. В. Кузьмин – д.т.н., чл.-корр. РАН, проф., ВолгГТУ, г. Волгоград
Ю. В. Левинский – д.т.н., проф., ИСМАН, г. Черноголовка
А. Е. Лигачев – д.ф.-м.н., проф., ИОФ РАН, г. Москва
А. А. Лозован – д.т.н., проф., МАИ (НИУ), г. Москва
В. Ю. Лопатин – к.т.н., доц., НИТУ МИСИС, г. Москва
В. И. Лысак – д.т.н., акад. РАН, проф., ВолгГТУ, г. Волгоград
А. В. Макаров – д.т.н., акад. РАН, ИФМ УрО РАН, УрФУ,
г. Екатеринбург
С. А. Оглезнева – д.т.н., проф., ПНИПУ, г. Пермь
И. Б. Пантелеев – д.т.н., проф., СПбГТИ (ТУ), г. Санкт-Петербург
М. И. Петржик – д.т.н., проф., НИТУ МИСИС, г. Москва
Ю. С. Погожев – к.т.н., доц., НИТУ МИСИС, г. Москва
В. В. Поляков – д.ф.-м.н., проф., АлтГУ, г. Барнаул
А. А. Попович – д.т.н., чл.-корр. РАН, проф., СПбГПУ,
г. Санкт-Петербург

С. Е. Порозова – д.т.н., проф., ПНИПУ, г. Пермь
А. А. Ремпель – д.ф.-м.н., акад. РАН, проф., ИМЕТ УрО РАН,
г. Екатеринбург
А. Н. Тимофеев – д.т.н., АО «Композит», г. Королев
М. В. Чукин – д.т.н., проф., МГТУ, г. Магнитогорск
С. Д. Шляпин – д.т.н., проф., МАИ (НИУ), г. Москва
Д. В. Штанский – д.ф.-м.н., проф., НИТУ МИСИС, г. Москва
H. Danningер – Dr. Sci., Prof., Vienna University of Technology,
Vienna, Austria
B. Derin – Dr. Sci. (Phil.), Assoc. Prof., Istanbul Technical University,
Maslak, Istanbul, Turkey
I. Konyashin – Dr. Sci. (Econ.), Prof., Element Six GmbH, Burghaun,
Germany
S. A. Kulinich – PhD (Chem.), Associate Prof., Tokai University, Hiratsuka,
Kanagawa, Japan
L. L. Mishnaevsky – Dr. Habil. (Eng.), Technical University of Denmark,
Roskilde, Denmark
A. S. Mukasyan – Dr. Sci. (Phys.-Math.), Prof., University of Notre Dame,
Notre Dame, USA
R. Orrù – Dr. Sci. (Eng.), Prof., University of Cagliari, Cagliari, Italy
F. Peizhong – Dr. Sci., Prof., China University of Mining and Technology,
Xuzhou, P.R. China
C. Pengwan – Dr. Sci., Prof., Beijing Institute of Technology,
Beijing, P.R. China
F. Rustichelli – Dr. Sci. (Phys.), Prof., University of Marches, Ancona, Italy
Zheng YongTing – Dr. Sci., Prof., Harbin Institute of Technology, Harbin,
P.R. China
F. Zhengyi – Dr. Sci., Prof., Wuhan University of Technology, Wuhan,
P.R. China

Редакция журнала

Адрес: 119049, Москва,
Ленинский пр-т, 4, стр. 1. НИТУ МИСИС

Тел.: +7 (495) 638-45-35. Эл. почта: izv.vuz@misis.ru

Свидетельство о регистрации № ФС77-27955 от 12.04.2007 г.
Перерегистрация 25.09.2020 г. ПИ № ФС77-79230



© НИТУ МИСИС, Москва, 2025



Статьи доступны под лицензией Creative Commons
Attribution Non-Commercial No Derivatives

Ведущий редактор: О.В. Соснина
Выпускающий редактор: А.А. Кудинова
Дизайн и верстка: В.В. Расенец

Подписано в печать 20.08.2025. Формат 60×90 1/8
Бум. офсетная № 1. Печать цифровая. Усл. печ. л. 12,5
Заказ 22789. Цена свободная
Отпечатано в типографии Издательского Дома МИСИС
119049, г. Москва, Ленинский пр-т, 4, стр. 1
Тел./факс: +7 (499) 236-76-17

Contents



Содержание

To the 100th anniversary of Academician O.V. Roman

Vityaz P.A., Pyushchenko A.F.
On the occasion of the centenary of Academician
Oleg Vladislavovich Roman, 1925–2013 6

Production Processes and Properties of Powders

Dyachkova L.N., Vityaz P.A.
Iron-based pseudosalloys for antifriction applications
with enhanced mechanical and tribological properties
developed at the O.V. Roman Powder Metallurgy
Institute of the National Academy of Sciences
of Belarus 16

Theory and Processes of Formation and Sintering of Powder Materials

**Dorofeyev V.Yu., Sviridova A.N.,
Sviridova S.V., Svistun L.I.**
Features of densification, structure formation,
and properties of powder titanium under hot die forging 28

Self-Propagating High-Temperature Synthesis

Vadchenko S.G., Rogachev A.S., Alymov M.I.
Mechanism of synthesis of ultra-high temperature
 Ta_4ZrC_5 carbide by thermal explosion
with preliminary mechanical alloying of metals 40

Refractory, Ceramic, and Composite Materials

**Oglezneva S.A., Kulmetyeva V.B.,
Smetkin A.A., Malyshev A.E.**
Effect of $ZrO_2-Y_2O_3$ powder morphology on CMAS
resistance of thermal barrier coatings 50

Nanostructured Materials and Functional Coatings

**Mukanov S.K., Petrzhik M.I., Kudryashov A.E.,
Loginov P.A., Shvyndina N.V., Sheveyko A.N.,
Kuptsov K.A., Levashov E.A.**
Combined technology of electrospray
and cathodic-arc formation of wear- and oxidation
resistant coatings 60

К 100-летию академика О.В. Романа

Витязь П.А., Ильющенко А.Ф.
К 100-летию со дня рождения академика
Олега Владиславовича Романа, 1925–2013 6

Процессы получения и свойства порошков

Дьячкова Л.Н., Витязь П.А.
Псевдосплавы на основе железа
антифрикционного назначения с повышенными
механическими и триботехническими свойствами,
разработанные в Институте порошковой металлургии
имени академика О.В. Романа НАН Беларуси 16

Теория и процессы формования и спекания порошковых материалов

**Дорофеев В.Ю., Свиридова А.Н.,
Свиридова С.В., Свистун Л.И.**
Особенности уплотнения, формирования структуры
и свойств порошкового титана при горячей штамповке 28

Самораспространяющийся высокотемпературный синтез

Вадченко С.Г., Рогачев А.С., Алымов М.И.
Механизм синтеза ультратугоплавкого
карбида Ta_4ZrC_5 в режиме теплового взрыва
с предварительным механическим сплавлением
металлов 40

Тугоплавкие, керамические и композиционные материалы

**Оглезнева С.А., Кульмetyева В.Б.,
Сметкин А.А., Малышев А.Е.**
Влияние морфологии керамических порошков
 $ZrO_2-Y_2O_3$, используемых в теплозащитных
покрытиях, на стойкость к силикатным отложениям 50

Наноструктурированные материалы и функциональные покрытия

**Муканов С.К., Петржик М.И., Кудряшов А.Е.,
Логинов П.А., Швындина Н.В., Шевейко А.Н.,
Купцов К.А., Левашов Е.А.**
Комбинированная технология электронно-лучевой
и катодно-дуговой формирования износостойких
и жаростойких покрытий 60

Contents



Содержание

**Materials and Coatings Fabricated Using
the Additive Manufacturing Technologies**

BorisoV E.V., Repnin A.V., Popovich A.A.

Additive manufacturing of functionally
graded products by selective laser melting:

A review 77

Baskov F.A., Logacheva A.I.,

Logachev I.A., Timofeev A.N.

Challenges in using powder feedstock

for laser powder bed fusion 91

**Материалы и покрытия, получаемые
методами аддитивных технологий**

Борисов Е.В., Репнин А.В., Попович А.А.

Аддитивное производство изделий
с функционально-градиентной структурой
по технологии селективного лазерного сплавления.

Обзор 77

Басков Ф.А., Логачёва А.И.,

Логачев И.А., Тимофеев А.Н.

О проблемах применения металлпорошковых
композиций в технологии селективного лазерного
сплавления 91



<https://doi.org/10.17073/1997-308X-2025-4-6-15>

Editorial article
Редакционная статья



On the occasion of the centenary of Academician Oleg Vladislavovich Roman 1925–2013

P. A. Vityaz¹, A. F. Ilyushchenko²

¹ Presidium of the National Academy of Sciences of Belarus
66 Nezavisimosti Prosp., Minsk 220072, Belarus

² State Research Institution O.V. Roman Powder Metallurgy Institute, National Academy of Sciences of Belarus
41 Platonov Str., Minsk 220005, Belarus

alexil@mail.belpak.by

For citation: Vityaz P.A., Ilyushchenko A.F. On the occasion of the centenary of Academician Oleg Vladislavovich Roman, 1925–2013. *Powder Metallurgy and Functional Coatings*. 2025;19(4):6–15. <https://doi.org/10.17073/1997-308X-2025-4-6-15>

К 100-летию со дня рождения академика Олега Владиславовича Романа 1925–2013

П. А. Витязь¹, А. Ф. Ильющенко²

¹ Президиум Национальной академии наук Беларуси
Беларусь, 220072, г. Минск, пр-т Независимости, 66

² Институт порошковой металлургии имени академика О.В. Романа
Беларусь, 220005, г. Минск, ул. Платонова, 41

alexil@mail.belpak.by

Для цитирования: Витязь П.А., Ильющенко А.Ф. К 100-летию со дня рождения академика Олега Владиславовича Романа, 1925–2013. *Известия вузов. Порошковая металлургия и функциональные покрытия*. 2025;19(4):6–15. <https://doi.org/10.17073/1997-308X-2025-4-6-15>



Oleg Vladislavovich Roman was born in 1925 in Vladivostok to a family of teachers. In 1934, the family moved to Minsk, and following his father's death in 1941 – to Ufa, where his mother worked at a defense plant while he attended school and simultaneously worked at a factory. After graduating from school in 1942, he entered the Ufa Aviation Institute. In 1945, the family returned to Minsk, where he continued his studies at the Belarusian Polytechnic Institute (BPI), majoring in mechanical engineering. Upon graduation in 1948, he entered postgraduate studies at the M.I. Kalinin Leningrad Polytechnic Institute (LPI). His academic advisor was the eminent scientist and founder of the Soviet school of manufacturing engineering, Professor Aleksandr Pavlovich Sokolovsky. At that time, LPI already had a strong team of well-known scholars.

In 1951, O.V. Roman successfully defended his Candidate of Technical Sciences dissertation at LPI on the topic “Vibration Control in Metal Cutting” and returned to the Belarusian Polytechnic Institute, where he joined the faculty.

From 1961 to 1962, Oleg Vladislavovich completed a research internship in the United States at Rensselaer Polytechnic Institute (RPI) under Professors F.V. Lenel

*Dedicated to our teacher,
colleague, and friend,
Academician O.V. Roman,
on the occasion of his centenary*

and G. Ansell, as well as Dr. H. Hausner. He later noted that he was fortunate to work with such prominent scholars, whose influence shaped his future scientific career. Their collaboration continued for many years; both Professor Ansell and Dr. Hausner visited Minsk and gave lectures at the Research Institute of Powder Metallurgy.

The rapid development of powder metallurgy in the Belarusian Soviet Socialist Republic (BSSR) was closely linked with O.V. Roman's name. In 1955, he became head of the Department of Metal Technology at BPI, which covered multiple areas of materials production and processing technologies, including powder metallurgy. At his initiative, a powder metallurgy laboratory was established within the department in 1956, marking the beginning of this field in the republic.

At the time, new industrial facilities were being built in Minsk: Minsk Tractor Works (MTZ), Minsk Automobile Plant (MAZ), Minsk Automatic Lines Plant (MZAL), and many others. This growing industrial sector required new specialists, advanced knowledge, novel materials, and modern manufacturing processes. As a result, close collaboration developed between educational institutions, research organizations, and industry.

The laboratory staff actively cooperated with Udarnik Road Machinery Plant, whose director, S.M. Kovnatsky, and chief engineer, BPI graduate M.Ya. Kutser, understood the importance of developing new materials. In 1957, at O.V. Roman's initiative, the plant allocated a small space for the laboratory and pilot production, where the first powder metallurgy components were manufactured to meet industrial orders. For Udarnik, this included production of self-lubricating bushings (sliding bearings). In 1959, the first industrial contract was signed for the production of oil pump gears from powder compositions for the Kharkov Tractor Plant. However, production space remained insufficient, and again through O.V. Roman's initiative, an industrial section was established at the Minsk Spare Parts Plant (now OJSC Minsk Gear Plant), where for the first time in the BSSR a broad range of powder metallurgy components was manufactured for MTZ and MAZ.

The development of powder metallurgy work was formalized by a Resolution of the Council of Ministers of the BSSR dated October 3, 1959, which also defined the key research directions for the BPI Powder Metallurgy Laboratory at the Udarnik plant.

The creation in 1960 of the USSR system of regional economic councils (Sovnarkhozes) further stimulated the field. A government resolution transferred the BPI Powder Metallurgy Laboratory from the department to the institute's Research Sector, and under a Sovnarkhoz decision it was renamed the Central Base Laboratory of Powder Metallurgy (Order No. 627 of the Ministry of Higher Education of the BSSR, September 23, 1960). This date is now regarded as the official birthday of powder metallurgy in Belarus. The laboratory was staffed with 40 employees and guided by a Scientific and Technical Council chaired by Department Head O.V. Roman, who also served as Scientific Supervisor. M.Ya. Kutser, chief engineer of Udarnik plant, was appointed head of the laboratory. From the outset, its work followed a full-cycle principle: “from scientific research – to pilot design – to pilot-scale production – to mass production”, with parallel training of engineering specialists and highly qualified researchers.

It is worth noting that this integrated approach has been maintained to the present day in the Research Institute of Powder Metallurgy (RI PM, now the O.V. Roman Powder Metallurgy Institute) and the State Research and Production Powder Metallurgy Association, both of which trace their origins to this laboratory.

To train engineering specialists in powder metallurgy, the BPI was already involving students in

relevant diploma projects as early as 1958. Two students from the Faculty of Mechanical Engineering – V.N. Gromovich and E.M. Dechko – completed their graduation projects in this field. Gromovich subsequently worked at the powder metallurgy section of Minsk Spare Parts Plant, while Dechko joined the Department of Machine Tools and Cutting Tools at BPI, continuing his academic career to become a Doctor of Technical Sciences and Professor.

By 1959, an entire group of students was actively engaged in powder metallurgy. One of them, T.K. Yurashkevich (later Garkavaya), was assigned upon graduation to the Central Base Laboratory of Powder Metallurgy, becoming its first full-time engineer among BPI graduates.

In 1960, a team of five students successfully developed and defended a joint diploma project for the design of a future powder metallurgy plant. Participants in this project, including V.S. Kovnatsky and L.G. Talako, actively took part in designing and implementing technological processes for the Powder Metallurgy Plant in Molodechno in the early 1980s.

At the Central Base Laboratory of Powder Metallurgy, new structural, antifriction, and friction materials were developed, along with pilot-scale technologies for their production. The laboratory also manufactured friction rings for power take-off shafts for the newly launched MTZ-50 tractor series. The laboratory expanded rapidly, creating a need for new personnel.

One of its first staff members was the future Academician P.A. Vityaz, who recalls:



O.V. Roman during his internship among leading RPI specialists, 1965

Стажер О.В.Роман среди ведущих специалистов РПИ, 1965 г.

“At that time, I was working as a foreman in the repair shop at the Udarnik plant, and I often assisted the laboratory with repairs of process equipment, presses, and furnaces. This led to my joining the laboratory in 1961. I began my work in powder metallurgy by studying the properties and production methods of friction products for MTZ. My first meeting with O.V. Roman took place in 1962, upon his return from a research internship in the United States. At a general meeting with the laboratory staff, O.V. Roman impressed me not only with his appearance but also with the persuasiveness of his speech about the prospects for developing powder metallurgy and its importance for introducing new technologies and products for both general engineering and specialized equipment. At that very first meeting, he emphasized the need to learn foreign languages, attend conferences, undertake research internships at leading scientific centers, and continuously acquire new knowledge. He pursued this process of mastering the new throughout his entire life”.

Following the abolition of the regional economic councils (Sovnarkhozes) in the USSR in 1962 and the return to a ministerial system, the laboratory was reorganized into an industry-level laboratory of powder metallurgy. Its staff actively improved their qualifications and collaborated closely with leading national and international scientific centers. Invaluable assistance was provided by prominent Soviet powder metallurgy specialists such as V.V. Saklinsky (Research Institute of the Automotive Industry, Moscow) and V.S. Rakovsky (All-Union Institute of Light Alloys, Moscow).

Laboratory staff also gained valuable scientific training through cooperation with the Academy of Sciences of Ukraine, particularly with the Institute for Problems of Materials Science under Academicians I.N. Frantsevich, I.M. Fedorchenko, and V.I. Trofilov, as well as Corresponding Member G.V. Samsonov. Productive and creative collaboration continued with Academicians V.V. Skorokhod, I.V. Novikov, I.K. Pokhodnya, A.G. Kostornov, K.A. Yushchenko, and many others. The laboratory consistently enjoyed strong support from the President of the Academy of Sciences of Ukraine, Academician B.E. Paton, which continued until the very end of his life.

The laboratory's research and development were evaluated by the Collegium of the Ministries of Higher Education of the BSSR and the USSR. By the mid-1960s, it had become one of the leading laboratories in the Soviet Union and, upon the recommendation

of the Collegium, was transformed by Resolution No. 11/34 of the Council of Ministers of the BSSR dated August 11, 1964 into the Problem Laboratory of Powder Metallurgy, designated as the lead laboratory within the USSR Ministry of Higher Education system. It was tasked with conducting theoretical research and assisting industrial enterprises in the republic with implementing powder metallurgy developments in production.

Under the leadership and active involvement of O.V. Roman, the laboratory staff established contacts with both Soviet and foreign scientists. Visitors included researchers from Moscow, Leningrad, and Kyiv, as well as international colleagues such as Kempton Roll, Director of the Metal Powder Industries Federation (USA); Professor Gerhard Bockstiegel (Sweden), a leading specialist with Hoeganaes, the world's largest producer of iron and low-alloy steel powders; Professor Richard Kieffer (Austria), a renowned expert in hard and heavy alloys; and many other distinguished specialists.

These international connections enabled staff from the laboratory and the Department of Metal Technology at BPI to work and train abroad through scientific exchange programs in the USA, Sweden, England, France, Finland, Austria, Italy, and Yugoslavia. They participated in and presented papers at international conferences on powder metallurgy. The laboratory's specialists were not only acquiring knowledge themselves but also sharing it with others. In 1961–1962, they designed and established a powder metallurgy production shop at an electromechanical plant in Riga. On O.V. Roman's initiative, the Eighth All-Union Conference on Professional Methods for Manufacturing Products by Powder Metallurgy was organized and successfully held in Minsk on September 7–10, 1966.

Thanks to O.V. Roman's active work and personal authority, the development of powder metallurgy enjoyed strong support from the republic's leadership, particularly from P.M. Masharov, First Secretary of the Central Committee of the Communist Party of Belorussia, who visited the laboratory on multiple occasions. Significant attention was also given to the field by V.P. Elyutin, USSR Minister of Higher Education, himself a powder metallurgy specialist who headed a department at the Moscow Institute of Steel and Alloys, where many well-known experts in the field worked and continue to work to this day.

In the early 1960s, the Department of Metal Technology at BPI saw its first postgraduate researchers: G.M. Zhdanovich, E.A. Doroshkevich, P.A. Vityaz, V.E. Perelman, V.G. Gorobtsov, A.P. Bogdanov,

L.S. Boginsky, L.N. Afanasyev, V.N. Kovalevsky, and others. They soon successfully defended their Candidate of Technical Sciences dissertations, and later Doctoral dissertations, becoming prominent scientists, specialists, educators, and leaders in research and industry.

All of this led to the adoption of Resolution No. 272 of the Council of Ministers of the BSSR on September 7, 1972, establishing the Research Institute of Powder Metallurgy (RI PM) at BPI on the basis of the Problem Laboratory of Powder Metallurgy. O.V. Roman was appointed Director and immediately raised the issue of building dedicated premises for the institute, including pilot-scale production facilities. The necessary financial resources for construction were secured by Oleg Vladislavovich and his disciples from various USSR ministries through what First Deputy Chairman of the USSR Council of Ministers K.T. Mazurov jokingly referred to as the “passing the hat around”. Considerable support in this matter came from I.M. Glazkov, Deputy Chairman of the Council of Ministers of the BSSR, as well as from A.V. Goryachkin, the republic’s Permanent Representative in Moscow, and his deputy A.Ya. Masalsky.

As a result, the RI PM buildings with pilot-scale production facilities were constructed in Minsk at 41 Platonova Street, along with an experimental field station for impulse-loading applications near Ostroshitsky Gorodok, 18 km from Minsk. Securing funding from USSR ministries, obtaining building quotas, and overseeing their utilization was a complex process. In each ministry, it was necessary to demonstrate that the institute possessed promising developments that would be applied in the interests of that ministry’s enterprises in return for the allocated funds. These issues were addressed collectively by O.V. Roman and his team of disciples and colleagues. The acquisition of modern scientific equipment for research, as well as industrial equipment such as presses and furnaces for producing pilot-scale batches of powder metallurgy products and refining industrial technologies, was also essential. To this end, and at O.V. Roman’s initiative, the first international exhibition on powder metallurgy in the USSR, Powder Metallurgy, was held in Minsk in 1973 – a true test of capabilities on the international stage. By that time, many of his disciples had completed research internships abroad, defended their Candidate dissertations, and were prepared to take on more complex challenges.

In May 1977, the institute’s pilot production building was completed, and it hosted the second highly representative exhibition with the participation of virtually

all major companies in the world engaged in powder metallurgy. At the same time, an international conference was organized, featuring presentations by scientists from Europe, the United States, and the USSR. In subsequent years, such exhibitions, along with their associated international conferences, became a regular event held every four years in Minsk. This helped to strengthen international ties, which have been maintained and continue to develop to this day.

Thanks to these events, the institute was able to acquire, for that time, unique research equipment such as the MS046 X-ray microprobe (Cameca, France), the QUANTIMET-720 image analyzer (Cambridge Instruments, UK), the MiniSEM scanning electron microscope (Japan), and others. Funding for their purchase was secured from the USSR State Committee for Science and Technology (GKNT), taking into account agreements to carry out developments for the benefit of various USSR ministries and industries of the BSSR.

This system of organizing and hosting exhibitions and scientific–practical conferences continued on a regular basis until the dissolution of the USSR. It made it possible to establish at the institute a physical and chemical research center – the best in the USSR – which operated actively then and continues to function successfully today.

Following the first Powder Metallurgy exhibition, the institute intensified its work on applying protective coatings by various methods, developing new materials from powder compositions, and mastering advanced technological processes. Dozens of powder metallurgy and protective coating production sections and shops were established at enterprises in the BSSR, elsewhere in the USSR, and in foreign countries. These activities developed within the framework of the ministries of education of these republics, whose main objectives included training both scientific personnel for research and engineers for industry.

The shortage of specialists in these areas prompted the Ministries of Higher Education of the USSR and the BSSR to decide to establish at BPI a special faculty for the retraining of engineers in powder metallurgy, protective coatings, and composite materials. The educational process was supported by staff from the department and the Research Institute of Powder Metallurgy. To integrate the institute’s research and pilot production capabilities into the educational process, particularly for research projects and practical training, a branch of the department headed by P.A. Vityaz was created. Graduates from universities in Russia, Uzbekistan, Tajikistan, Kazakhstan, and other Soviet republics –

more than 100 specialists in total – completed retraining at this faculty.

In 1978, the BPI established a Department of Materials Research and Testing, which in 1996 became the basis for the creation of the Materials Research and Testing Center. In 1997, this center was accredited by the State Standardization Committee of the Republic of Belarus for technical competence and independence. It focused on conducting certification testing in the field of general materials science. Today, the institute operates a certification body for metallic and non-metallic materials and products made from them, enabling customers to obtain quality certificates in accordance with the National Certification System.

Since powder metallurgy products are used in virtually all industries, and their production requires specialized knowledge of technological processes, it is economically advantageous to create interdepartmental production facilities. In the 1980s, to accelerate the introduction of scientific achievements, associations and scientific–technical complexes were established, bringing together organizations from both science and industry.

The growth of research activities, the creation of new materials and technologies, and the resulting demand from industrial enterprises meant that the pilot production facilities of the Research Institute of Powder Metallurgy, along with the sections created at various plants, could no longer meet industry needs. The institute's leadership began exploring the possibility of building a dedicated powder metallurgy plant. There was no prior experience in constructing such a facility, and at that time very few existed worldwide. This raised the questions of who would design and build the plant, provide financing, and then manage it. The matter was given careful consideration at the governmental level in both the BSSR and the USSR.

At the initiative of O.V. Roman, a meeting was held at the Research Institute of Powder Metallurgy in 1980, attended by P.M. Masharov, First Secretary of the Central Committee of the Communist Party of Belorussia (CPB); I.M. Glazkov, CPB Central Committee member responsible for science and education; A.N. Aksenov, Chairman of the Council of Ministers of the BSSR; G.N. Artyushevsky, Head of the Science and Education Directorate of the Council of Ministers of the BSSR; V.D. Tkachev, Rector of BPI; O.V. Roman, Director of the Research Institute of Powder Metallurgy and Head of the Department, along with his deputies P.A. Vityaz and M.Ya. Kutser.

After reviewing the institute's work and holding a thorough discussion on the creation of a scientific and production association for powder metallurgy, and on the proposal of P.M. Masharov with the agreement of Chairman of the Council of Ministers A.N. Aksenov, and with the support of USSR Academy of Sciences President A.P. Aleksandrov and USSR Minister of Higher Education V.P. Elyutin, a decision was made to establish the Belorussian Research and Production Powder Metallurgy Association (BRPPMA), reporting directly to the Council of Ministers of the BSSR. Oleg Vladislavovich Roman was appointed General Director of the newly created association, while retaining his positions as Director of the institute and Head of the Department. P.A. Vityaz was appointed First Deputy Director-General for Research, and M.Ya. Kutser – Deputy Director-General for Production and Technology Implementation. It should be noted that O.V. Roman's concurrent leadership of the association, the institute, and the department proved highly effective, enabling a focused policy for training engineering and research personnel, carrying out essential R&D with the participation of students and postgraduate researchers, and transferring completed developments into industrial production.

At the same time, by Resolution No. 52 of the Council of Ministers of the BSSR dated February 13, 1980, BPI established a special faculty, New Materials, to train specialists in powder metallurgy, composite materials, and protective coatings. The faculty operated within the framework of the association, with E.A. Doroshkevich appointed as Dean.

The BRPPMA comprised the Research Institute of Powder Metallurgy (its head organization), a Special Design and Technology Bureau with pilot production facilities, an experimental field station (near Ostroshitsky Gorodok), and the planned Molodechno Powder Metallurgy Plant (MolZPM) for manufacturing products from metal powders.

Implementing the resolution required major effort and the resolution of entirely new, complex tasks. It was necessary to design the plant, choose a construction site, and prepare technical specifications for a facility capable of producing 10,000 tons of powder metallurgy products annually for machine-building plants and special-purpose equipment manufacturers across all Soviet republics. All institute laboratories were engaged in these tasks. O.V. Roman insisted that every development of the RI PM be implemented at the plant. By then, the institute had achieved notable results in creating new powder compositions for manufacturing structural, antifriction, friction, and porous products. The specific product range for enterprises in

the BSSR and for various USSR ministries had to be defined. Based on required quantities and specifications, the necessary equipment, production capacities, and operating conditions were determined, forming the basis for the plant's technical specifications.

In managing these efforts, O.V. Roman displayed exceptional organizational skill, delegating responsibilities and ensuring timely, high-quality execution. Not everything went smoothly. One telling example involved selecting the plant site. After extensive searches and numerous meetings, Molodechno was chosen. Working with the Molodechno City Executive Committee, the site was inspected and preparations began for its transfer for construction in autumn 1980. Funding had been secured, and construction quotas allocated with annual distribution over the building period. However, formal land allocation was delayed, and forecasts predicted severe frosts. Oleg Vladislavovich gathered his team, warning that if the topsoil was not removed before the freeze, construction could not start the following year, resulting in the loss of both funding and quotas – an unacceptable outcome. The decision was made to begin site preparation immediately. The work was completed before the frost, even though official land allocation documents had not yet been issued. For this breach of regulations, O.V. Roman and P.A. Vityaz received an official reprimand from the People's Control Committee of the BSSR. Roman's response was characteristically pragmatic:

“They gave the reprimand today, tomorrow it will be lifted, but the important job will have been done. The funds and construction quotas will be used”.

And so it proved.

The choice of Molodechno was driven by restrictions on new industrial construction in Minsk, the availability of local labor, and the supportive attitude of the city's leadership, which greatly accelerated the process.

On January 20, 1981, the directorate for the plant under construction was established, headed by N.P. Ivanov. Work began on the plant itself alongside the simultaneous development of housing for its workforce. The first residential building was occupied by plant employees in 1984.

The plant was built and brought into operation in parallel. In 1982, a section for manufacturing non-standard equipment was set up in temporarily commissioned facilities. By December 1983, construction of the main production building and installation of process equipment had been completed. In January 1984, A.S. Sivets was appointed Plant Director, and

the first phase of the facility, with an annual capacity of 5,000 tons of powder metallurgy products, was commissioned. In March 1984, the first batch of products was manufactured using the full technological cycle – powder mixing, blank compaction, sintering, and calibration. That year, production began for 37 types of structural and antifriction components for MAZ, BelAZ, and ZIL trucks, MTZ tractors, Gomselmash agricultural machinery, and other applications.

In January 1985, the plant mastered titanium nitride protective coating technology for dental prostheses and surgical instruments. Two months later, it launched production of friction discs for tractors and agricultural machinery, expanding the product range to 123 items.

The following year saw the introduction of 104 new products, including filter elements with specified pore size distributions for liquid and gas filtration, phase separation, and sound-damping silencers. In 1986, the plant produced 227 types of filter products for 187 enterprises in Belarus, Ukraine, and the Baltic republics.

In 1987, the plant became the first in the USSR to launch serial production of heat pipes with a capillary-porous structure and heat sinks for cooling high-power semiconductor devices, as well as components made from hard alloys. That year, it reached full design capacity, employing 1,473 people and producing a wide range of structural, antifriction, and porous components. These included commutators for electric machines, friction discs manufactured by free-pouring composite powder onto a steel base, large-diameter friction discs (over 300 mm), and hydraulic pump components made from multicomponent composite materials. The plant's products were supplied not only across the Soviet republics but also to Italy, Poland, Bulgaria, Czechoslovakia, and Germany.

Cooperation with the Council for Mutual Economic Assistance (CMEA) countries developed actively. The Research Institute of Powder Metallurgy played a leading role in multilateral international scientific and technical programs on hydrodynamic pressing of powder materials, porous materials, and protective powder coatings. Meetings of CMEA representatives on these topics were regularly held in Minsk, with institute staff also participating in similar events abroad.

The institute established productive ties with firms, research centers, and organizations in Bulgaria, the German Democratic Republic, Hungary, Poland, Czechoslovakia, and Romania. From 1982, all CMEA member countries shifted this cooperation to a contractual basis. Under this framework, the Research Institute of Powder Metallurgy with Pilot Production Facilities

(Director O.V. Roman, Minsk, USSR) partnered with the Metal Ceramics Scientific and Production Complex (Director R.P. Todorov, Sofia, Bulgaria). Four contracts – two import and two export – were concluded, balanced in both value and cost. As part of these agreements, the RI PM acquired PA-series automatic presses for compacting products of complex shape and an atomization unit for producing powders for wear- and corrosion-resistant coatings, while Bulgaria's NPC MK received a hydrodynamic pressing unit developed by the institute and manufactured at the All-Union Scientific Research Institute MetMash (Moscow), along with equipment for applying protective coatings.

O.V. Roman, together with his disciples, maintained extensive international contacts. Particularly fruitful was cooperation with Indian researchers. Between 1967 and 1969, he worked at the Indian Institute of Technology in Kharagpur, where he lectured and established a powder metallurgy laboratory. For his contribution to the field, his role in training specialists, and his efforts to advance science in India, the Government of India awarded him the Jawaharlal Nehru Prize.

O.V. Roman's connection with India was rooted in both genuine affection for the country and long-standing friendships with influential figures, including Professor A.P.J. Abdul Kalam – the “father” of India's space program and future President of India. At the time, Abdul Kalam worked at the Defence Metallurgical Research Laboratory (DMRL) in Hyderabad. O.V. Roman's visit to DMRL in the early 1980s, and his subsequent collaboration with Abdul Kalam, proved highly productive. This partnership led to an exhibition in Hyderabad in the late 1980s showcasing the achievements of the Academies of Sciences

of the USSR, the Belorussian SSR, and the Ukrainian SSR, during which an agreement was reached to establish the International Center for Powder Metallurgy and New Materials in Hyderabad.

Later, Indian postgraduate students S. Basu and Kumar studied at the Department of Powder Metallurgy at BPI, defending their Candidate of Technical Sciences dissertations at the Research Institute of Powder Metallurgy, where a specialized Dissertation Council for the specialty 05.16.06 “Powder Metallurgy and Composite Materials” had been established in 1986. This council continues to operate to this day. S. Basu went on to earn his doctoral degree and serve as Vice President of Sandvik Asia, the world's largest producer of hard alloys, in Pune, India. Kumar became a professor and now teaches at a university in Delhi.

After the dissolution of the USSR, Russia and Ukraine withdrew from the agreement, leaving the RI PM team, led by O.V. Roman, to carry out the work jointly with DMRL staff. In 1992, another exhibition was held in Hyderabad, and the newly established center was commissioned in cooperation with the Indian side. Active collaboration between RI PM and the center continues today under joint contracts.

The onset of perestroika and the collapse of the USSR brought sharp industrial decline to Belarus and a significant reduction in demand for powder metallurgy products. As the Republic of Belarus became an independent state, adaptation to the new conditions was essential. Thanks to the strong team built by O.V. Roman at the Belarusian Research and Production Powder Metallurgy Association (now the State Research and Production Powder Metallurgy Association, SRPPMA), the organization not only survived but continued to grow. Today it includes



O.V. Roman at the Indian Institute of Technology, Kharagpur, 1968

О.В. Роман в Индийском технологическом институте, г. Харагпур, 1968 г.



O.V. Roman and future President of India (2002–2007) Professor A.P.J. Abdul Kalam, Hyderabad, 1998

О.В. Роман и будущий Президент Индии (2002–2007 гг.) профессор Абдул Калам, г. Хайдарабад, 1998 г.

the O.V. Roman Powder Metallurgy Institute; three self-financing divisions – the Institute of Pulse Processes, the Institute of Welding and Protective Coatings, and the Scientific Instrument Engineering Design Bureau; the state production unitary enterprise Molodechno Powder Metallurgy Plant; and two state enterprises – the Center of Utilization of Aviation Means of Destruction and the Center of Utilization of Artillery and Engineering Ammunition.

O.V. Roman's active stance and ability to connect with people across diverse professional backgrounds earned him respect in both scientific and governmental circles. His relationships with colleagues went beyond formalities – he was deeply responsive to personal hardships and difficulties, often taking a direct role in helping those in need. This human quality, combined with his professional achievements, defines him as much as his scientific legacy.

Through creativity, tireless work, and determination, O.V. Roman founded the field of powder metallurgy in Belarus. What began as a small laboratory within the Department of Metal Technology at BPI grew into the State Research and Production Powder Metallurgy Association. The association reached its peak in 1987, with a staff of 2,727, including 1,254 research personnel – among them 237 research scientists, 4 Doctors of Sciences, and 74 Candidates of Sciences – and 1,473 plant employees. The leadership of SRPPMA has included General Directors O.V. Roman (1980–1993), E.A. Doroshkevich (1993–2003), V.K. Sheleg (2003–2005), and A.Ph. Ilyushchanka (2005–present), as well as Directors of O.V. Roman Powder Metallurgy Institute (1972–1992), P.A. Vityaz (1992–1997), and A.Ph. Ilyushchanka (1997–present).

Under the guidance of O.V. Roman and his disciples – P.A. Vityaz, E.A. Doroshkevich, A.Ph. Ilyushchanka, and V.K. Sheleg – 74 Candidate and 39 Doctoral dissertations were defended. Overall, to date, more than 100 Candidate and 54 Doctoral dissertations have been defended under the leadership of O.V. Roman, his school of disciples, and their academic descendants. Among them are five Corresponding Members of the National Academy of Sciences of Belarus, including three Academicians – O.V. Roman, P.A. Vityaz, and A.Ph. Ilyushchanka. Many of his disciples have gone on to become heads of organizations, department chairs at universities, educators, and creative professionals for whom Oleg Vladislavovich played a decisive role in career choice and life philosophy. From all his disciples – deepest gratitude and everlasting memory. On their initiative, on May 28, 2014, a memorial plaque to Academician O.V. Roman – founder of powder metallurgy in Belarus – was installed on the main facade of the State Research and Production Powder Metallurgy Association and the Powder Metallurgy Institute.

On September 6, 2018, by decision of the Presidium of the National Academy of Sciences of Belarus, the Powder Metallurgy Institute was named after Academician O.V. Roman. In 2020, by decision of the Scientific and Technical Council of the SRPPMA, a prestigious prize bearing his name was established, awarded annually to specialists who have made the most significant contributions to the development of powder metallurgy.

In this commemorative account, we have sought to highlight the role of Academician O.V. Roman as the organizer of the formation and growth of powder



Ceremonial unveiling of the memorial plaque to Academician O.V. Roman on the main building of the Powder Metallurgy Institute, May 28, 2014

Торжественное открытие мемориальной доски академику О.В. Роману на здании главного корпуса Института порошковой металлургии, 28 мая 2014 г.

metallurgy in Belarus, as a teacher who built a school of disciples in powder metallurgy – including protective coatings and the application of impulse loading – a school that continues to function and develop successfully to this day. We have not touched upon the scientific areas and achievements of O.V. Roman and his disciples, which are documented in dozens of monographs, thousands of articles published in domestic and international journals, and hundreds of Author's Certificates and patents. For their scientific and practical achievements, O.V. Roman and his disciples have received numerous national and international prizes

and governmental awards, both in the Soviet period and in the present day.


Oleg Vladislavovich will forever be remembered by his disciples and by those they have trained in turn. We trust that among future generations of researchers working in the fields founded by Academician O.V. Roman and his disciples, his name will endure as a source of inspiration – driving them to achieve outstanding results and to promote the creative, collaborative development of science, education, and industry for the benefit of the Republic of Belarus, the Union State, and international cooperation.

Information about the Authors



Сведения об авторах

Pyotr A. Vityaz – Dr. Sci. (Eng.), Academician of the National Academy of Sciences of Belarus, Professor, Head of the Department of Aerospace Activities of the Apparatus of the National Academy of Sciences of Belarus

 **ORCID:** 0000-0001-9950-2120

 **E-mail:** vitiaz@presidium.bas-net.by

Aleksander F. Ilyushchenko – Dr. Sci. (Eng.), Academician of the National Academy of Sciences of Belarus, Professor, general director of the State Research and Production Association, director of the Institute of Powder Metallurgy n.a. acad. O.V. Roman

 **E-mail:** alexil@mail.belpak.by

Петр Александрович Витязь – д.т.н, профессор, академик НАН Беларуси, начальник управления аэрокосмической деятельности аппарата НАН Беларуси

 **ORCID:** 0000-0001-9950-2120

 **E-mail:** vitiaz@presidium.bas-net.by

Александр Фёдорович Ильющенко – д.т.н, профессор, академик НАН Беларуси, ген. директор ГНПО ПМ, директор Института порошковой металлургии им. акад. О.В. Романа

 **E-mail:** alexil@mail.belpak.by

Received 23.03.2025
Revised 29.04.2025
Accepted 11.05.2025

Статья поступила 23.03.2025 г.
Доработана 29.04.2025 г.
Принята к публикации 11.05.2025 г.



UDC 621.762.8

<https://doi.org/10.17073/1997-308X-2025-4-16-27>

Research article
Научная статья



Iron-based pseudosalloys for antifriction applications with enhanced mechanical and tribological properties developed at the O.V. Roman Powder Metallurgy Institute of the National Academy of Sciences of Belarus

L. N. Dyachkova¹✉, P. A. Vityaz²

¹ State Research Institution O.V. Roman Powder Metallurgy Institute, National Academy of Sciences of Belarus

41 Platonov Str., Minsk 220005, Belarus

² Presidium of the National Academy of Sciences of Belarus

66 Nezavisimosti Prosp., Minsk 220072, Belarus

✉ dyachkova@tut.by

Abstract. The paper presents the results of research carried out at the O.V. Roman Powder Metallurgy Institute (Belarus) on the production of iron-based pseudosalloys for antifriction applications and the development of methods for improving their mechanical and tribological properties. A computational model of parametrically non-stationary high-temperature infiltration was developed, enabling the calculation of pore-filling time and optimization of the pseudosalloy fabrication mode. The features of carbon distribution in the iron skeleton of the pseudosalloy during isothermal holding and subsequent heat treatment under the influence of the copper phase were identified. It was shown that after isothermal holding, the carbon content in the region of the skeleton adjacent to the copper phase is lower than in its center, whereas after quenching and high-temperature tempering, a carbon-enriched zone forms at the interface with the copper phase. The mechanisms responsible for improving the mechanical and tribological properties of pseudosalloys using the developed methods were established. These include: stamping at the optimum temperature; extended holding during high-temperature tempering after quenching; high- and low-temperature thermomechanical treatments under optimized conditions; alloying the iron matrix with nickel or chromium; and structural modification through the introduction of ultradispersed diamonds, ultradispersed aluminum oxide, nanodispersed zirconium oxide, mixtures of nanosized oxides of iron, nickel, and zinc, single- or two-phase aluminides of nickel, iron, or titanium and their composites, calcium molybdate, or hexagonal boron nitride, as well as alloying the infiltrate with tin, nickel, or chromium and the addition of ultradispersed aluminum oxide. The obtained strength, hardness, impact toughness, friction coefficient, limit seizure pressure, wear resistance, and PV parameter values are reported. The wear mechanism of pseudosalloys with enhanced properties was determined. It was demonstrated that during friction, nanoscale porosity and voids form, serving as additional reservoirs for lubricant, thereby improving friction conditions, preventing copper transfer into these areas, reducing the coefficient of friction, and increasing wear resistance.

Keywords: iron-based pseudosalloys, infiltration, structure, phase composition, mechanical properties, tribotechnical properties, heat treatment, thermomechanical treatments, additives

For citation: Dyachkova L.N., Vityaz P.A. Iron-based pseudosalloys for antifriction applications with enhanced mechanical and tribological properties developed at the O.V. Roman Powder Metallurgy Institute of the National Academy of Sciences of Belarus. *Powder Metallurgy and Functional Coatings*. 2025;19(4):16–27. <https://doi.org/10.17073/1997-308X-2025-4-16-27>

Псевдосплавы на основе железа антифрикционного назначения с повышенными механическими и триботехническими свойствами, разработанные в Институте порошковой металлургии имени академика О.В. Романа НАН Беларуси

Л. Н. Дьячкова¹, П. А. Витязь²

¹ Институт порошковой металлургии имени академика О.В. Романа
Беларусь, 220005, г. Минск, ул. Платонова, 41

² Президиум Национальной академии наук Беларуси
Беларусь, 220072, г. Минск, пр-т Независимости, 66

✉ dyachkova@tut.by

Аннотация. Представлены результаты проведенных в Институте порошковой металлургии имени академика О.В. Романа (Беларусь) работ по изучению процессов получения псевдосплавов антифрикционного назначения с каркасом на основе железа и разработке способов повышения их механических и триботехнических свойств. Создана расчетная модель параметрически нестационарной высокотемпературной инфильтрации, позволившая рассчитать время заполнения пор и оптимизировать режим получения псевдосплавов. Выявлены особенности распределения углерода в стальном каркасе псевдосплава при изотермической выдержке и термической обработке из-за воздействия медной фазы. Показано, что после изотермической выдержки содержание углерода в приграничной с медной фазой области стального каркаса меньше, чем в центре, а после закалки и высокотемпературного отпуска на границе с медной фазой образуется область с повышенным содержанием углерода. Установлены механизмы, обеспечивающие повышение механических и триботехнических свойств псевдосплавов на основе железа с помощью разработанных способов: штамповкой при оптимальной температуре; увеличением выдержки при высокотемпературном отпуске после закалки; высоко- и низкотемпературной термомеханической обработкой при оптимальных режимах; легированием стального каркаса никелем или хромом; модифицированием структуры введением ультрадисперсных алмазов, ультрадисперсного оксида алюминия, нанодисперсного оксида циркония, смеси наноразмерных оксидов железа, никеля и цинка, а также алюминидов никеля, железа, титана (однофазных или двухфазных) и композитов на их основе, молибдата кальция или гексагонального нитрида бора; легированием инфильтрата оловом, никелем, хромом и введением в него ультрадисперсного оксида алюминия. Приведены достигнутые значения прочности, твердости, ударной вязкости, коэффициента трения, предельного давления схватывания, износостойкости, параметра PV . Установлен механизм изнашивания псевдосплавов с повышенными свойствами. Показано, что в процессе трения происходит образование наноразмерной пористости и лагун, являющихся дополнительными резервуарами для смазки, что улучшает условия трения, препятствует переносу в эти места меди, обеспечивает снижение коэффициента трения и повышения износостойкости.

Ключевые слова: псевдосплавы на основе железа, инфильтрация, структура, фазовый состав, механические, триботехнические свойства, термическая, термомеханическая обработки, добавки

Для цитирования: Дьячкова Л.Н., Витязь П.А. Псевдосплавы на основе железа антифрикционного назначения с повышенными механическими и триботехническими свойствами, разработанные в Институте порошковой металлургии имени академика О.В. Романа НАН Беларуси. *Известия вузов. Порошковая металлургия и функциональные покрытия*. 2025;19(4):16–27. <https://doi.org/10.17073/1997-308X-2025-4-16-27>

Introduction

This article is dedicated to the memory of Oleg Vladislavovich Roman – the founder of powder metallurgy in Belarus, the first Director of the Powder Metallurgy Institute, and the first General Director of the State Research and Production Powder Metallurgy Association. His main scientific interests included theoretical and experimental studies of impulse processes in materials processing, such as explosive welding. At the same time, he devoted considerable attention to the theory and practice of classical powder

metallurgy processes, in particular, the development of powder-based antifriction materials with enhanced mechanical and tribological properties for components of heavily loaded friction units. The present article continues this line of research.

In heavily loaded friction units operating under high pressures and across a wide temperature range, a thin boundary lubrication film does not adequately protect the surface of sliding bearings from plastic deformation, leading to a marked increase in wear [1]. Therefore, antifriction materials must combine high bulk mechanical strength with stability at operating

temperatures, advanced tribological characteristics, and high thermal conductivity for efficient heat dissipation from the friction zone. They must also exhibit corrosion resistance and oxidation stability at elevated temperatures. Consequently, minimal porosity is a primary requirement.

Powder antifriction materials based on iron have found the widest application in heavily loaded friction units, owing to their high wear resistance and permissible load capacity. To increase their strength, alloying with carbon, copper, manganese, chromium, nickel, molybdenum, and other elements is employed, along with heat treatment and thermochemical treatment [2]. A low coefficient of friction and high wear resistance are achieved by introducing solid lubricants and various solid ultra- or nanosized inclusions (carbides, borides, oxides, glass, intermetallics, etc.) [3]. Porosity reduction methods include plastic deformation processes, hot dynamic or isostatic pressing [4], and sintering in the presence of a liquid phase [5].

A particularly promising method for reducing porosity and enhancing the mechanical, tribological, and thermal conductivity properties is the infiltration of an iron skeleton with copper alloys [6], producing so-called pseudosplloys. In addition to the properties listed above, they are also characterized by high thermal and heat resistance, damping capacity under vibrational loading, resistance to electrical erosion, and thermal stability. Pseudosplloys are used to manufacture both antifriction and structural components.

The aim of this article is to review the studies conducted at the O.V. Roman Powder Metallurgy Institute on the production of iron-skeleton-based antifriction pseudosplloys and the development of methods for improving their mechanical and tribological performance.

Research methodology

The powders of iron, copper, tin, and graphite (commercial grade) were used in the as-received state. The additives introduced to improve the properties are described below. A hydraulic press was employed for compaction, and a continuous furnace with an endogas atmosphere was used for infiltration.

The material structure was examined using a MEF-3 metallographic microscope (Austria) and a high-resolution Mira scanning electron microscope (Czech Republic) equipped with an INCA 350 micro-X-ray spectral analyzer (UK). The phase composition and fine structure were studied on an Ultima IV Rigaku high-resolution diffractometer with a cobalt anode (Japan) under $\text{CuK}\alpha$ radiation. Mechanical properties were determined using standard methods, while tribologi-

cal characteristics were evaluated on an MT-2 friction testing machine at a sliding speed of 2.5–7.0 m/s. Tests were carried out on three samples (10 mm in diameter, 12 mm in height) with a moderate lubricant supply (6–8 drops per minute of industrial oil I-20) directed to the center of the counterbody. The wear of the samples was measured on an optimeter with an accuracy of 0.001 mm. Hardened steel 45 discs (42–45 HRC) were used as the counterbody.

Results and discussion

In studying the processes of pseudalloy fabrication, a computational model of parametrically non-stationary high-temperature infiltration was developed. The model accounts for changes in the structural parameters of the skeleton and in the physical properties of the liquid phase, caused by diffusion, dissolution, and liquid-phase rearrangement of skeleton particles. The model showed that, depending on pore size and infiltrant viscosity, capillary forces fill the pore space with copper alloy within 30–60 s [7]. However, this time is insufficient for the formation of a stable skeleton structure, particularly in the case of unsintered skeletons, which prevents achieving the required material properties. Therefore, isothermal holding at the infiltration temperature was applied. During this process, a homogeneous skeleton structure, the required morphology of the copper phase, and transition layers in the interfacial regions (Fe solid solution in Cu and Cu solid solution in Fe) are formed, and micropores are also filled with copper alloy. These phenomena provide high strength, wear resistance, thermal conductivity, and a low friction coefficient [8; 9], thus confirming the validity of the proposed antifriction material model.

The presence of copper in the pseudalloy significantly affects the formation of the skeleton structure of carbon steel during isothermal holding, especially when infiltrating an unsintered skeleton, where the formation of the Fe–C solid solution and the infiltration process occur simultaneously. As shown previously [10], copper located at the particle boundaries of the skeleton slows down grain-boundary diffusion of carbon into iron and drives carbon deeper into the particles. As a result, the carbon content in the layer adjacent to the copper phase is lower. Micro-X-ray spectral analysis revealed that in the regions of the steel skeleton near the copper infiltrant, the intensity of the carbon signal was more than two times lower than in the center of the steel skeleton (Fig. 1).

The microstructure obtained after infiltration and isothermal holding ensured high performance. Depending on the skeleton composition as well as the composition, content, and morphology of the infil-

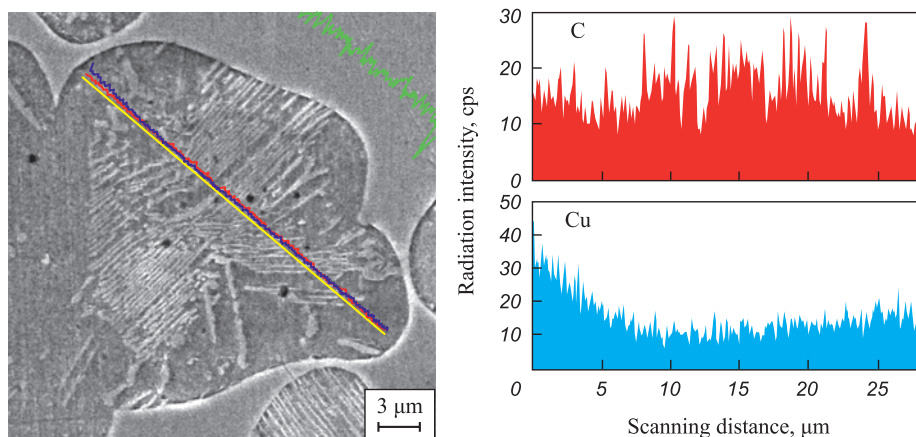


Fig. 1. Microstructure of a section of the steel skeleton of a pseudalloy with a skeleton of grade ZhGr1.2Ms1 (Fe-1.2 % C-1 % Cu), infiltrated with BrO5 bronze (Cu-5 % Sn), and the distribution of carbon and copper

Рис. 1. Структура участка стального каркаса псевдосплава с каркасом состава ЖГр1,2Мс1, инфильтрированным бронзой БрО5, и распределение в нем углерода и меди

rant, the tensile strength was 400–600 MPa, impact toughness 30–40 kJ/m², hardness 140–280 HB, and thermal conductivity 45–79 W/m·K. Under boundary lubrication at $PV = 30\text{--}38 \text{ MPa} \cdot \text{m/s}$, the wear rate was 0.08–0.20 μm/km – more than five times lower than that of dense bronze. The friction coefficient was 0.007–0.009, and the maximum operating temperature reached 800 °C.

To further improve the properties of the pseudalloys, plastic deformation (hot die forging), heat treatment, and thermomechanical treatment were applied. Hot die forging at the optimum temperature of 850–900 °C eliminated residual porosity and increased the tensile

strength to 670–980 MPa, while hardness and impact toughness rose by a factor of 1.5–2.5 [11].

After quenching, depending on the copper-phase content, maximum strength was achieved at tempering temperatures of 550–650 °C (Fig. 2) [12]. Extending the holding time to 3 h at these temperatures further increased the hardness of the pseudalloys, particularly those with a higher copper content. This effect is attributed to aging in the copper phase due to the precipitation of Fe₄Cu₃ intermetallic and copper-tin compounds (Table 1). As a result, the microhardness of the infiltrant phase increased from 1450 to 1750 MPa. At high-temperature tempering, carbon diffuses into the more

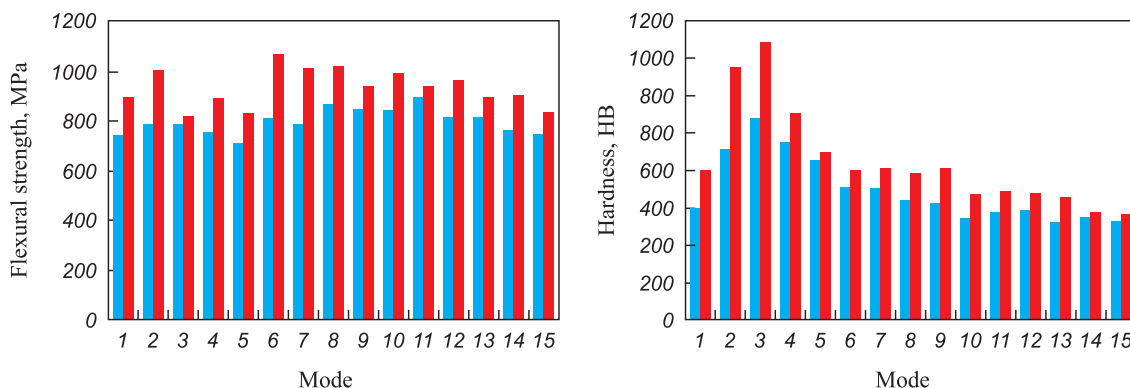


Fig. 2. Effect of heat treatment modes (1–15) on the properties of a pseudalloy with a skeleton of PK80 (Fe-0.8 % C) steel infiltrated with BrO5 bronze

■ – skeleton density 75 %; ■ – 85 %;
1 – infiltration; 2 – quenching; 3 – tempering at $t = 200 \text{ °C}$ (3); 300 °C (4); 400 °C (5); 500 °C, 1 h (6); 500 °C, 3 h (7); 550 °C, 1 h (8); 550 °C, 3 h (9); 600 °C, 1 h (10); 600 °C, 3 h (11); 650 °C, 1 h (12); 650 °C, 3 h (13); 700 °C, 1 h (14); 700 °C, 3 h (15)

Рис. 2. Влияние режимов (1–15) термообработки на свойства псевдосплава с каркасом из стали ПК80, инфильтрированным бронзой БрО5

■ – плотность каркаса 75 %; ■ – 85 %;
1 – инфильтрация; 2 – закалка; 3–15: отпуск при $t = 200 \text{ °C}$ (3); 300 °C (4); 400 °C (5); 500 °C, 1 ч (6); 500 °C, 3 ч (7); 550 °C, 1 ч (8); 550 °C, 3 ч (9); 600 °C, 1 ч (10); 600 °C, 3 ч (11); 650 °C, 1 ч (12); 650 °C, 3 ч (13); 700 °C, 1 ч (14); 700 °C, 3 ч (15)

Table 1. Phase composition of material with a PK80 steel skeleton infiltrated with a Cu–Sn alloy, depending on heat treatment conditions

Таблица 1. Зависимость фазового состава материала с каркасом из стали ПК80, инфильтрированным медно-оловянным сплавом, от режимов термической обработки

Heat treatment mode	Content, wt. %								
	α' -Fe (quenched martensite)	α -Fe (tempered martensite)	γ -Fe	Fe_3C	Fe_2C	Fe_4Cu_3	Cu α -(Cu ₃ Sn)	η -Cu ₆ Sn ₅	δ -Cu ₃ Sn ₈
Quenching	21	35	12	13	–	–	14	–	5
Tempering – 200 °C	15	29	8	20	–	–	25	–	3
Tempering – 550 °C, 1 h	12	42	5	15	6	4	13	3	–
Tempering – 550 °C, 3 h	13	50	3	12	1	2	14	5	–

defect-rich region adjacent to the copper phase, forming a carbon-enriched layer (visible as a dark rim in Fig. 3). In high-carbon steel skeletons, carbon segregation within the grain interior was less pronounced. The microhardness in the particle center was 3030 MPa, while in the dark rim zone it reached 4120 MPa.

The formation of a two-layer structure in the pseudoalloy skeleton after heat treatment, together with aging of the copper phase, enhanced not only the mechanical but also the tribological properties. The seizure pressure doubled, wear resistance increased by more than 2.5 times, and the PV parameter rose by 1.5–1.7 times.

Application of thermomechanical treatment (TMT) further improved the properties of the pseudoalloys [13]. Deformation during TMT was carried out by free upsetting on a mechanical press with a strain of $\varepsilon = 30, 45$, and 65 % at 900 and 700 °C (high-temperature thermomechanical treatment, HTMT) and at 550 °C (low-temperature thermomechanical treatment, LTMT). Heating was performed by high-frequency currents, and quenching after deformation

was carried out in water. At HTMT with 900 °C and a strain of 65 %, samples fractured due to high stress levels at the Fe–Cu interphase boundaries. At HTMT at 700 °C, softening was less pronounced: the structure retained a well-developed polygonal substructure of deformed austenite, which ensured higher strength.

The greatest strengthening was achieved with LTMT (Fig. 4), owing to hardening not only of the steel phase (formation of a two-layer structure within grains, increased dislocation density, and development of a cell-polygonal substructure) (Table 2), but also of the copper phase through aging.

During TMT, macrotexture formation, structural refinement in the steel skeleton, and the development of an even more pronounced gradient structure compared with heat treatment were observed (Fig. 5).

The wear resistance of the pseudoalloy after HTMT at 700 °C increased by 1.5 times at $\varepsilon = 45$ % and by 2.0 times at $\varepsilon = 65$ %. The seizure pressure

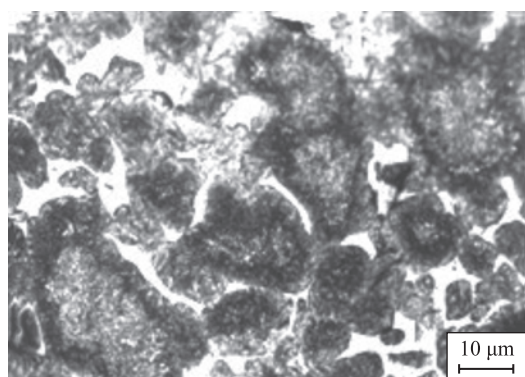


Fig. 3. Microstructure of a pseudoalloy with a skeleton of PK80 steel infiltrated with BrO5 bronze after quenching and tempering at 550 °C for 3 h

Рис. 3. Структура псевдосплава с каркасом из стали ПК80, инфильтрированным бронзой БрО5, после закалки и отпуска при $t = 550$ °C, $\tau = 3$ ч

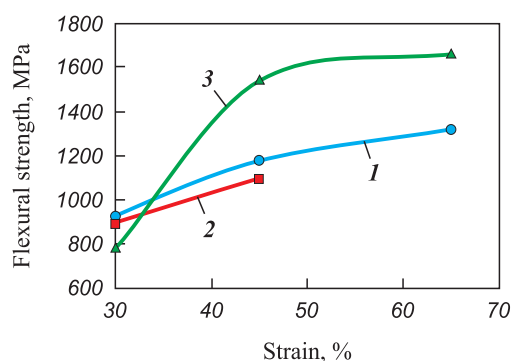


Fig. 4. Effect of strain and deformation temperature during TMT on the strength of a pseudoalloy with a skeleton of 80 % density made of PK80N4M (Fe–0.8 % C–4 % Ni–Mo) steel, infiltrated with BrO5 bronze
Deformation temperature: 700 °C (1), 900 °C (2), 550 °C (3)

Рис. 4. Влияние степени и температуры деформации при ТМО на прочность псевдосплава с каркасом плотностью 80 % из стали ПК80Н4М, инфильтрированным БрО5
Температура деформации при 700 °C (1), 900 °C (2), 550 °C (3)

Table 2. Fine-structure parameters of the skeleton of PK80N4M steel in the initial state and after low-temperature thermomechanical treatment**Таблица 2. Параметры тонкой структуры каркаса из стали ПК80Н4М псевдосплава в исходном состоянии и после низкотемпературной термомеханической обработки**

Treatment condition	(hkl)	Coherent scattering domain size, Å	Relative root-mean-square microstrain ($\langle E^2 \rangle^{1/2}$), $\cdot 10^{-4}$	Dislocation density $\times 10^8$, $1/\text{cm}^2$	Integral line width $\beta_{1/2}$, deg	Lattice parameter a , Å
After infiltration	(110) (220)	208 ± 8	1.69 ± 0.37	0.4375	0.0565	2.8732
After LTMT with $\varepsilon = 45\%$	(110) (220)	201 ± 8	8.44 ± 3.46	10.2875	0.2830	2.8695
After LTMT with $\varepsilon = 65\%$	(110) (220)	177 ± 2	24.32 ± 14.08	71.7391	0.8127	2.8681

increased by 1.9 and 2.1 times, respectively. After LTMT at 550 °C, wear resistance increased threefold at $\varepsilon = 45\%$ and fourfold at $\varepsilon = 65\%$, while the seizure pressure increased by 2.4 and 2.5 times, respectively. The PV parameter after TMT was 1.8–1.9 times higher than without treatment.

A key advantage of iron-based antifriction pseudosalloys obtained by infiltration with copper alloys followed by isothermal holding is the ability to tailor their properties by varying:

– the composition of the skeleton through alloying, microalloying, and the introduction of additives of different types;

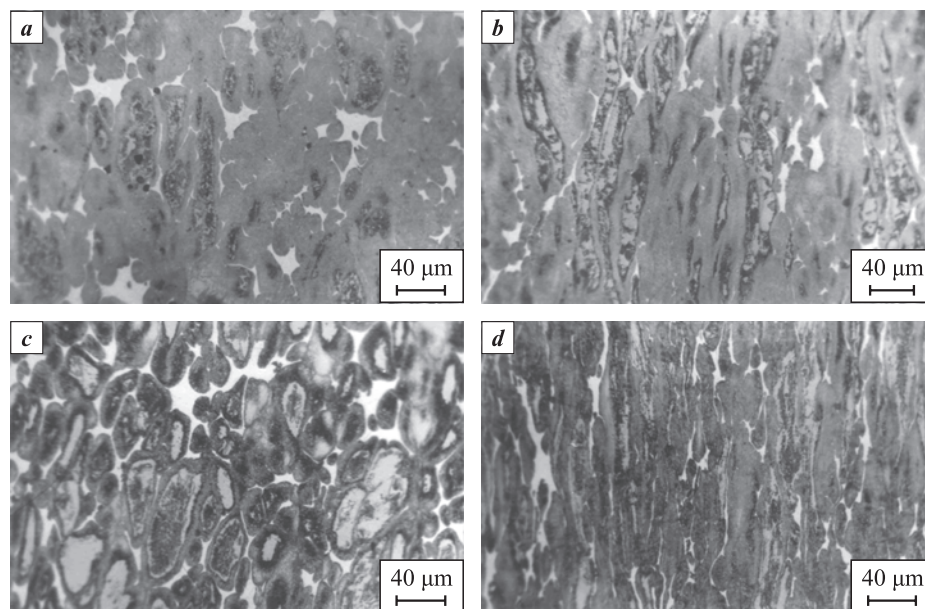
– the composition of the infiltrant by alloying;

– the copper-phase content, which is determined by the initial porosity of the skeleton;

– the morphology of the copper phase, which depends on the type of skeleton used – either a sintered skeleton with well-developed interparticle contacts or an unsintered skeleton with more defective contacts;

– the duration of isothermal holding after infiltration.

Studies of wear intensity showed that the wear resistance of the pseudalloy was 3.0–3.5 times higher than that of sintered steel of the same composition as the pseudalloy skeleton [14; 15]. Micro-X-ray spect-

**Fig. 5. Microstructure of a pseudalloy with a skeleton of PK80N4M steel infiltrated with BrO5 bronze after HTMT at 700 °C (a, b) and LTMT at 550 °C (c, d)**

a, c – strain $\varepsilon = 45\%$; b, d – strain $\varepsilon = 65\%$

Рис. 5. Структура псевдосплава с каркасом из стали ПК80Н4М, инфильтрированным бронзой БрО5, после ВТМО при $t = 700\text{ °C}$ (a, b) и НТМО при 550 °C (c, d)

a, c – степень деформации 45 %; b, d – 65 %

ral analysis of worn counterbody surfaces paired with pseudalloys revealed that copper content reached 6–7 % due to selective mass transfer. The worn surfaces of pseudalloys were homogeneous, without signs of erosion (Fig. 6, *a*), and exhibited a spongy-capillary structure (Fig. 6, *b*). Three-dimensional images (Fig. 6, *c*, *d*) revealed the formation of nanoscale voids that act as additional lubricant reservoirs, improving friction conditions and preventing copper transfer into these areas. Copper was located only on the protrusions of the voids.

Surface roughness studies of sintered and infiltrated samples showed that the initial roughness parameters differed by 30–40 %. After testing, vertical roughness parameters decreased 3.5–4.0 times for sintered materials and threefold for infiltrated materials [16; 17].

A significant increase in the strength of the steel skeleton was achieved by the introduction of:

- 2 and 4 %¹ Ni or 3 % Cr [18];
- 0.2–1.0 % ultradispersed diamond (UDD) [19];
- 0.5–0.8 μm Al_2O_3 and 100–200 nm ZrO_2 powders [20; 21];
- mechanically activated mixture of 300–500 nm Fe_2O_3 with 40–70 nm NiO and ZnO [22];
- single-phase aluminides (Ni_3Al , Ti_3Al , Fe_3Al), and two-phase aluminides ($(\text{Al}_3\text{Ni}-\text{Al}_3\text{Ni}_2)$, $(\text{TiAl}_2-\text{TiAl}_3)$, $(\text{Fe}_2\text{Al}_5-\text{FeAl}_3)$);

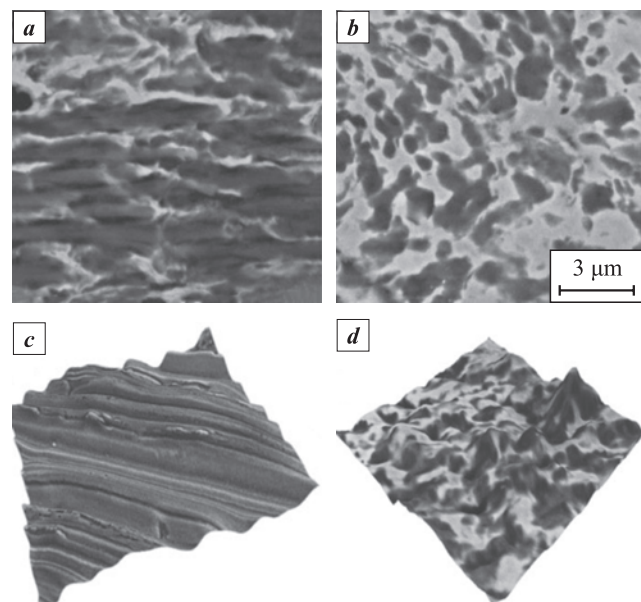


Fig. 6. Worn surfaces of samples made of sintered (*a*, *c*) and infiltrated (*b*, *d*) material

Рис. 6. Изношенные поверхности образцов из спеченного (*a*, *c*) и инфильтрованного (*b*, *d*) материалов

¹ Here and throughout the text, wt. % is implied.

• TiCrAl, NiTiAl, and FeMo/TiB₂ composites obtained by SHS with preliminary mechanical activation [10; 23];

- 3–5 μm CaMoO_4 ;
- 2–8 μm hexagonal BN [24].

When ultradispersed mixtures of Al_2O_3 and ZrO_2 oxides were added, strength, fracture toughness (from 31 to 40–43 $\text{MPa}\cdot\text{m}^{1/2}$), total fracture energy (from $1.7\cdot 10^5$ to $(1.8-1.93)\cdot 10^5$ J/m^2), and skeleton hardness (*HV*) (from 680–965 to 1100–1230 MPa) increased. This strengthening was attributed not only to grain refinement of the skeleton but also to the effect of ZrO_2 nanoparticles at grain boundaries (Table 3). The most pronounced increase in strength of both iron and carbon steel (flexural strength increased by 50–100 MPa and compressive yield strength by 350–500 MPa) was observed when 0.5 % of the Fe–Ni–Zn oxide mixture was added (Table. 3).

The dependence of strength on microadditive content was parabolic, with an optimum range of 0.2–0.5 %.

The greatest strengthening of powder steel, by a factor of 1.2–1.5, is achieved with the introduction of nanosized particles that form a denser, defect-free contact with the matrix. Micro-X-ray spectral analysis showed that the introduced dispersed particles are located mainly along grain boundaries, where they retard collective recrystallization and promote grain refinement. The increase in strength of powder steel with the addition of 0.5 wt. % chromium boride is further explained by the fact that, during sintering, its particles interact with the iron matrix to form complex borides, and, by reacting with carbon, they form chromium carboborides.

Table 3. Compressive strength of sintered iron and PK80 steel with ultradispersed additives (sintered in endogas atmosphere)

Таблица 3. Предел прочности при сжатии спеченного железа и стали ПК80 с ультрадисперсными добавками (спекание в эндогазе)

Material	σ_c , MPa
Fe	2020
PK80	3100 ($\sigma_f = 220$)
Fe + 0.5 % UDD	3200
PK80 + 0.5 % Al_2O_3	4340
PK80 + 0.5 % (Al_2O_3 + 20 % ZrO_2)	4540
PK80 + 0.5 % CrB_2	4320
PK80 + 1.0 % CrB_2	3460
Fe + 0.5 % ($\text{Fe}_3\text{Ni}_2\text{Zn}_0$)	3560
PK80 + 0.5 % ($\text{Fe}_3\text{Ni}_2\text{Zn}_0$)	4250
PK80 + 0.5 % CaMoO_4	$\sigma_f = 275$

The introduction of nickel, titanium, and iron aluminides also enhances strength and hardness by significantly refining the structure, with the degree of refinement depending on the quantity and composition of the additive. The most pronounced strengthening is obtained with 0.2–0.5 % FeMo/TiB₂ or up to 5 % FeAl/Al₂O₃, as well as with two-phase iron aluminide and both single- and two-phase nickel aluminides. The strengthening effect of FeAl/Al₂O₃ is attributed to the formation of alloyed regions with an austenitic structure, whereas FeMo/TiB₂ promotes the formation of molybdenum solid solutions in iron and complex borides (TiFeMo)B₂. These borides exhibit a coherent interface with the iron matrix through transitional layers with variable element concentrations between the matrix and the aluminide particle.

Nickel aluminides increase strength more effectively (by a factor of 1.5–2.0) compared to titanium aluminides, while iron aluminide additions are even more effective. The strongest strengthening occurs with the introduction of intermetallics having lower melting points or polymorphic transformation temperatures (Ni₃Al, Fe₂Al₅–FeAl₃, TiAl₂–TiAl₃). Tribological tests showed that aluminide additions reduce the friction coefficient of powder steel and significantly increase its seizure pressure (Figs. 7 and 8). The most effective additives in this regard were two-phase nickel and iron aluminides.

Examination of powder steel without aluminide additions revealed wide seizure bands on the wear sur-

face (Fig. 9, *a*). With aluminide additions, the surface was smooth (Fig. 9, *b, c*). In this case, micropores were formed on the surface, which gradually developed into voids acting as additional micro-reservoirs for lubricant, thereby increasing wear resistance, as confirmed by micro-*X*-ray spectral analysis (Fig. 9, *d*).

The introduction of calcium molybdate or hexagonal boron nitride increased the strength and wear resistance of powder carbon steels by ~30 %. In the first case, the effect was associated with the formation of CaO precipitates during CaMoO₄ decomposition, which promoted structural refinement, while in the second case it was due to the formation of carboborides. Even greater effects of CaMoO₄ and BN were observed in high-chromium steels: the maximum increase in strength was 34 % in the first case and 2.1-fold in the second [24].

The gas atmosphere also influences infiltration processes and the properties of iron-based pseudosalloys. Increasing the hydrogen content in endogas slowed infiltration due to a reduction in the surface tension of the copper alloy. Introducing 25–50 % nitrogen into the endogas reduced the hydrogen and oxidizing components, which promoted a more uniform distribution of the copper phase in the pseudalloy and improved strength [25].

During contact infiltration, diffusion interaction of the iron skeleton with the compacted copper alloy caused erosion of the skeleton surface. To prevent this, specific additives to the infiltrant were developed and applied [10].

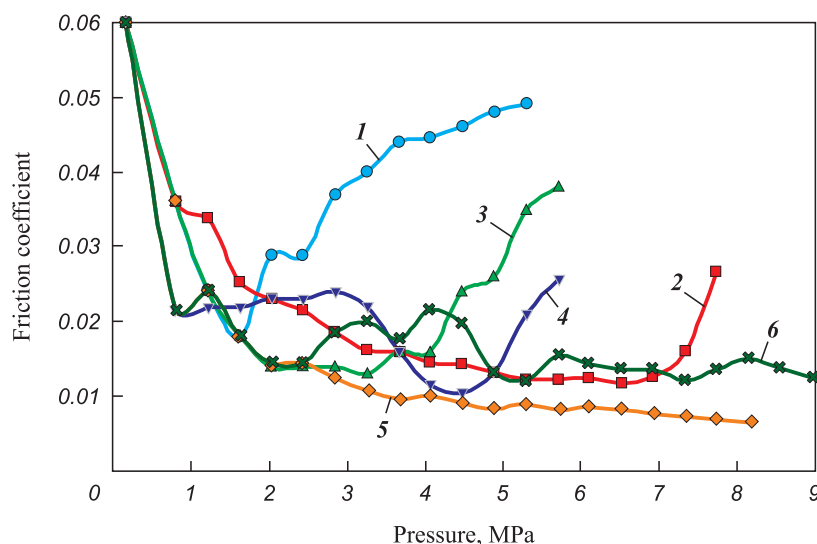


Fig. 7. Dependence of the friction coefficient of PK40 (Fe–0.31–0.6 % C) powder steel with additions of single phase and two phase nickel aluminides on pressure

1 – without additive; 2 – 0.2 % Ni₃Al; 3 – 0.5 % Ni₃Al; 4 – 1 % Ni₃Al; 5 – 0.2 % Ni₅Al₃–NiAl; 6 – 1 % Ni₅Al₃–NiAl

Рис. 7. Зависимость коэффициента трения порошковой стали ПК40 с добавками однофазных и двухфазных алюминидов никеля от давления

1 – без добавки; 2 – 0,2 % Ni₃Al; 3 – 0,5 % Ni₃Al; 4 – 1 % Ni₃Al; 5 – 0,2 % Ni₅Al₃–NiAl; 6 – 1 % Ni₅Al₃–NiAl

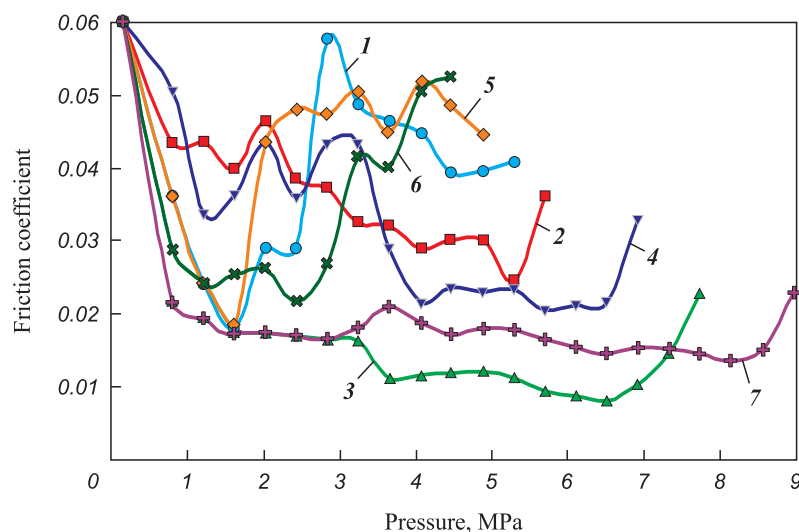
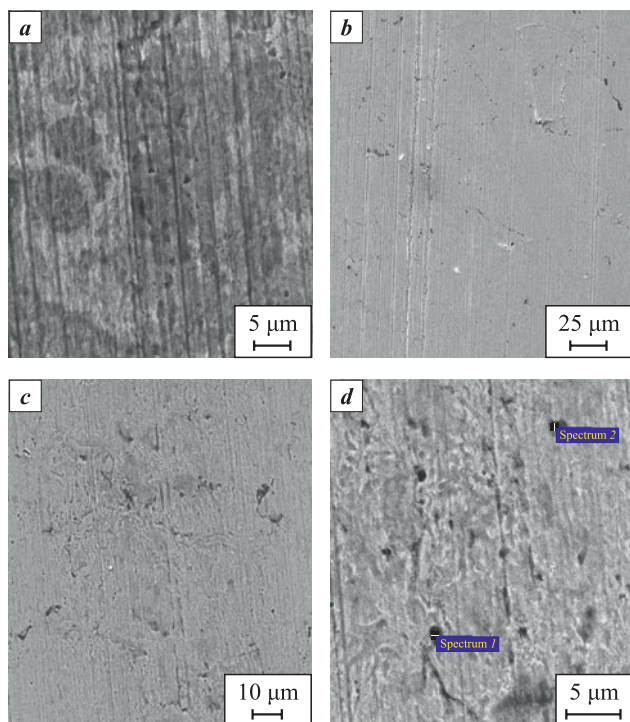


Fig. 8. Dependence of the friction coefficient of PK40 powder steel with additions of single phase and two phase iron aluminides on pressure

1 – without additive; 2 – 0.2 % Fe_3Al ; 3 – 0.5 % Fe_3Al ; 4 – 1 % Fe_3Al ; 5 – 0.2 % $\text{Fe}_2\text{Al}_5\text{-FeAl}_3$; 6 – 0.5 % $\text{Fe}_2\text{Al}_5\text{-FeAl}_3$; 7 – 1 % $\text{Fe}_2\text{Al}_5\text{-FeAl}_3$

Рис. 8. Зависимость коэффициента трения порошковой стали ПК40 с добавками однофазных и двухфазных алюминидов железа от давления

1 – без добавки; 2 – 0,2 % Fe_3Al ; 3 – 0,5 % Fe_3Al ; 4 – 1 % Fe_3Al ; 5 – 0,2 % $\text{Fe}_2\text{Al}_5\text{-FeAl}_3$; 6 – 0,5 % $\text{Fe}_2\text{Al}_5\text{-FeAl}_3$; 7 – 1 % $\text{Fe}_2\text{Al}_5\text{-FeAl}_3$



Spectrum	C + O, %	Al, %	P, S, Ca, %	Fe, %
1	36.6	6.9	8.4	balance
2	24.2	0.3	3.7	balance

Fig. 9. Worn surfaces of PK40 powder steel with and without intermetallic additions

a – without additive; b – $\text{Ni}_5\text{Al}_3\text{-NiAl}$; c, d – $\text{Fe}_2\text{Al}_5\text{-FeAl}_3$

Рис. 9. Поверхности износа порошковой стали ПК40 с добавкой интерметаллидов и без нее

a – без добавки; b – $\text{Ni}_5\text{Al}_3\text{-NiAl}$; c, d – $\text{Fe}_2\text{Al}_5\text{-FeAl}_3$

In the production of pseudalloys by infiltration of unsintered skeletons, methods were developed to accelerate diffusion processes in order to obtain a homogeneous skeleton structure and, consequently, higher strength. These methods are based on the introduction of high-molecular compounds derived from polypropylene glycol (poly(diethylene glycol adipate), polypropylene glycol adipate, polypropylene glycol succinate, polypropylene glycol sebacinate) and on the use of alkali metal compounds (sodium, lithium). The latter promote the formation of atomic carbon through redox reactions during their decomposition in the heating process [10]. The most pronounced activation of diffusion of both carbon and alloying elements into iron was achieved by the introduction of alkali metal bicarbonates.

A study of the diffusion coefficient of carbon in iron, performed by radiometric analysis using the radioactive isotope C-14 (in the form of $\text{BaC}^{14}\text{O}_3$ or elemental C-14) and the integral residue method, showed that the addition of sodium bicarbonate nearly doubled the diffusion coefficient of carbon. Transmission electron microscopy of foils in secondary and Auger electrons revealed that sodium formed nanodispersed ferrite-type compounds $\text{Na}_3\text{Fe}_5\text{O}_9$. Owing to their strong affinity for grain boundaries and structural heterogeneities, thereby hindering collective recrystallization and promoting the formation of a fine-grained structure. In addition, because of its high affinity for metalloids, sodium interacted with impurities. Sulfur,

phosphorus, and silicon were detected at sodium-rich sites. This promoted the removal of impurity segregations from grain boundaries, thereby strengthening intergranular cohesion and increasing the strength of powder steels by a factor of 1.4–1.5.

The mechanical and tribological properties of iron-based pseudosalloys were improved not only by modifying the skeleton composition but also by alloying the infiltrant with Sn, Ni, Cr, or Pb, as well as by introducing Al_2O_3 particles with a dispersion of 400–700 nm [26].

All developed pseudosalloy compositions and processing modes for producing friction unit components have been patented.

Conclusion

The processing modes for iron-based pseudosalloys and the methods for improving their mechanical and tribological performance, developed at the O.V. Roman Powder Metallurgy Institute (Minsk, Belarus), provided the property levels required for reliable operation in heavily loaded friction units. A computational model of parametrically non-stationary high-temperature infiltration was proposed, which accounted for structural changes and property variations of the interacting phases. This model enabled calculation of pore-filling times and optimization of infiltration parameters, including the use of extended isothermal holding.

It was shown that the copper phase plays a key role in structure formation within the steel skeleton of pseudosalloys during isothermal holding, heat treatment, and thermomechanical treatment. After isothermal holding, the carbon content near the copper phase was 0.2–0.4 % lower than in the central regions of the skeleton. Following quenching and high-temperature tempering, a carbon-enriched layer formed at the Fe–Cu interface.

A comprehensive set of approaches was developed to enhance the mechanical and tribological properties of iron-based pseudosalloys, and the mechanisms responsible for these improvements were identified. Increases in strength, hardness, impact toughness, seizure pressure, wear resistance, and PV parameter, along with a reduction in the friction coefficient, were achieved through the following measures:

- hot die forging at the optimum temperature (850–900 °C);
- extended tempering (550–650 °C) after quenching;
- HTMT at 700 °C with strain $\varepsilon = 45\text{--}65\%$ or LTMT at 550 °C with $\varepsilon = 45\%$;
- alloying of the steel skeleton with 2–4 wt. % Ni or Cr;

– structural modification by introducing 0.2–1.0 wt. % ultradispersed diamond (UDD), ultradispersed Al_2O_3 (0.5–0.8 μm) or ZrO_2 (100–200 nm), and mechanically activated mixtures of nanosized Fe (300–500 nm), Ni, and Zn oxides (40–70 nm);

– additions of single-phase aluminides (Ni_3Al , Ti_3Al , Fe_3Al), two-phase aluminides (Al_3Ni – Al_3Ni_2 , TiAl_2 – TiAl_3 , Fe_2Al_5 – FeAl_3), and composites based on TiCrAl, NiTiAl, and FeMo/TiB₂, intermetallics obtained by SHS with mechanical activation;

– additions of CaMoO_4 (3–5 μm) or hexagonal BN (2–8 μm);

– alloying of the infiltrant with Sn, Ni, or Cr, and introducing 3–5 wt. % ultradispersed Al_2O_3 (400–700 nm).

The wear mechanism of pseudosalloys with enhanced properties was also established. During friction, nanoscale porosity and voids form, serving as additional lubricant reservoirs. These structural features improve lubrication, hinder copper transfer into the contact zone, reduce friction, and increase wear resistance.



References / Список литературы



1. Garkunov D.N. Tribotechnics (wear and wear-free). Moscow: Moscow Agricultural Academy, 2001. 616 p. (In Russ.).
Гаркунов Д.Н. Триботехника (износ и безызносность). М.: МСХА, 2001. 616 с.
2. Fedorchenko I.M., Frantsevich I.N., Radomyselsky I.D., Kovalchenko M.S., Kisly P.S., Kosolapova T.Ya., May V.K., Shcherban N.I. Powder metallurgy, materials, technology, properties, areas of application: Handbook. Kyiv: Naukova Dumka, 1985. 624 p. (In Russ.).
Федорченко И.М., Францевич И.Н., Радомысельский И.Д., Ковальченко М.С., Кислый П.С., Косолапова Т.Я., Май В.К., Щербань Н.И. Порошковая металлургия, материалы, технология, свойства, области применения: Справочник. Киев: Наукова думка, 1985. 624 с.
3. Savich V.V., Oglezneva S.A. Powder metallurgy: current state and development prospects. Perm: Publishing house of Perm National Research Polytechnic University, 2021. 695 p. (In Russ.).
Савич В.В., Оглезнева С.А. Порошковая металлургия: Современное состояние и перспективы развития. Пермь: Изд-во ПНИПУ, 2021. 695 с.
4. Dorofeev Yu.G. Dynamic hot pressing of porous powder blanks. Moscow: Metallurgiya, 1977. 216 p. (In Russ.).
Дорофеев Ю.Г. Динамическое горячее прессование пористых порошковых заготовок. М.: Металлургия, 1977. 216 с.
5. Eremenko V.N., Naidich Yu.V., Lavrinenko P.A. Sintering in the presence of a liquid metal phase. Kyiv: Naukova Dumka, 1968. 123 p. (In Russ.).

- Еременко В.Н., Найдич Ю.В., Лавриненко П.А. Спекание в присутствии жидкой металлической фазы. Киев: Наукова думка, 1968. 123 с.
6. Tuchinsky L.I. Composite materials obtained by impregnation. Moscow: Metallurgiya, 1986. 208 p. (In Russ.).
Тучинский Л.И. Композиционные материалы, получаемые методом пропитки. М.: Металлургия, 1986. 208 с.
7. Dyachkova L.N., Vityaz P.A., Leonov A.N., Dechko M.M. Regularities of high-temperature infiltration in the production of antifriction materials of the iron-copper system. *Doklady Natsional'noi akademii nauk Belarusi*. 2012;56(4):103–110. (In Russ.).
Дьячкова Л.Н., Витязь П.А., Леонов А.Н., Дечко М.М. Закономерности высокотемпературной инфильтрации при получении антифрикционных материалов системы железо–медь. *Доклады Национальной академии наук Беларуси*. 2012;56(4):103–110.
8. Dyachkova L.N., Vityaz P.A. The structure and properties formation in iron-carbon powder composite materials during infiltration. *Metal Powder Report Journal*. 2019;24(2):90–94.
<https://doi.org/10.1016/j.2018/12/078>
9. Dyachkova L.N., Vityaz P.A. Regularities of formation of the structure of pseudoalloys of the powder steel–copper alloy system obtained by infiltration. *Doklady Natsional'noi akademii nauk Belarusi*. 2012;56(5):106–114. (In Russ.).
Дьячкова Л.Н., Витязь П.А. Закономерности формирования структуры псевдосплавов системы порошковая сталь – медный сплав, получаемых инфильтрацией. *Доклады Национальной академии наук Беларуси*. 2012;56(5):106–114.
10. Dyachkova L.N. Iron-based powder materials with enhanced mechanical and tribotechnical properties. Minsk: Belarusian Science, 2020. 203 p. (In Russ.).
Дьячкова Л.Н. Порошковые материалы на основе железа с повышенными механическими и триботехническими свойствами. Минск: Белорусская наука, 2020. 203 с.
11. Dyachkova L.N. Peculiarities of hardening of steel – copper alloy pseudo-alloys obtained by infiltration during hot plastic deformation. *Izvestiya Natsional'noi akademii nauk Belarusi. Seriya fiziko-tekhnikeskikh nauk*. 2022;67(2):156–166. (In Russ.).
<https://doi.org/10.29235/1561-8358-2022-67-2-156-166>
Дьячкова Л.Н. Закономерности упрочнения псевдосплавов сталь – медный сплав, получаемых инфильтрацией, при горячей пластической деформации. *Известия Национальной академии наук Беларуси. Серия физико-технических наук*. 2022;67(2):156–166.
<https://doi.org/10.29235/1561-8358-2022-67-2-156-166>
12. Dyachkova L.N. Influence of heat treatment on the structure and properties of pseudo-alloy steel – copper alloy obtained by infiltration. *Izvestiya Natsional'noi akademii nauk Belarusi. Seriya fiziko-tekhnikeskikh nauk*. 2022;67(1):27–38. (In Russ.).
<https://doi.org/10.29235/1561-8358-2022-67-1-27-38>
- Дьячкова Л.Н. Влияние термической обработки на структуру и свойства псевдосплава сталь–медный сплав, получаемого инфильтрацией. *Известия Национальной академии наук Беларуси. Серия физико-технических наук*. 2022;67(1):27–38.
<https://doi.org/10.29235/1561-8358-2022-67-1-27-38>
13. Dyachkova L.N., Vityaz P.A., Zverko A.A. Features of structure formation in antifriction composite powder infiltrated with copper alloy material based on iron (pseudoalloy) under high-temperature thermomechanical treatment. *Izvestiya Natsional'noi akademii nauk Belarusi. Seriya fiziko-tekhnikeskikh nauk*. 2023;68(3):196–207. (In Russ.).
<https://doi.org/10.29235/1561-8358-2023-68-3-196-207>
Дьячкова Л.Н., Витязь П.А., Зверко А.А. Особенности структурообразования в антифрикционном композиционном порошковом инфильтрированном медным сплавом материале на основе железа (псевдосплаве) при высокотемпературной термомеханической обработке. *Известия Национальной академии наук Беларуси. Серия физико-технических наук*. 2023;68(3):196–207.
<https://doi.org/10.29235/1561-8358-2023-68-3-196-207>
14. Dyachkova L.N., Kerzhentseva L.F., Markova L.V. Iron-based powder materials. Minsk: Tonpik, 2004. 228 p. (In Russ.).
Дьячкова Л.Н., Керженцева Л.Ф., Маркова Л.В. Порошковые материалы на основе железа. Минск: ОДО «Тонпик», 2004. 228 с.
15. Dyachkova L.N., Feldshtein E.E. Microstructures, strength characteristics and wear behavior of the Fe-based P/M composites after sintering or infiltration with Cu–Sn alloy. *Journal of Materials Science & Technology, China*. 2015;31(12):1226–1231.
<https://doi.org/10.1016/j.jmst.2015.10.007>
16. Dyachkova L.N., Feldshtein E.E. Morphology of worn surfaces of iron–graphite materials sintered or infiltrated with tin bronze. *Journal of Friction and Wear*. 2015;36(5):395–399.
<https://doi.org/10.3103/S1068366615050037>
17. Feldshtein E.E., Dyachkova L.N. Wear minimization for highly loaded iron-based MMCs due to the formation of spongy-capillary texture on the friction surface. *Wear*. 2020;444–445:203161.
<https://doi.org/10.1016/j.wear.2019.203161>
18. Dyachkova L.N., Kerzhentseva L.F., Vityaz P.A. Effect of steel skeleton composition on the triboengineering properties of steel–copper pseudoalloys produced by infiltration. *Journal of Friction and Wear*. 2010;31(4):270–275.
<https://doi.org/10.3103/S1068366610040045>
19. Dyachkova L.N. The effect of the nanodiamonds introduction on the properties of powder carbon steel. *Magazin «INŻYNERIA PRODUKCJI Metody i techniki usprawniania procesów produkcyjnych»*, Zielona Góra. 2019;16:103–112.
20. Dyachkova L.N., Feldshtein E.E., Vityaz P.A., Mikhalski M. Tribological properties of iron-based powder composite materials with addition of graphite, alumina and zirconia nanoparticles. *Journal of Friction and Wear*. 2020;41(3):198–203.
<https://doi.org/10.3103/S1068366620030046>



21. Feldshtein E.E., Dyachkova L.N. On the properties and tribological behaviors of P/M iron based composites reinforced with ultrafine particulates. *Composites Part B: Engineering*. 2013;58:16–24.
<https://doi.org/10.1016/j.compositesb.2013.10.015>
22. Dyachkova L.N., Letsko A.I. Study of the process of increasing the mechanical and tribological properties of iron-based powder materials by introducing ultrafine additives. *Izvestiya Natsional'noi Akademii nauk Belarusi. Seriya fiziko-tehnicheskikh nauk*. 2007. 3. 21–26. (In Russ.).
Дьячкова Л.Н., Лецко А.И. Исследование процесса повышения механических и триботехнических свойств порошковых материалов на основе железа введением ультрадисперсных добавок. *Известия Национальной академии наук Беларуси. Серия физико-технических наук*. 2007;3:21–26.
23. Dyachkova L.N., Vityaz P.A., Plyushchenko A.F., Voronetskaya L.Ya., Letsko A.I., Parnitsky N.M. Influence of the ultrafine iron aluminide additive on the structure and properties of iron and copper powder materials. *Doklady Natsional'noi akademii nauk Belarusi*. 2019;63(3): 360–369. (In Russ.).
<https://doi.org/10.29235/1561-8323-2019-63-3-360-369>
Дьячкова Л.Н., Витязь П.А., Ильющенко А.Ф., Воронцовская Л.Я., Лецко А.И., Парницкий Н.М. Влияние ультрадисперсной добавки алюминиды железа на структуру и свойства порошковых материалов на основе железа и меди. *Доклады Национальной академии наук Беларуси*. 2019;63(3):360–369.
<https://doi.org/10.29235/1561-8323-2019-63-3-360-369>
24. Dyachkova L.N., Dechko M.M. Influence of dispersed microadditives on the structure and properties of powder carbon and high-chromium steels. *Russian Journal of Non-Ferrous Metals*. 2016;57(5):477–483.
<https://doi.org/10.3103/S1067821216050047>
Дьячкова Л.Н., Дечко М.М. Влияние дисперсных микродобавок на структуру и свойства порошковых углеродистой и высокохромистой сталей. *Известия вузов. Порошковая металлургия и функциональные покрытия*. 2016;57(5):477–483.
<https://doi.org/10.3103/S1067821216050047>
25. Дьячкова Л.Н., Волчек А.Я., Лецко И.Н. Исследование влияния состава атмосферы спекания на структуру и механические свойства порошковых низколегированных сталей. В сб.: *Порошковая металлургия*. Минск: Национальная академия наук Беларуси, 2007. Т. 30. С. 64–66.
26. Dyachkova L.N., Volchek A.Ya., Letsko I.N. Study of the influence of the sintering atmosphere composition on the structure and mechanical properties of low-alloy powder steels. In the collection: *Powder Metallurgy*. Minsk: National Academy of Sciences of Belarus, 2007. Vol. 30. P. 64–66. (In Russ.).
Dyachkova L.N. Structure and properties of antifriction pseudo-alloys of the powder steel–copper alloy, infiltrated with materials of various compositions. *Friction and Wear*. 2023;44(4):197–203.
<https://doi.org/10.3103/S1068366623040050>



Information about the Authors

Larisa N. Dyachkova – Dr. Sci. (Eng.), Professor, Chief Researcher, State Research Institution O.V. Roman Powder Metallurgy Institute, National Academy of Sciences of Belarus
 **ORCID:** 0000-0003-1850-6221
 **E-mail:** dyachkova@tut.by

Piotr A. Vityaz – Dr. Sci. (Eng.), Academician of the National Academy of Sciences of Belarus, Professor, Head of the Department of Aerospace Activities of the Apparatus of the National Academy of Sciences of Belarus
 **ORCID:** 0000-0001-9950-2120
 **E-mail:** vitiaz@presidium.bas-net.by

Сведения об авторах

Лариса Николаевна Дьячкова – д.т.н., профессор, гл. науч. сотрудник, Институт порошковой металлургии имени академика О.В. Романа» НАН Беларуси
 **ORCID:** 0000-0003-1850-6221
 **E-mail:** dyachkova@tut.by

Петр Александрович Витязь – д.т.н., профессор, академик НАН Беларуси, начальник управления аэрокосмической деятельности аппарата НАН Беларуси
 **ORCID:** 0000-0001-9950-2120
 **E-mail:** vitiaz@presidium.bas-net.by

Contribution of the Authors

L. N. Dyachkova – formation of the main concept, goal and objectives of the study; writing the text, formulation of the conclusions.
P. A. Vityaz – scientific guidance, correction of the text and conclusions.

Вклад авторов

Л. Н. Дьячкова – формирование основной концепции, постановка цели и задачи исследования, подготовка текста, формулировка выводов
П. А. Витязь – научное руководство, корректировка текста

Received 16.04.2025
 Revised 21.05.2025
 Accepted 26.05.2025

Статья поступила 16.04.2025 г.
 Доработана 21.05.2025 г.
 Принята к публикации 26.05.2025 г.



UDC 621.762.016

<https://doi.org/10.17073/1997-308X-2025-4-28-39>

Research article
Научная статья



Features of densification, structure formation, and properties of powder titanium under hot die forging

V. Yu. Dorofeyev¹✉, A. N. Sviridova¹,
S. V. Sviridova², L. I. Svistun³

¹Platov South-Russian State Polytechnic University (NPI)
132 Prosveshcheniya Str., Rostov region, Novocherkassk 346428, Russia

²Tamбов State University named after G.R. Derzhavin
33 Internatsionalnaya Str., Tambov 392000, Russia

³Kuban State Technological University
2 Moskovskaya Str., Krasnodar 350072, Russia

✉ dvyu56.56@mail.ru


Abstract. Research in the field of titanium powder metallurgy has been ongoing for more than 60 years. Nevertheless, there are relatively few examples of the practical application of powder titanium, which is associated with insufficient reliability and durability of the manufactured products. The ability of titanium parts to withstand static and dynamic loads is determined by residual porosity, non-metallic inclusions, and microstructural characteristics. At present, the most widely used method for producing powder titanium components is the press–sinter route. However, the porosity of sintered titanium typically ranges from 3 to 15 %, which reduces its load-bearing capacity and highlights the need for effective methods to minimize porosity. Hot working methods, particularly hot die forging of porous preforms, hold considerable potential in addressing this issue. This study presents the results of investigating the features of densification, structure formation, and properties of powder titanium under hot die forging. A technology for producing hot-forged powder titanium is proposed, which includes hydriding–dehydriding of porous preforms. This operation promotes the reduction of oxides localized on the surfaces of open pores by hydrogen and their activation, thereby improving conditions for interparticle bonding during subsequent hot repressing. As a result, the obtained samples demonstrate higher fracture toughness and ductility compared with reference samples. The values of the maximum specific work of hot densification of porous powder titanium, required to achieve monolithic density at different preheating temperatures of the preforms, were determined. It was shown that the non-monotonic temperature dependence of the maximum specific densification work is associated with the formation of a coarse-grained structure and with reduced ductility of the deformable material in the temperature range of the $\alpha \rightarrow \beta$ phase transformation.

Keywords: hot die forging, porous preforms, powder titanium, densification work, fracture toughness, ductility, strength, ductile fracture, interparticle fracture, oxide reduction, hydriding, dehydriding, interparticle bonding, activation

Acknowledgements: The SEM images were obtained using a Quanta 200 i 3D microanalyzer at the Nanotechnology Shared Research Facility of Platov South-Russian State Polytechnic University. The authors express their gratitude to Höganäs Eastern Europe for providing the ABC100.30 iron powder manufactured by Höganäs AB.

For citation: Dorofeyev V.Yu., Sviridova A.N., Sviridova S.V., Svistun L.I. Features of densification, structure formation, and properties of powder titanium under hot die forging. *Powder Metallurgy and Functional Coatings*. 2025;19(4):28–39.
<https://doi.org/10.17073/1997-308X-2025-4-28-39>

Особенности уплотнения, формирования структуры и свойств порошкового титана при горячей штамповке

В. Ю. Дорофеев¹ , А. Н. Свиридова¹,
С. В. Свиридова², Л. И. Свистун³

¹ Южно-Российский государственный политехнический университет (НПИ) имени М.И. Платова
Россия, 346428, Ростовская обл., г. Новочеркасск, ул. Просвещения, 132

² Тамбовский государственный университет имени Г.Р. Державина
Россия, 392000, г. Тамбов, ул. Интернациональная, 33

³ Кубанский государственный технологический университет
Россия, 350072, г. Краснодар, ул. Московская, 2

 dvyu56.56@mail.ru

Аннотация. Работы в области порошковой металлургии титана проводятся уже более 60 лет. Несмотря на это, примеров практического использования порошкового титана не так много, что связано с неудовлетворительным характером показателей надежности и долговечности получаемых изделий. Способность титановых изделий сопротивляться воздействию статических и динамических нагрузок определяется наличием остаточной пористости, неметаллических включений, а также характеристиками микроструктуры. В настоящее время при изготовлении изделий из порошкового титана наибольшее распространение получила технология прессования–спекания. Однако пористость спеченного титана составляет 3–15 %, что снижает его сопротивляемость действию нагрузок и обуславливает актуальность разработки эффективных методов снижения пористости. Большой потенциал в решении указанной задачи имеют методы горячей обработки давлением, в частности горячая штамповка пористых заготовок. В работе представлены результаты исследования особенностей уплотнения, формирования структуры и свойств порошкового титана при горячей штамповке. Предложена технология получения горячештампованного порошкового титана, включающая выполнение операций гидрирования–дегидрирования пористой заготовки, обеспечивающих восстановление оксидов, локализованных на поверхностях открытых пор, водородом и их активизацию, что способствует улучшению условий формирования межчастичного сращивания при последующей горячей допрессовке и повышению трещиностойкости и пластичности получаемых образцов в сравнении с образцами-свидетелями. Установлены значения величины максимальной приведенной работы горячего уплотнения пористого порошкового титана, необходимой для достижения плотности монолита, при разных температурах преддеформационного нагрева заготовок. Показано, что немонотонность температурной зависимости максимальной приведенной работы уплотнения связана с формированием крупнозернистой структуры и с уменьшением пластичности деформируемого материала в интервале температур фазового $\alpha \rightarrow \beta$ -превращения.

Ключевые слова: горячая штамповка, пористые заготовки, порошковый титан, работа уплотнения, трещиностойкость, пластичность, прочность, вязкий излом, межчастичное разрушение, восстановление оксидов, гидрирование, дегидрирование, межчастичное сращивание, активация

Благодарности: Снимки на растровом микроскопе-микроанализаторе Quanta 200 i 3D получены в Центре коллективного пользования «Нанотехнологии» ЮРГПУ (НПИ). Авторы выражают благодарность компании «Хёганес Восточная Европа» за предоставленный железный порошок ABC100.30 производства фирмы Höganäs AB.

Для цитирования: Дорофеев В.Ю., Свиридова А.Н., Свиридова С.В., Свистун Л.И. Особенности уплотнения, формирования структуры и свойств порошкового титана при горячей штамповке. *Известия вузов. Порошковая металлургия и функциональные покрытия*. 2025;19(4):28–39. <https://doi.org/10.17073/1997-308X-2025-4-28-39>

Introduction

The unique properties of titanium – its high specific strength, corrosion resistance, and good biocompatibility – determine the wide application of this metal and its alloys in aerospace, automotive engineering, medicine, and other industries [1]. The prospects of powder metallurgy technologies for manufacturing titanium and titanium alloy products are largely driven by the high cost of alternative casting technolo-

gies [2; 3]. The production of cast titanium is further complicated by significant losses during machining. The average material utilization factor in manufacturing titanium products from wrought stock does not exceed 18 % and is often much lower [4].

Research in titanium powder metallurgy has been ongoing for more than 60 years. Nevertheless, there are still relatively few examples of its practical application. In many cases, consumers prefer cast titanium over powder-based titanium due to unsatisfactory

mechanical properties and/or high cost of the latter [1]. Reducing the cost of powder titanium products requires the development of economically efficient technologies both for producing titanium powder and for fabricating finished parts [5].

One promising approach to lowering the cost of titanium powder is the use of by-products from sponge titanium production as the raw material. Another promising route is the *hydride–dehydride* (HDH) process, which involves mechanical milling of pre-hydrided sponge titanium, turnings, scrap, and other machining waste, followed by dehydrogenation of the milled material [6–8].

Improving the mechanical properties of powder titanium products during processing is also of critical importance, although success in this area often directly depends on the quality of the starting powder [9]. The ability of titanium products to resist static and dynamic loads is determined by the presence of residual porosity, non-metallic inclusions, and microstructural characteristics [10]. The residual porosity of powder titanium depends on the production technology. In recent decades, the press–sinter method has become the most widespread [1; 11; 12]. Porosity in sintered (undeformed) titanium typically ranges from 3 to 15 %. Since pores act as stress concentrators, they reduce the effective cross-section of the sample and diminish its load-bearing capacity. Therefore, improving the physical and mechanical properties of powder titanium requires the development of effective methods to reduce porosity [1].

The use of fine, amorphous, and nanostructured powders, thermocycling in the $\alpha \rightarrow \beta$ phase transformation range ($t = 800\text{--}1100\text{ }^{\circ}\text{C}$), thermomechanical treatment, and spark plasma sintering are effective methods of sintering activation [11; 13–15]. In addition, the use of activating additives also provides positive results; these are conventionally divided into two types [16].

Additives of the first type activate self-diffusion of the base element, thereby improving densification conditions during sintering. The diffusion rates of transition metals and phosphorus in α -Ti are 3–5 orders of magnitude higher than its self-diffusion [17]. Self-diffusion of titanium is also enhanced by elements that reduce the solidus temperature of the alloy [16].

The second type of additives includes elements that promote the formation of a transient liquid phase, which disappears during sintering and provides effective diffusion pathways for mass transport, thereby increasing the density of sintered products. Moreover, liquid-phase formation may be related to eutectic reactions between two precipitated phases (solid–liquid

sintering). Significant sintering activation is observed during liquid-phase sintering of amorphous titanium powders [13]. Powders of iron, nickel, silicon, cobalt, and copper are used as activators [18–26]. However, liquid-phase sintering technology has several drawbacks: distortion of the shape of preforms, segregation of solid and liquid phases, and rapid grain growth, all of which negatively affect the mechanical and service properties of the products.

High diffusion rates are also observed during sintering of titanium powder produced by the hydride–dehydride process [27]. This is due to the formation of a large number of lattice defects during dehydrogenation, which promote diffusion processes [28].

Among the more recent technologies of sintering activation for powder titanium are induction vacuum sintering methods and FAST (*Field-assisted sintering technology*), which employs strong electromagnetic fields [29; 30]. A major limitation of these methods is the need for expensive specialized equipment, which significantly increases production costs [31].

Limiting factors also include the low ductility and toughness of powder titanium and its alloys, which adversely affect their fracture toughness and fatigue strength [32; 33]. In this regard, it is worth recalling a recent event. At the 2021 Tokyo Olympics, an accident occurred involving the bicycle of an Australian rider, caused by the fatigue failure of handlebars manufactured by additive technology from Ti–6Al–4V powder alloy [34; 35].

Although the specific strength of powder titanium is about four times higher than that of steels, its resistance to cyclic loading is often low due to its limited ductility. In addition to porosity, ductility, fracture toughness, and fatigue strength are negatively affected by interstitial impurities (O, H, N, C) and microstructural characteristics [32]. The presence of impurities is associated with the high chemical affinity of titanium for these elements, necessitating heating operations in vacuum or inert atmospheres.

The dependence of fatigue life on microstructural characteristics is determined by the slip length during plastic shear of the crystal lattice. In titanium-based materials, this corresponds to the α -phase grain diameter in equiaxed structures, the α -phase plate width in basket-weave structures, or the colony size in lamellar structures [33]. A reduction in slip length due to microstructural refinement contributes to improved fatigue strength. It should be noted that prolonged high-temperature exposure during sintering leads to grain growth. This highlights the relevance of employing methods in powder titanium processing that enable

simultaneous reduction of porosity and refinement of structural constituents.

A promising approach to addressing this challenge lies in hot deformation methods. The first studies in this area were carried out in the late 1950s to early 1960s. At Novocherkassk Polytechnic Institute, I.N. Goncharov proposed a method of hammer forging titanium powder particles or crushed titanium sponge to achieve welding [36]. Densification was performed under isothermal conditions in a preheated die at 900–920 °C. The resulting samples exhibited high density (4.46–4.48 g/cm³), along with high ductility and deformability of forged powder titanium. Since the starting material subjected to hot deformation was powder or sponge particles, this method developed by I.N. Goncharov can, in modern terminology, be classified as *direct powder forging* (DPF).

In industrial practice, hot forging of loose powder preppacked into cans was introduced later, in the 1970s, for the production of high-alloy tool steels [37]. More recently, studies have investigated the feasibility of applying DPF technology to titanium powder processing [31; 38]. A high-density Ti–6Al–4V powder material with a homogeneous lamellar two-phase ($\alpha + \beta$) structure was obtained, characterized by high ductility, low impurity content both on the surface and in the bulk of the experimental samples, and only minor deviations from the chemical composition of the starting powder. Using this technology, a femoral implant was fabricated that meets the requirements of ASTM F136-13 (2021) [39].

One advantage of the DPF process is that the high stresses and strains generated during forging at the powder – can interface promote the fracture of intermetallics and oxides formed there, facilitating subsequent can removal. However, this advantage may present a problem: after can removal, the powder material surface exhibits a fracture-like relief, necessitating additional machining.

Research on hot forging of porous titanium preforms (HFPTP) was conducted by S.S. Kiparisov and co-authors in the late 1960s to early 1970s [11, pp. 47, 48]. These studies established the optimal parameters for HFPTP: heating temperature of 900 °C and impact energy of 2000–2500 kJ/m². However, the upper limit of the heating temperature range did not exceed 900 °C, and the impact energy values were expressed per unit area rather than per volume of the sample in the compact state, which complicates their practical application for densification.

Subsequently, V.A. Pavlov and co-authors carried out research on hot deformation of titanium powders and other non-ferrous metals [40; 41]. They examined

the forging behavior of porous titanium preforms in open and closed dies, heating under various conditions (unprotected, protected with glass coatings, in argon, and in vacuum), as well as deformability characteristics and energy consumption during cold hydrostatic pressing of titanium powder. However, the energy requirements for densifying powder titanium to a pore-free state by hot forging were not determined. Such data are also absent in the works of Yu.G. Dorofeev and his scientific school. The lack of information on the parameter W_{\max} (maximum specific densification work, i.e., the work required to reach monolithic density [42; 43]) for HFPTP complicates the selection of technological modes, since densification energy is one of the key control parameters in dynamic consolidation of powder materials [44].

The aim of this work was to study the densification behavior, microstructure formation, and properties of powder titanium during *hot die forging* (HDF).

Experimental procedure

The experimental samples were fabricated from electrolytic titanium powder grade PTES-1 according to TU 48–10–22–85. A powder fraction of $-0.63 + 0.18$ mm with a bulk density of $1.5 \cdot 10^3$ kg/m³ was used. The processing flowcharts for sample fabrication are shown in Fig. 1. At the initial stage of the study, the energy characteristics of hot densification were determined using cylindrical samples with dimensions $\varnothing 20 \times 8$ mm (scheme 1). The ratio of the final height of the sample (h_f) to its diameter (d) was kept constant ($h_f/d = 0.4 = \text{const}$). The porosity of the cold-pressed billets was in the range of 22–25 %. After heating to various temperatures (800–1050 °C), the billets were further compacted on a laboratory drop hammer with a falling weight of 50 kg. The densification work (W) was varied in the range of 30–150 MJ/m³. Preheating of the billets before further compaction was carried out in a portable heat-resistant steel container into which helium was supplied. The container with the sample was then placed into a laboratory muffle furnace with silicon carbide heating elements, which was also purged with helium.

The value of W_{\max} was determined by a graphical–analytical method, processing the plots of $\lg W = f(\lg \beta)$ according to Dorofeev’s methodology (β – relative volume) [42; 43]. The density of the samples was measured by hydrostatic weighing in accordance with GOST 18898–89.

At the next stage of the study, prismatic samples with dimensions $130 \times 26 \times 15$ mm were fabricated to determine the mechanical properties and conduct microstructural analysis. To reduce the probability

of oxidation, the billets for prismatic samples were made bimetallic. The outer layer (sheath) of the billets was produced from high-pressibility iron powder grade ABC100.30 (Höganäs AB).

After HDF, the billets were subjected to machining. The fracture toughness (K_{Ic}) was determined on type 4 samples (GOST 25.506–85) with dimensions $12.5 \times 25 \times 112.5$ mm containing a pre-induced crack using the three-point bending method. The crack was initiated under cyclic loading. The values of K_{Ic} were calculated according to the procedure [45]. Tensile tests were carried out on type II Gagarin samples (GOST 1497–84) with a working section diameter $d_0 = 5$ mm and a gauge length $l_0 = 25$ mm.

Based on the results of the first stage of HDF testing, the mechanical properties and fracture toughness were determined at a specific densification work of $W = 195 \text{ MJ/m}^3$. Since fully dense samples were not obtained in the first stage, the pre-deformation heating temperature of the billets was varied in the range of $t_{HDF} = 1000\text{--}1200$ °C.

During the fabrication of samples according to technological scheme 3, porous cold-pressed billets were subjected to hydrogenation in hydrogen, followed by dehydrogenation during vacuum sintering. This step was intended to reduce impurity content and acti-

vate interparticle surfaces for subsequent hot forging, similar to the previously observed effect of hydrogenation–dehydrogenation of initial titanium powders during sintering [27]. For comparative analysis, control samples were produced according to technological scheme 2, which did not include the hydrogenation step of cold-pressed billets.

The fracture surfaces of the samples were examined using a Quanta 200 i 3D scanning electron microscope–microanalyzer and an MBS 9 binocular microscope. The fraction of fracture surface components was determined by grid and area methods applied to electron microscopic images [46], with 10–12 fields analyzed. Metallographic studies were performed with an AltamiMET 1M optical microscope (Altami Ltd., Russia) on both etched and unetched polished sections. Kroll's reagent (2 ml HNO_3 + 2 ml HF + 96 ml H_2O) was used as the etchant, with an etching time of 20 s.

Results and discussion

Fig. 2 presents the $\lg W = f(\lg \beta)$ dependences for porous titanium billets subjected to different pre-deformation heating temperatures. The relationships between the relative volume of powder titanium and the specific densification work, plotted in logarithmic coordinates, exhibit a linear form, which is characteris-

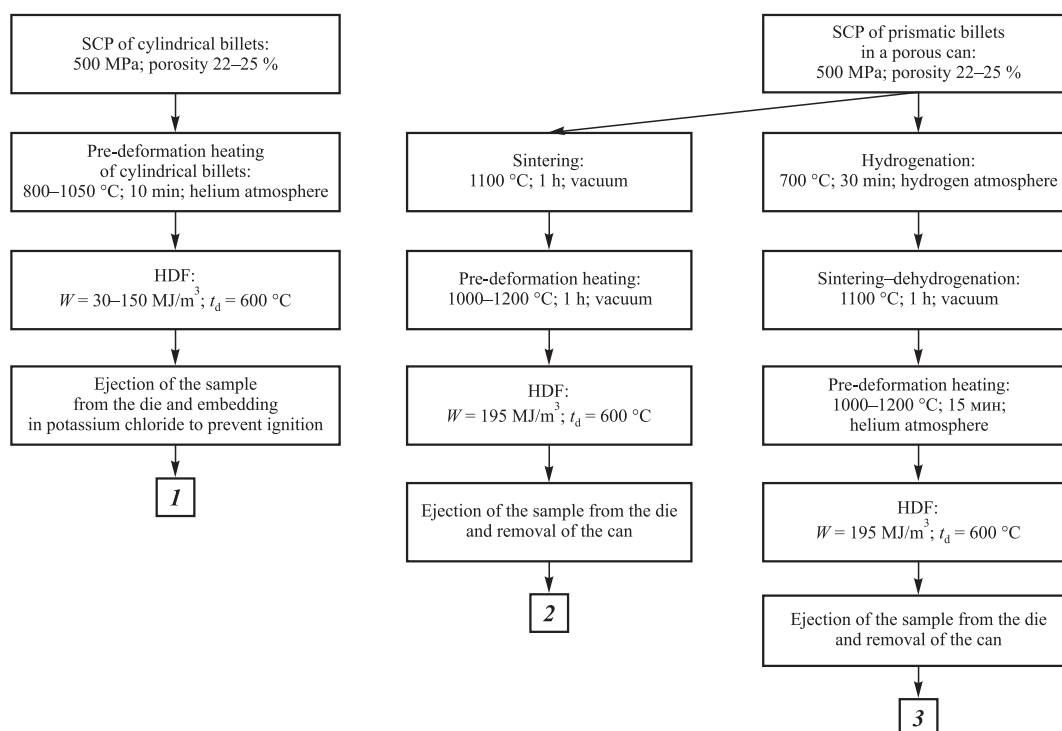


Fig. 1. Processing flowcharts for producing hot die forged powder titanium

SCP – static cold pressing; t_d – preheating temperature of the die matrix for HDF; W – specific densification work

Рис. 1. Технологические схемы получения горячештампованного порошкового титана

SCP – статическое холодное прессование; t_d – температура подогрева матрицы пресс-формы для ГШ; W – приведенная работа уплотнения

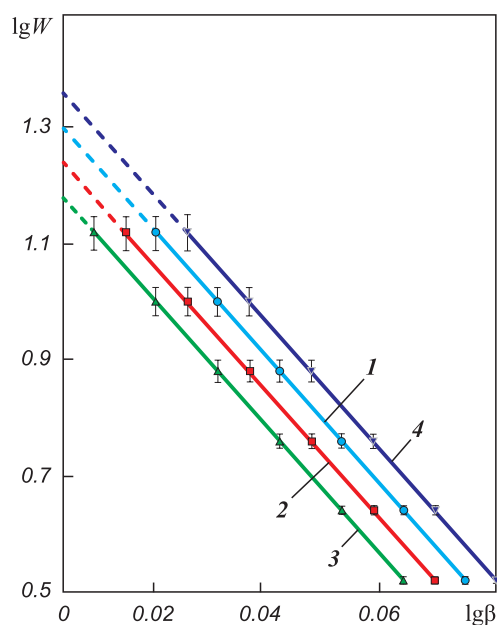


Fig. 2. $\lg W = f(\lg \beta)$ dependences during hot die forging of cold-pressed titanium powder billets

$t_{\text{HDF}}, ^\circ\text{C}$: 1 – 800, 2 – 900, 3 – 950, 4 – 1000; $h_f/d = 0.4$

Рис. 2. Зависимости $\lg W = f(\lg \beta)$ при горячей штамповке холоднопрессованных заготовок из титанового порошка

$t_{\text{HDF}}, ^\circ\text{C}$: 1 – 800, 2 – 900, 3 – 950, 4 – 1000; $h_f/d = 0.4$

tic of ductile materials [42]. The W_{max} were determined by extrapolating curves 1–4 to their intersection with the ordinate axis (dashed lines).

The dependence of the W_{max} values determined in this way on the hot die forging temperature is shown in Fig. 3. It is evident that the dependence is nonmonotonic. Increasing t_{HDF} in the 800–950 $^\circ\text{C}$ range leads to a decrease in W_{max} due to the enhanced plasticity of the α -phase. At $t_{\text{HDF}} = 950$ –1000 $^\circ\text{C}$, the W_{max} value increases, which is attributed to the $\alpha \rightarrow \beta$ phase transformation and the formation of the β -phase, characterized at these temperatures by reduced plasticity

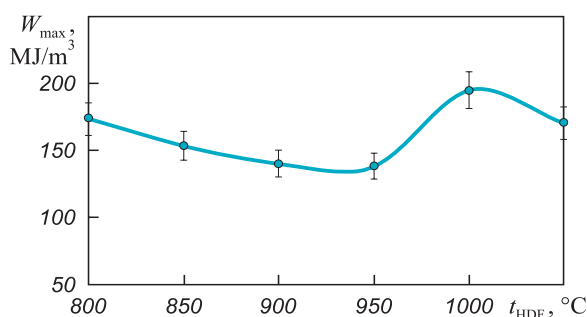


Fig. 3. Dependence of the maximum specific densification work on the heating temperature of porous titanium billets

Рис. 3. Зависимость максимальной приведенной работы уплотнения от температуры нагрева пористых заготовок из титана

and higher strength. At $t_{\text{HDF}} > 1000$ $^\circ\text{C}$, the plasticity of the β -phase increases, resulting in a decrease in W_{max} .

The effect of phase transformations on densification behavior and deformability has been previously reported in studies of dynamic and explosive hot pressing of porous iron-based billets [42; 43]. With regard to titanium and its alloys, the literature data remain contradictory [11]. Some authors indicate a monotonic increase in plasticity with temperature across all titanium alloys [47], whereas others note a nonmonotonic trend [48]. The reduction in plasticity in the $\alpha \rightarrow \beta$ transformation range has been linked to the development of a coarse-grained structure [49].

In our experiments, the grain size of samples fabricated at $t_{\text{HDF}} = 950$ $^\circ\text{C}$, was 10–20 μm (Fig. 4, a), corresponding to grades 2–3 on the titanium alloy microstructure scale used for metallurgical quality control [49]. At $t_{\text{HDF}} = 1000$ $^\circ\text{C}$, the grain size increased to 25–35 μm (grades 5–6) (Fig. 4, b). This provides sufficient grounds to assume that the nonmonotonic

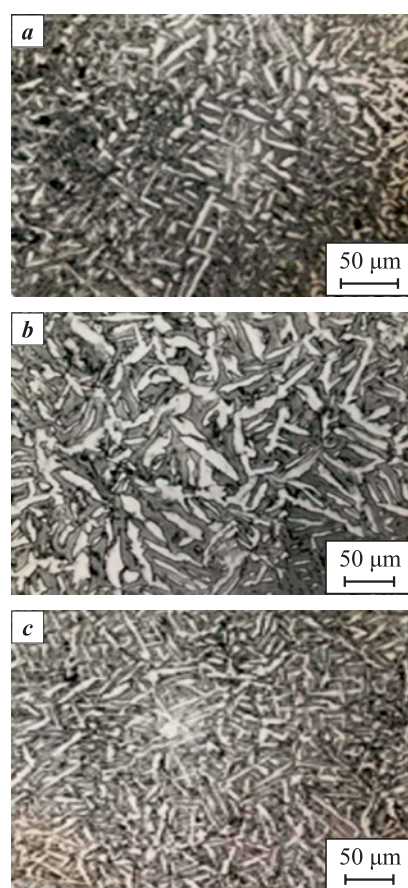


Fig. 4. Microstructure of hot die forged powder titanium
a, b – scheme 1, c – scheme 2; $t_{\text{HDF}}, ^\circ\text{C}$: 950 (a), 1000 (b) and 1200 (c)

Рис. 4. Микроструктура горячештампованного порошкового титана

a, b – схема 1, c – схема 2; $t_{\text{HDF}}, ^\circ\text{C}$: 950 (a), 1000 (b) и 1200 (c)

$W_{\max} = f(t_{\text{HDF}})$ dependence is also associated with grain growth during phase transformation. The samples exhibited a lamellar intragranular α -phase structure with areas of basket-weave microstructure. This morphology is related to the temperature distribution within the billet during deformation and subsequent cooling.

A similar lamellar α -phase intragranular structure is observed in titanium castings under slow cooling conditions [48]. In our experiments, cooling was relatively slow: after removal from the die preheated to 600 °C, further cooling proceeded under a layer of potassium chloride. Consequently, the formation of the lamellar structure can be attributed to $\beta \rightarrow \alpha$ recrystallization. In this process, α -phase lamellae nucleate at β -grain boundaries and grow inward. The formation of basket-weave regions is apparently associated with cooling of the billet surface layers in contact with the die walls during hot forging. Deformation of these zones begins in the β -region and ends in the $\alpha + \beta$ region, which provides favorable conditions for basket-weave formation [50].

The W_{\max} values obtained in the investigated pre-deformation heating range were 150–200 MJ/m³, whereas the heat of fusion of titanium in comparable units is significantly higher – 1411 MJ/m³ [51]. This indicates that in powder titanium processing by hot die forging, as in other metals, the energy expenditure is considerably lower than during melting, since only part of the particle material undergoes plastic deformation, determined by the material's ductility [43]. The measured W_{\max} values are also much lower than the reported activation energy of powder titanium sintering (~15,000 MJ/m³) [52], which approximately corresponds to the activation energy of self-diffusion in β -Ti.

Fig. 5 presents the dependence of fracture toughness and mechanical properties of powder metallurgy titanium on the hot die forging temperature. Samples were fabricated according to technological schemes 2 and 3. The $K_{\text{Ic}} = f(t_{\text{HDF}})$ dependences are nonmonotonic. Increasing t_{HDF} to 1150 °C leads to higher K_{Ic} due to improved deformability of the porous billet material. A further increase in t_{HDF} to 1200 °C results in a decrease in K_{Ic} , which is attributed to grain refinement (see Fig. 4, c).

Grain refinement in samples fabricated at $t_{\text{HDF}} > 1150$ °C, is associated with the higher post-deformation cooling rate caused by the increasing temperature gradient between the heated porous billet and the die. Throughout the studied t_{HDF} range, the fracture toughness of samples fabricated according to scheme 3 was consistently higher than that

of control samples fabricated according to scheme 2 (cf. curves 1 and 2 in Fig. 5, a). This difference can be explained by distinct fracture mechanisms in the compared types of samples.

Raising the hot die forging temperature also altered the fracture characteristics of the samples. In control samples fabricated at $t_{\text{HDF}} = 1000$ –1100 °C, the fracture surface of the initial fatigue crack contained secondary cracks in the failure origin (Fig. 6, a). In the final fracture zone, which formed under static loading, the fracture was of a ductile fine-dimple type with areas of interparticle fracture (Fig. 6, b, c). Dimple sizes ranged from 4 to 6 μm . At $t_{\text{HDF}} > 1100$ °C, secondary cracks in the fracture origin were not observed; however, interparticle fracture areas remained present in the final fracture zone. The dimples of ductile fracture in this zone were larger – 10–12 μm – than in control samples fabricated at 1000–1100 °C, indicating higher material ductility (Fig. 6, d).

The fracture surfaces of samples fabricated according to scheme 3 were characterized by the absence of secondary cracks in the fracture origin at all studied t_{HDF} values (Fig. 6, e). In the final fracture zone, interparticle fracture was not detected, which indicates higher fracture energy compared to control samples.

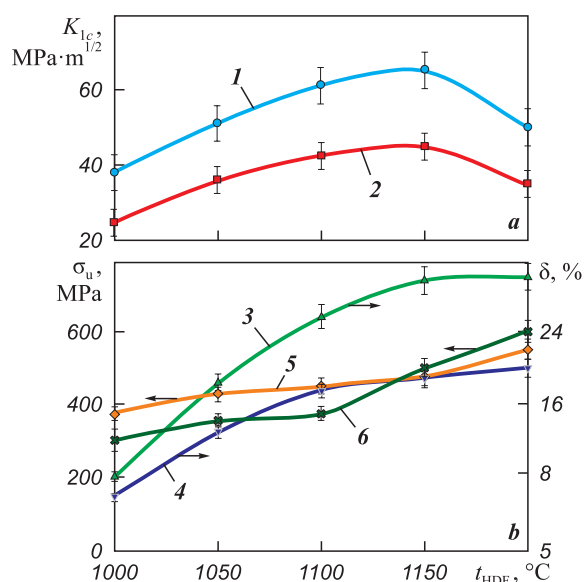


Fig. 5. Effect of pre-deformation heating temperature of porous titanium billets on fracture toughness (a) and mechanical properties (b)

1 – K_{Ic} (scheme 3), 2 – K_{Ic} (scheme 2); 3 – δ (scheme 3);
4 – δ (scheme 2); 5 – σ_u (scheme 3);
6 – σ_u (scheme 2); $W = 195 \text{ MJ/m}^3$

Рис. 5. Влияние температуры преддеформационного нагрева пористых заготовок из титана на трещиностойкость (a) и механические свойства (b)

1 – K_{Ic} (схема 3), 2 – K_{Ic} (схема 2); 3 – δ (схема 3), 4 – δ (схема 2),
5 – σ_u (схема 3), 6 – σ_u (схема 2); $W = 195 \text{ МДж/м}^3$

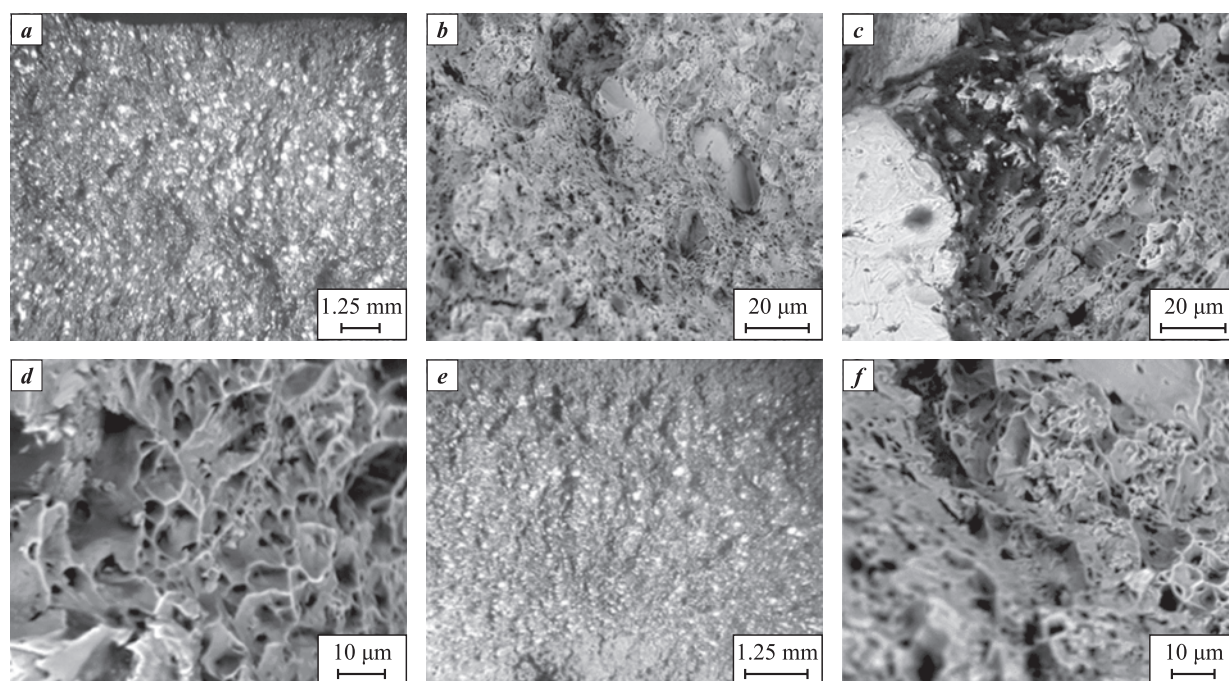


Fig. 6. Fracture surfaces of powder titanium samples fabricated by schemes 2 (*a–d*) and 3 (*e, f*) after fracture toughness tests

a, e – fracture panorama; *b, c, d, f* – final static fracture zone:
b – area of ductile fine-dimple fracture, *c* – area of interparticle fracture,
d – large dimples of ductile fracture with interparticle fracture areas, *f* – ductile fracture
 t_{HDF} , °C: 1000 (*a, b, c*); 1100 (*e, f*); 1200 (*d*)

Рис. 6. Поверхности разрушения образцов порошкового титана, полученных по схемам 2 (*a–d*) и 3 (*e, f*), после испытаний на трещиностойкость

a, e – панорама излома; *b, c, d, f* – зона статического долома:
b – участок вязкого мелкоячеичного разрушения, *c* – участок межчастичного разрушения,
d – крупные ямки вязкого излома с участками межчастичного разрушения, *f* – вязкий излом
 t_{HDF} , °C: 1000 (*a, b, c*); 1100 (*e, f*); 1200 (*d*)

The trend in dimple size variation with t_{HDF} was similar to that observed for control samples (see Fig. 6, *f*). Thus, the predominant factor influencing the fracture toughness characteristics of scheme 3 samples is the hydrogenation–dehydrogenation treatment. An analysis of impurity composition in the initial titanium powder and in the fabricated samples showed that under scheme 2, the oxygen concentration in the resulting material increased by about two fold (see Table).

In samples obtained according to scheme 3, the oxygen content was significantly reduced, while no substantial changes were observed in the amount of other impurities. This is explained by the fact that

hydrogen released from titanium hydrides during vacuum sintering of porous billets after hydrogenation promotes the reduction and activation of oxides localized on the surfaces of open pores. A similar sintering activation effect when using hydrogenated titanium powder was reported earlier [27]. In our experiments, the activation of pore surfaces and their refinement from oxides improved the conditions for interparticle bonding during subsequent hot die forging [53]. In contrast, the relatively high oxygen content in control samples (scheme 2), associated with the presence of oxides on the collapsing pore surfaces during hot die forging, impaired interparticle contact conditions and

Impurity content in titanium powder and materials produced from it

Содержание примесей в порошке титана и материалах на его основе

Material/ processing scheme	Content, wt. %						
	Fe	Cl ₂	N ₂	O ₂	C	Si	H ₂
PTES-1 powder	0.06	0.03	0.020	0.06	0.02	0.02	0.010
Scheme 2	0.06	0.02	0.011	0.15	0.03	0.02	0.003
Scheme 3	0.06	0.01	0.008	0.03	0.02	0.02	0.002

led to lower fracture toughness compared to scheme 3 samples (Fig. 5, a).

Strength and ductility characteristics were less sensitive to the quality of interparticle bonding and were mainly determined by grain size. Accordingly, the dependences of σ_u and δ on t_{HDF} were monotonic: increasing temperature led to growth of these properties throughout the studied range (see Fig. 5, b). In this case, the dominant factor was grain refinement with increasing t_{HDF} (see Fig. 4, c). Improved interparticle bonding conditions during hot die forging of billets subjected to hydrogenation–dehydrogenation resulted in higher ductility of scheme 3 samples compared to control samples (cf. curves 3 and 4 in Fig. 5, b).

Conclusions

1. The maximum specific densification work required to achieve monolithic density in porous powder titanium was determined for different pre-deformation heating temperatures of billets. The nonmonotonic character of the W_{max} dependence on t_{HDF} is associated with the formation of a coarse-grained structure and reduced ductility of the deforming material in the $\alpha \rightarrow \beta$ phase transformation temperature range.

2. A processing technology was proposed for producing hot die forged powder titanium, involving hydrogenation–dehydrogenation of porous billets. This treatment promotes hydrogen-assisted reduction by hydrogen of oxides localized on the surfaces of open pores and their activation, thereby improving interparticle bonding during subsequent hot die forging and enhancing the fracture toughness and ductility of the resulting samples compared to control samples.

3. Increasing the hot die forging temperature of porous titanium billets contributes to higher fracture energy and improved ductility of the samples. At the same time, the likelihood of secondary crack formation in the origin of the initial fatigue crack is reduced, and the size of dimples in the final ductile fracture zone increases.

References / Список литературы


1. Fang Z.Z., Paramore J.D., Sun P., Chandrana K.S.R., Zhang Y., Xia Y., Cao F., Koopman M.M., Free M.M. Powder metallurgy of titanium – past, present, and future. *International Materials Reviews*. 2018;63(7):407–459. <https://doi.org/10.1080/09506608.2017.1366003>
2. Froes F.H., Eylon D. Powder metallurgy of titanium alloys. *International Materials Reviews*. 1990;35(1):162–184. <https://doi.org/10.1179/095066090790323984>
3. Fang Z.Z., Sun P. Pathways to optimize performance/cost ratio of powder metallurgy titanium – a perspective. *Key Engineering Materials*. 2012;520:15–23. <https://doi.org/10.4028/www.scientific.net/KEM.520.15>
4. Seong S., Younossi O., Goldsmith B.W., Lang Th., Neumann M. Titanium – industrial base, price trends, and technology initiatives. Santa Monica (CA): RAND Corporation; 2009. 128 p. <https://doi.org/10.7249/MG789>
5. Froes F.H.S., Gungor M.N., Ashraf Imam M. Cost-affordable titanium: The component fabrication perspective. *Journal of the Minerals, Metals and Materials Society*. 2007;59(6):28–31. <https://doi.org/10.1007/s11837-007-0074-8>
6. Rubtsov A.N., Olesov Yu.G., Antonova M.M. Hydrogenation of titanium materials. Kyiv: Naukova Dumka, 1971. 128 p. (In Russ.).
Рубцов А.Н., Олесов Ю.Г., Антонова М.М. Гидрирование титановых материалов. Киев: Наукова думка, 1971. 128 с.
7. Zhu L., Kong L., Yang B., Xu B. Production of low-oxygen titanium powder by thermochemical and electrochemical processes: Current state and perspectives. *Journal of Materials Research and Technology*. 2025;36:1522–1535. <https://doi.org/10.1016/j.jmrt.2025.03.226>
8. Barbis D., Gasior R.M., Walker G.P., Capone J.A., Schaeffer T.S. Titanium powders from the hydride-dehydride process. In: *Titanium powder metallurgy: science, technology and applications*. Oxford: Butterworth-Heinemann, 2015. P. 101–116. <https://doi.org/10.1016/B978-0-12-800054-0.00007-1>
9. Hidalgo A.A., Frykholm R., Ebel Th., Pyczak F. Powder metallurgy strategies to improve properties and processing of titanium alloys: A review. *Advanced Engineering Materials*. 2017;19(6):1600743. <https://doi.org/10.1002/adem.201600743>
10. Wang H., Fang Z.Z., Sun P. A critical review of mechanical properties of powder metallurgy titanium. *International Journal of Powder Metallurgy*. 2010;46(5):45–57.
11. Antsiferov V.N., Ustinov V.S., Olesov Yu.G. Sintered titanium-based alloys. Moscow: Metallurgiya, 1984. 168 p. (In Russ.).
Анциферов В.Н., Устинов В.С., Олесов Ю.Г. Спеченные сплавы на основе титана. М.: Металлургия, 1984. 168 с.
12. Majima K., Hirata T., Shouji K. Effects of purity of titanium powder and porosity on static tensile properties of sintered titanium specimens. *Journal of The Japan Institute of Metals*. 1987;51(12):194–1200. https://doi.org/10.2320/JINSTMET1952.51.12_1194
13. Liu L.H., Yang C., Kang L.M., Qu S.G., Li X.Q., Zhang W. W., Chen W.P., Li Y.Y., Li P.J., Zhang L.C. A new insight into high-strength $\text{Ti}_{62}\text{Nb}_{12.2}\text{Fe}_{13.6}\text{Co}_{6.4}\text{Al}_{5.8}$ alloys with bimodal microstructure fabricated by semi-solid sintering. *Scientific Reports*. 2016;6(1):23467. <https://doi.org/10.1038/srep23467>
14. Panigrahi B.B., Godkhindi M.M. Sintering of titanium: Effect of particle size. *International Journal of Powder Metallurgy*. 2006;42(2):35–42.
15. Robertson I., Schaffer G. Some effects of particle size on the sintering of titanium and a master sintering curve model. *Metallurgical and Materials Transactions A*.

- 2009;40(8):1968–1979.
<https://doi.org/10.1007/s11661-009-9894-1>
16. Qian M., Yang Y.F., Luo S.D., Tang H.P. Pressureless sintering of titanium and titanium alloys: sintering densification and solute homogenization. In: *Titanium powder metallurgy: science, technology and applications*. Oxford: Butterworth-Heinemann, 2015. P. 201–218.
<https://doi.org/10.1016/B978-0-12-800054-0.00012-5>
17. Pereloma E.V., Savvakina D.G., Carman A., Gazder A., Ivasishin O.M. Microstructure development and alloying elements diffusion during sintering of near- β titanium alloys. In: *Powder Metallurgy of Titanium*. Brisbane, Australia: Trans Tech Publications Ltd, 2012. P. 49–56.
<https://doi.org/10.4028/b-HGgP7a>
18. Panigrahi B.B. Sintering behaviour of Ti–2Ni and Ti–5Ni elemental powders. *Materials Letters*. 2007;61(1):152–155.
<https://doi.org/10.1016/j.matlet.2006.04.025>
19. Xia Y., Schaffer G. B., Qian M. The effect of a small addition of nickel on the sintering, sintered microstructure, and mechanical properties of Ti–45Al–5Nb–0.2C–0.2B alloy. *Journal of Alloys and Compounds*. 2013;578:195–201.
<https://doi.org/10.1016/j.jallcom.2013.05.104>
20. Liu H.-W., Bishop D. P., Plucknett K. P. A comparison of Ti–Ni and Ti–Sn binary alloys processed using powder metallurgy. *Materials Science and Engineering A*. 2015;644:392–404.
<https://doi.org/10.1016/j.msea.2015.07.085>
21. Robertson I.M., Schaffer G.B. Design of titanium alloy for efficient sintering to low porosity. *Powder Metallurgy*. 2009;52(4): 311–315.
<https://doi.org/10.1179/003258909X12502872942499>
22. Liu Y., Chen L.F., Tang H.P., Liu C.T., Liu B., Huang B.Y. Design of powder metallurgy titanium alloys and composites, *Materials Science and Engineering: A*. 2006;418:25–35.
<https://doi.org/10.1016/j.msea.2005.10.057>
23. Esteban P.G., Bolzoni L., Ruiz-Navas E.M., Gordo E. PM processing and characterisation of Ti–7Fe low cost titanium alloys. *Powder Metallurgy*. 2011;54(3):242–252.
<https://doi.org/10.1179/174329009X457063>
24. Yang Y.F., Luo S.D., Bettles C.J., Schaffer G.B., Qian M. The effect of Si additions on the sintering and sintered microstructure and mechanical properties of Ti–3Ni alloy. *Materials Science and Engineering: A*. 2011;528(24):7381–7387.
<https://doi.org/10.1016/j.msea.2011.06.029>
25. Xia Y., Yu P., Schaffer G.B., Qian M. Cobalt-doped Ti–48Al–2Cr–2Nb alloy fabricated by cold compaction and pressureless sintering. *Materials Science and Engineering: A*. 2013;574:176–185.
<https://doi.org/10.1016/j.msea.2013.03.023>
26. Xia Y., Luo S.D., Wu X., Schaffer G.B., Qian M. The sintering densification, microstructure and mechanical properties of gamma Ti–48Al–2Cr–2Nb alloy with a small addition of copper. *Materials Science and Engineering: A*. 2013;559:293–300.
<https://doi.org/10.1016/j.msea.2012.08.100>
27. Savvakina D.H., Humenyak M.M., Matviichuk M.V. Molyar O.H. Role of hydrogen in the process of sintering of titanium powders. *Materials Science*. 2012;47(5):651–661.
<https://doi.org/10.1007/s11003-012-9440-y>
28. Ivasishin O.M., Savvakina D.G., Gumenyak N.M. Dehydrogenation of powder titanium hydride and its role in the activation of sintering. *Metallofizika i Noveishie Tekhnologii*. 2011;33:899–917. (In Russ.).
Ивасишин О.М., Саввакин Д.Г., Гуменяк Н.М. Дегидрирование порошкового гидрида титана и его роль в активации спекания. *Металлофизика и новейшие технологии*. 2011;33(7):899–917.
29. Raynova S., Yang F., Bolzoni L. Mechanical behaviour of induction sintered blended elemental powder metallurgy Ti alloys. *Materials Science and Engineering: A*. 2020;799:140–157.
<https://doi.org/10.1016/j.msea.2020.140157>
30. Weston N., Jackson M. FAST-forge – A new cost-effective hybrid processing route for consolidating titanium powder into near net shape forged components. *Journal of Materials Processing Technology*. 2017;243:335–346.
<https://doi.org/10.1016/j.jmatprotec.2016.12.013>
31. Careau S.G., Ulate-Kolitsky E., Tougas B. Direct powder forging – A new approach for near net shape processing of titanium. *Powders*. 2023;2(1):21–31.
<https://doi.org/10.3390/powders2010002>
32. Singh A.P., Gabbitas B., Zhang D. Fracture toughness of powder metallurgy and ingot titanium alloys – A review. *Key Engineering Materials*. 2013;551:143–160.
<https://doi.org/10.4028/www.scientific.net/KEM.551.143>
33. Romero C., Yang F., Bolzoni L. Fatigue and fracture properties of Ti alloys from powder-based processes – A review. *International Journal of Fatigue*. 2018;117:407–419.
<https://doi.org/10.1016/j.ijfatigue.2018.08.029>
34. Weston R. Anatomy of an AM part failure: Lessons for managers, designers and producers from 2021’s Olympic bike crash. *Additive Manufacturing*. 2022;8(2):115–125. URL: <https://www.metal-am.com/articles/anatomy-of-an-am-part-failure-lessons-for-managers-designers-and-producers-from-2021s-olympic-bike-crash/>
35. Baker J. An investigation into the handlebar failure that occurred in the Australian men’s team pursuit race at the Tokyo 2020 Olympics. *Report*. 2022. 171 p. URL: https://assets.ausecycling.org.au/s3fs-public/2022-02/handlebar-9_21-ev-3_5-combined-inc-annexes-appendicies.pdf?utm_source=Metal+AM&utm_medium=magazine (Accessed: 30.04.2025).
36. Goncharov I.N. Method for processing titanium sponge and device for implementing the method: Author’s certificate 132409 (USSR). 1960.
Гончаров И.Н. Способ переработки титановой губки и устройство для осуществления способа: Авт. св-во 132409 (СССР). 1960.
37. Olsson L.R., Lampe V., Fischmeister H. Direct forging of high-alloy steel powders to bar stock. *Powder Metallurgy*. 1974;17(34):347–362.
<https://doi.org/10.1179/pom.17.34.1974.007>
38. Careau S.G., Bernard Tougas B., Ulate-Kolitsky E. Effect of direct powder forging process on the mechanical properties and microstructural of Ti–6Al–4V ELI. *Materials*. 2021;14(16):4499.
<https://doi.org/10.3390/ma14164499>
39. ASTM F136-21. Standard specification for wrought titanium–6aluminium–4vanadium ELI (Extra Low Interstitial)

- alloy for surgical implant applications (UNS R56401). West Conshohocken, PA: ASTM International, 2018. 5 p.
40. Pavlov V.A., Kiparisov S.S., Shcherbina V.V. Pressure treatment of non-ferrous metal powders. Moscow: Metallurgiya, 1977. 170 p. (In Russ.).
Павлов В.А., Кипарисов С.С., Щербина В.В. Обработка давлением порошков цветных металлов. М.: Metallurgiya, 1977. 170 с.
 41. Pavlov V.A. Pressure processing of non-ferrous metal powders. Zaporozhye: Motor Sich OJSC, 2010. 347 p. (In Russ.).
Павлов В.А. Обработка давлением порошков цветных металлов. Запорожье: ОАО «Мотор Сич», 2010. 347 с.
 42. Dorofeyev Yu.G. Dynamic hot pressing of porous materials. Moscow: Nauka, 1968. 120 p. (In Russ.).
Дорофеев Ю.Г. Динамическое горячее прессование пористых материалов. М.: Наука, 1968. 120 с.
 43. Dorofeyev Yu.G. Dynamic hot pressing in metal ceramics. Moscow: Metallurgiya, 1972. 176 p. (In Russ.).
Дорофеев Ю.Г. Динамическое горячее прессование в металлокерамике. М.: Metallurgiya, 1972. 176 с.
 44. Roman O.V., Shuganov A.D., Smirnov G.V. High-energy technologies based on the use of explosives. In: *50 years of powder metallurgy in Belarus. History, achievements, prospects*. Minsk: PM SSPA, 2010. P. 583–601. (In Russ.).
Роман О.В., Шуганов А.Д., Смирнов Г.В. Высокоэнергетические технологии, основанные на применении взрывчатых веществ. В сб.: *50 лет порошковой металлургии Беларуси. История, достижения, перспективы*. Минск: ГНПО порошковой металлургии, 2010. С. 583–601.
 45. Brown W.F.Jr., Srawley J.E. Plane strain crack toughness testing of high strength metallic materials. In: *Plane Strain Crack Toughness Testing of High Strength Metallic Materials*. Ed. Committee E-24. West Conshohocken, PA: ASTM International, 1966. 129 p.
<https://doi.org/https://doi.org/10.1520/STP44663S>
 46. Murphy Th.F., Lindsley B. Metallographic analysis of PM fracture surfaces. 15 p. URL: <https://studylib.net/doc/10702066/metallographic-analysis-of-pm-fracture-surfaces--hoeganae...> (Accessed: 30.04.2025).
 47. Mazharova G.E., Komanovskii A.Z., Chechulin B.B., Vazhenin S.F. Pressure treatment of titanium alloys. Moscow: Metallurgiya, 1977. 96 p. (In Russ.).
Мажарова Г.Е., Комановский А.З., Чечулин Б.Б., Вазенин С.Ф. Обработка титановых сплавов давлением. М.: Metallurgiya, 1977. 96 с.
 48. Ilarionov A.G., Popov A.A. Technological and operational properties of titanium alloys. Yekaterinburg: Publishing house of the Ural University, 2014. 137 p. (In Russ.).
Илларионов А.Г., Попов А.А. Технологические и эксплуатационные свойства титановых сплавов. Екатеринбург: Изд-во Уральского ун-та, 2014. 137 с.
 49. Salishchev G.A., Kajbyshev O.A., Gordienko E.G., Chernyakov M.I. Influence of initial structure on superplasticity effect of VTZ-1 titanium alloy. *Izvestiya. Non-Ferrous Metallurgy*. 1976;4:104–107. (In Russ.).
Салищев Г.А., Кайбышев О.А., Гордиенко Е.Г., Черняков М.И. Влияние исходной структуры на эффект сверхпластичности титанового сплава ВТЗ-1. *Известия вузов. Цветная металлургия*. 1976;4:104–107.
 50. Aleksandrov V.K., Anoshkin N.F., Belozеров A.P., Bovchar G.A., Brun M.Ya., Ermanok M.Z. Semi-finished products from titanium alloys. Moscow: ONTI VILS, 1996. 581 p. (In Russ.).
Александров В.К., Аношкин Н.Ф., Белозеров А.П., Бовчар Г.А., Брун М.Я., Ерманок М.З. Полуфабрикаты из титановых сплавов. М.: ОНТИ ВИЛС, 1996. 581 с.
 51. Berdonosov S.S. Titan. In: *Physical Encyclopedia*. (Ed. A.M. Prokhorov). Moscow: Bol'shaya rossiiskaya entsiklopediya, 1994. Vol. 4. 704 p.
Бердоносоев С.С. Титан. В кн.: *Физическая энциклопедия*. В 5 т. (гл. ред. А.М. Прохоров). М.: Большая российская энциклопедия, 1994. Т. 4. 704 с.
 52. Robertson I.M., Schaffer G.B. Some Effects of particle size on the sintering of titanium and a master sintering curve model. *Metallurgical and Materials Transactions A*. 2009;40A: 1968–1979.
<https://doi.org/10.1007/s11661-009-9894-1>
 53. Dorofeyev Yu.G., Popov S.N. Welding together of metals during dynamic hot pressing. *Soviet Powder Metallurgy and Metal Ceramics*. 1971;10(2):118–124.
<https://doi.org/10.1007/BF00796409>
Дорофеев Ю.Г., Попов С.Н. Исследование сращивания металлов при динамическом горячем прессовании. *Порошковая металлургия*. 1971;98(2):44–51.

Information about the Authors

Vladimir Yu. Dorofeyev – Dr. Sci. (Eng.), Professor of the Department of material science and engineering technology, Platov South-Russian State Polytechnic University (NPI), (PSRSPU (NPI))

 **ORCID:** 0000-0001-6743-1727

 **E-mail:** dvuyu56.56@mail.ru

Anna N. Sviridova – Cand. Sci. (Eng.), Associate Prof. of the Department of Automobiles and Transport-Technological Complexes, PSRSPU (NPI)

 **ORCID:** 0000-0002-9851-1073

 **E-mail:** anysviridova@yandex.ru

Сведения об авторах

Владимир Юрьевич Дорофеев – д.т.н., профессор кафедры «Материаловедение и технология машиностроения», Южно-Российский государственный политехнический университет (НПИ) имени М.И. Платова (ЮРГПУ (НПИ))

 **ORCID:** 0000-0001-6743-1727

 **E-mail:** dvuyu56.56@mail.ru

Анна Николаевна Свиридова – к.т.н., доцент кафедры «Автомобили и транспортно-технологические комплексы», ЮРГПУ (НПИ)

 **ORCID:** 0000-0002-9851-1073


 **E-mail:** anysviridova@yandex.ru


Svetlana V. Sviridova – Resident of the Institute of Medicine and Health Preservation, Tambov State University named after G.R. Derzhavin

 **ORCID:** 0009-0007-5260-3726


 **E-mail:** dr.sviridova27@inbox.ru

Lev I. Svistun – Dr. Sci. (Eng.), Professor of the Department of Engineering of Control Systems, Materials and Technologies in Mechanical Engineering, Kuban State Technological University

 **ORCID:** 0009-0001-8552-2582

 **E-mail:** levsvistun45@gmail.com

Светлана Владимировна Свиридова – ординатор института медицины и здоровьесбережения, Тамбовский государственный университет имени Г.Р. Державина

 **ORCID:** 0009-0007-5260-3726

 **E-mail:** dr.sviridova27@inbox.ru

Лев Иванович Свистун – д.т.н., профессор кафедры инженерии систем управления, материалов и технологий в машиностроении, Кубанский государственный технологический университет

 **ORCID:** 0009-0001-8552-2582

 **E-mail:** levsvistun45@gmail.com

Contribution of the Authors



Вклад авторов

V. Yu. Dorofeyev – scientific supervision, formulation of research objectives and tasks, manuscript preparation, and drafting of conclusions.

A. N. Sviridova – mechanical testing and analysis of research results.

S. V. Sviridova – structural and compositional analysis of experimental samples.

L. I. Svistun – preparation and execution of the experiment, supervision of experimental work.

В. Ю. Дорофеев – научное руководство, постановка цели и задачи исследования, подготовка текста, формулировка выводов.

А. Н. Свиридова – проведение механических испытаний, анализ результатов исследований.

С. В. Свиридова – проведение исследований структуры и состава опытных образцов.

Л. И. Свистун – подготовка и проведение эксперимента, руководство проведением эксперимента.

Received 11.05.2025

Revised 19.05.2025

Accepted 30.05.2025

Статья поступила 11.05.2025 г.

Доработана 19.05.2025 г.

Принята к публикации 30.05.2025 г.



Self-Propagating High-Temperature Synthesis Самораспространяющийся высокотемпературный синтез



UDC 621.762

<https://doi.org/10.17073/1997-308X-2025-4-40-49>

Research article
Научная статья



Mechanism of synthesis of ultra-high temperature Ta_4ZrC_5 carbide by thermal explosion with preliminary mechanical alloying of metals

S. G. Vadchenko[✉], A. S. Rogachev, M. I. Alymov

Merzhanov Institute of Structural Macrokinetics and Materials Science of the Russian Academy of Sciences
8 Akademian Osip'yan Str., Chernogolovka, Moscow region 142432, Russia

[✉] vadchenko@ism.ac.ru

Abstract. Tantalum–zirconium carbide Ta_4ZrC_5 was synthesized by the method of self-propagating high-temperature synthesis (SHS) in the thermal explosion mode. The mechanism of its formation was investigated, including processes occurring during the heating of precursor mixtures to the ignition temperature, which proceed in the solid phase. The interaction of molten bimetallic Ta_4Zr particles with carbon was also studied. The initial powder mixtures were prepared in two stages. In the first stage, high-energy ball milling (HEBM) in an AGO-2 mill under an argon atmosphere was employed to carry out mechanical alloying (MA) of tantalum with zirconium, resulting in the formation of bimetallic Ta_4Zr particles representing a solid solution of zirconium in tantalum. Upon heating, ordering of the solid solution occurred, accompanied by a small exothermic effect depending on the MA duration. In the second stage, the obtained Ta_4Zr powder was mixed with carbon black and heated to the thermal explosion temperature (900–1250 °C), leading to the formation of Ta_4ZrC_5 . For the first time, to study the mechanism of high-temperature interaction of Ta_4Zr bimetallic particles with carbon, the particles were deposited onto a graphite substrate and heated in vacuum at a residual pressure of 10^{-3} Pa, with the substrate temperature reaching up to 3000 °C. Depending on particle size, two modes of interaction of molten Ta_4Zr particles with the graphite substrate were observed. Particles smaller than 10 μm , due to surface tension forces, did not spread on the substrate upon melting; instead, they absorbed carbon and sank into it. Larger particles spread over the substrate, with the melt being depleted in zirconium, which more actively interacted with carbon.

Keywords: refractory compounds, high-energy ball milling (HEBM), mechanical alloying (MA), carbides

For citation: Vadchenko S.G., Rogachev A.S., Alymov M.I. Mechanism of synthesis of ultra-high temperature Ta_4ZrC_5 carbide by thermal explosion with preliminary mechanical alloying of metals. *Powder Metallurgy and Functional Coatings*. 2025;19(4):40–49. <https://doi.org/10.17073/1997-308X-2025-4-40-49>

Механизм синтеза ультратугоплавкого карбида Ta_4ZrC_5 в режиме теплового взрыва с предварительным механическим сплавлением металлов

С. Г. Вадченко[✉], А. С. Рогачев, М. И. Алымов

Институт структурной макрокинетики и проблем материаловедения им. А.Г. Мерзанова РАН
Россия, 142432, Московская обл., г. Черноголовка, ул. Академика Осипьяна, 8

[✉] vadchenko@ism.ac.ru

Аннотация. Методом самораспространяющегося высокотемпературного синтеза (СВС) в режиме теплового взрыва получен карбид Ta_4ZrC_5 . Изучен механизм его формирования, включающий процессы в ходе нагрева смесей прекурсоров до температуры воспламенения, протекающие в твердой фазе. Исследовано взаимодействие расплавленных биметаллических частиц состава Ta_4Zr с углеродом. Исходные смеси порошков готовили в две стадии. На первой – методом высокоэнергетической механической обработки (ВЭМО) в активаторе АГО-2 в атмосфере аргона происходило механическое сплавление (МС)

смеси тантала с цирконием и формировались биметаллические частицы состава Ta_4Zr , представляющие собой твердый раствор циркония в тантале. При их нагреве происходило упорядочение твердого раствора и наблюдалось небольшое тепловыделение, зависящее от времени МС. На второй стадии полученный порошок Ta_4Zr смешивали с сажей и нагревали до температуры теплового взрыва (900–1250 °С), в результате которого образовывалось соединение Ta_4ZrC_5 . Впервые для исследования механизма высокотемпературного взаимодействия биметаллических частиц Ta_4Zr с углеродом их нанесли на подложку из графита и нагревали в вакууме при остаточном давлении 10^{-3} Па и температуре подложки до 3000 °С. В зависимости от размера частиц наблюдались два режима взаимодействия расплавленных частиц Ta_4Zr с подложкой из графита. Частицы размером менее 10 мкм из-за сил поверхностного натяжения при плавлении не растекались по подложке, а, растворяя в себе углерод, в нее погружались. Частицы большего размера растекались по подложке, причем расплав обеднялся цирконием, который более активно взаимодействовал с углеродом.

Ключевые слова: тугоплавкие соединения, высокоэнергетическая механическая обработка (ВЭМО), механическое сплавление (МС), карбиды

Для цитирования: Вадченко С.Г., Рогачев А.С., Алымов М.И. Механизм синтеза ультратугоплавкого карбида Ta_4ZrC_5 в режиме теплового взрыва с предварительным механическим сплавлением металлов. *Известия вузов. Порошковая металлургия и функциональные покрытия*. 2025;19(4):40–49. <https://doi.org/10.17073/1997-308X-2025-4-40-49>

Introduction

Binary carbides of the Ta–Zr–C system are considered promising candidates for the development of ultra-high temperature ceramics (UHTCs) [1–8]. Despite extensive research on this system, the available literature data remain contradictory, with the central question concerning the possibility of forming a single-phase carbide $Ta_{1-x}Zr_xC$. Calculation of the phase diagram of the binary Ta–Zr system has shown that below 800 °C these two metals are practically immiscible [6]. In this temperature range, a mixture of two solid solutions is formed: one based on α -zirconium with an HCP structure and the other based on tantalum with a BCC structure. The solubility of tantalum in zirconium does not exceed 2 at. %, while that of zirconium in tantalum is less than 9 at. %. A continuous series of solid solutions with a BCC structure is formed only near 1700 °C [6].

Thermodynamic investigation of the Ta–Zr–C system using the CALPHAD method led to the paradoxical conclusion that no ternary phases exist within the temperature range of 200–3600 °C [7]. This conclusion contradicts the results obtained using the CASTEP (*Cambridge Serial Total Energy Package*) code, which demonstrated the stability of $Ta_{1-x}Zr_xC$ and its structural similarity to the ultra-high temperature carbide Ta_4HfC_5 [8]. The stability of the $Ta_{1-x}Zr_xC$ phase was also demonstrated by first-principles calculations and confirmed experimentally in [9]. In particular, binary carbides with $x = 0.9, 0.8, 0.6$, and 0.3 , synthesized by self-propagating high-temperature synthesis (SHS) from mechanically activated Ta–Zr–C mixtures and consolidated by hot pressing, showed no signs of decomposition into simple carbides after annealing at 800 °C for 40 h. Preliminary mechanical activation promotes the formation of a more homogeneous reactive mixture, enabling the synthesis of binary carbide

under SHS conditions [10–12]. Along with hot pressing, a highly promising method for consolidating complex UHTCs is spark plasma sintering (SPS), in which synthesis and densification occur simultaneously [13–18]. Samples of $Ta_{1-x}Zr_xC$ UHTCs have also been produced using an original electrothermal explosion technique [19].

In studies devoted to the synthesis of $Ta_{1-x}Zr_xC$ by SHS, the primary focus has been placed on ignition and combustion parameters. The processes occurring during the preheating stage prior to ignition and the mechanism of molten metal interaction with carbon remain largely unexplored.

The aim of this work was to experimentally investigate the macrokinetic characteristics of mechanical alloying, thermal explosion, and heating of the resulting Ta_4Zr bimetallic particles, as well as the high-temperature interactions in the Ta–Zr–C system leading to the formation of $Ta_{1-x}Zr_xC$ carbide.

Materials and methods

Commercially produced powders manufactured in the Russian Federation were used in this study:

- tantalum powder, grade TaP-1 (TU 1870-258-00196109-01), 99.9 wt. % purity, particle size $d = 40\text{--}63\text{ }\mu\text{m}$;
- zirconium powder, grade PTsRK (TU 48-4-234-84), 99.6 wt. % purity, particle size $d = 40\text{--}63\text{ }\mu\text{m}$;
- carbon black, grade P804T, particle size $d < 2.2\text{ }\mu\text{m}$.

High-energy ball milling (HEBM) of tantalum and zirconium powder mixtures in a molar ratio of 4Ta:Zr was carried out in an AGO-2 planetary ball mill under an argon atmosphere. The rotational speed of the steel vials was 2220 rpm, the mass of powder mixtures was 10 g, and the mass of steel balls was 200 g. The mill-

ing time varied from 2 to 30 min. After processing and removal of the vials from the mill, their surface was heated to above 100 °C; therefore, the vials were opened only after several hours of cooling to room temperature.

As a result of HEBM, a Ta₄Zr alloy powder was obtained, a significant portion of which (up to 50 wt. %) adhered to the balls and vial walls. To grind and recover more of the alloy powder, 30 ml of hexane was added to the vials, followed by additional HEBM for 3 min. After drying, carbon black was added to the Ta₄Zr alloy powder in stoichiometric proportion to obtain Ta₄ZrC₅, and the mixture was homogenized in the AGO-2 planetary ball mill for 3–5 min.

The processes occurring during heating of Ta₄Zr alloy and during thermal explosion in the Ta₄Zr + 5C and 4Ta + Zr + 5C mixtures were studied using the setup described in [20]. Cylindrical samples, 3 mm in diameter and up to 1.5 mm in height, were pressed from the powder mixtures and placed in a boron nitride crucible on a WRe 5/20 thermocouple rolled to a thickness of 30 µm. The crucible was positioned on a graphite strip heated by electric current. The samples were heated under constant electrical power supplied to the graphite strip, in argon at atmospheric pressure. The heating rate and maximum temperature were controlled by adjusting the electrical power. After ignition of the pellets, heating of the strip was stopped. The accuracy of temperature measurement, determined

using the melting points of Zn, Al, and Cu as reference standards, was ±10 °C.

Melting and reaction of Ta₄Zr alloy powders with carbon were investigated in a VUP-5 vacuum system at a pressure of 1.3·10⁻³ Pa. The powders were placed on substrates (25×5×1 mm) of fine-pored graphite (GMP) or glassy carbon (SU-2500), which were heated by direct current with a power of 1–4 kW [21]. The substrate had a fillet-like shape, allowing the narrow section to reach temperatures above 3000 °C. Before the reaction, the substrate was degassed by heating in vacuum to ~3000 °C. After cooling, bimetallic powders were deposited on its surface.

Results and discussion

Mechanical alloying

During high-energy ball milling (HEBM) of the 4Ta + Zr powder mixture, the combined effects of friction, rolling, and impacts result in mechanical alloying (MA) of tantalum and zirconium particles. Adhesion of the powder mixture to the milling balls allows observation of alloy formation in their cross-sections (Fig. 1, *a*). Initially, bimetallic layers form on the balls, which, after repeated cycles of deformation, detachment, and fracture, produce particles with a structure similar to that shown in Fig. 1, *b–d*. With increasing milling time, both the coating and the alloy particles formed upon its fracture become

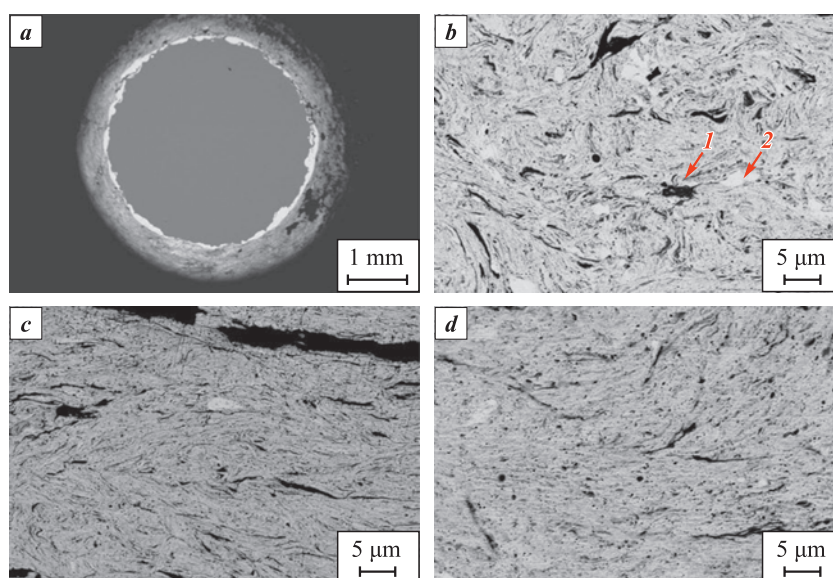


Fig. 1. Cross-section of a ball after MA of the 4Ta + Zr mixture (*a*) and fragments of the cross-section of the coating layer after HEBM for 2 (*b*), 3 (*c*) and 5 min (*d*)

1 – pore, 2 – tantalum particle. The light regions correspond to a higher tantalum concentration

Рис. 1. Сечение шара после МС смеси 4Ta + Zr (*a*) и фрагменты сечения слоя смеси после ВЭМО в течение 2 (*b*), 3 (*c*) и 5 мин (*d*)

1 – пора, 2 – частица тантала. Светлые слои содержат более высокую концентрацию тантала

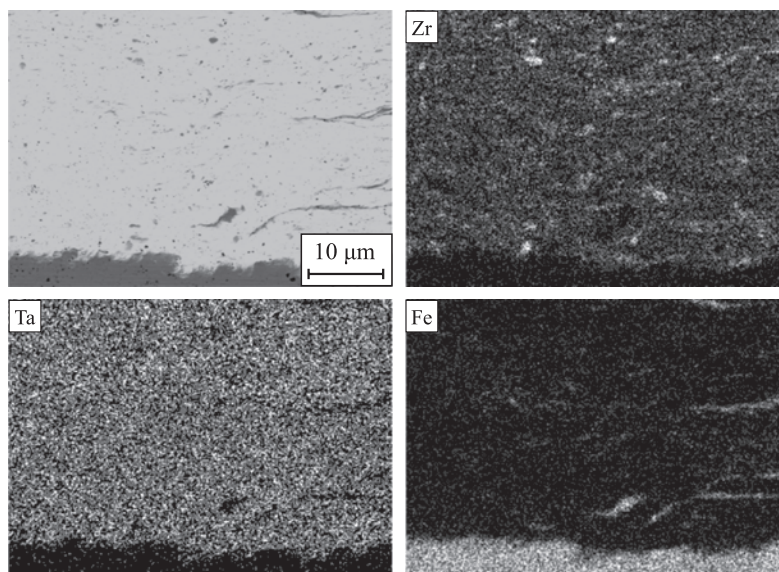


Fig. 2. Elemental distribution maps after MA of the 4Ta + Zr mixture for 10 min

Рис. 2. Карты распределения элементов после МС смеси 4Ta + Zr в течение 10 мин

more homogeneous (Fig. 2). Elemental distribution maps across particle cross-sections reveal that after 10 min of HEBM, large zirconium particles and steel fragments abraded from the milling balls are not fully broken down. Iron contamination originating from the abrasion of the steel balls and vials is an undesirable characteristic of HEBM, as it contaminates the product. The processes of particle fragmentation and iron contamination become especially pronounced during HEBM in hexane, due to the wedge action of the liquid (Rebinder effect).

At mechanical alloying times up to 5 min, complete homogenization of the alloy was not achieved; therefore, the duration was increased to 10–30 min. However, even in this case, the elemental distribution remained insufficiently uniform (see Fig. 2). Further prolongation of milling time led to significant contamination of the Ta₄Zr alloy with iron, and thus the MA time was limited to 30 min.

Results of X-ray diffraction analysis of the bimetallic powders

Fig. 3 shows the diffraction patterns of powders at different stages of mechanical alloying. The zirconium powder used contains some zirconium hydride, originating from the hydride–calcium reduction process by which it was produced. During MA, zirconium hydride decomposes with the release of hydrogen, and its diffraction peaks, along with those of zirconium, disappear after only 3 min of MA. This disappearance may be associated both with the refinement of zirconium crystallites and with its dissolution in tantalum.

As shown in Fig. 2, complete dissolution of zirconium does not occur even after 10 min of milling, and moreover, the mutual solubility of Zr and Ta is quite limited [6]. Therefore, the most likely reason for the disappearance of the peaks is intensive plastic deformation of zirconium, which results in crystallite refinement (reduction of coherent scattering domain size) and peak broadening. After 30 min of MA, the dif-

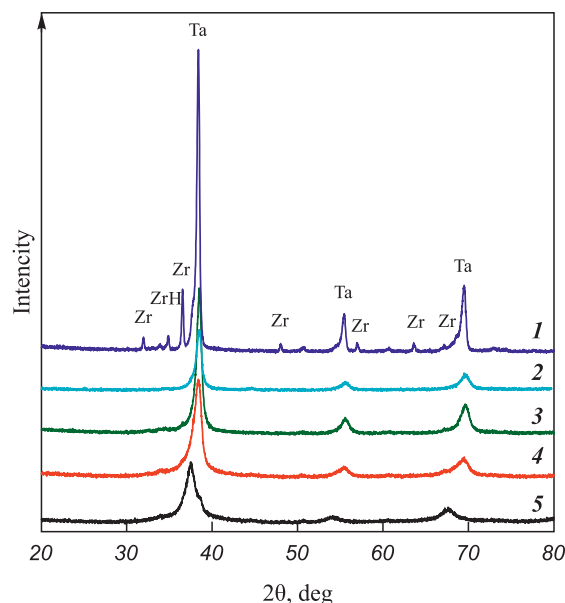


Fig. 3. XRD patterns of powders after different durations of MA
 τ_{MA} , min: 0 (1), 3 (2), 10 (3), 20 (4) and 30 (5)

Рис. 3. Дифрактограммы порошков после различной длительности МС
 $\tau_{МС}$, мин: 0 (1), 3 (2), 10 (3), 20 (4) и 30 (5)

fraction pattern exhibits three strongly broadened peaks characteristic of the BCC structure. The asymmetric shape of the most intense peak suggests the presence of two phases with closely spaced interplanar distances. Such a diffraction pattern may indicate the coexistence of two BCC solid solutions based on Ta.

Heating of bimetallic powders and ignition of their mixtures with carbon black

Fig. 4 shows the thermograms of primary and repeated heating of samples prepared from the initial $4Ta + Zr$ mixtures (curves *1a* and *1b*), Ta_4Zr bimetallic particles obtained by MA for 10 and 30 min (curves *2a*, *2b* and *3a*, *3b*, respectively), and the $Ta_4Zr + 5C$ mixture (curves *4a*, *4b*). The inflections in the thermograms in the temperature range of 700–900 °C (curve 3) are associated with the $\alpha \rightarrow \beta$ phase transition in zirconium. Tantalum lowers the transition temperature from 863 to 800–785 °C [22; 23]. According to the phase diagram of the Zr–Fe system, dissolution of more than 4 at. % Fe in tantalum also reduces the $\alpha \rightarrow \beta$ transition temperature in zirconium to 785 °C [22]. Increasing the MA time to 30 min leads to a clearer manifestation of this phase transition during powder heating. Above the phase transition temperature, an exothermic effect is observed. Heat release is proportional to the area under the Δt curve, which repre-

sents the temperature difference between the primary and repeated heating of the mixtures (curves *1c–4c*). The exothermic effect increases with milling time and is most likely caused by the interaction of Ta_4Zr alloy with the abraded iron. During ignition and combustion, however, this reaction contributes only a small fraction of the heat release. For example, the enthalpy of formation of Zr_3Fe ($\Delta H(298.15) = -13.51$ kJ/mol) [6] is an order of magnitude smaller than that for the carbides ZrC ($\Delta H(298.15) = -207.1$ kJ/mol) and TaC ($\Delta H(298.15) = -141.8$ kJ/mol) [24]. This is confirmed by the heating curves of the $Ta_4Zr + 5C$ mixture (see Fig. 4, curves *4a*, *4b*, *4c*).

Fig. 5 presents the results of studying the effect of heating and thermal explosion on the phase composition of powders. Curves 1 and 2 correspond to a BCC solid solution, while curve 3 represents the Ta_4ZrC_5 compound with an FCC structure. During heating of $Ta_4Zr + 5C$ mixtures to the ignition temperature, ordering of the alloy structure occurs. This is evident from the reduced peak broadening and peak shifts in the diffraction pattern of Ta_4Zr bimetallic particles after short-term heating in argon (curve 2 in Fig. 5). Their reaction with carbon leads to the formation of an alloy close in composition to Ta_4ZrC_5 , although in some experiments traces of Ta and its carbide Ta_2C were observed at the background level in the diffraction patterns. This can be attributed to incomplete homogeni-

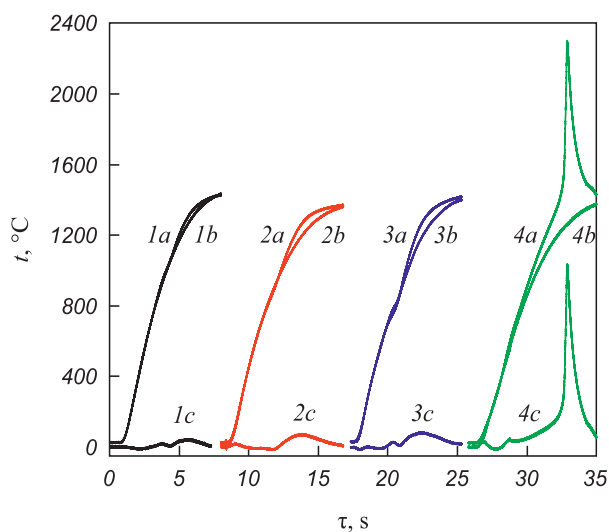


Fig. 4. Thermograms of heating of the initial $4Ta + Zr$ mixture (*1a*), Ta_4Zr bimetallic particles after 10 min of MA (*2a*) and 30 min of MA (*3a*), and the $Ta_4Zr + 5C$ mixture (*4a*)

1b–4b – repeated heating; *1c–4c* – temperature difference (Δt)

Рис. 4. Термограммы нагрева исходной смеси $4Ta + Zr$ (*1a*), биметаллических частиц Ta_4Zr после 10 мин МС (*2a*) и 30 мин МС (*3a*), а также смеси $Ta_4Zr + 5C$ (*4a*)

1b–4b – повторный нагрев; *1c–4c* – разность температур (Δt)

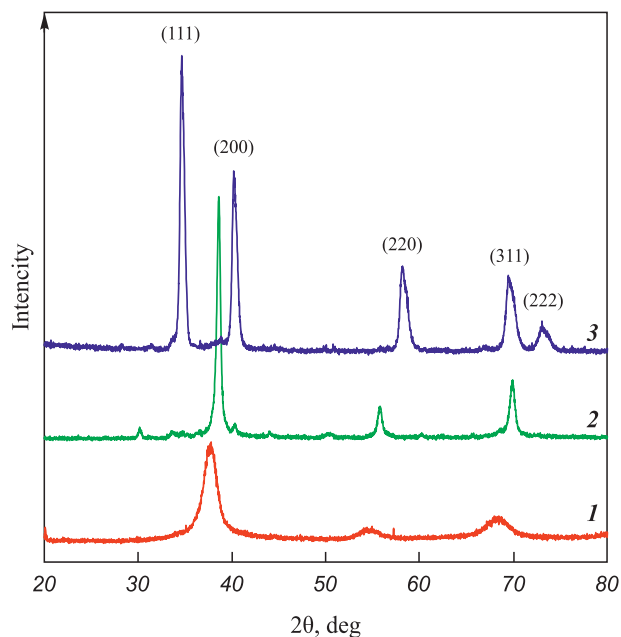


Fig. 5. XRD patterns of bimetallic powder after 30 min of MA (*1*), heating to 1400 °C for 10 s (*2*), and thermal explosion products (*3*)

Рис. 5. Дифрактограммы биметаллического порошка после 30 мин МС (*1*), нагрева до 1400 °C в течение 10 с (*2*) и продуктов теплового взрыва (*3*)

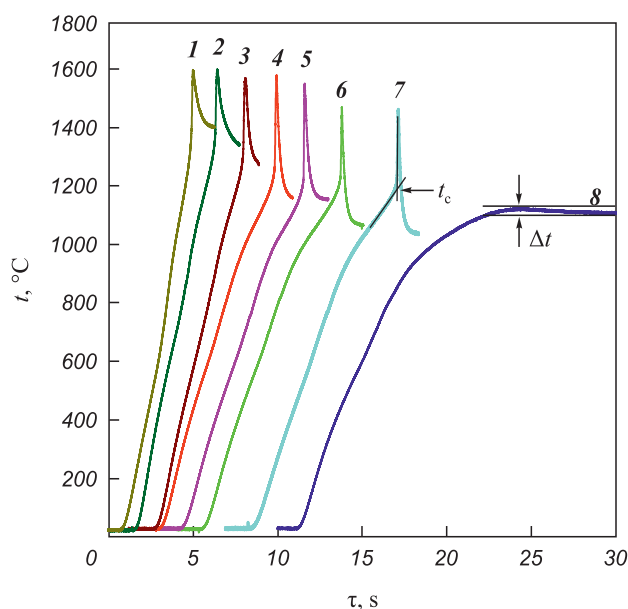


Fig. 6. Thermograms of ignition of $\text{Ta}_4\text{Zr} + 5\text{C}$ mixtures at different average initial heating rates

ν , $^{\circ}\text{C/s}$: 277 (1), 275 (2), 260 (3), 205 (4), 195 (5), 190 (6), 185 (7), 180 (8)

Рис. 6. Термограммы воспламенения образцов из смеси $\text{Ta}_4\text{Zr} + 5\text{C}$ при изменении средней начальной скорости нагрева

ν , $^{\circ}\text{C/c}$: 277 (1), 275 (2), 260 (3), 205 (4), 195 (5), 190 (6), 185 (7), 180 (8)

zation of the Ta_4Zr alloy at HEBM times shorter than 60 min.

Fig. 6 shows the thermograms of Ta_4Zr bimetallic particles ($\tau_{\text{MC}} = 5$ min) mixed with carbon black and heated at different heating rates (ν). Below 1100°C , heating does not lead to ignition (Fig. 6, curve 8). The critical ignition temperature (t_c) corresponds to the intersection of tangents drawn to the heating section of the sample and to the steep temperature rise. The value of t_c depends on the duration of MA and the mixing time of bimetallic powders with carbon black, and may vary within $900\text{--}1250^{\circ}\text{C}$. With increasing heating rate, the ignition temperature t_c also increases (Fig. 7).

Experimental results show that the ignition temperature of the mixture is significantly lower than the melting points of zirconium (1852°C) and Ta_4Zr alloy ($1855\text{--}2600^{\circ}\text{C}$, depending on the degree of homogeneity) [14]. Thermodynamic calculations for the ternary system [7] also indicate that a liquid phase appears only above 1800°C . The heating of $\text{Ta}_4\text{Zr} + 5\text{C}$ powder mixtures observed in the $900\text{--}1100^{\circ}\text{C}$ range, followed by their ignition, demonstrates that the reaction initiates in the solid state. The calculated adiabatic combustion temperatures using the Thermo software [25] for the reaction $4\text{Ta} + \text{Zr} + 5\text{C} = 4\text{TaC} + \text{ZrC}$ are 2640 and 3180°C at initial temperatures of 25 and 900°C ,

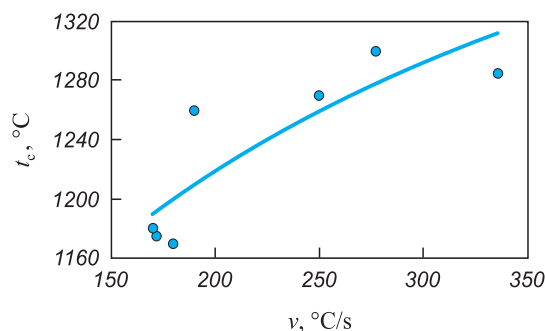


Fig. 7. Dependence of the critical ignition temperature of $\text{Ta}_4\text{Zr} + 5\text{C}$ mixtures on the heating rate

Рис. 7. Зависимость критической температуры воспламенения смесей $\text{Ta}_4\text{Zr} + 5\text{C}$ от скорости нагрева образцов

respectively. Thus, during thermal explosion and in the combustion wave, the melting point of the bimetallic particles is reached, and the reaction proceeds via mass transport through the liquid phase.

X-ray diffraction analysis of the thermal explosion products shows the formation of a single-phase double carbide with a face-centered cubic (FCC) structure (curve 3 in Fig. 5).

High-temperature interaction of Ta_4Zr melt with carbon

The study of high-temperature reaction mechanisms is complicated by the rapid processes occurring in the combustion wave. To investigate the interaction of Ta_4Zr melt with carbon, model experiments were conducted. In these, Ta_4Zr and Ta particles were placed on graphite or glassy carbon substrates, heated to the melting point of tantalum, and held for $10\text{--}30$ s. The melting of Ta (99.9% purity, melting point 2996°C) served as a reference for estimating substrate temperature. Energy-dispersive X-ray analysis showed that iron impurities present in the initial particles were absent after heating, explained by their evaporation.

The interaction of particles with the substrate depends on particle size. Small particles ($d < 10\ \mu\text{m}$) did not spread under the action of surface tension forces but instead dissolved carbon and sank into the substrate (Fig. 8). This behavior is governed by the ratio between the spreading time (τ_s) and the carburization time (τ_d). For small particles, $\tau_s > \tau_d$, for large particles, $\tau_s < \tau_d$. The critical spreading time is determined by the relation $\tau_s \sim R^2/D$, where R is particle radius and D is the diffusion coefficient of carbon in the melt [26].

Melting begins at the contact point between the particle and the hot substrate. Therefore, during melting and spreading of particles larger than $10\ \mu\text{m}$, the reac-

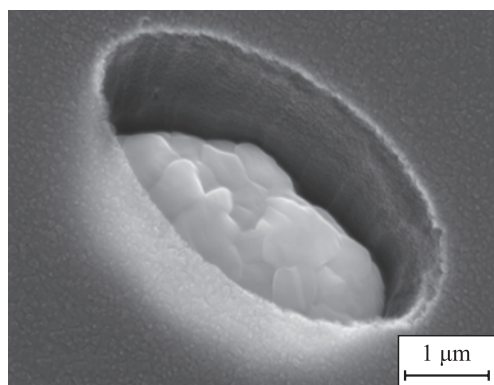


Fig. 8. Photograph of a Ta_4Zr particle that penetrated into a glassy carbon substrate upon melting

Рис. 8. Фотография частицы Ta_4Zr , погрузившейся при расплавлении в подложку из стеклогуглерода

tion initiates in the central region of the contact spot, producing a crater-like ring structure (Fig. 9).

The resulting droplets typically move along the substrate surface, leaving a trace. A characteristic feature of these structures is a reduced zirconium concentration on the surface of the spread droplet and an increased zirconium concentration in the imprint. This structure is most likely associated with the higher diffusivity of zirconium atoms in the melt and their strong affinity for carbon. In some cases, nearly all zirconium diffuses into the substrate (Fig. 10). In such cases, regions with zirconium concentrations close to the initial composition coexist with zirconium-depleted regions, which differ significantly in structure. The crater edges also exhibit high carbon content.



Spectrum	Content, at. %			
	C	Zr	Ta	Σ
1	9.6	3.3	87.1	100.0
2	35.7	1.7	62.6	100.0
3	15.6	16.6	67.8	100.0
4	11.3	10.4	78.3	100.0
5	98.1	1.2	0.7	100.0

Fig. 9. Photograph of a molten Ta_4Zr particle and results of its elemental analysis

Рис. 9. Фотография расплавленной частицы Ta_4Zr и результаты ее элементного анализа

Conclusions

An experimental study was conducted on the formation of the ultra-high temperature carbide Ta_4ZrC_5 by mechanical alloying in a planetary ball mill, fol-

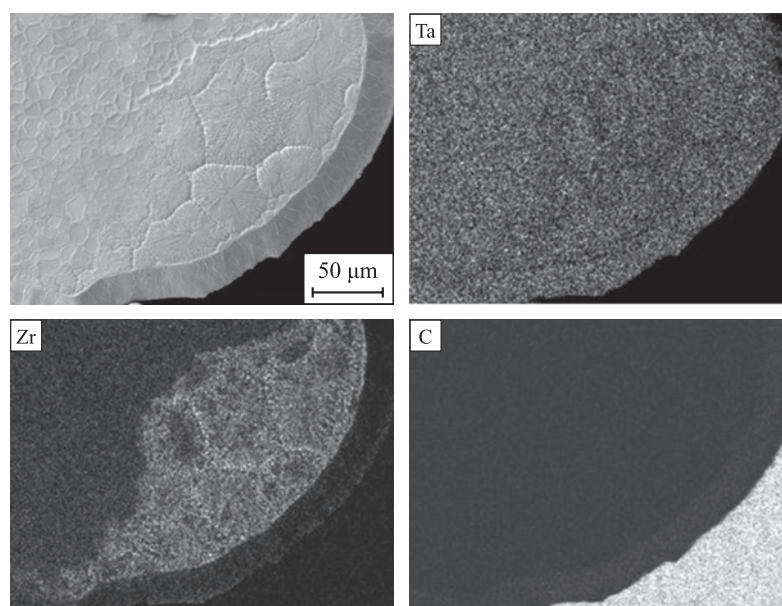


Fig. 10. Elemental distribution map of a molten particle

Рис. 10. Карты распределения элементов в расплавленной частице

lowed by synthesis in the thermal explosion mode. Model experiments simulating the processes of ignition and combustion in the high-temperature zone were also performed. The data obtained on the formation of bimetallic particles, ignition of their mixtures with carbon black, and high-temperature interaction with carbon provide new insights into the synthesis mechanism of ultra-high temperature carbides and their ceramic materials for high-temperature applications. The following conclusions can be drawn.

1. High-energy ball milling of 4Ta + Zr powder mixtures in a planetary mill yields BCC solid solutions that serve as initial reactants for subsequent synthesis. The mechanically alloyed powder consists of bimetallic particles with a characteristic layered (“compositional”) structure.

2. Mixtures of bimetallic powders with carbon black undergo self-ignition upon heating in argon at 900–1250 °C, depending on heating conditions. Since these temperatures are below the melting point of the bimetallic particles, the self-sustaining reaction is initiated by solid-phase interaction.

3. As a result of the exothermic reaction of the bimetallic particles with carbon, the temperature rapidly increases beyond the melting point of the metals. The final product is formed through the interaction of the metallic melt with carbon.

4. The product of synthesis in the thermal explosion mode is the ultra-high temperature carbide Ta₄ZrC₅.

5. Model high-temperature experiments in the “molten Ta₄Zr bimetallic particles–carbon” system revealed two size-dependent interaction mechanisms: large particles spread across the carbon substrate surface with preferential zirconium diffusion into the substrate, whereas small particles predominantly absorbed carbon.

References / Список литературы

- Andrievskii R.A., Strel'nikova N.S., Poltoratskii N.I., Kharkhardin E.D., Smirnov V.S. Melting point in systems ZrC–HfC, TaC–ZrC, TaC–HfC. *Powder Metallurgy and Metal Ceramics*. 1967;(6):65–67.
<https://doi.org/10.1007/BF00773385>
- Gusev A.I. Phase diagrams of the pseudo-binary TiC–NbC, TiC–TaC, ZrC–NbC, ZrC–TaC, and HfC–TaC carbide systems. *Russian Journal of Physical Chemistry A*. 1985;59:336–340.
Гусев А.И. Диаграммы состояния псевдобинарных карбидных систем TiC–NbC, TiC–TaC, ZrC–NbC, ZrC–TaC и HfC–TaC. *Журнал физической химии*. 1985; 59(3):579–584.
- Fan Z., Zhilin T., Bin L. Research progress on carbide ultra-high temperature ceramic anti-ablation coatings for thermal protection system. *Journal of Inorganic Materials*. 2025; 40(1):1–16.
<https://doi.org/10.15541/jim20240317>
- Farhadizadeh A., Ghomi H. Mechanical, structural, and thermodynamic properties of TaC–ZrC ultra-high temperature ceramics using first principle methods. *Materials Research Express*. 2020;7(3):1–10.
<https://doi.org/10.1088/2053-1591/ab79d2>
- Wang Y., Wen B., Jiao X., Li Y., Chen L., Wang Y., Dai F.-Z.. The highest melting point material: Searched by Bayesian global optimization with deep potential molecular dynamics. *Journal of Advanced Ceramics*. 2023;12(4):803–814.
<https://doi.org/10.26599/JAC.2023.9220721>
- Guillermet A.F. Phase diagram and thermochemical properties of the Zr–Ta system. An assessment based on Gibbs energy modeling. *Journal of Alloys and Compounds*. 1995;226(1–2):174–184.
[https://doi.org/10.1016/0925-8388\(95\)01582-5](https://doi.org/10.1016/0925-8388(95)01582-5)
- Zhou P., Peng Y., Du Y., Wang S., Wen G., Xie W., Chang K. A thermodynamic description of the C–Ta–Zr system. *International Journal of Refractory Metals and Hard Materials*. 2013;41:408–415.
<https://doi.org/10.1016/j.jrmhm.2013.05.015>
- Zhang S., Liu S., Yan D., Yu Q., Ren H., Yu B., Li D. Structural stability, hardness, fracture toughness and melting points of Ta_{1-x}Hf_xC and Ta_{1-x}Zr_xC ceramics from first-principles. *Research Square*. 25 March 2020, PREPRINT.
<https://doi.org/10.21203/rs.3.rs-19083/v1>
- Vorotilo S., Sidnov K., Mosyagin I. Yu., Khvan A.V., Levashov E.A., Patsera E.I., Abrikosov I.A. *Ab-initio* modeling and experimental investigation of properties of ultra-high temperature solid solutions Ta_xZr_{1-x}C. *Journal of Alloys and Compounds*. 2019;778:480–486.
<https://doi.org/10.1016/j.jallcom.2018.11.219>
- Kurbatkina V.V., Patsera E.I., Levashov E.A., Vorotylo S.A., Timofeev A.N. Impact of mechanical activation pattern and conditions on carbide formation in Ta–Zr–C SHS system. *Powder Metallurgy and Functional Coatings*. 2016;(2):30–40. (In Russ.).
<https://doi.org/10.17073/1997-308X-2016-2-30-40>
Курбаткина В.В., Пацера Е.И., Левашов Е.А., Воротыло С.А., Тимофеев А.Н. Влияние схемы и условий механического активирования на карбидообразование в СВС-системе Та–Зр–С. *Известия вузов. Порошковая металлургия и функциональные покрытия*. 2016;2:30–40.
<https://doi.org/10.17073/1997-308X-2016-2-30-40>
- Kurbatkina V.V., Patsera E.I., Vorotilo S., Levashov E.A., Timofeev A.N. Conditions for fabricating single-phase (Ta,Zr)C carbide by SHS from mechanically activated reaction mixtures. *Ceramic International Journal*. 2016;42(15):16491–16498.
<https://doi.org/10.1016/j.ceramint.2016.06.207>
- Patsera E.I., Levashov E.A., Kurbatkina V.V., Kovalev D.Yu. Production of ultra-high temperature carbide (Ta,Zr)C by self-propagating high-temperature synthesis of mechanically activated mixtures. *Ceramic International Journal*. 2015;41(7):8885–8893.
<https://doi.org/10.1016/j.ceramint.2015.03.146>

13. Demirskyi D., Nishimura T., Suzuki T.S., Yoshimi K., Vasylykiv O. Consolidation and high-temperature properties of ceramics in the TaC–NbC system. *Journal of the American Ceramic Society*. 2022;105:7567–7581. <https://doi.org/10.1111/jace.18660>
14. Demirskyi D., Suzuki T.S., Yoshimi K., Vasylykiv O. Synthesis and high-temperature properties of medium-entropy (Ti,Ta,Zr,Nb)C using the spark plasma consolidation of carbide powders. *Open Ceramics*. 2020;2:100015. <https://doi.org/10.1016/J.OCERAM.2020.100015>
15. Demirskyi D., Borodianska H., Suzuki T.S., Sakka Y., Yoshimi K., Vasylykiv O. High-temperature flexural strength performance of ternary high-entropy carbide consolidated via spark plasma sintering of TaC, ZrC and NbC. *Scripta Materialia*. 2019;164:2–16. <https://doi.org/10.1016/J.SCRIPTAMAT.2019.01.024>
16. Stacy J., Hilmas G., Watts J., Taylor B., Rosales J. Spark plasma sintering of (Zr,Nb)C ceramics. *Journal of Alloys and Compounds*. 2025;1013:178630. <https://doi.org/10.1016/j.jallcom.2025.178630>
17. Wang X.G., Liu J.X., Kan Y.M., Zhang G.J. Effect of solid solution formation on densification of hot-pressed ZrC ceramics with MC (M = V, Nb, and Ta) additions. *Journal of the European Ceramic Society*. 2012;32:1795–1802. <https://doi.org/10.1016/J.JEURCERAMSOC.2011.10.045>
18. Orrù R., Cao G. Comparison of reactive and non-reactive spark plasma sintering routes for the fabrication of monolithic and composite ultra high temperature ceramics (UHTC) materials. *Materials*. 2013;6(5):1566–1583. <https://doi.org/10.3390/ma6051566>
19. Shcherbakov V.A., Gryadunov A.N., Vadchenko S.G., Alymov M.I. Exothermic synthesis and consolidation of single-phase ultra-high temperature composite Ta₄ZrC₅. *Doklady Chemistry*. 2019;488(1):242–245. <https://doi.org/10.1134/S0012500819090027>
 Щербakov В.А., Грядунев А.Н., Вадченко С.Г., Алымов М.И. Экзотермический синтез и консолидация однофазного ультратугоплавкого композита Ta₄ZrC₅. *Доклады РАН*. 2019;488(2):153–156. <https://doi.org/10.31857/S0869-56524882153-156>
20. Vadchenko S.G. Induction period of a thermal explosion in titanium and aluminum powder mixtures. *Combustion, Explosion, and Shock Waves*. 2023;59(4):447–456. <https://doi.org/10.1134/S001050822304007X>
 Вадченко С.Г. Период индукции теплового взрыва в смесях порошков титана и алюминия. *Физика горения и взрыва*. 2023;(4):60–70.
21. Vadchenko S.G., Shchukin A.S., Sytshev A.E., Boyarchenko O.D. Peculiarities of structure formation in Ni–C, Al–C, and Ni–Al–C systems at high-temperature heating. *Inorganic Materials: Applied Research*. 2022;13(1):1–6. <https://doi.org/10.1134/S2075113322010385>
22. Okamoto H. Desk Edition: Phase diagram for binary alloys. 2nd ed. ASM International. 900 p.
23. Lyakishev N.P. Constitution Diagrams of Binary Metallic Systems. In 3 vols. Vol. 3, book 2. Moscow: Mashinostroenie, 2000. 448 p. (In Russ.).
 Диаграммы состояния двойных металлических систем: Справочник. В 3 т. Т. 3, кн. 2. Под общ. ред. Н.П. Лякишева. М: Машиностроение, 2000. 448 с.
24. Aristova N.M., Belov G.V. Thermodynamic properties of ZrC_{0.95–0.99} zirconium carbide in a condensed state. *Teplofizika vysokikh temperatur*. 2022;60(1):23–32. (In Russ.). <https://doi.org/10.31857/S004036442201001X>
 Аристова Н.М., Белов Г.В. Термодинамические свойства карбида циркония ZrC_{0.95–0.99} в конденсированном состоянии. *Теплофизика высоких температур*. 2022;60(1):23–32. <https://doi.org/10.31857/S004036442201001X>
25. Shiryayev A. Program for thermodynamics equilibrium calculations “Thermo”. <http://www.ism.ac.ru/thermo>
26. Vadchenko S.G., Grigoriev Yu.M., Merzhanov A.G. Study of the ignition and combustion mechanism of Ti + C, Zr + C systems by the electrothermographic method. *Fizika goreniya i vzryva*. 1976;12(5):676–682. (In Russ.).
 Вадченко С.Г., Григорьев Ю.М., Мержанов А.Г. Исследование механизма воспламенения и горения систем Ti + C, Zr + C электротермографическим методом. *Физика горения и взрыва*. 1976;12(5):676–682.

Information about the Authors

Sergei G. Vadchenko – Cand. Sci. (Phys.-Math.), Leading Researcher, Microheterogenic Process Dynamics Laboratory, Merzhanov Institute of Structural Macrokinetics and Materials Science of the Russian Academy of Sciences (ISMAN)

 **ORCID:** 0000-0002-2360-2114


 **E-mail:** vadchenko@ism.ac.ru

Aleksander S. Rogachev – Dr. Sci. (Phys.-Math.), Professor, Senior Researcher, Head of the Microheterogenic Process Dynamics Laboratory, ISMAN

 **ORCID:** 0000-0003-1554-0803

 **E-mail:** rogachev@ism.ac.ru

Mikhail I. Alymov – Dr. Sci. (Eng.), Professor, Corresponding Member of Russian Academy of Sciences, Director of ISMAN

 **ORCID:** 0000-0001-6147-5753

 **E-mail:** director@ism.ac.ru

Сведения об авторах

Сергей Георгиевич Вадченко – к.ф.-м.н., вед. науч. сотрудник лаборатории динамики микрогетерогенных процессов, Институт структурной макрокинетики и проблем материаловедения им. А.Г. Мержанова Российской академии наук (ИСМАН)

 **ORCID:** 0000-0002-2360-2114

 **E-mail:** vadchenko@ism.ac.ru

Александр Сергеевич Рогачев – д.ф.-м.н., гл. науч. сотрудник, профессор, зав. лабораторией динамики микрогетерогенных процессов, ИСМАН

 **ORCID:** 0000-0003-1554-0803

 **E-mail:** rogachev@ism.ac.ru

Михаил Иванович Алымов – д.т.н., профессор, чл. корр. РАН, директор ИСМАН

 **ORCID:** 0000-0001-6147-5753

 **E-mail:** director@ism.ac.ru

Contribution of the Authors



Вклад авторов

S. G. Vadchenko – preparation and conduct of the experiment, preparing the text, formulating conclusions.

A. S. Rogachev – scientific guidance, the formation of the main concept, text correction, correction of conclusions.

M. I. Alymov – setting the goal and objectives of the study, text correction, correction of conclusions.

С. Г. Вадченко – подготовка и проведение эксперимента, подготовка текста, формулировка выводов.

А. С. Рогачев – научное руководство, формирование основной концепции, корректировка текста, корректировка выводов.

М. И. Алымов – постановка цели и задачи исследования, корректировка текста, корректировка выводов.

Received 15.05.2025

Revised 16.06.2025

Accepted 20.06.2025

Статья поступила 15.05.2025 г.

Доработана 16.06.2025 г.

Принята к публикации 20.06.2025 г.



UDC 666-492.2: 620.193: 549.6

<https://doi.org/10.17073/1997-308X-2025-4-50-59>Research article
Научная статья

Effect of $ZrO_2-Y_2O_3$ powder morphology on CMAS resistance of thermal barrier coatings

S. A. Oglezneva[✉], V. B. Kulmetyeva, A. A. Smetkin, A. E. MalyshevPerm National Research Polytechnic University
29 Komsomolskiy Prosp., Perm 614990, Russia svetlana.iron@yandex.ru

Abstract. Corrosion of thermal barrier coatings on gas turbine engine components made of heat-resistant alloys, caused by interaction with molten silicate deposits (CMAS), reduces their high-temperature stability and leads to premature failure during service. The problem of CMAS resistance in coatings with an outer ceramic layer of yttria-stabilized zirconia (YSZ) remains highly relevant, and its solution has important practical implications. The present study focused on zirconia-based ceramic materials used for the deposition of thermal barrier coatings. The interaction of ceramic coatings with silicate deposits was investigated at temperatures up to 1300 °C. Scanning electron microscopy, energy-dispersive spectroscopy, thermogravimetric/differential thermal analysis, and X-ray diffraction were employed to study the interaction of CMAS with YSZ on model samples prepared from powders of grades Z7Y10-80A, Zr7Y20-60, and Metco 204NS with different morphologies. The interaction mechanism between CMAS and YSZ at 1200–1300 °C was established. It was shown that the nature and intensity of the interaction strongly depend on the structure and morphology of the ceramic particles. The dense particle structure of ceramics based on Z7Y10-80A and Metco 204NS powders reduces CMAS penetration, in contrast to Zr7Y20-60 powders with a more porous particle structure. The interaction mechanism between CMAS and YSZ was found to be the same for all ceramics studied and occurs through dissolution–precipitation of zirconia in the glass melt. It was demonstrated that with increasing temperature, the degree of zirconia tetragonality changes due to the reduction of yttrium content caused by its diffusion into the glass. This can lead to a polymorphic transformation of zirconia accompanied by volume expansion, followed by cracking and spallation of the thermal barrier coating.

Keywords: gas turbine engine, thermal barrier coatings, ceramic layer, zirconia, silicate deposits, powder morphology

For citation: Oglezneva S.A., Kulmetyeva V.B., Smetkin A.A., Malyshev A.E. Effect of $ZrO_2-Y_2O_3$ powder morphology on CMAS resistance of thermal barrier coatings. *Powder Metallurgy and Functional Coatings*. 2025;19(4):50–59.
<https://doi.org/10.17073/1997-308X-2025-4-50-59>

Влияние морфологии керамических порошков $\text{ZrO}_2\text{-Y}_2\text{O}_3$, используемых в теплозащитных покрытиях, на стойкость к силикатным отложениям

С. А. Оглезнева , В. Б. Кульметьева, А. А. Сметкин, А. Е. Малышев

Пермский национальный исследовательский политехнический университет
Россия, 614990, г. Пермь, Комсомольский пр-т, 29

 svetlana.iron@yandex.ru

Аннотация. Коррозия теплозащитных покрытий деталей газотурбинных двигателей, выполненных из жаропрочных сплавов, обусловленная взаимодействием с расплавленными силикатными отложениями (CMAS), снижает их устойчивость к высоким температурам и приводит к преждевременным отказам в эксплуатации. Проблема стойкости к CMAS покрытий с внешним керамическим слоем из диоксида циркония, стабилизированного иттрием, остается весьма актуальной, и ее решение имеет важное практическое применение. Объектом изучения в настоящей работе являлись керамические материалы на основе диоксида циркония, используемые для нанесения теплозащитных покрытий. Исследовано взаимодействие керамических покрытий с силикатными отложениями при температурах до 1300 °С. С помощью сканирующей электронной микроскопии, энергодисперсионной спектроскопии, дериватографии и рентгеноструктурного анализа выполнены исследования взаимодействия CMAS с керамикой YSZ на модельных образцах из порошков марок Z7Y10-80A, Zr7Y20-60 и Metco 204NS различной морфологии. Установлен механизм взаимодействия CMAS и YSZ при $t = 1200\div 1300$ °С. Показано, что характер и интенсивность взаимодействия существенно зависят от строения и морфологии частиц керамики. Плотная структура частиц керамики на основе порошков Z7Y10-80A и Metco 204NS снижает проникновение CMAS в отличие от Zr7Y20-60 с более пористой структурой частиц. Установлено, что характер взаимодействия между CMAS и YSZ один для всех исследуемых керамик и происходит по механизму растворения–осаждения оксида циркония в расплаве стекла. Показано, что с ростом температуры происходит изменение степени тетрагональности оксида циркония, обусловленное снижением содержания иттрия из-за его диффузии в стекло. Это может привести к полиморфной трансформации диоксида циркония с увеличением объема, последующим растрескиванием и отслоением теплозащитного покрытия.

Ключевые слова: газотурбинный двигатель, теплозащитные покрытия, керамический слой, оксид циркония, силикатные отложения, морфология порошков

Для цитирования: Оглезнева С.А., Кульметьева В.Б., Сметкин А.А., Малышев А.Е. Влияние морфологии керамических порошков $\text{ZrO}_2\text{-Y}_2\text{O}_3$, используемых в теплозащитных покрытиях, на стойкость к силикатным отложениям. *Известия вузов. Порошковая металлургия и функциональные покрытия*. 2025;19(4):50–59. <https://doi.org/10.17073/1997-308X-2025-4-50-59>

Introduction

The efficiency of gas turbine engines (GTEs) is directly related to the gas temperature at the inlet of the high-pressure turbine (HPT), which exceeds 1200 °C [1; 2]. Such high operating temperatures impose stringent requirements on the protection of components made of heat-resistant alloys used in GTEs. Thermal barrier coatings (TBCs), applied to turbine blades and vanes as well as combustion chamber components, reduce the temperature by approximately 100 °C [3–6].

Modern TBCs consist of an outer ceramic layer and an intermediate metallic bond coat based on nickel superalloys. The outer ceramic layer must combine a range of high-temperature properties, including low thermal conductivity in the operating temperature range, high resistance to thermal shock, phase and structural stability, a high coefficient of thermal expansion,

and strong adhesion to the bond coat [7–10]. In current aerospace engine manufacturing, yttria-stabilized zirconia (YSZ) is employed as the outer ceramic layer. This material exhibits low thermal conductivity (2.3 W/(m²·K) at 1000 °C) for a dense ceramic, a high melting point (2680 °C), and a favorable coefficient of thermal expansion (11·10⁻⁶ K⁻¹ at ~1000 °C) [5; 11].

It should be noted that YSZ coatings are susceptible to failures, which are classified as internal and external. Internal failures include defect formation due to phase transformation or excessive temperature gradients during sintering [12]. External failures are usually associated with TBC damage caused by erosion from small (<75 μm) solid particles in the environment or from foreign object damage. Such fine particles typically enter GTEs from dust storms, volcanic ash, and airport runways, where their concentration is relatively high and generally ranges from 350 to 13,000 μg/m³ [13].

These particles penetrate into the low-pressure compressor and eventually reach the combustion chamber. Under high operating temperatures, they melt, decompose, and deposit on component surfaces, leading to structural degradation and chemical alteration of the TBC. The particles mainly consist of $CaO-MgO-Al_2O_3-SiO_2$ compounds (*Calcium-Magnesium-Alumina-Silicate* – CMAS). Their detrimental effects on aircraft engine components are well established. Therefore, further research is required to better understand the mechanisms of CMAS interaction with HPT blade coatings [14–16].

Deposition of ceramic top coats for TBCs is carried out using electron-beam physical vapor deposition (EB-PVD) and atmospheric plasma spraying (APS). APS has become the primary method for applying multilayer TBCs due to its high deposition rate, a wide range of adjustable process parameters, relative cost-effectiveness, and suitability for a broad spectrum of powder feedstocks [17–21]. By injecting powders into the plasma jet with a carrier gas, the porosity of the resulting TBC can be controlled. APS technology thus provides flexibility in tailoring the microstructure, particularly of ceramic coatings. The most common microstructure is lamellar, containing microcracks and about 15 % porosity [5; 8].

Coatings produced by APS can develop either porous microstructures or dense ones with vertical cracks. The properties of the feedstock powders play a decisive role in achieving effective TBCs. Typically, the particle size of APS powders ranges from 10 to 100 μm . Oversized particles often fail to melt completely, while undersized ones may bypass the plasma jet and remain in cooler regions, leading to insufficient heating during spraying.

Powder morphology has a strong influence on both processing behavior and in flight dynamics in the plasma jet. To tailor coating properties and functionality, ceramic powders are prepared using methods such as melt crushing, agglomeration-sintering, and agglomeration-spheroidization. These processes produce powders with distinct morphologies: fractured, spherical, or hollow spherical [22–25].

The role of powder morphology in determining resistance to CMAS corrosion has not been adequately investigated and remains a critical issue. The present work therefore aimed to examine the structural and phase evolution of powders with different morphologies, used for TBC deposition, under high temperature exposure to $CaO-MgO-Al_2O_3-SiO_2$ glass melts. The findings provide insight into the mechanisms of phase evolution in stabilized zirconia powders and lay the groundwork for further studies on full thermal barrier coating systems.

Materials and methods

As starting materials, we used thermal barrier ceramic powders based on yttria stabilized zirconia (YSZ):

– Z7Y10-80A (T: SP LLC, Russia) – agglomerated, sintered, and crushed powder with fractured morphology;

– Zr7Y20-60 (T SFERA LLC, Russia) – agglomerated and sintered powder with spheroidal morphology;

– Metco 204NS (Oerlikon Metco, USA) – agglomerated, plasma treated (HOSP) powder with hollow spherical morphology.

The particle size distribution of the YSZ powders was determined by laser diffraction (Analizette 22 NanoTech, Fritsch, Germany) and is summarized in Table 1.

For CMAS investigations, a model glass was prepared. According to X-ray fluorescence analysis (EDX 800HS spectrometer, Shimadzu, Japan), its composition was (wt. %): SiO_2 – 53.3, CaO – 30.4, Al_2O_3 – 10.7, MgO – 5.4. The glass was first ground in a jasper mortar and then milled in a planetary ball mill in water for 2 h at a rotation speed of 160 rpm. The dried powder was sieved. Its chemical composition closely matched the CMAS glass reported in the literature [26–28], which represents the average composition of deposits found on turbine blades in service (SiO_2 – 48.5, CaO – 33.2, Al_2O_3 – 11.8, MgO – 6.5 wt. %). Simultaneous thermal analysis (ZCT H, Jing Yi Gao Ke) showed that melting started at 1200 °C and reached its maximum at 1244 °C.

Table 1. Particle size distribution of YSZ ceramic powders

Таблица 1. Гранулометрический состав керамических порошков YSZ

Powder grade	Production method	Particle size distribution, μm		
		d_{10}	d_{50}	d_{90}
Z7Y10-80A	Sintering, crushing	4.0	48.9	75.3
Zr7Y20-60	Agglomeration-sintering	11.2	28.1	37.9
Metco 204NS	Agglomeration, plasma treatment (HOSP)	13.4	41.9	62.8

Model samples for studying CMAS infiltration and microstructural evolution were fabricated by pressing YSZ powders followed by sintering. For binder preparation, a 4% polyvinyl alcohol solution (GOST 10779-78) was added in an amount corresponding to 10 wt. % of the powder. Pressing was performed on a manual hydraulic press (Carl Zeiss, Germany) under a specific pressure of 1.5 t/cm². Sintering was carried out in a HT 64/17 furnace (Nabertherm, Germany) at 1700 °C for 2 h.

On the surface of the sintered samples (Z7Y10-80A, Zr7Y20-60, and Metco 204NS), a suspension of CMAS powder in ethanol was applied at a loading of 20 mg/cm². High temperature tests of the samples with surface applied suspensions were performed in air in the HT 64/17 electric furnace. The heating rate was 10 °C/min, and the exposure temperature ranged from 1200–1300 °C with holding times ranging from 2 to 24 h.

To analyze high temperature chemical reactions between YSZ and CMAS in more detail, powder mixtures were prepared at a 3:1 ratio. The mixtures were homogenized in ethanol, dried, and pressed into pellets at 50 MPa, followed by isothermal treatment at 1200–1300 °C for 2 h.

Microstructural analysis of cross sections was performed using a scanning electron microscope (SEM EM 30AX, Coxem Co. Ltd., Republic of Korea) equipped with an energy dispersive spectrometer (EDS). Phase composition and structural parameters were determined on an X-ray diffractometer (XRD 6000, Shimadzu, Japan) using full profile analysis. Diffraction patterns were recorded over a 2θ range of 20–90° with CuK_α radiation, a step size of 0.02°, and a counting time of 2 s per step. Qualitative phase analysis was carried out using the Crystallographica Search Match (CSM) program and the PDF database of the International Centre for Diffraction Data (ICDD).

Results and discussion

Structure of YSZ ceramic powders

Analysis of the particle size distribution (Table 1) showed that the average particle sizes of powders Z7Y10-80A and Metco 204NS are comparable, with d_{50} values of 48.9 and 41.9 μm, respectively. However, Z7Y10-80A contains the largest fraction of fine particles compared with the other powders. The smallest average particle size, $d_{50} = 28.1$ μm, was observed for Zr7Y20-60.

SEM images of powder morphology and cross-sections are presented in Fig. 1. Based on morphometric

parameters, Z7Y10-80A exhibits a fractured morphology, Zr7Y20-60 is nearly spherical, and Metco 204NS is predominantly hollow spherical. Particles of all powders, except Metco 204NS, are porous throughout their volume. Metco 204NS contains both hollow spherical particles and non hollow porous particles similar in structure to the other powders. The shells of the hollow spheres are notably denser compared to the non hollow particles.

XRD analysis (Fig. 2) showed that the Z7Y10-80A and Zr7Y20-60 powders are composed of tetragonal ZrO_2 (space group $P4_2/nmc$, No. 137). The results of Rietveld full-profile refinement of the structural parameters and phase composition are presented in Table 2. The lattice parameters of the tetragonal phase are nearly identical to the reference values (PDF card No. 80-2155). The Metco 204NS powder consists of tetragonal ($P4_2/nmc$, No. 137) and monoclinic ZrO_2 ($P2_1/c$, No. 14) in proportions of 79 and 21 %, respec-

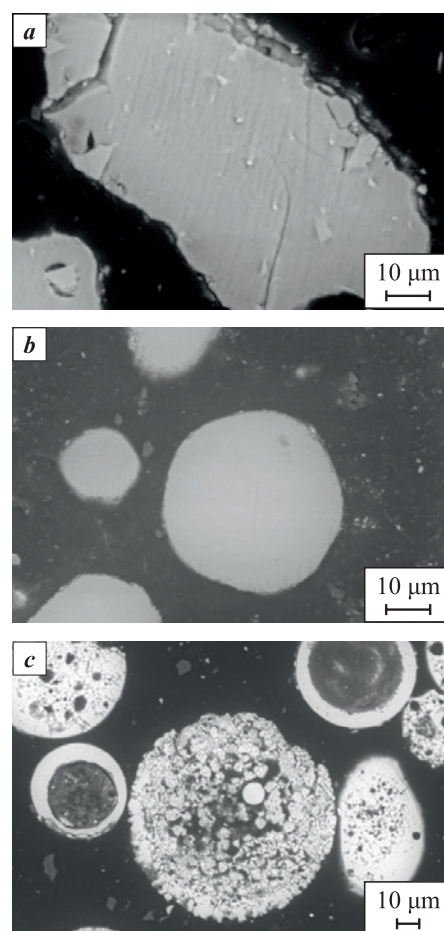


Fig. 1. SEM images of the morphology and cross sections of YSZ ceramic powder particles
Z7Y10-80A (a), Zr7Y20-60 (b) and Metco 204NS (c)

Рис. 1. СЭМ-изображения морфологии и поперечных сечений частиц керамических порошков
Z7Y10-80A (a), Zr7Y20-60 (b) и Metco 204NS (c)

Table 2. Structural parameters of YSZ powders
Таблица 2. Структурные параметры порошков YSZ

Powder grade	Phase	Lattice parameters, nm			Crystallite size D , nm	Lattice microstrain da/a , %
		a	b	c		
Z7Y10-80A	t	0.36142	0.36142	0.51706	21	0.14
Zr7Y20-60	t	0.36131	0.36131	0.51670	51	0.06
Metco 204NS	t	0.36143	0.36143	0.51580	200	0.01
	m	0.51617	0.52052	0.53221	65	0.05

tively. The smallest crystallite size was observed for Z7Y10-80A, while the largest was for Metco 204NS. The evaluation of lattice microstrain da/a indicated the highest distortions in Z7Y10-80A, which can be attributed to mechanical crushing.

XRD analysis of the model samples sintered at 1700 °C for 2 h showed that their phase composition did not differ from that of the as received powders.

The mechanism of interaction between YSZ ceramics and CMAS has been widely investigated and described in numerous studies [13; 15; 26; 27; 29–31]. In general, YSZ dissolves into the CMAS melt, followed by the reprecipitation of ZrO_2 grains in various polymorphic forms and compositions, depending on the local melt chemistry. Since Y^{3+} ions have much higher solubility in CMAS than Zr^{4+} ions, they readily diffuse into the melt, leading to zirconia depletion. This depletion facilitates the phase transformation of YSZ from tetragonal to monoclinic.

Interaction of Z7Y10 80A with CMAS

The interaction of CMAS with ceramic powders begins at temperatures below the melting point of the glass due to the formation of a eutectic in the SiO_2 – CaO – Al_2O_3 system [29; 32]. As a result, regardless of particle morphology, interaction with CMAS is already observed at 1200 °C.

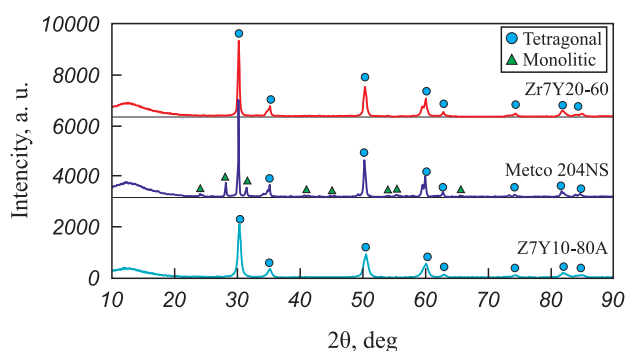


Fig. 2. XRD patterns of YSZ powders

Рис. 2. Дифрактограммы исходных порошков YSZ

As shown above, the particles of the Z7Y10-80A powder (Fig. 1, *a*) possess a dense structure determined by the production method, which strongly influences their interaction with CMAS. At 1200 °C, interaction is confined to a near-surface layer up to ~2 μm thick, while the dense particle structure remains largely intact (Fig. 3, *a*). When the temperature is raised to 1300 °C, dissolution/precipitation processes in YSZ are activated, resulting in loosening of the particle structure (Fig. 3, *b*). The glass melt penetrates from the interparticle space into the particle interior, causing the particle boundaries to blur.

Since the sensitivity of XRD to detect subtle phase composition changes during CMAS interaction is relatively low when glass is simply applied to the surface of Z7Y10-80A, additional mixed samples with a Z7Y10-80A:CMAS ratio of 3:1 were prepared. These were heated in air at 1200, 1250, and 1300 °C for 2 h. This approach enabled a more precise analysis of the CMAS–ceramic interaction mechanisms.

Fig. 4 shows the XRD patterns of the Z7Y10-80A:CMAS samples after exposure to these temperatures. The incorporation of 6–8 wt. % Y_2O_3 into ZrO_2 results in the formation of a metastable tetragonal t' -phase (the so called non transformable phase), in contrast to the less stable tetragonal t -phase. To distinguish between the two tetragonal modifications (t and t'), the $c/a\sqrt{2}$ ratio – reflecting the degree of tetragonality – is used. For the t' -phase, this ratio approaches 1.010 [33].

The as received Z7Y10-80A powder consists of tetragonal zirconia, with no characteristic doublets observed at $2\theta \approx 35^\circ$ and 60° . After testing, the XRD patterns clearly show peak splitting at these angles, along with the emergence of the cubic (400) reflection in the 2θ range of 72–76°. In the as received powder, the degree of tetragonality was 1.0116 and remained unchanged after exposure at 1200 °C. Raising the temperature to 1250 °C led to an increase in tetragonality, associated with yttrium depletion in YSZ, i.e., the decomposition of the t -phase into t - and c -phases.

At 1300 °C, counter diffusion of Ca and Mg from the glass into YSZ causes a reduction in tetragonality,

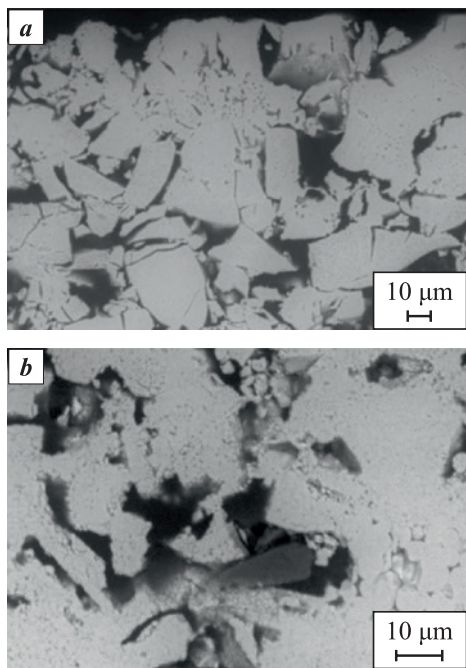


Fig. 3. SEM images of Z7Y10-80A samples after interaction with CMAS at 1200 °C for 2 h (a) and 1300 °C for 12 h (b)

Рис. 3. СЭМ-изображения образцов Z7Y10-80A после взаимодействия с CMAS при $t = 1200\text{ °C}$, $\tau = 2\text{ ч}$ (a), $t = 1300\text{ °C}$, $\tau = 12\text{ ч}$ (b)

although it does not return to its original value (Table 3). The variation in tetragonality as a function of yttrium content is consistent with the findings reported in [34], where it was shown that, irrespective of the synthesis method, the tetragonal character of YSZ powders diminishes with increasing yttrium content.

Table 3. Lattice parameters of the tetragonal phase in YSZ

Таблица 3. Параметры кристаллической решетки тетрагональной фазы YSZ

Powder grade	t , °C	a , nm	c , nm	$c/a\sqrt{2}$
Z7Y10-80A	20	0.36142	0.51706	1.0116
	1200	0.36145	0.51707	1.0115
	1250	0.36087	0.51710	1.0132
	1300	0.36104	0.51692	1.0124
Zr7Y20-60	20	0.36131	0.51670	1.0112
	1200	0.36091	0.51661	1.0122
	1250	0.36094	0.51659	1.0120
	1300	0.36041	0.51701	1.0143
Metco 204NS	20	0.36143	0.51580	1.0091
	1200	0.36135	0.51663	1.0110
	1250	0.36150	0.51724	1.0117
	1300	0.36179	0.51767	1.0118

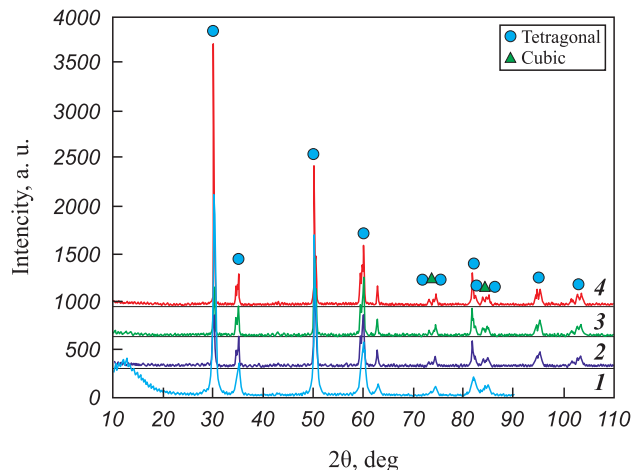


Fig. 4. XRD patterns of Z7Y10-80A samples after interaction with CMAS at different temperatures

1 – as-received, 2 – 1200 °C, 3 – 1250 °C, 4 – 1300 °C

Рис. 4. Дифрактограммы образцов Z7Y10-80A после взаимодействия с CMAS при различных температурах

1 – исходный, 2 – 1200 °C, 3 – 1250 °C, 4 – 1300 °C

Interaction of Zr7Y20-60 with CMAS

The Zr7Y20-60 ceramic particles have a porous surface surrounding a dense core (Fig. 1, b). This morphology makes them prone to CMAS melt infiltration, not only into the macropores but also deeper into the particle volume. Interaction between YSZ and CMAS is already evident at 1200 °C (Fig. 5), and at 1300 °C it becomes more pronounced, with the boundaries between individual ceramic grains disappearing and an extensive reaction zone forming.

The as received Zr7Y20-60 powder consists of tetragonal zirconia; however, the characteristic doublets are already distinguishable at $2\theta \approx 35^\circ$ and 60° (Fig. 6). After exposure at 1200 °C, these doublets become clearly resolved. As the temperature increases, the degree of tetragonality rises from 1.0112 to 1.0143 (Table 3). At 1300 °C, the emergence of the cubic phase is indicated by the appearance of the (400) peak between the tetragonal (004) and (220) reflections.

Interaction of Metco 204NS with CMAS

The Metco 204NS ceramic powder consists of both hollow spherical particles with a dense shell and non hollow particles with a porous structure. The latter interact most intensively with CMAS due to glass infiltration (Fig. 7). As the temperature increases to 1300 °C, the boundaries between individual non hollow particles gradually disappear, leading to the formation of an extensive reaction zone. In contrast, the dense

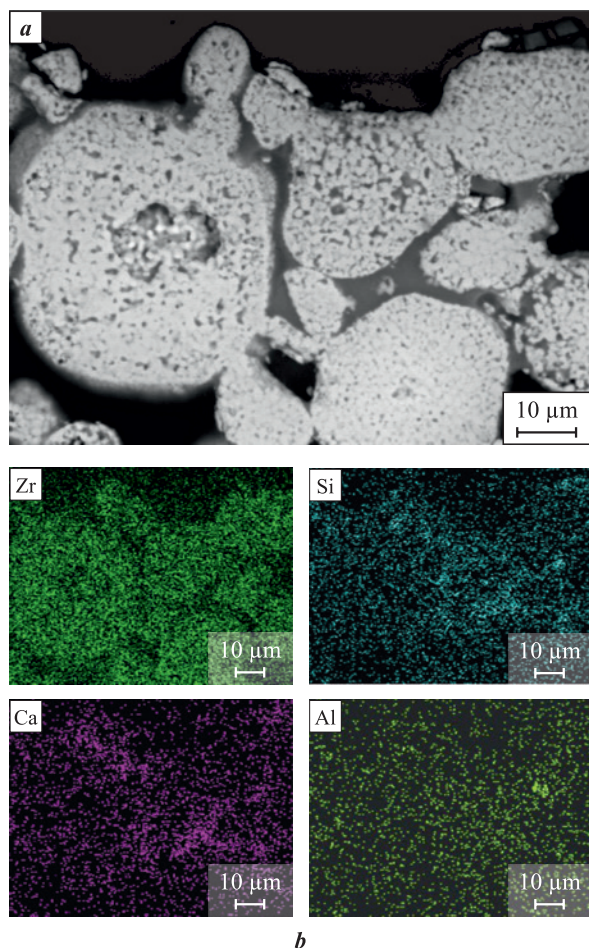


Fig. 5. SEM image (a) and EDS analysis (b) of Zr7Y20-60 samples after interaction with CMAS at 1200 °C for 2 h

Рис. 5. СЭМ-изображение (a) и результаты EDS-анализа (b) образцов Zr7Y20-60 после взаимодействия с CMAS при $t = 1200$ °C в течение 2 ч

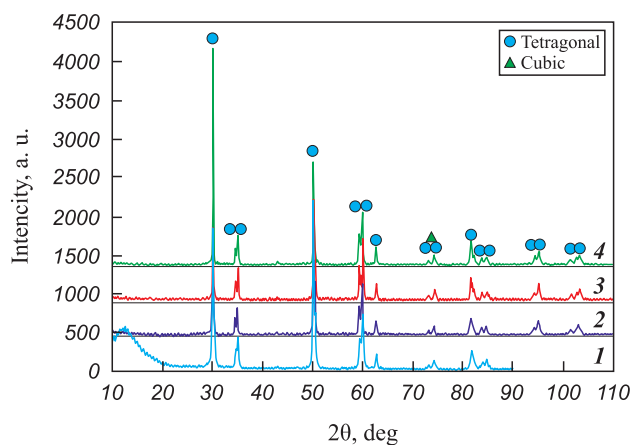


Fig. 6. XRD patterns of Zr7Y20-60 samples after interaction with CMAS at different temperatures
1 – as-received, 2 – 1200 °C, 3 – 1250 °C, 4 – 1300 °C

Рис. 6. Дифрактограммы образцов Zr7Y20-60 после взаимодействия с CMAS при различных температурах
1 – исходный, 2 – 1200 °C, 3 – 1250 °C, 4 – 1300 °C

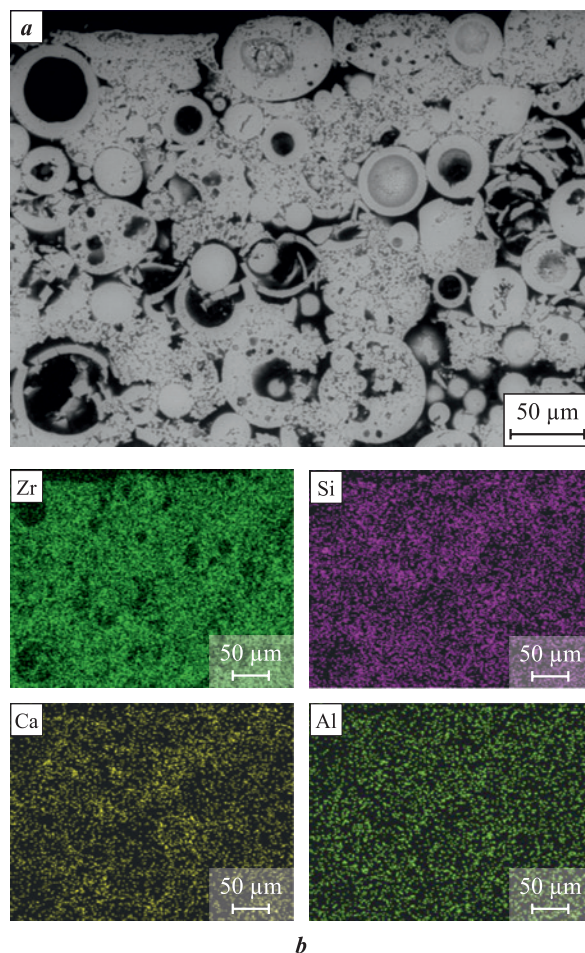


Fig. 7. SEM image (a) and EDS analysis (b) of Metco 204NS samples after interaction with CMAS at 1300 °C for 24 h

Рис. 7. СЭМ-изображение (a) и результаты EDS-анализа (b) образцов Metco 204NS после взаимодействия с CMAS при $t = 1300$ °C в течение 24 ч

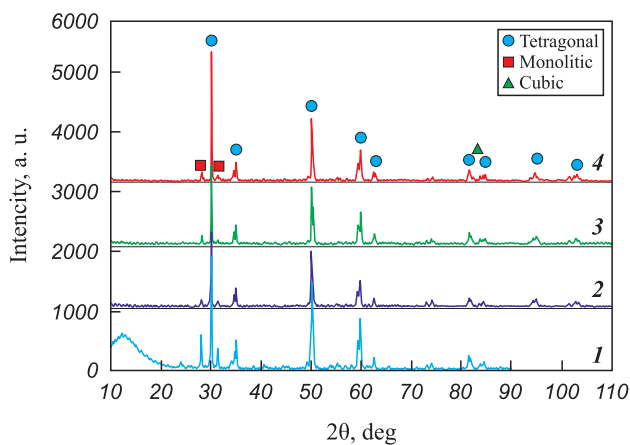


Fig. 8. XRD patterns of Metco 204NS samples after interaction with CMAS at different temperatures
1 – as-received, 2 – 1200 °C, 3 – 1250 °C, 4 – 1300 °C

Рис. 8. Дифрактограммы образцов Metco 204NS после взаимодействия с CMAS при различных температурах
1 – исходный, 2 – 1200 °C, 3 – 1250 °C, 4 – 1300 °C

shells of the spherical particles remain the most resistant to CMAS attack up to 1300 °C, preserving their structural integrity.

XRD analysis revealed that after CMAS corrosion testing the monoclinic phase fraction ($m\text{-ZrO}_2$) decreased from 20.6 to 10.0 % (Fig. 8). This was accompanied by a reduction in the intensity of the $(\bar{1}11)$ and (111) reflections and an increase in the degree of tetragonality (see Table 2). These changes are attributed to additional stabilization of zirconia by calcium and magnesium oxides. At 1300 °C, the cubic (400) reflection was also detected.

Conclusion

The study of CMAS interaction with TBC ceramics based on Z7Y10-80A, Zr7Y20-60, and Metco 204NS powders using model samples has demonstrated that the interaction mechanism between CMAS and YSZ is the same for all yttria containing ceramics. It is governed by the dissolution–precipitation of zirconia in the glass melt. Exposure to CMAS at 1200–1300 °C leads to the formation of a new yttria depleted tetragonal zirconia phase as a result of yttrium diffusion into the glass. With increasing temperature, the degree of tetragonality changes due to further yttrium depletion. However, the counter diffusion of Ca and Mg ions from the glass into zirconia is insufficient to restore the initial tetragonality values. As a result, zirconia may undergo polymorphic transformation accompanied by volume expansion, cracking, and eventual spallation of the TBC.

The extent and character of CMAS–YSZ interaction were shown to depend strongly on the structure and morphology of the ceramic particles. A dense particle structure, as in ceramics produced from Z7Y10-80A and Metco 204NS powders, reduces CMAS infiltration, whereas the more porous structure of Zr7Y20-60 particles promotes deeper penetration and more extensive interaction.

References / Список литературы

- Kablov E.N. Cast blades of gas turbine engines: Alloys, technologies, coatings. 2nd ed. Moscow: Nauka, 2006. 632 p. (In Russ.).
Каблов Е.Н. Литые лопатки газотурбинных двигателей: Сплавы, технология, покрытия. 2-е изд. М.: Наука, 2006. 632 с.
- Zeraati M., Oganov A., Fan T., Solodovnikov S. Searching for low thermal conductivity materials for thermal barrier coatings: A theoretical approach. *Physical Review Materials*. 2024;8(3):033601.
<https://doi.org/10.1103/PhysRevMaterials.8.033601>
- Huang L.L., Meng H.M., Tang J., Li S., Yu Z.Q. Overview on double ceramic layer thermal barrier coatings. *Advanced Materials Research*. 2014;1053:364–372.
<https://doi.org/10.4028/www.scientific.net/amr.1053.364>
- Liu B., Liu Y., Zhu C., Xiang H., Chen H., Sun L., Gao Y., Zhou Y. Advances on strategies for searching for next generation thermal barrier coating materials. *Journal of Materials Science and Technology*. 2019;35(5):833–851.
<https://doi.org/10.1016/j.jmst.2018.11.016>
- Vaßen R., Bakan E., Mack D.E., Guillon O.A Perspective on thermally sprayed thermal barrier coatings: current status and trends. *Journal of Thermal Spray Technology*. 2022;31(4):685–698.
<https://doi.org/10.1007/s11666-022-01330-2>
- Pankov V.P., Babayan A.L., Kulikov M.V., Kossoy V.A., Varlamov B.S. Heat-protective coatings for turbine blades of aircraft gas turbine engines. *Polzunovskiy vestnik*. 2021;1:161–172. (In Russ.).
<https://doi.org/10.25712/ASTU.2072-8921.2021.01.023>
Панков В.П., Бабаян А.Л., Куликов М.В., Коссои В.А., Варламов Б.С. Теплозащитные покрытия лопаток турбин авиационных газотурбинных двигателей. *Ползуновский Вестник*. 2021;1:161–172.
<https://doi.org/10.25712/ASTU.2072-8921.2021.01.023>
- Dudnik E., Lakiza S., Hrechanyuk I., Ruban A.K., Redko V.P., Marek I.O., Shmibelsky V.B., Makudera A.A., Hrechanyuk N.I. Thermal barrier coatings based on ZrO_2 solid solutions. *Powder Metallurgy and Metal Ceramics*. 2020;59(3):179–200.
<https://doi.org/10.1007/s11106-020-00151-8>
- Bakan E., Vaßen R. Ceramic top coats of plasma-sprayed thermal barrier coatings: materials, processes, and properties. *Journal of Thermal Spray Technology*. 2017;26(12):992–1010. <https://doi.org/10.1007/s11666-017-0597-7>
- Sezavar A., Sajjadi S.A. A review on the performance and lifetime improvement of thermal barrier coatings. *Journal of the European Ceramic Society*. 2025;45(1):117274.
<https://doi.org/10.1016/j.jeurceramsoc.2025.117274>
- Iqbal A., Moskal G., Cavaleiro A., Amjad A., Khan M.J. The current advancement of zirconate based dual phase system in thermal barrier coatings (TBCs): New modes of the failures: Understanding and investigations. *Alexandria Engineering Journal*. 2024;91:161–196.
<https://doi.org/10.1016/j.aej.2024.01.063>
- Bogdan M., Peter I. A comprehensive understanding of thermal barrier coatings (TBCs): applications, materials, coating design and failure mechanisms. *Metals*. 2024;14(5):575.
<https://doi.org/10.3390/met14050575>
- Pakseresht A., Sharifianjazi F., Esmaeilkhani A., Bazli L., Reisi Nafchi M., Bazli M., Kirubaharan K. Failure mechanisms and structure tailoring of YSZ and new candidates for thermal barrier coatings: A systematic review. *Materials and Design*. 2022;222:111044.
<https://doi.org/10.1016/j.matdes.2022.111044>
- Nieto A., Agrawal R., Bravo L., Hofmeister-Mock C., Pepi M., Ghoshal A. Calcia–magnesia–alumina–silicate (CMAS) attack mechanisms and roadmap towards Sandphobic thermal and environmental barrier coatings. *Inter-*

- national Materials Reviews*. 2021;66(7):451–492.
<https://doi.org/10.1080/09506608.2020.1824414>
14. Guo L., Xin H., Li Y., Yu Y. Self-crystallization characteristics of calcium-magnesium-alumina-silicate (CMAS) glass under simulated conditions for thermal barrier coating applications. *Journal of the European Ceramic Society*. 2020;40(15):5683–5691.
<https://doi.org/10.1016/j.jeurceramsoc.2020.07.025>
 15. Tolmachev Ya.V., Zavarzin S.V., Loshchinina A.O., Knyazev A.V. High temperature oxide corrosion of ceramic materials in turbine engines. *Trudy VIAM*. 2023;7: 69–83. (In Russ.).
<https://doi.org/10.18577/2307-6046-2023-0-7-69-83>
 Толмачев Я.В., Заварзин С.В., Лощинина А.О., Князев А.В. Высокотемпературная окисная коррозия керамических материалов ГТД. *Труды ВИАМ*. 2023;7:69–83.
<https://doi.org/10.18577/2307-6046-2023-0-7-69-83>
 16. Nair R.B., Brabazon D. Calcia magnesia alumino silicate (CMAS) corrosion attack on thermally sprayed thermal barrier coatings: A comprehensive review. *npj Materials Degradation*. 2024;8:44.
<https://doi.org/10.1038/s41529-024-00462-w>
 17. Kadam N.R., Karthikeyan G., Jagtap P.M., Kulkarni D.M. An atmospheric plasma spray and electron beam-physical vapour deposition for thermal barrier coatings: a review. *Australian Journal of Mechanical Engineering*. 2022;21(5):1729–1754.
<https://doi.org/10.1080/14484846.2022.2030088>
 18. Vaßen R., Bakan E., Mack D., Guillon O. A perspective on thermally sprayed thermal barrier coatings: current status and trends. *Journal of Thermal Spray Technology*. 2022;31(4):685–698.
<https://doi.org/10.1007/s11666-022-01330-2>
 19. Kubaszek T., Goral M., Pedrak P. Influence of air plasma spraying process parameters on the thermal barrier coating deposited with micro- and nanopowders. *Materials Science-Poland*. 2022;40(3):80–92.
<https://doi.org/10.2478/msp-2022-0034>
 20. Puzryakov A.F. Theoretical foundations of plasma spraying technology. Moscow: Publishing House of Bauman Moscow State Technical University, 2003. 360 p. (In Russ.).
 Пузряков А.Ф. Теоретические основы технологии плазменного напыления. М.: Изд. МГТУ им. Н.Э. Баумана, 2003. 360 с.
 21. Bernard B.A., Quet A., Bianchi L., Joulia A., Malie A., Schick V., Remy B. Thermal insulation properties of YSZ coatings: suspension plasma spraying (SPS) versus electron beam physical vapor deposition (EB-PVD) and atmospheric plasma spraying (APS). *Surface and Coatings Technology*. 2017;318:122–128.
<https://doi.org/10.1016/j.surfcoat.2016.06.010>
 22. Il'inkova T.A., Barsukova E.A., Tagirov A.T. The relationship between the characteristics of powder materials and the mechanical properties of plasma thermal barrier coatings. *Vestnik Kazanskogo tekhnologicheskogo universiteta*. 2015;18(15):116–121. (In Russ.).
 Ильинкова Т.А., Барсукова Е.А., Тагиров А.Т. Взаимосвязь характеристик порошковых материалов и механических свойств плазменных теплозащитных покрытий. *Вестник Казанского технологического университета*. 2015;18(15):116–121.
 23. Qiu J., Yu D., Chen Y., Li D., Islam M.S., Peng X. Controllable preparation of YSZ-STHS in arc plasma spheroidization: exploring the plasma flow characteristics' impact on powder quality. *Ceramics International*. 2024;50(15):26569–26582.
<https://doi.org/10.1016/j.ceramint.2024.04.385>
 24. Guo H.B., Murakami H., Kuroda S. Effect of hollow spherical powder size distribution on porosity and segmentation cracks in thermal barrier coatings. *Journal of the American Ceramic Society*. 2006;89(12):3797–3804.
<https://doi.org/10.1111/j.1551-2916.2006.01322.x>
 25. Zhao L., Zhang Z., Duan Y., Cui H., Gao Y. Preparation of yttria-stabilized zirconia hollow sphere with reduced shell thickness by controlling ambient temperature during plasma process. *Coatings*. 2018;8(7):245.
<https://doi.org/10.3390/coatings8070245>
 26. Kraemer S., Yang J., Levi C., Johnson C. Thermomechanical interaction of thermal barrier coatings with molten CaO – MgO – Al_2O_3 – SiO_2 (CMAS) Deposits. *Journal of the American Ceramic Society*. 2006;89: 3167–3175.
<https://doi.org/10.1111/j.1551-2916.2006.01209.x>
 27. Morelli S., Testa V., Bolelli G., Ligabue O., Molinari E., Antolotti N., Lusvardi L. CMAS corrosion of YSZ thermal barrier coatings obtained by different thermal spray processes. *Journal of the European Ceramic Society*. 2020;40(12):4084–4100.
<https://doi.org/10.1016/j.jeurceramsoc.2020.04.058>
 28. Wu Y., Luo H., Cai C., Wang Y., Zhou Y., Yang L., Zhou G. Comparison of CMAS corrosion and sintering induced microstructural characteristics of APS thermal barrier coatings. *Journal of Material Science and Technology*. 2019;35(3):440–447.
<https://doi.org/10.1016/j.jmst.2018.09.046>
 29. Vidal-Setif M.H., Rio C., Boivin D., Lavigne O. Microstructural characterization of the interaction between 8YPSZ (EB-PVD) thermal barrier coatings and a synthetic CAS. *Surface and Coatings Technology*. 2014; 239:41–48.
<https://doi.org/10.1016/j.surfcoat.2013.11.014>
 30. Ramachandran C.S., Balasubramanian V., Ananthapadmanabhan P.V. Thermal cycling behaviour of plasma sprayed lanthanum zirconate based coatings under concurrent infiltration by a molten glass concoction. *Ceramics International*. 2013;39(2):1413–1431.
<https://doi.org/10.1016/j.ceramint.2012.07.084>
 31. Boissonnet G., Chalk C., Nicholls J., Bonnet G., Pedraza F. Thermal insulation of CMAS (Calcium-Magnesium-Alumino-Silicates)-attacked plasma-sprayed thermal barrier coatings. *Journal of the European Ceramic Society*. 2020;40(5):2042–2049.
<https://doi.org/10.1016/j.jeurceramsoc.2019.12.040>
 32. Pratskova S.E., Burmistrov V.A., Starikova A.A. Thermodynamic modeling of oxide melts of CaO – Al_2O_3 – SiO_2 systems. *Izvestiya vysshikh uchebnykh zavedeniy. Khimiya i khimicheskaya tekhnologiya*. 2020;63(1): 45–50. (In Russ.).
<https://doi.org/10.6060/ivkkt.20206301.6054>

Працкова С.Е., Бурмистров В.А., Старикова А.А. Термодинамическое моделирование оксидных расплавов системы $CaO-Al_2O_3-SiO_2$. *Известия высших учебных заведений. Химия и химическая технология*. 2020;63(1):45–50.

<https://doi.org/10.6060/ivkkt.20206301.6054>

33. Tolkachev O.S., Dvili E.S., Alishin T.R., Khasanov O.L., Miheev D.A., Chzhan T. Assessment of the hydrothermal resistance of Y-TZP ceramics by the degree of tetragonality of major phases. *Pis'ma o materialakh*. 2020;10(4): 416–421. (In Russ.).
<https://doi.org/10.22226/2410-3535-2020-4-416-421>

Толкачев О.С., Двилис Э.С., Алишин Т.Р., Хасанов О.Л., Михеев Д.А., Чжан Ц. Оценка гидротермальной стойкости керамики Y-TZP по степени тетрагональности основных фаз. *Письма о материалах*. 2020;10(4):416–421.

<https://doi.org/10.22226/2410-3535-2020-4-416-421>

34. Viazzi C., Bonino J.-P., Ansart F., Barnabe A. Structural study of metastable tetragonal YSZ powders produced via a sol-gel route. *Journal of Alloys and Compounds*. 2008;452(2):377–383.
<https://doi.org/10.1016/j.jallcom.2006.10.155>

Information about the Authors



Svetlana A. Oglezneva – Dr. Sci. (Eng.), Associate Professor of the Department of mechanics of composite materials and structures, Perm National Research Polytechnic University (PNRPU)

ORCID: 0000-0002-5529-4259

E-mail: svetlana.iron@yandex.ru

Valentina B. Kulmetyeva – Cand. Sci. (Eng.), Associate Professor of the Department of mechanics of composite materials and structures, PNRPU

ORCID: 0000-0002-5214-0932

E-mail: kulmetevavb@pstu.ru

Andrey A. Smetkin – Cand. Sci. (Eng.), Associate Professor of the Department of Mechanics of composite materials and structures, PNRPU

ORCID: 0000-0001-8736-0575

E-mail: smetkinaa@pstu.ru

Alexander E. Malyshev – Master's Degree Student at the Advanced Engineering School "Higher School of Aviation Engine Engineering", PNRPU

ORCID: 0009-0004-6923-9316

E-mail: malyshev.4lex@yandex.ru

Сведения об авторах

Светлана Аркадьевна Оглезнева – д.т.н., профессор, доцент кафедры механики композиционных материалов и конструкций, Пермский национальный исследовательский политехнический университет (ПНИПУ)

ORCID: 0000-0002-5529-4259

E-mail: svetlana.iron@yandex.ru

Валентина Борисовна Кульметьева – к.т.н., доцент кафедры механики композиционных материалов и конструкций, ПНИПУ

ORCID: 0000-0002-5214-0932

E-mail: kulmetevavb@pstu.ru

Андрей Алексеевич Сметкин – к.т.н., доцент кафедры механики композиционных материалов и конструкций, ПНИПУ

ORCID: 0000-0001-8736-0575

E-mail: smetkinaa@pstu.ru

Александр Евгеньевич Малышев – студент магистратуры Передовой инженерной школы «Высшая школа авиационного двигателестроения», ПНИПУ

ORCID: 0009-0004-6923-9316

E-mail: malyshev.4lex@yandex.ru

Contribution of the Authors



S. A. Oglezneva – scientific supervision, analysis of research results, manuscript revision, revision of conclusions.

V. B. Kulmetyeva – development of the main concept, formulation of the research aim and objectives, manuscript drafting, analysis of research results, formulation of conclusions.

A. A. Smetkin – experiment preparation, conducting experiments, formulation of the research objectives, manuscript drafting, formulation of conclusions.

A. E. Malyshev – sample testing, manuscript drafting

Вклад авторов

С. А. Оглезнева – научное руководство, анализ результатов исследований, корректировка текста, корректировка выводов.

В. Б. Кульметьева – формирование основной концепции, постановка цели и задачи исследования, подготовка текста, анализ результатов исследований, формулировка выводов.

А. А. Сметкин – подготовка эксперимента, проведение экспериментов, постановка цели и задачи исследования, подготовка текста, формулировка выводов.

А. Е. Малышев – проведение испытаний образцов, подготовка текста статьи.

Received 12.05.2025

Revised 18.06.2025

Accepted 20.06.2025

Статья поступила 12.05.2025 г.

Доработана 18.06.2025 г.

Принята к публикации 20.06.2025 г.



UDC 669.717: 669.718: 621.9.048

<https://doi.org/10.17073/1997-308X-2025-4-60-76>

Research article
Научная статья



Combined technology of electrospark and cathodic-arc formation of wear- and oxidation resistant coatings

S. K. Mukanov , M. I. Petrzhik, A. E. Kudryashov, P. A. Loginov,
N. V. Shvyndina, A. N. Sheveyko, K. A. Kuptsov, E. A. Levashov

National University of Science and Technology “MISIS”
1 Bld, 4 Leninskiy Prosp., Moscow 119049, Russia

 smukanov@isis.ru


Abstract. The regularities of formation of wear- and oxidation-resistant coating under combined electrospark and cathodic-arc treatment (ESCAT) of AZhK superalloy were studied. The effect of electrode polarity and rare-earth (Ce, Er) microalloying of Al–Ca-based rod electrodes on the structure, strengthening and oxidation resistance of the deposited coatings was studied. It was found that anodic polarity secures the formation of crack-free coatings predominantly composed of γ' -Ni₃Al intermetallic (L1₂-type structure, 3.600 Å). These coatings reached a thickness of 15–20 μm due to the oriented growth of crystallites with a transverse size below 300 nm. In contrast, the coatings formed at cathodic polarity have consisted of two intermetallic phases: β-NiAl (B2 structure, 2.895 Å) and γ' -Ni₃Al (L1₂, 3.595 Å). Structural and phase transformations occurring during the treatment of a AZhK substrate (initial hardness of 5.2 GPa) using electrodes of different polarities constitute the dominant strengthening factors. The maximum hardness (12.3 GPa) was recorded for coatings composed of β-NiAl and γ' -Ni₃Al phases. Coatings obtained with anodic electrode polarity exhibited relatively lower hardness values (7.3 GPa) accompanied by low elastic modulus values (112 GPa). The wear rate of these coatings ranged from 6 to $7.5 \cdot 10^{-5}$ mm³/(N·m), representing a sixfold improvement of wear resistance compared to the untreated AZhK alloy. *In-situ* TEM studies revealed excellent thermal stability of the γ' -Ni₃Al intermetallic structure upon heating the coating lamellae cut of the coating obtained under anodic polarity up to 700 °C. Results of high-temperature oxidation tests at 1000 °C indicate that the coating the AZhK alloy change the oxidation law from linear to logarithmic one. The minimum thickness of the oxide layer (about 3 μm) was found in the coatings obtained by ESCAT using Al–Ca–Er electrode with anodic polarity. That is 10 times less than the thickness of the oxide layer of AZhK alloy. The change of oxidation law during annealing to the logarithmic one is due to in-situ formed the NiAl₂O₄/α-Al₂O₃ barrier layer strengthened with CaMoO₄ particles. It slowing down of oxygen diffusion in bulk of substrate providing its excellent oxidation resistance.

Keywords: electrospark treatment, cathodic arc deposition, fusible electrodes, rare-earth metals microalloying, electrode polarity, intermetallic compounds, hardness, wear resistance, barrier oxide layer, high-temperature oxidation resistance

Acknowledgements: This work was supported by the Ministry of Science and Higher Education of the Russian Federation under state research assignment, project No. FSME-2025-0003.

For citation: Mukanov S.K., Petrzhik M.I., Kudryashov A.E., Loginov P.A., Shvyndina N.V., Sheveyko A.N., Kuptsov K.A., Levashov E.A. Combined technology of electrospark and cathodic-arc formation of wear- and oxidation resistant coatings. *Powder Metallurgy and Functional Coatings*. 2025;19(4):60–76. <https://doi.org/10.17073/1997-308X-2025-4-60-76>

Комбинированная технология электроискрового и катодно-дугового формирования износо- и жаростойких покрытий

С. К. Муканов , М. И. Петржик, А. Е. Кудряшов, П. А. Логинов,
Н. В. Швындина, А. Н. Шевейко, К. А. Купцов, Е. А. Левашов

Национальный исследовательский технологический университет «МИСИС»
Россия, 119049, г. Москва, Ленинский пр-т, 4, стр. 1

 smukanov@isis.ru

Аннотация. Изучены закономерности формирования стойких к износу и окислению покрытий при комбинированной электроискровой и катодно-дуговой обработке (ЭИКДО) жаропрочного сплава АЖК. Исследовано влияние полярности стержневых электродов на основе Al–Ca и их микролегирования РЗМ (Ce, Er) на структуру, упрочнение и жаростойкость полученных покрытий. Установлено, что при подключении электрода с анодной полярностью формируются покрытия без трещин на основе интерметаллида γ' -Ni₃Al (тип L1₂, 3,600 Å). Их толщина достигает 15–20 мкм в результате направленного роста кристаллитов с поперечным размером менее 300 нм. При подключении к электроду катодной полярности формируются покрытия, в структуре которых найдены зерна двух интерметаллидов: β -NiAl (тип B2, 2,895 Å) и γ' -Ni₃Al (тип L1₂, 3,595 Å). Структурно-фазовые превращения, происходящие при обработке электродами с разной полярностью подложки из АЖК с твердостью 5,2 ГПа, являются доминирующими факторами упрочнения. Максимальное значение твердости (12,3 ГПа) зафиксировано в покрытиях, состоящих из β -NiAl и γ' -Ni₃Al. При анодной полярности электрода твердость покрытий составляет 7,3 ГПа, и при этом они имеют низкие (112 ГПа) значения модуля упругости. Величина приведенного износа покрытий находится в пределах от $6,0 \cdot 10^{-5}$ до $7,5 \cdot 10^{-5}$ мм³/(Н·м), что в 6 раз меньше, чем у необработанного сплава АЖК. При *in-situ* ПЭМ-исследовании установлена превосходная термическая стабильность интерметаллидной структуры γ' -Ni₃Al при нагреве до $t = 700$ °С ламели, вырезанной из покрытия, полученного при анодном режиме обработки. Результаты испытаний на стойкость к высокотемпературному окислению при $t = 1000$ °С свидетельствуют, что покрытия меняют закон окисления сплава АЖК с линейного на логарифмический. Минимальная толщина оксидного слоя (около 3 мкм) установлена у покрытий, полученных при ЭИКДО электродом Al–Ca–Er с анодной полярностью, что в 10 раз меньше таковой для сплава АЖК. Переход к логарифмическому закону окисления обусловлен замедлением диффузии кислорода через образующийся при отжиге барьерный слой NiAl₂O₄/α-Al₂O₃, упрочненный частицами CaMoO₄, что обеспечивает превосходную стойкость к окислению сплава АЖК.

Ключевые слова: электроискровая обработка, катодно-дуговое испарение, легкоплавкие электроды, микролегирование РЗМ, полярность электродов, интерметаллиды, твердость, износостойкость, барьерный оксидный слой, жаростойкость

Благодарности: Работа выполнена при финансовой поддержке Министерства науки и высшего образования РФ в рамках государственного задания (проект FSME-2025-0003).

Для цитирования: Муканов С.К., Петржик М.И., Кудряшов А.Е., Логинов П.А., Швындина Н.В., Шевейко А.Н., Купцов К.А., Левашов Е.А. Комбинированная технология электроискрового и катодно-дугового формирования износо- и жаростойких покрытий. *Известия вузов. Порошковая металлургия и функциональные покрытия*. 2025;19(4):60–76.
<https://doi.org/10.17073/1997-308X-2025-4-60-76>

Introduction

Over the past decades, considerable attention has been devoted to developing methods for extending the service life of superalloys used in high-temperature applications [1; 2], which are essential for the advancement of aerospace, chemical, and power engineering. One of the key limitations of superalloys in the manufacture of critical components is their insufficient wear and oxidation resistance, necessitating the development of effective surface modification techniques [3].

Electrospark treatment (EST) is a promising technology for strengthening and restoring working surfaces, as well as for producing coatings with enhanced wear

and oxidation resistance [4–6]. An important advantage of EST is its localized action of electrical discharges, which makes it possible to treat specific areas of critical components without overheating. A distinctive feature of the technology is the need for careful selection and control of processing modes to ensure the formation of crack-free coatings.

The versatility of EST is determined by the wide range of developed electrode compositions, which allows selecting specific alloys to improve surface-sensitive properties of components. In particular, the use of fusible electrodes Al–Si, Al–Ca–Si, and Al–Ca–Mn in [7; 8] or EST of EP741NP alloy samples fabricated by selective laser melting (SLM) resulted

in the formation of coatings containing intermetallic Ni_xAl_y particles synthesized during EST. This not only increased wear resistance by a factor of 4.5 through intermetallic strengthening but also reduced surface roughness to $R_a = 3 \mu\text{m}$ due to the healing of surface defects typical of SLM. In addition, the *in-situ* synthesis of $(\text{Al}, \text{Ca})\text{O}$ nanoparticles during oxidative annealing of the coatings at 1000°C provided a four-fold increase in oxidation resistance of the EP741NP alloy [8]. The oxidation rate can be further reduced [9] by improving the crack resistance and adhesion of the oxide layer to the substrate through microalloying the coatings with rare-earth (RE) metals. In this context, particular interest lies in studying the effect of Al–Ca–RE electrodes, where RE = Ce or Er. Such additives are especially relevant for coatings applied to superalloys in order to extend their operating temperature range.

A promising approach is to combine, within a single technological cycle, electrospark and cathodic-arc treatment (ESCAT) [10]. The clear advantages of computer-controlled combined processing include improved reproducibility of the technology and intensified mass transfer during cathodic arc evaporation of the electrode.

The aim of this study was to investigate the conditions for forming wear- and oxidation-resistant coatings by combining electrospark and cathodic-arc treatment (ESCAT) of the AZhK superalloy.

Methods

Rod electrodes 4 mm in diameter, made of near-eutectic Al–Ca–Ce and Al–Ca–Er alloys prepared in accordance with TU 24.45.30–042–11301236–2024, were used for the combined process of ESCAT.

The electrodes were produced by a two-stage process: (1) remelting of the charge components into an ingot in a resistance furnace; (2) induction melting of the ingot followed by casting of the melt into a copper mold in a vacuum chamber filled with argon at a pressure of 0.2 atm.

Substrates were made of the AZhK nickel-based superalloy, fabricated by selective laser melting (SLM) at JSC Komposit (Russia). The chemical composition of the AZhK alloy substrates is given below [11], wt. %:

Ni	59.9–66.2	Al	4.0–5.0
Cr	15.0–16.0	Nb	2.5–3.5
Mo	7.0–9.0	Hf	0.1–0.4
Co	5.0–7.0	C	0.02–0.05

ESCAT were carried out in a single cycle using a modified cap-type UVN-2M unit (Russia), equipped with a CNC system for programmed lateral movement of the sample during processing under specified conditions. After reaching forevacuum, the vacuum chamber was filled with argon to a pressure of 20 Pa, in accordance with TI 65–11301236–2024. This pressure ensures the simultaneous initiation of an arc discharge and electrospark discharges [10]. A schematic of the ESCAT process is shown in Fig. 1.

The microstructure and composition of the samples were examined using a Hitachi S-3400N scanning electron microscope equipped with a NORAN System 7 X-ray microanalysis system (Thermo Scientific, USA). For detailed microstructural studies, cross-sectional samples were prepared using standard metallographic methods (grinding, polishing), followed by electrochemical etching at a constant voltage of 10 V in an aqueous 10 % H_2SO_4 solution.

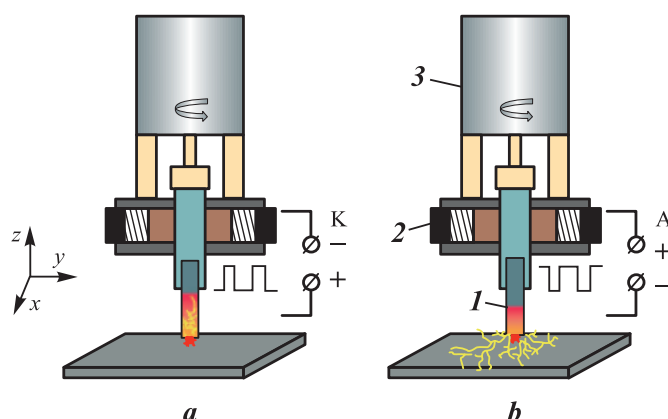


Fig. 1. Schematic diagram of the automated ESCAT setup under cathodic (a) and anodic (b) electrode polarity
1 – electrode, 2 – brush unit, 3 – motor

Рис. 1. Схема автоматизированной ЭИКДО при катодной (a) и анодной (b) полярностях
1 – электрод, 2 – щеточный узел, 3 – двигатель

X-ray diffraction (XRD) phase analysis was performed using diffractograms obtained on a DRON-4 diffractometer (Burevestnik, Russia) with monochromatic CuK_α radiation (1.5418 \AA), and in the case of oxide layers, CoK_α radiation (1.7902 \AA), in the 2θ range of $20\text{--}110^\circ$. For detailed analysis of coating substructures, a JEM-2100 transmission electron microscope (Jeol, Japan) equipped with an Oxford Instruments X-Max 80 energy-dispersive detector was employed. Lamellae were cut from the coating surface layer using a focused ion beam system (Quanta 200 3D FIB, FEI Company, USA). TEM foils were additionally thinned by ion etching on a PIPS II system (Gatan, Inc., USA). *In-situ* studies of structural–phase transformations in the coatings under thermal exposure at 400, 600, and 700°C were carried out directly in the microscope column. The heating rate was $50^\circ\text{C}/\text{min}$. Bright-field images and electron diffraction patterns were obtained with a dwell time of about 15 min at each heating step.

Mechanical properties (hardness H and elastic modulus E) of the coatings were measured on cross-sectional samples using a Nano-Hardness Tester (CSM Instruments, Switzerland) at a maximum load of 10 mN. Tribological tests were performed on a CSM Tribometer (Switzerland) in accordance with ASTM G133-22 under reciprocating sliding at room temperature in air. A 3-mm diameter 100Cr6 steel ball (analog of ShKh15) was used as the stationary counterbody. The test parameters were: track length – 4 mm, applied

load – 2 N, maximum speed – 5 cm/s. Wear tracks were examined using a WYKO NT1100 optical profilometer (Veeco, USA).

Oxidation resistance tests at high temperature were carried out under cyclic heating–cooling in a SNOL 7.2/1200 muffle furnace (Lithuania), exposing the samples in air at 1000°C . The total isothermal holding time in air was 30 h. After each cycle of “heating – isothermal hold – cooling”, the samples were weighed on an ALC-210d4 analytical balance (Acculab, USA) with an accuracy of 10^{-5} g . The specific mass gain (K) was calculated as:

$$K = \Delta m / S_0,$$

where Δm is the mass difference before and after oxidation, mg; S_0 is the total surface area of the sample before testing, cm^2 .

Results

Structure of fusible Al–Ca–RE (Ce, Er) electrodes

Figs. 2, *a* and *b* show the microstructures of the fusible electrodes, while the diffraction spectrum (Fig. 2, *c*) displays the lines corresponding to their phase constituents. It can be seen that the Al–Ca–Ce electrodes have a near-eutectic structure, which is con-

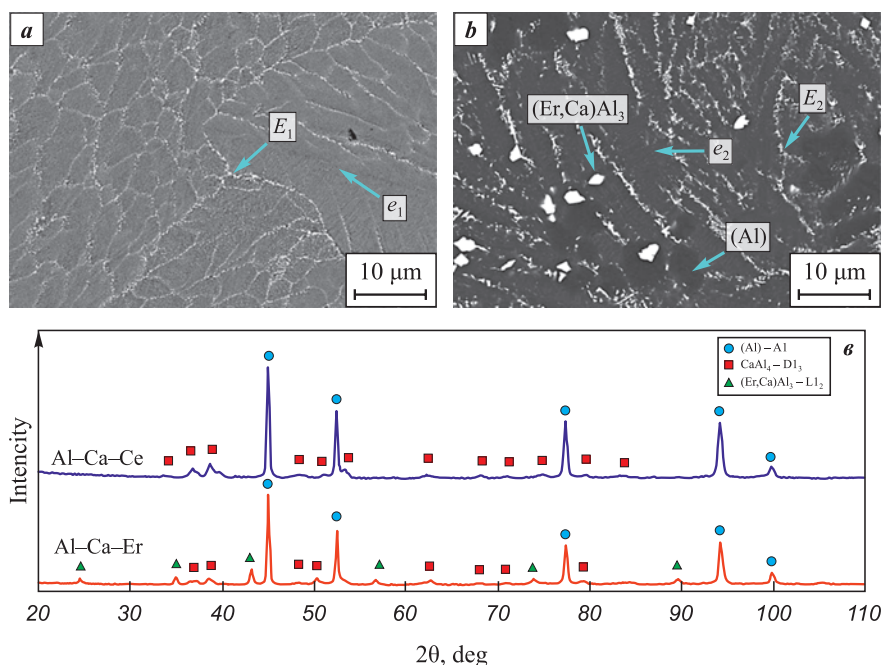


Fig. 2. SEM backscattered electron images of the microstructure of Al–Ca–Ce (*a*) and Al–Ca–Er (*b*), and diffraction patterns of the electrodes (*c*)

Рис. 2. РЭМ-изображения в режиме обратноотраженных электронов микроstructures Al–Ca–Ce (*a*) и Al–Ca–Er (*b*), а также дифрактограммы электродов (*c*)

Table 1. Elemental distribution across structural constituents according to EDS data (see Fig. 2)

Таблица 1. Распределение элементов по структурным составляющим по данным ЭДС (см. рис. 2)

Structural constituent	Elemental composition, at. %			
	Al	Ca	Ce	Er
$e_1 [(Al) + CaAl_4]$	94.8	4.3	0.8	–
$E_1 [(Al) + CaAl_4 + (Ca,Ce)Al_4]$	93.8	5.2	1.0	–
$e_2 [(Al) + CaAl_4]$	93.9	6.1	–	–
$E_2 [(Al) + CaAl_4 + (Er,Ca)Al_3]$	93.5	3.8	–	2.8
$(Er,Ca)Al_3$	81.8	2.3	–	15.7
(Al)	100.0	–	–	–

sistent with the results of [12]. As shown in Table 1, this structure consists of fine two-phase eutectics $e_1 [(Al) + CaAl_4]$ and three-phase eutectics $E_1 [(Al) + CaAl_4 + (Ca,Ce)Al_4]$, as well as dendrites of a solid solution based on aluminum (Al).

As shown in Fig. 2, *b*, the addition of Er to the Al–Ca–Er electrode promotes the formation of bright, faceted primary $Al_3(Er,Ca)$ crystals. Consequently, the principal structural constituents of the Al–Ca–Er electrode are fine two-phase eutectics $[(Al) + CaAl_4]$, three-phase eutectics $[(Al) + CaAl_4 + (Er,Ca)Al_3]$, primary $Al_3(Er,Ca)$ crystals, and (Al) dendrites. The elemental distribution among the structural constituents of the Al–Ca–Ce and Al–Ca–Er electrodes is summarized in Table 1.

Kinetics of coating formation and structure

The kinetic curves of mass transfer as a function of electrode polarity are shown in Fig. 3. The maximum specific mass gain of the substrate, corresponding to the greatest coating thickness, is observed after 5 min of treatment, regardless of electrode polarity. However, the specific erosion after 5 min of treatment under cathodic electrode connection ($\Delta A_5 = -94.9 \cdot 10^{-4}$ g) is an order of magnitude higher than that under anodic polarity ($\Delta A_5 = -7.1 \cdot 10^{-4}$ g). The mass gain curve obtained under anodic polarity (ACe) indicates a low contribution of mass transfer ($\Delta K_5 = 4.8 \cdot 10^{-4}$ g). In this case, an increase in mass is observed only after 3 min of treatment.

On the surface of the ACe series coatings, elongated solidified droplets can be observed (Fig. 3, *c*), some of which are marked with yellow arrows. Their formation under anodic polarity can be attributed to local melting of fusible structural constituents within cathode spot [12]. In addition, oxide particles approximately 15 μm in size were found on the surface of these coatings (highlighted with orange arrows). According to EDS data, these particles, in addition to oxygen, contain high concentrations of Al (28–33 at. %) and Ca (6–10 at. %). They also contain about 1 at. % Ce and Er, which is expected given their high affinity for oxygen. Under cathodic polarity, the surfaces of the coatings (KEr and KCe) exhibit overlapping solidified melt droplets, but they

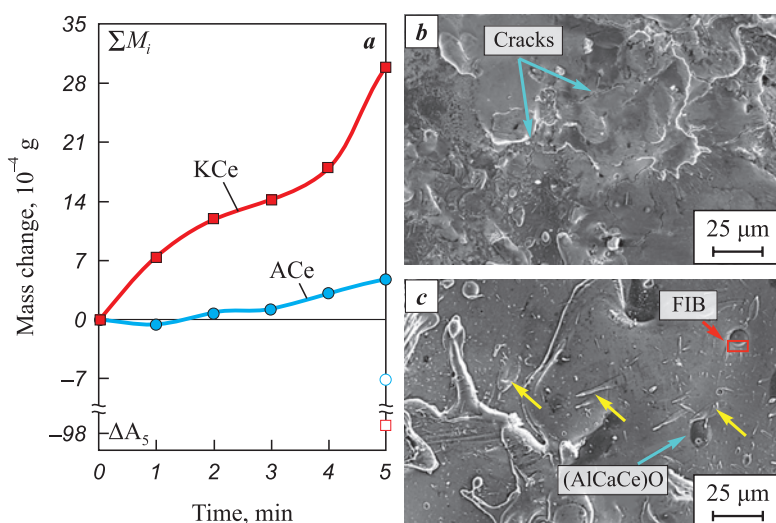


Fig. 3. Kinetic curves of mass transfer for the Al–Ca–Ce electrode during ESCAT on the AZhK alloy substrate (*a*) and SEM images of the surface of coatings: KEr (*b*) and ACe (*c*)

$\Sigma \Delta M_i$ – mass gain of the substrate; ΔA_5 – electrode erosion after 5 min of treatment

Рис. 3. Кинетические кривые массопереноса электрода Al–Ca–Ce при ЭИДКО подложки из сплава АЖК (*a*) и РЭМ-изображения поверхности покрытий KEr (*b*) и ACe (*c*)

$\Sigma \Delta M_i$ – привес массы подложки; ΔA_5 – эрозия электрода после 5 мин обработки

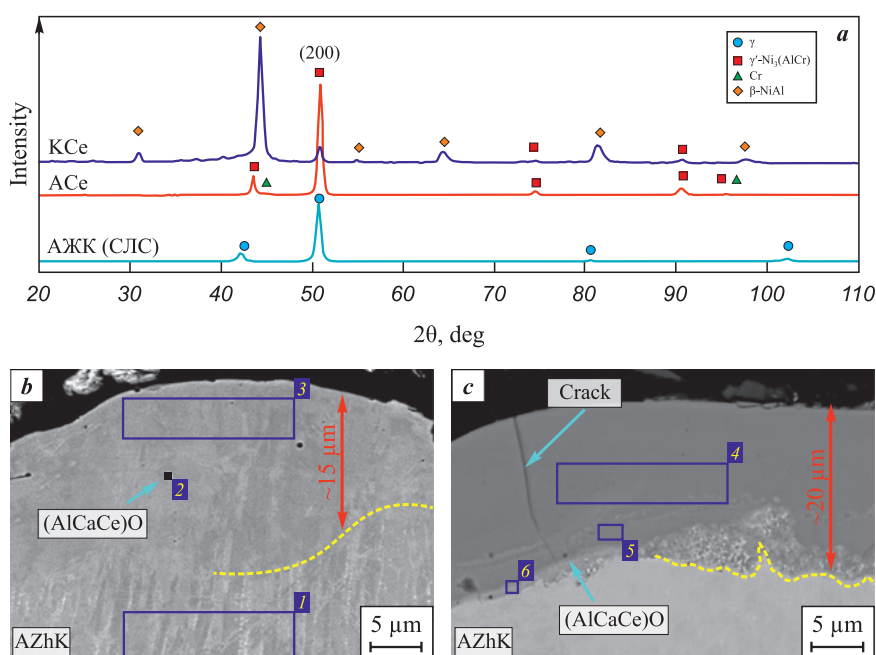


Fig. 4. Diffraction patterns of the initial AZhK alloy and after ESCAT with an Al–Ca–Ce electrode (a), and typical cross-sectional images of the ACe (b) and KCe (c) coatings

Рис. 4. Дифрактограммы исходного и подвергнутого ЭИКДО сплава АЖК электродом Al–Ca–Ce (a), типичные изображения поперечных шлифов покрытий АСс (b) и КСс (c)

are less homogeneous in composition. It is worth noting that, unlike the A-series, cracks were observed on the surfaces of the K-series coatings.

XRD patterns (Fig. 4, a) of the initial and ESCAT-treated substrates revealed differences in the phase composition of the coatings depending on electrode polarity. Under cathodic polarity (sample KCe), the coating consists of β-NiAl, which has an ordered cubic B2 crystal structure, and γ'-Ni₃(AlCr) with an ordered L1₂ superstructure. The β-phase fraction is dominant (Table 2), amounting to 84.6 wt. %.

Anodic polarity (sample ACe) results in the formation of a coating predominantly composed of γ'-Ni₃(AlCr) (97.6 wt. %). Diffraction peaks of the β-phase were not detected in the diffractogram. This indicates an insufficient amount of free Al in the EST melt to form the equiatomic NiAl intermetallic.

As shown in Figs. 4, b and c, typical cross-sectional images of the coatings are presented. The ACe and AEr coatings do not display a distinct interface with the substrate, which can be attributed to their similar elemental concentrations (Table 3). According to EDS data (regions 1 and 3), however, the Al content in the coatings (15 at. %) is nearly twice that of the AZhK alloy (9 at. %). No Ca was detected in the bulk of the coating, and the Ce content did not exceed 0.2 at. %. The coating structure nevertheless contains small black inclusions identified by EDS as (AlCaCe)O (Table 3, region 2). Larger particles of the same composition were also found on the surfaces of these coatings (see Fig. 3, c).

The thickness of the coatings formed under cathodic polarity (18–20 μm) is greater than that of the anodic ACe and AEr coatings (15 μm). The microstructure

Table 2. Phase composition of the AZhK alloy – initial and after ESCAT

Таблица 2. Фазовый состав сплава АЖК – исходного и подвергнутого ЭИКДО

Sample	Phase	Space group (structure type)	Fraction, wt. %	Lattice perimeter <i>a</i> , Å
AZhK	γ	<i>Fm-3m</i> (Cu)	100.0	3.609
ACe	γ'-Ni ₃ (AlCr)	<i>Pm-3m</i> (L1 ₂)	97.6	3.600
	Cr	<i>Im-3m</i> (W)	2.4	2.870
KCe	B-NiAl	<i>Pm-3m</i> (B2)	84.6	2.895
	γ'-Ni ₃ (AlCr)	<i>Fm-3m</i> (L1 ₂)	15.4	3.595

Table 3. EDS results for coating regions ACe and KCe shown in Fig. 4

Таблица 3. Результаты ЭДС областей покрытий ACe и KCe, показанных на рис. 4

Region	Elemental composition, at. %									
	Al	Ni	Ca	Cr	Co	Mo	Nb	Ce	O	Hf
1	9.3	60.9	–	16.3	7.6	4.1	1.8	–	–	–
2 (ACe)	24.7	1.5	12.8	0.6	–	–	–	1.0	58.9	0.6
3 (ACe)	15.0	57.4	–	15.7	5.9	4.1	1.7	0.2	–	–
4 (KCe)	74.4	14.9	2.9	4.1	1.4	1.3	0.4	0.6	–	–
5 (KCe)	67.8	19.8	1.5	6.0	1.9	1.8	0.7	0.5	–	–
6 (KCe)	55.5	31.6	1.2	6.2	3.0	1.7	0.5	0.3	–	–

of the cathodic coatings (Fig. 4, c) exhibits pronounced differences due to the increased incorporation of elements from the Al–Ca–RE electrodes. As shown in Table 3, the Al concentration in the K-series coatings reaches 74 at. %, while the Ni content decreases to 15 at. %. A distinct interface between the AZhK substrate and the coatings is evident; it is heterogeneous in both structure and composition, with the Ni concentration in this region at about 30 at. %. It should also be noted that under cathodic polarity, Ca and RE metals are distributed more uniformly throughout the coatings compared with the ACe and AEr samples, although the total RE metal content does not exceed 0.6 at. %.

The microstructure of the A-series coatings (Figs. 5, a and b) consists of uniform fine columnar crystals, which differ entirely from the microstructures of both the electrodes and the substrate. Yellow dashed lines indicate the boundaries of solidified melt droplets. The crystallite orientation coincides with the growth

direction of the AZhK alloy, which is also reflected in the increased intensity of the 200 γ' peak at $2\theta \approx 50^\circ$ (Fig. 4, a). During crystallization of the melt droplets, the columnar crystallites grow from the interface toward the surface.

The coatings formed under cathodic polarity (Figs. 5, c and d) exhibit a different structure, characterized by a less pronounced metallographic texture. Compared with the substrate, these coatings are less susceptible to chemical etching, which indicates higher corrosion resistance.

To investigate the structure of crack-free coatings obtained under anodic polarity in greater detail, the fine structure of the ACe sample was analyzed. A bright-field TEM image of a lamella cut from its surface is shown in Fig. 6, a (see also Fig. 3, c). The coating consists of columnar crystals with a strongly oriented growth direction along the [01–1] zone axis. An oxide particle located above the columnar crystals

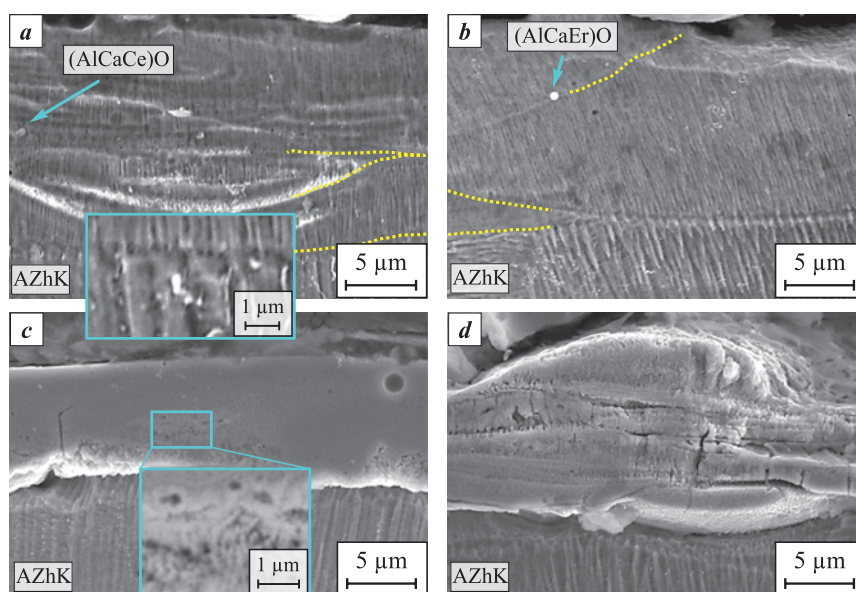


Fig. 5. SEM secondary electron images of coating microstructures: ACe (a), AEr (b), KCe (c), and KEr (d)

Рис. 5. РЭМ-изображения в режиме вторичных электронов микроstructures покрытий ACe (a), AEr (b), KCe (c), KEr (d)

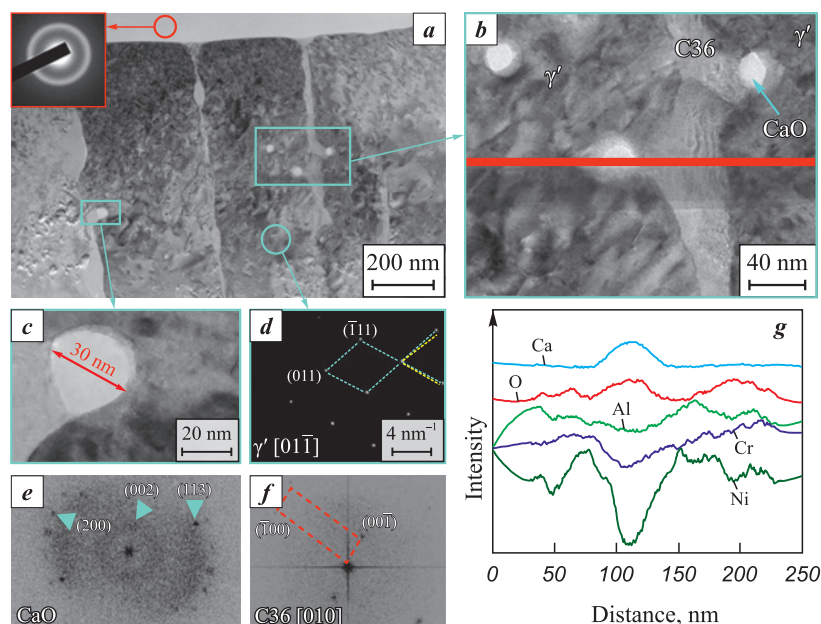


Fig. 6. Fine structure of the ACe sample obtained under anodic polarity in ESCAT

a – TEM image of the ACe coating lamella; *b* – HRTEM image of γ' columnar crystal boundaries; *c* – CaO nanoparticles; *d* – electron diffraction pattern of a columnar crystal; *e* – Fourier transform of a CaO particle; *f* – C36 Laves phase; *g* – elemental distribution map corresponding to Fig. *b*

Рис. 6. Тонкая структура образца АСс, полученного при анодной полярности ЭИО

a – ПЭМ-изображение ламели покрытия АСс; *b* – ПЭМ ВР изображение границы столбчатых кристаллов γ' ; *c* – наночастицы CaO; *d* – электронная дифракция столбчатого кристалла; *e* – Фурье-преобразования частицы CaO; *f* – фазы Лавеса C36; *g* – распределение элементов из рис. *b*

on the coating surface exhibits an amorphous structure, confirmed by electron diffraction showing an amorphous halo (inset in Fig. 6, *a*).

The columnar crystals, ~ 300 nm in cross-section, consist of the γ' phase with an ordered $L1_2$ crystal structure, as confirmed by electron diffraction. Analysis of the corresponding diffraction pattern (Fig. 6, *d*) revealed displacements of atomic planes, which may result from dislocation motion in the γ' matrix.

Spherical nanoparticles up to 30 nm in size are mainly located along the boundaries of the columnar crystals (Fig. 6, *c*). Analysis of these particles (Figs. 6, *b* and *g*) showed that they are enriched in calcium and oxygen, while the concentrations of all other elements are significantly reduced. According to Fig. 6, *d*, these oxides have an orthorhombic lattice with a CaO-type structure.

In addition, the γ' grain boundaries contain a highly distorted secondary phase (Fig. 6, *b*). EDS analysis determined its composition as $\text{Ni}_{53.21}\text{Al}_{20}\text{Cr}_{15.85}\text{Co}_{6.5}\text{Mo}_{4.45}$. The large interplanar spacing ($d = 5.7$ Å), obtained from the Fourier transform (Fig. 6, *e*), suggests that the diffraction originates from the $[10\text{--}10]$ plane of a hexagonal Laves phase (AB2) of the C36 structure type. The calculated lattice parameters for this phase are $a = 6.63$ Å and $c = 11.05$ Å. Based on the elemen-

tal ratio, it can be assumed that the Laves phase has the composition $(\text{Ni,Co})_2(\text{Al,Cr,Mo})$.

Fig. 7 shows the overall appearance of the lamella and enlarged images of the selected region before and after vacuum annealing at 700 °C. A distinct change in contrast in some areas indicates relaxation of internal stresses (Fig. 7, *b*). The series of electron diffraction patterns presented in Fig. 7, *c*, obtained from γ' columnar crystals during lamella heating up to 700 °C, confirm the high thermal stability of this phase. At the same time, at 600 °C nanocrystalline particles appeared in the amorphous (AlCaCe)O particle located on the coating surface (Fig. 7, *d*). Their interplanar spacings (3.05 Å, 2.90 Å) correspond to a monoclinic CaAl_2O_4 mixed oxide.

Mechanical and tribological properties of the coatings

The results of instrumented nanoindentation (Fig. 8, *a*) showed that ESCAT increases the hardness and decreases the Young's modulus (E) of the AZhK alloy substrate. The presence of Er in the coatings has a more pronounced effect on hardness compared with Ce alloying of the electrode. The maximum hardness values (12.3 ± 0.3 and 10.2 ± 0.3 GPa, respectively) were

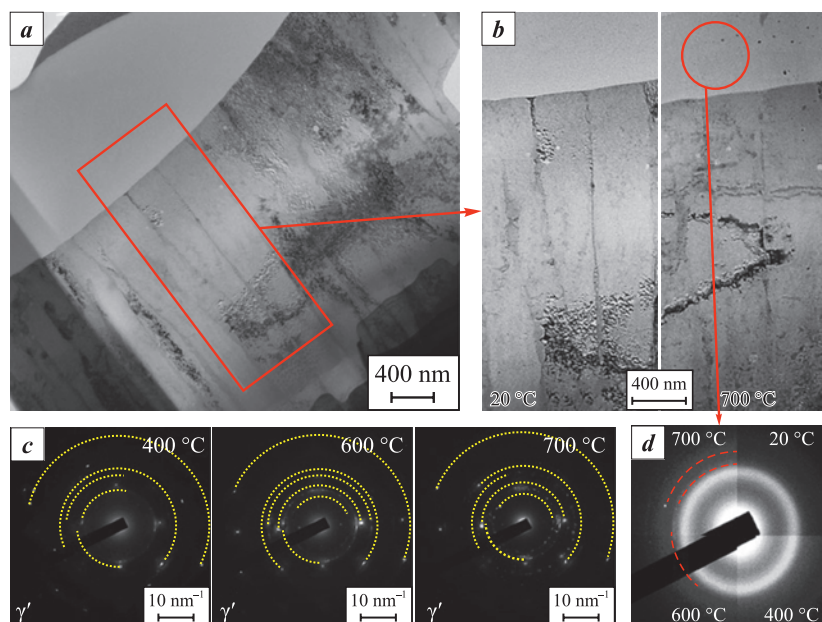


Fig. 7. Overall view of the lamella (*a*), images before and after vacuum heating to 400 and 700 °C in the TEM column (*b*), electron diffraction patterns from γ' columnar crystal zones (*c*), and from the amorphous oxide (*d*)

Рис. 7. Общий вид ламели (*a*), увеличенные ее изображения до и после вакуумного нагрева от 400 до 700 °C в колонне ПЭМ (*b*), а также картины дифракции от зон столбчатых кристаллов γ' (*c*) и аморфного оксида (*d*)

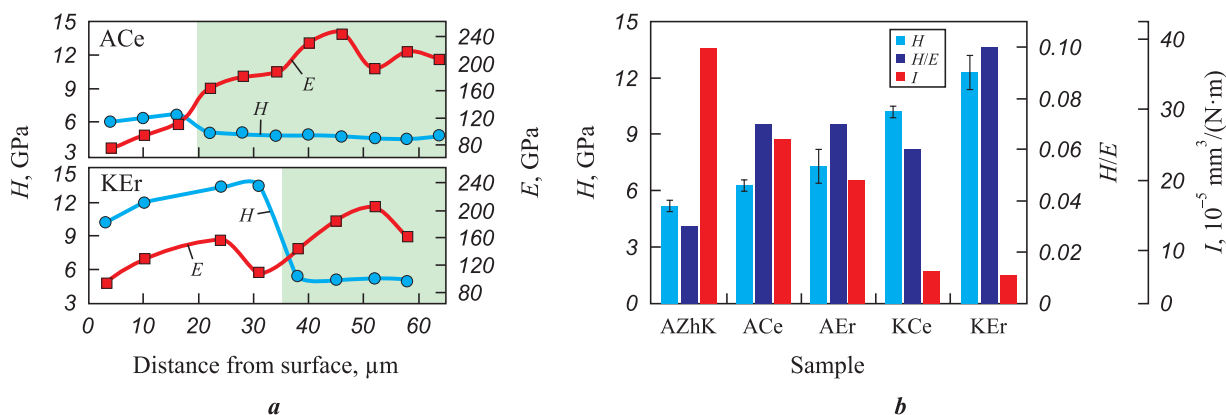


Fig. 8. Profiles of hardness (*H*) and Young's modulus (*E*) across the sample thickness (*a*) and comparison of hardness, *H/E* ratio, and wear rate of the samples (*b*)

Рис. 8. Распределение твердости и модуля упругости по толщине образца (*a*) и сопоставление значений *H*, *H/E* и приведенного износа образцов (*b*)

recorded when cathodic polarity was applied. Fig. 8, *b* also presents the *H/E* ratio, which is commonly used as an indicator of the damage tolerance of coatings. The coatings exhibit relatively low Young's modulus values ($E \leq 160$ GPa), which is atypical for intermetallics: 178 GPa for Ni_3Al and 284 GPa for NiAl [14].

As shown in Figs. 8, *b* and 9, *b*, ESCAT significantly improves the wear resistance of the nickel alloy, with the effect being stronger under cathodic polarity (up to a sixfold increase) compared with anodic polarity (up to a twofold increase). Erbium in the coating has a stronger influence on enhancing these proper-

ties. The effects of RE additions and electrode polarity on the wear resistance of the coatings correlate with the formation of a dual-intermetallic structure. In particular, coatings with a $(\beta\text{-NiAl} + \gamma'\text{-Ni}_3\text{Al})$ structure, which exhibit the highest hardness, are characterized by excellent wear resistance, with values ranging from 6.0 to $7.5 \cdot 10^{-5} \text{ mm}^3/(\text{N}\cdot\text{m})$.

The friction coefficient versus cycle number curves shown in Fig. 9, *a* demonstrate the higher amplitude of friction fluctuations in contact with the steel ball for both the untreated AZhK alloy and after anodic ESCAT. The average friction coefficient values range

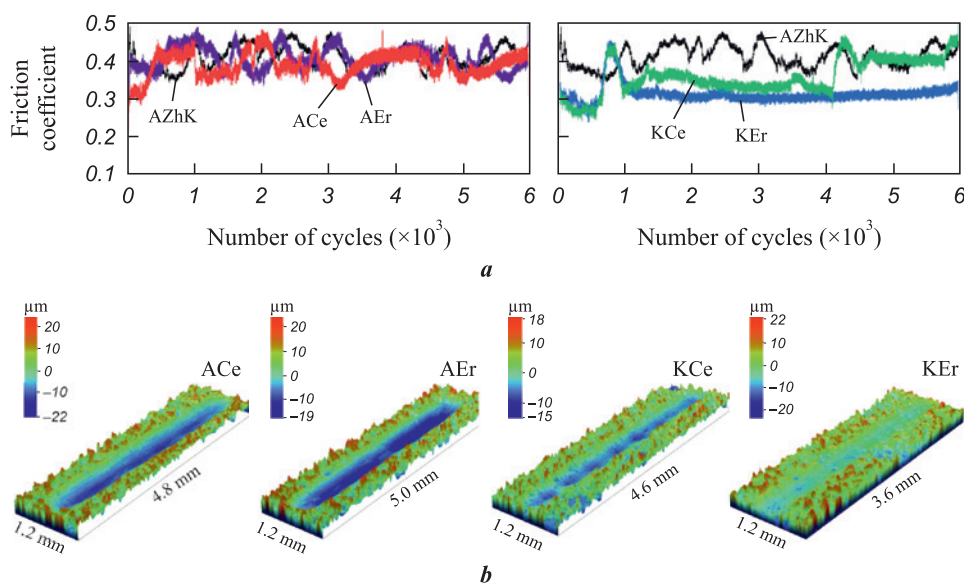


Fig. 9. Friction coefficient curves (a) and 3D images of wear tracks (b)

Рис. 9. Кривые коэффициента трения (a) и 3D-изображения дорожек износа (b)

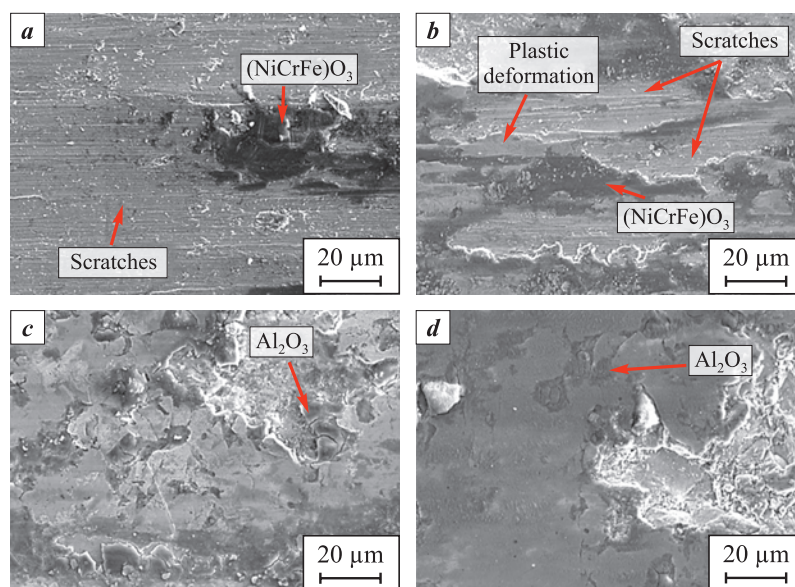


Fig. 10. SEM secondary electron images of wear tracks for the samples: ACe (a), AEr (b), KCe (c), and KEr (d)

Рис. 10. РЭМ-изображения во вторичных электронах дорожек износа образцов ACe (a), AEr (b), KCe (c), KEr (d)

from 0.45 to 0.35, while a further reduction to ~ 0.3 is observed for coatings produced under cathodic polarity (K-series).

To investigate the wear mechanisms in greater detail, SEM images of the wear tracks were obtained (Fig. 10), and EDS analysis was performed. The results suggest two dominant wear mechanisms, which correlate with the coating structures determined by electrode polarity during ESCAT. In the case of A-series coatings, ball sliding is accompanied by the formation of deep grooves and numerous ridges, associated with local plastic deformation (Figs. 10, a and b).

In contrast, the wear track surfaces of the K-series coatings display a different morphology, characterized by compacted wear debris formed under load during testing (Figs. 10, c and d). According to EDS data, the bottoms of the wear tracks are depleted in aluminum (28.2 at. % Al and 47.9 at. % Ni). At the same time, the wear debris consists mainly of Al₂O₃, formed by selective oxidation of aluminum. Thus, wear of the K-series coatings is primarily governed by aluminum oxidation and compaction of the oxidized debris, processes which together promote the formation of a protective tribolayer.

High-temperature oxidation resistance of the coatings

Fig. 11 and Table 4 show the results of qualitative and quantitative phase analysis of the samples after 30 h of oxidative annealing at 1000 °C. The XRD pattern of the AZhK alloy exhibits diffraction peaks corresponding to Cr_2O_3 and spinel phases NiCr_2O_4 , NiMoO_4 , and NiNb_2O_6 .

Although the ESCAT coatings show a similar qualitative phase composition after long-term oxidative annealing, the quantitative phase ratios differ markedly (Table 4) and are dependent on electrode polarity. In the annealed coated samples, a large fraction of the γ' phase is retained (30–72 wt. %). This suggests that the oxide layers formed on the coating surfaces are relatively thin and remain fully penetrable by X -rays under Bragg–Brentano geometry. Thus, after isothermal holding of the ACe and AEr coatings, the surface layer is dominated by $\alpha\text{-Al}_2\text{O}_3$ and NiAl_2O_4 phases, while CaMoO_4 is detected only in small amounts (up to 3 wt. %). In contrast, oxidation of the KCe and KEr coatings results in an increase in CaMoO_4 content up to 15 wt. %, while the combined content of $\alpha\text{-Al}_2\text{O}_3$ and NiAl_2O_4 reaches 25–56 wt. %.

Cross-sectional images (Fig. 12) of the oxidized samples confirm the XRD results. The total thickness of the oxide layers formed on the coatings reaches 2.5 μm , which is up to 10 times thinner than the oxide layer on the AZhK alloy ($\sim 25 \mu\text{m}$). The minimum oxide layer thickness was recorded for coatings produced under anodic polarity.

The oxide layers exhibit a bilayer structure. The outer continuous NiAl_2O_4 layer has a spinel structure and contains finely dispersed CaMoO_4 particles. Beneath it lies a layer of $\alpha\text{-Al}_2\text{O}_3$, whose boundaries (highlighted with blue arrows in the inset of Fig. 12, *b*) are enriched in Er and Ce. According to EDS (region 1, Table 5), the oxygen-free zone of the coating is depleted in Al (7.8 at. %). These results indicate that beneath the oxide layers there is a zone composed not of pure γ' phase, as identified by XRD, but of $\gamma' + \gamma$ grains.

The oxide layers of the coatings produced under cathodic polarity (Figs. 12, *c* and *d*) also show a heterogeneous structure. CaMoO_4 grains are found on the surface, beneath which lies a continuous $\text{NiAl}_2\text{O}_4 + \alpha\text{-Al}_2\text{O}_3$ layer, also containing dispersed CaMoO_4 particles. The oxygen-free zone of these coatings consists of γ' grains, indicating a $\beta \rightarrow \gamma'$ phase transformation driven by the interaction of aluminum with oxygen. Additionally, agglomerates of particles are present at the coating–substrate interface, a feature not observed in the A-series coatings. According to EDS

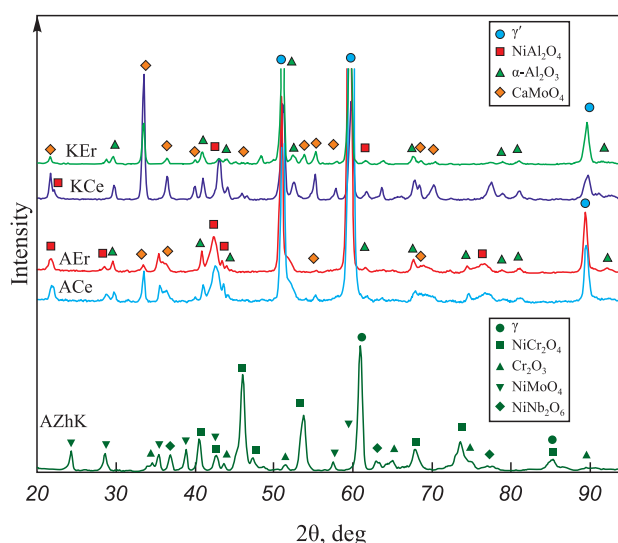


Fig. 11. XRD patterns of the samples after 30 h of oxidative annealing at 1000 °C

Рис. 11. Дифрактограммы образцов после 30 ч окислительного отжига при $t = 1000 \text{ }^\circ\text{C}$

Table 4. Phase composition of the samples after 30 h of oxidative annealing at 1000 °C

Таблица 4. Фазовый состав образцов после 30 ч окислительного отжига при $t = 1000 \text{ }^\circ\text{C}$

Sample	Phase	Fraction, wt. %	Lattice parameter, Å	
			<i>a</i>	<i>c</i>
AZhK-substrate	NiCr_2O_4	46.2	8.276	—
	γ	19.1	3.588	—
	NiMoO_4	14.3	—	—
	Cr_2O_3	14.3	4.965	13.556
	NiNb_2O_6	6.2	4.696	3.032
ACe	$\gamma'\text{-Ni}_3\text{Al}$	72.2	3.596	—
	$\alpha\text{-Al}_2\text{O}_3$	12.7	4.763	13.004
	NiAl_2O_4	12.2	8.160	—
	CaMoO_4	2.9	—	—
AEr	$\gamma'\text{-Ni}_3\text{Al}$	61.8	3.596	—
	NiAl_2O_4	18.1	8.172	—
	$\alpha\text{-Al}_2\text{O}_3$	17.2	4.769	13.007
	CaMoO_4	2.9	—	—
KCe	$\gamma'\text{-Ni}_3\text{Al}$	29.6	3.594	—
	NiAl_2O_4	28.9	8.094	—
	$\alpha\text{-Al}_2\text{O}_3$	26.7	4.771	13.033
	CaMoO_4	14.8	5.244	11.470
KEr	$\gamma'\text{-Ni}_3\text{Al}$	46.7	3.585	—
	NiAl_2O_4	23.0	8.078	—
	$\alpha\text{-Al}_2\text{O}_3$	21.2	4.773	13.040
	CaMoO_4	9.1	—	—

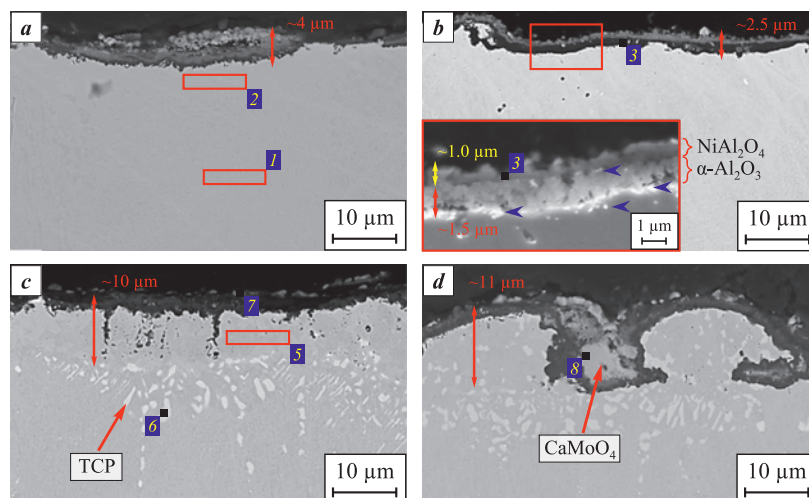


Fig. 12. SEM backscattered electron images of cross-sections of ACE (*a*), AEr (*b*), KCe (*c*), and KEr (*d*) coatings after 30 h of oxidative annealing at 1000 °C

Inset: magnified secondary electron image

Рис. 12. РЭМ-изображения в обратноотраженных электронах поперечных шлифов покрытий ACE (*a*), AEr (*b*), KCe (*c*), KEr (*d*) после 30 ч окислительного отжига при $t = 1000\text{ °C}$. На вставке увеличенное изображение во вторичных электронах

Table 5. EDS results of the regions shown in Fig. 12

Таблица 5. Результаты ЭДС областей, показанных на рис. 12

Region	Elemental composition, at. %									
	O	Al	Ni	Cr	Co	Mo	Nb	Ca	Ce	Er
1	–	7.8	63.4	16.1	6.2	4.5	2.0	–	–	–
2	–	5.6	62.3	18.5	6.9	5.7	1.0	–	–	–
3	60.7	37.5	1.0	0.5	–	0.2	0.1	–	–	–
4	57.6	25.8	9.8	5.4	1.1	–	0.1	–	–	–
5	–	18.9	68.4	6.1	3.9	1.5	1.2	–	–	–
6	–	1.5	29.1	40.5	8.5	20.4	–	–	–	–
7	70.4	0.8	–	–	–	14.0	0.2	13.5	1.0	–
8	65.3	2.3	0.9	0.3	–	15.3	–	14.8	–	1.1

(region 6, Table 5), these particles contain refractory elements consistent with topologically close-packed (TCP) phases.

Fig. 13 shows the oxidation kinetics curves of the untreated and EST-treated samples during 30 h of isothermal exposure at 1000 °C. For comparison, the oxidation kinetics of a coating obtained under anodic polarity of ESCAT with an Al–7 at. % Ca–1 at. % Mn electrode (sample AMn) are also included. In Fig. 13, *a*, the experimental data are shown by solid lines, while the dashed lines represent approximations calculated by an empirical method using the equations given in Table 6. The relationship between mass gain and oxidation time for the AZhK alloy follows a linear law, as confirmed by approximation coefficients close to unity. For this sample (Fig. 14, *b*), after 30 h of iso-

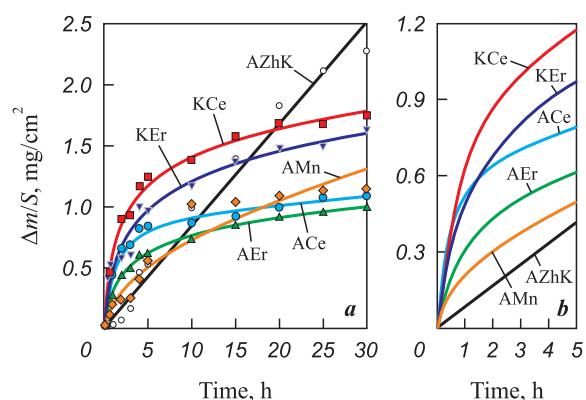


Fig. 13. Oxidation kinetics curves of the samples (*a*) and approximation curves of the initial oxidation stage (5 h) (*b*)

Рис. 13. Кинетика окисления образцов (*a*) и аппроксимационные кривые начальной стадии (5 ч) окисления (*b*)

Table 6. Regression equation parameters for the oxidation kinetics curves of the samples

Таблица 6. Параметры уравнения регрессии кинетических кривых окисления образцов

Sample	Oxidation rate constant K_p	Fitting equation	Approximation coefficient R
AZhK	0.08	$K = 0.08t$	0.979
ACe	0.16	$K = 0.16\ln t$	0.971
AEr	0.22	$K = 0.22\ln t$	0.995
KCe	0.34	$K = 0.34\ln t$	0.983
KEr	0.36	$K = 0.36\ln t$	0.971
AMn	0.26	$K = 0.25t^{0.5}$	0.921

K is the specific mass gain of the samples, mg/cm²; t is the exposure time, h.

thermal exposure, a degraded green-colored surface is observed, which is most likely due to the formation of nickel or chromium oxides.

The oxidation kinetics curves confirm (Fig. 13) that the use of combined ESCAT with Al–Ca-based electrodes significantly improves the oxidation resistance of the AZhK superalloy at 1000 °C. While the mass gain of the AMn coating follows a parabolic law (Table 6), the oxidation of RE-containing coatings follows a logarithmic law. Overall, the oxidation curves of the coatings can be divided into two stages: an initial stage (0–5 h) and a steady stage (5–30 h). Despite the parabolic kinetics of the initial oxidation stage of the AMn sample, it shows the lowest slope of the curve (Fig. 13, *b*), indicating the slowest oxidation rate at this stage. In contrast, other samples with logarithmic oxidation show rapid mass gain during the initial stage, but in the steady stage the rate slows down as the oxide layer thickens. Thus, the transition from parabolic to logarithmic behavior is explained by the retardation of oxygen diffusion through the already formed oxide layer.

Discussion

The role of rare-earth metals in both coatings and nickel-based superalloys has been widely investigated [9; 16; 17]. However, a unified theory explaining the beneficial effects of such alloying has not yet been established. Alloying nickel-based superalloys with RE metals (Y, Ce, La, Hf, and Er), as well as applying RE-modified coatings, reduces oxidation rates by improving the crack resistance and adhesion of the oxide layer to the substrate. Small RE metals additions accelerate the nucleation of chromium and aluminum oxides [18], thereby promoting rapid formation

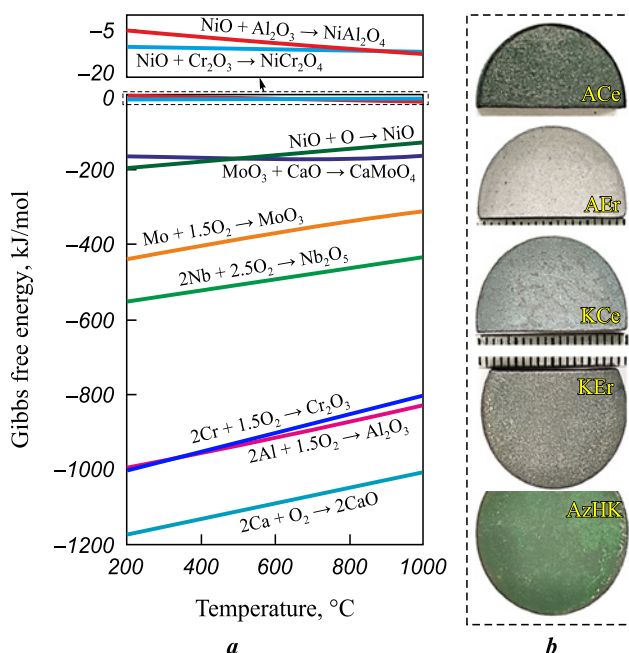


Fig. 14. Gibbs free energy of oxide formation (ΔG) as a function of temperature (calculated using FactSage database [15]) (*a*) and surface appearance of the samples after 30 h of isothermal exposure at 1000 °C (*b*)

Рис. 14. Свободная энергия образования (ΔG) оксидов в зависимости от температуры (построена по результатам базы данных FactSage [15]) (*a*) и внешний вид образцов после 30 ч изотермической выдержки при $t = 1000$ °C (*b*)

of a protective layer. Owing to their large atomic radii and high chemical activity, RE form dispersed phases in coatings (e.g., $\text{Ni}_x\text{Al}_y(\text{Hf,Zr})_z$ [19], LaCrO_3 [20]) that hinder grain boundary diffusion of cations (Al^{3+} , Cr^{3+} , Ni^{2+} , Ta^{5+} [21; 22]). For instance, [23] reported that the presence of Ce (0.038 wt. %) increases aluminum activity in the IC21 superalloy with an Al–Si coating after oxidative annealing at 1150 °C, reducing the Al content required for the formation of a protective $\alpha\text{-Al}_2\text{O}_3$ layer. Ce also retards the polymorphic transformation of metastable $\theta\text{-Al}_2\text{O}_3$ into stable $\alpha\text{-Al}_2\text{O}_3$, thereby suppressing volumetric shrinkage of the oxide layer [24] and lowering the likelihood of crack formation.

Excessive RE additions, however, coarsen the microstructure and degrade the mechanical properties of alloys [25], and may also lead to degradation of the oxide scale. Therefore, electrode compositions were selected to be close to the eutectic point on the phase diagram, allowing the formation of a fluid reactive melt on the metal surface during ESCAT that actively interacts with substrate elements. Although the RE content in the coatings does not exceed 0.5 at. %, this level is sufficient to significantly influence their properties.

The polarity of the electrodes during ESCAT governs the structural and phase transformations in the coatings. Since this processing is carried out in vacuum [10; 12], spark breakdown during electrode retraction is accompanied not only by energy release at the anode, but also by pulsed arc evaporation of the cathode (Fig. 15). Under cathodic polarity, additional electrode sputtering increases the substrate mass gain and coating thickness, whereas anodic polarity leads to partial evaporation of the coating surface.

β -NiAl-based coatings can only be obtained under cathodic polarity, because intensive electrode evaporation enriches the coating with aluminum. Such coatings, however, are prone to cracking due to the mismatch between the thermal expansion coefficients of β -NiAl ($15 \cdot 10^{-6} \text{ K}^{-1}$ [26]) and Ni-based superalloys ($12 \cdot 10^{-6} \text{ K}^{-1}$ [27]). They also exhibit a weaker crystallographic texture (Figs. 6, *c* and *d*), resulting from stronger substrate heating.

Anodic polarity promotes the formation of γ' -Ni₃(AlCr)-based coatings. Minimal substrate heating under these conditions enables efficient heat dissipation into the bulk [28; 29], supporting uniform grain growth with a dominant $\langle 100 \rangle$ crystallographic orientation. The reduced cross-section of the columnar crystallites compared with the AZhK alloy (inset in Fig. 5, *a*) is associated with the ultrahigh solidification rates typical of ESCAT [30; 31], which overall enhances hardness and wear resistance. In addition, *in-situ* formation of (Al–Ca–RE)O nanoparticles along grain boundaries restricts dislocation motion by generating dislocation loops. The strengthening role of oxide inclusions has also been noted in [32].

Regardless of electrode polarity, oxidation of the coatings follows a logarithmic law: a rapid mass gain during the initial stage is followed by a slower increase

as the oxide layer thickens. The high oxidation rate at the early stage is associated with selective oxidation of Al, accompanied by Al_2O_3 formation (-890.4 kJ/mol) (Fig. 14, *a*). The presence of (Al–Ca–RE)O nanoparticles appears to accelerate Al_2O_3 formation. The solubility of RE in Al_2O_3 or Cr_2O_3 is very low [19], so their oxides segregate at the metal–oxide interface (Fig. 13, *b*). Furthermore, as shown in Fig. 7, vacuum annealing of the coatings results in the crystallization of CaAl_2O_4 nanoparticles, which are isostructural with alumina. Owing to their lower energy, these particles accelerate Al_2O_3 grain growth. At the boundaries of the thin α - Al_2O_3 layer, RE-enriched particles improve oxide adhesion and reduce stress concentrations, thereby preventing crack formation.

Prolonged isothermal exposure of ACe and AEr coatings in oxygen-containing environments leads to the formation of NiAl_2O_4 (-12.5 kJ/mol) through Ni diffusion across the thin Al_2O_3 film to the surface. Thus, in these coatings oxygen diffusion is strongly restricted by the heterogeneous $\text{NiAl}_2\text{O}_4/\alpha$ - Al_2O_3 layer, reinforced by CaMoO_4 particles. This interpretation is consistent with the low oxidation rate constants ($K_p = 0.16\text{--}0.22$) compared with those of the KCe and KEr coatings (Table 6).

Despite the presence of cracks, the KCe and KEr coatings exhibit lower mass gain than the AZhK alloy. Oxygen diffusion along cracks occurs during the first $\sim 15 \text{ h}$ of oxidation, after which the growth of CaMoO_4 grains within the cracks blocks further diffusion. The cracks thus act as channels for upward Mo diffusion, necessary for CaMoO_4 grain nucleation and subsequent coalescence into a continuous layer. According to [8], these grains with the tetragonal scheelite structure $\text{I}4_1/a$ exhibit excellent thermal stability and ultralow thermal conductivity at $400\text{--}1000 \text{ K}$ ($0.6\text{--}1.2 \text{ W/(m}\cdot\text{K)}$), values even lower than those of thermal barrier coatings such as YSZ ($1.5\text{--}3.0 \text{ W/(m}\cdot\text{K)}$).

Conclusion

The formation behavior of wear- and oxidation-resistant coatings produced by combined electrospark and cathodic arc treatment (ESCAT) on AZhK nickel-based superalloy samples was investigated. Optimal ESCAT modes with Al–Ca–Er and Al–Ca–Ce electrodes were identified, enabling the formation of $15\text{--}20 \mu\text{m}$ thick coatings composed of columnar crystallites with a cross-section below 300 nm , containing γ' -Ni₃Al and β -NiAl phases. These coatings increased substrate hardness from 5.2 to 12.3 GPa and improved wear resistance sixfold. The use of Al–Ca–Er electrodes provided enhanced oxidation resistance of the AZhK alloy at 1000°C by changing

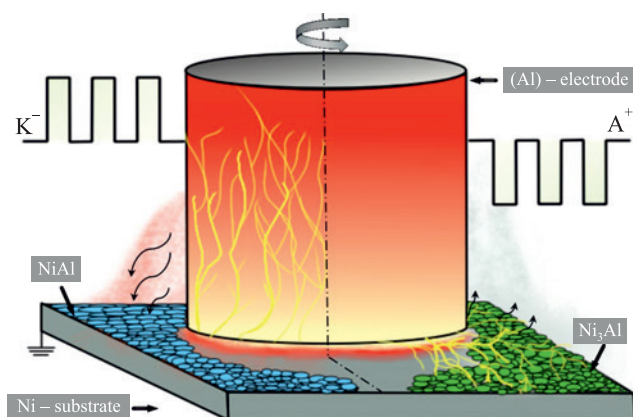


Fig. 15. Schematic illustration of the ESCAT process as a function of electrode polarity

Рис. 15. Схематическое изображение процесса ЭИДТО в зависимости от полярности электрода

the oxidation law from linear to logarithmic one due to the formation of a protective $\text{NiAl}_2\text{O}_4/\alpha\text{-Al}_2\text{O}_3$ layer $\sim 3 \mu\text{m}$ thick, reinforced by CaMoO_4 particles.

References / Список литературы

- Kablov E.N. Strategical areas of developing materials and their processing technologies for the period up to 2030. *Aviatsionnye materialy i tekhnologii*. 2012;(S):7–17. (In Russ.).
Каблов Е.Н. Стратегические направления развития материалов и технологий их переработки на период до 2030 года. *Авиационные материалы и технологии*. 2012;(S):7–17.
- Long H., Mao S., Liu Y., Zhang Z., Han X. Microstructural and compositional design of Ni-based single crystalline superalloys. A review. *Journal of Alloys and Compounds*. 2018;743:203–220.
<https://doi.org/10.1016/j.jallcom.2018.01.224>
- Sirotnin N.N., Marchukov E.Yu., Novikov A.S. Damageability and operability of aviation gas turbine engines: Handbook. Moscow: Nauka; 2015. 551 p. (In Russ.).
Сиротин Н.Н., Марчуков Е.Ю., Новиков А.С. Повреждаемость и работоспособность авиационных ГТД: Справочник. М.: Наука; 2015. 551 с.
- Xie Yu., Wang M. Epitaxial MCrAlY coating on a Ni-base superalloy produced by electrospark deposition. *Surface and Coatings Technology*. 2006; 201(6):3564–3570.
<https://doi.org/10.1016/j.surfcoat.2006.08.107>
- Zamulaeva E.I., Levashov E.A., Sviridova T.A., Shvynina N.V., Petrzhik M.I. Pulsed electrospark deposition of MAX phase Cr_2AlC based coatings on titanium alloy. *Surface and Coatings Technology*. 2013;235:454–460.
<https://doi.org/10.1016/j.surfcoat.2013.08.002>
- Burkov A.A., Chigrin P.G., Kulik M.A. Effect of TaC content on microstructure and wear behavior of PRMMC Fe-TaC coating manufactured by electrospark deposition on AISI304 stainless steel. *Surface and Coatings Technology*. 2024;494(2):131446.
<https://doi.org/10.1016/j.surfcoat.2024.131446>
- Mukanov S.K., Petrzhik M.I., Loginov P.A., Levashov E.A. Influence of manganese alloying on the structure and properties of electrospark coatings of EP741NP heat-resistant nickel LPBF alloy. *Izvestiya. Non-Ferrous Metallurgy*. 2024;(2):70–84.
<https://doi.org/10.17073/0021-3438-2024-2-70-84>
Муканов С.К., Петржик М.И., Логинов П.А., Левашов Е.А. Влияние легирования марганцем на структуру и свойства электроискровых покрытий на никелевом жаропрочном СЛС-сплаве ЭП741НП. *Известия вузов. Цветная металлургия*. 2024;(2):70–84.
<https://doi.org/10.17073/0021-3438-2024-2-70-84>
- Mukanov S.K., Petrzhik M.I., Kudryashov A.E., Naumova E.A., Baskov F.A., Loginov P.A., Levashov E.A. Enhancing high-temperature oxidation resistance of nickel superalloy obtained by laser powder bed fusion via reactive electric spark treatment. *Transactions of Nonferrous Metals Society of China*. 2024;34(12):3935–3948.
[https://doi.org/10.1016/S1003-6326\(24\)66649-5](https://doi.org/10.1016/S1003-6326(24)66649-5)
- Li J.G., Wang N., Liu J.D., Xu W. Influence of rare earth elements (Y, La and Ce) on the mechanical properties and oxidation resistance of nickel-based superalloys: A critical review. *Journal of Materials Science & Technology*. 2024;195:9–21.
<https://doi.org/10.1016/j.jmst.2023.11.077>
- Kuptsov K.A., Sheveyko A.N., Sidorenko D.A., Shtansky D.V. Electro-spark deposition in vacuum using graphite electrode at different electrode polarities: Peculiarities of microstructure, electrochemical and tribological properties. *Applied Surface Science*. 2021;566:150722.
<https://doi.org/10.1016/j.apsusc.2021.150722>
- Baskov F.A., Sentyurina Zh.A., Logachev I.A., Krutikov N.I., Levashov E.A. Influence of HIP and heat treatment on the structure and properties of AJKh nickel heat-resistant alloy obtained by SLM. In: *Proceedings of the 12th International Symposium "Powder Metallurgy: Surface Engineering, New Powder Composite Materials, Welding"* (Minsk, April 7–9, 2021). Minsk: Belaruskaya navuka; 2021. Part 1. P. 136–141. (In Russ.).
Басков Ф.А., Сентюрин Ж.А., Логачев И.А., Крутиков Н.И., Левашов Е.А. Влияние ГИП и ТО на структуру и свойства никелевого жаропрочного сплава АЖК, полученного методом СЛС. В кн.: *Сборник докладов 12-го Международного симпозиума «Порошковая металлургия: Инженерия поверхности. новые порошковые композиционные материалы. сварка»* (Минск, 7–9 апреля 2021 г.). Ч. 1. Под ред. А.Ф. Ильющенко и др. Минск: Беларуская навука; 2021. С. 136–141.
- Naumova E.A., Vasina M.A., Chernogorova O.P., Rogachev S.O., Zadorozhnyi M.Yu., Bobrysheva A.O. Investigation of the effect of cerium on the structure and properties of calcium-containing aluminum alloys. *Metallurgist*. 2024;67:1302–1314.
<https://doi.org/10.1007/s11015-024-01622-8>
- Sheveyko A.N., Kuptsov K.A., Kiryukhantsev-Korneev Ph.V., Kaplansky Yu.Yu., Orekhov A.S., Levashov E.A. Protective coatings for LPBF Ni-based superalloys using a combination of electrospark deposition and pulsed arc evaporation methods. *Applied Surface Science*. 2022;581:152357.
<https://doi.org/10.1016/j.apsusc.2021.152357>
- Buntushkin V.P., Bazyleva O.A., Burkina V.I. High-temperature heat-resistant alloys based on the Ni_3Al intermetallic compound for hot section parts of gas turbine engines. *Aviatsionnaya promyshlennost'*. 2007;(2):41–43. (In Russ.).
Бунтушкин В.П., Базылева О.А., Буркина В.И. Высокотемпературные жаропрочные сплавы на основе интерметаллида Ni_3Al для деталей горячего тракта ГТД. *Авиационная промышленность*. 2007;(2):41–43.
- Bale C.W., Bélisle E., Chartrand P., Decterov S.A., Eriksen G., Gheribi A.E., Hack K., Jung I.H., Kang Y.B., Melançon J., Pelton A.D., Petersen S., Robelin C., Sangster J., Spencer P., Van Ende M.A. Reprint of: FactSage thermochemical software and databases. *Calphad*. 2016;55(1):1–19.
<https://doi.org/10.1016/j.calphad.2016.07.004>
- Thanneeru R., Patil S., Deshpande S., Seal S. Effect of trivalent rare earth dopants in nanocrystalline ceria coatings

- for high-temperature oxidation resistance. *Acta Materialia*. 2007;55(10):3457–3466.
<https://doi.org/10.1016/j.actamat.2007.01.043>
17. Pint B.A. Experimental observations in support of the dynamic-segregation theory to explain the reactive-element effect. *Oxidation of Metals*. 1996;45(1):1–37.
<https://doi.org/10.1007/BF01046818>
 18. Dai J., Zhu J., Chen C., Weng F. High temperature oxidation behavior and research status of modifications on improving high temperature oxidation resistance of titanium alloys and titanium aluminides: A review. *Journal of Alloys and Compounds*. 2016;685:784–798.
<https://doi.org/10.1016/j.jallcom.2016.06.212>
 19. Chevalier S. What did we learn on the reactive element effect in chromia scale since Pfeil's patent? *Materials and Corrosion*. 2014;65(2):109–115.
<https://doi.org/10.1002/maco.201307310>
 20. Guo H., Li D., Zheng L., Gong S., Xu H. Effect of co-doping of two reactive elements on alumina scale growth of β -NiAl at 1200 °C. *Corrosion Science*. 2014;88:197–208.
<https://doi.org/10.1016/j.corsci.2014.07.036>
 21. Song X., Wang L., Liu Y., Ma H. Effects of temperature and rare earth content on oxidation resistance of Ni-based superalloy. *Progress in natural science: Materials International*. 2011;21(3):227–235.
[https://doi.org/10.1016/S1002-0071\(12\)60035-5](https://doi.org/10.1016/S1002-0071(12)60035-5)
 22. Daroonparvar M., Yajid M.A.M., Kay C.M., Bakhsheshi-Rad H., Gupta R.K., Yusof N.M., Ghandvar H., Arshad A., Zulkifli I.S.M. Effects of Al_2O_3 diffusion barrier layer (including Y-containing small oxide precipitates) and nanostructured YSZ top coat on the oxidation behavior of HVOF NiCoCrAlTaY/APS YSZ coatings at 1100 °C. *Corrosion Science*. 2018;144:13–34.
<https://doi.org/10.1016/j.corsci.2018.07.013>
 23. Pang X.J., Li S.S., Qin L., Pei Y.L., Gong Sh.K. Effect of trace Ce on high-temperature oxidation behavior of an Al–Si-coated Ni-based single crystal superalloy. *Journal of Iron and Steel Research International*. 2019;26(1):78–83.
<https://doi.org/10.1007/s42243-018-0214-0>
 24. Pint B.A., Treska M., Hobbs L.W. The effect of various oxide dispersions on the phase composition and morphology of Al_2O_3 scales grown on β -NiAl. *Oxidation of Metals*. 1997;47(1):1–20.
<https://doi.org/10.1007/BF01682369>
 25. Wang H., Wang A., Li C., Yu X., Xie J., Liang T., Liu C. Effects of rare earth metals on microstructure, mechanical properties, and pitting corrosion of 27 % Cr hyper duplex stainless steel. *Reviews on Advanced Materials Science*. 2022;61(1):873–887.
<https://doi.org/10.1515/rams-2022-0284>
 26. Yuan J., Wang Q., Liu X., Lou S., Li Q., Wang Z. Microstructures and high-temperature wear behavior of NiAl/WC- Fe_x coatings on carbon steel by plasma cladding. *Journal of Alloys and Compounds*. 2020;842:155850.
<https://doi.org/10.1016/j.jallcom.2020.155850>
 27. Sung P.K., Poirier D.R. Estimation of densities and coefficients of thermal expansion of solid Ni-base superalloys. *Materials Science and Engineering: A*. 1998;245:135–141.
[https://doi.org/10.1016/S0921-5093\(97\)00699-0](https://doi.org/10.1016/S0921-5093(97)00699-0)
 28. Xie Y.J., Wang M.C. Epitaxial MCrAlY coating on a Ni-base superalloy produced by electrospark deposition. *Surface and Coatings Technology*. 2006;201(6):3564–3570.
<https://doi.org/10.1016/j.surfcoat.2006.08.107>
 29. Xie Y.J., Wang M.C. Microstructural morphology of electrospark deposition layer of a high gamma prime superalloy. *Surface and Coatings Technology*. 2006;201(3–4):691–698.
<https://doi.org/10.1016/j.surfcoat.2005.12.034>
 30. Petrzhik M., Molokanov V., Levashov E. On conditions of bulk and surface glass formation of metallic alloys. *Journal of Alloys and Compounds*. 2017;707:68–72.
<https://doi.org/10.1016/j.jallcom.2016.12.293>
 31. Mukanov S.K., Petrzhik M.I., Kudryashov A.E., Basikov F.A., Levashov E.A. Improving the wear and heat resistance of niobium substrate via reactive electrospark treatment using fusible AlCaSiY electrode. *Applied Surface Science*. 2024;670:160663.
<https://doi.org/10.1016/j.apsusc.2024.160663>
 32. Liu Y., Yang L., Yang X., Zhang T., Sun R. Optimization of microstructure and properties of composite coatings by laser cladding on titanium alloy. *Ceramics International*. 2021;47(2):2230–2243.
<https://doi.org/10.1016/j.ceramint.2020.09.063>

Information about the Authors



Сведения об авторах

Samat K. Mukanov – Cand. Sci. (Eng.), Research Scientist of the Scientific Educational Center of Self-Propagating High-Temperature Synthesis (SHS-Center) of MISIS–ISMAN, National University of Science and Technology “MISIS” (NUST MISIS)

 **ORCID:** 0000-0001-6719-6237

 **E-mail:** smukanov@sisis.ru

Mikhail I. Petrzhik – Dr. Sci. (Eng.), Professor of Department at Powder Metallurgy and Functional Coatings (PM&FC), NUST MISIS; Leading Research Scientist of the SHS-Center, MISIS–ISMAN

 **ORCID:** 0000-0002-1736-8050


 **E-mail:** petrzhik@shs.misis.ru

Alexander E. Kudryashov – Cand. Sci. (Eng.), Leading Research Scientist of the SHS-Center, MISIS–ISMAN

 **ORCID:** 0000-0001-6222-4497

 **E-mail:** aekudr@rambler.ru

Самат Куандыкович Муканов – к.т.н., науч. сотрудник научно-учебного центра (НУЦ) СВС, МИСИС–ИСМАН, Национальный исследовательский технологический университет «МИСИС» (ННТУ МИСИС)

 **ORCID:** 0000-0001-6719-6237

 **E-mail:** smukanov@sisis.ru

Михаил Иванович Петржи́к – д.т.н., профессор кафедры порошковой металлургии и функциональных покрытий (ПМиФП); вед. науч. сотрудник НУЦ СВС, МИСИС–ИСМАН

 **ORCID:** 0000-0002-1736-8050

 **E-mail:** petrzhik@shs.misis.ru

Александр Евгеньевич Кудряшов – к.т.н., вед. науч. сотрудник НУЦ СВС, МИСИС–ИСМАН

 **ORCID:** 0000-0001-6222-4497

 **E-mail:** aekudr@rambler.ru

Pavel A. Loginov – Dr. Sci. (Eng.), Senior Lecturer of the Department of PM&FC, NUST MISIS; Senior Research Scientist of SHS-Center, MISIS-ISMAN

 **ORCID:** 0000-0003-2505-2918

 **E-mail:** pavel.loginov.misis@list.ru

Nataliya V. Shvyndina – Leading Engineer of SHS-Center, MISIS-ISMAN

 **ORCID:** 0000-0002-4662-544X


 **E-mail:** natali19-03@list.ru

Aleksandr N. Sheveyko – Research Scientist of the SHS-Center, MISIS-ISMAN

 **ORCID:** 0000-0003-3704-515X

 **E-mail:** sheveyko@mail.ru

Konstantin A. Kuptsov – Cand. Sci. (Eng.), Senior Research Scientist of the SHS-Center, MISIS-ISMAN

 **ORCID:** 0000-0003-2585-0733

 **E-mail:** kuptsov.k@gmail.com

Evgeny A. Levashov – Dr. Sci. (Eng.), Professor, Corresponding Member of the RAS, Head of the Department PM&FC, NUST MISIS; Head of SHS-Center, MISIS-ISMAN

 **ORCID:** 0000-0002-0623-0013

 **E-mail:** levashov@shs.misis.ru

Павел Александрович Логинов – д.т.н., ст. преподаватель кафедры ПМиФП, НИТУ МИСИС; ст. науч. сотрудник НУЦ СВС, МИСИС-ИСМАН

 **ORCID:** 0000-0003-2505-2918

 **E-mail:** pavel.loginov.misis@list.ru

Наталья Владимировна Швындина – вед. инженер НУЦ СВС, МИСИС-ИСМАН

 **ORCID:** 0000-0002-4662-544X

 **E-mail:** natali19-03@list.ru

Александр Николаевич Шевейко – науч. сотрудник НУЦ СВС, МИСИС-ИСМАН

 **ORCID:** 0000-0003-3704-515X


 **E-mail:** sheveyko@mail.ru

Константин Александрович Купцов – к.т.н., ст. науч. сотрудник НУЦ СВС, МИСИС-ИСМАН

 **ORCID:** 0000-0003-2585-0733

 **E-mail:** kuptsov.k@gmail.com

Евгений Александрович Левашов – д.т.н., чл.-корр. РАН, профессор, зав. кафедрой ПМиФП, НИТУ МИСИС; директор НУЦ СВС МИСИС-ИСМАН

 **ORCID:** 0000-0002-0623-0013

 **E-mail:** levashov@shs.misis.ru

Contribution of the Authors



S. K. Mukanov – preparation and execution of experiments, manuscript writing, visualization, discussion of results.

M. I. Petrzhik – formulation of research goals and objectives, mechanical properties testing, data analysis, manuscript revision, formulation of conclusions.

A. E. Kudryashov – analysis and discussion of results.

P. A. Loginov – transmission electron microscopy experiments, discussion of results.

N. V. Shvyndina – microscopic investigations.

A. N. Sheveiko – coating deposition experiments, discussion of results.

K. A. Kuptsov – coating deposition experiments, discussion of results.

E. A. Levashov – development of the main concept, manuscript and conclusion revision.

Вклад авторов

С. К. Муканов – подготовка и проведение экспериментов, написание текста статьи, визуализация, обсуждение результатов.

М. И. Петржик – постановка цели и задачи исследования, проведение экспериментов по исследованию механических свойств, анализ данных, корректировка текста, формулировка выводов.

А. Е. Кудряшов – анализ и обсуждение результатов.

П. А. Логинов – проведение экспериментов по просвечивающей электронной микроскопии, обсуждение результатов.

Н. В. Швындина – проведение микроскопических исследований.

А. Н. Шевейко – проведение экспериментов по осаждению покрытий, обсуждение результатов.

К. А. Купцов – проведение экспериментов по осаждению покрытий, обсуждение результатов.

Е. А. Левашов – формирование основной концепции, корректировка текста и выводов.

Received 23.04.2025

Revised 21.05.2025

Accepted 26.05.2025

Статья поступила 23.04.2025 г.

Доработана 21.05.2025 г.

Принята к публикации 26.05.2025 г.



UDC 621.762

<https://doi.org/10.17073/1997-308X-2025-4-77-90>

Review article

Обзорная статья



Additive manufacturing of functionally graded products by selective laser melting: A review

E. V. Borisov, A. V. Repnin , A. A. Popovich

Peter the Great St. Petersburg Polytechnic University (SPbPU)
29 Politekhnikeskaya Str., St. Petersburg 195251, Russia repnin_arseniy@mail.ru

Abstract. This paper presents a review of recent advances in functionally graded additive manufacturing using selective laser melting (SLM, also referred to as laser powder bed fusion, LPBF). The fundamental principles of producing functionally graded products by SLM are discussed, including approaches to forming compositional and structural gradients. Particular attention is given to the formation of the transition layer in the synthesized material, which is crucial for achieving the desired properties of the products. Methods of design and numerical modeling of functionally graded structures are analyzed, including the use of artificial intelligence and machine learning. It is demonstrated that applying bio-inspired design principles enables the development of parts with enhanced mechanical, thermal, and functional properties. Examples are provided of successful fabrication of multi-material products with tailored property anisotropy, as well as products with controlled porosity gradients. The promising application areas of functionally graded products are identified, including aerospace, medicine, mechanical engineering, and energy.

Keywords: selective laser melting, functionally graded materials, multi-materials, metamaterials, design, artificial intelligence

Acknowledgements: The research was supported by the Russian Science Foundation, project No. 23-79-30004,
<https://rscf.ru/en/project/23-79-30004/>.

For citation: Borisov E.V., Repnin A.V., Popovich A.A. Additive manufacturing of functionally graded products by selective laser melting: A review. *Powder Metallurgy and Functional Coatings*. 2025;19(4):77–90.
<https://doi.org/10.17073/1997-308X-2025-4-77-90>

Аддитивное производство изделий с функционально-градиентной структурой по технологии селективного лазерного сплавления Обзор

Е. В. Борисов, А. В. Репнин , А. А. Попович

Санкт-Петербургский политехнический университет Петра Великого
Россия, 195251, г. Санкт-Петербург, ул. Политехническая, 29 repnin_arseniy@mail.ru

Аннотация. Представлен обзор современных достижений в области функционально-градиентного аддитивного производства по технологии селективного лазерного сплавления (СЛС). Рассмотрены основные принципы создания изделий с функционально-градиентной структурой методом СЛС, включая способы формирования градиентного состава и структуры. Описан процесс формирования переходного слоя синтезируемого материала, который является ключевым для обеспечения требуемых свойств изделий. Проанализированы методы проектирования и моделирования изделий с функционально-градиентной структурой, в том числе с использованием искусственного интеллекта и машинного обучения. Показано, что применение природоподобных принципов строения позволяет создавать изделия с улучшенными механическими,

тепловыми и функциональными свойствами. Рассмотрены примеры успешного получения мультиматериальных структур с заданной анизотропией свойств, а также изделий с контролируемым градиентом пористости. Определены перспективные направления применения изделий с функционально-градиентной структурой, включая аэрокосмическую отрасль, медицину, машиностроение и энергетику.

Ключевые слова: селективное лазерное сплавление (СЛС), функционально-градиентные материалы, мультиматериалы, метаматериалы, проектирование, искусственный интеллект

Благодарности: Исследование выполнено за счет гранта Российского научного фонда № 23-79-30004, <https://rscf.ru/project/23-79-30004/>.

Для цитирования: Борисов Е.В., Репнин А.В., Попович А.А. Аддитивное производство изделий с функционально-градиентной структурой по технологии селективного лазерного сплавления. Обзор. *Известия вузов. Порошковая металлургия и функциональные покрытия*. 2025;19(4):77–90. <https://doi.org/10.17073/1997-308X-2025-4-77-90>

Introduction

Functionally graded materials (FGMs) are an advanced class of materials distinguished by a continuous variation of composition, structure, and properties along one or more directions [1]. The concept was first introduced in Japan in the 1980s for aerospace applications, as a means of producing heat-resistant materials capable of withstanding steep thermal gradients and high mechanical loads [2]. Unlike conventional composites, where sharp interfaces separate the constituent phases, FGMs exhibit smooth transitions in properties. This reduces stress concentrations at the interfaces and improves the overall reliability of parts [3]. In recent years, additive manufacturing – particularly selective laser melting (SLM, also referred to as laser powder bed fusion, LPBF) – has become one of the most effective approaches for fabricating FGMs [4]. The ability to precisely control process parameters and material composition at the microscale makes it possible to design functionally graded products with tailored distributions of density, porosity, hardness, thermal and electrical conductivity, corrosion resistance, biocompatibility, and other properties [5]. Such control enables practical solutions to engineering challenges, including reducing structural weight without sacrificing strength, enhancing thermal cycling resistance, improving damping capacity, and producing biomedical implants with porosity gradients to promote osseointegration [6].

The potential of FGMs is further expanded through bio-inspired design principles. Bio-inspired materials emulate strategies refined by nature over millions of years of evolution [7–11]. Natural systems achieve exceptional performance and multifunctionality by combining heterogeneous structures in complex hierarchical architectures. While biological materials are limited to naturally available constituents, modern researchers can draw from a vast range of synthetic options [12; 13]. Organisms organize materials from the nano- to the macroscale, displaying distinct mechanical, electrical, optical, and surface properties, as

well as adaptive shape-changing capabilities. Notable examples include fish scales with excellent protective functions, spider silk and nacre with outstanding strength, and plants or animals capable of shape transformation for survival [14–17]. Inspired by these natural designs, engineers are developing commercial parts across mechanical engineering, robotics, aerospace, and architecture. The degree to which biomimetic concepts can be realized, however, depends directly on the precision of available fabrication technologies [18–23].

Research on the design and production of functionally graded products is now being actively pursued worldwide. The Fraunhofer Institute in Germany has accumulated extensive expertise in fabricating such structures from metals, ceramics, and polymers. Similar research is carried out at the University of Minho (Braga, Portugal), Washington State University, Harbin Engineering University, Huazhong University of Science and Technology, Delft University of Technology, Singapore University of Technology and Design, and Peter the Great St. Petersburg Polytechnic University, among others.

This review summarizes current progress in functionally graded additive manufacturing using SLM. It highlights the fundamental principles of gradient formation in structure and composition, the role of transition layers in synthesized materials, advances in design and modeling methods, and emerging directions for application.

Functionally graded materials with variable microstructure

The key SLM process parameters that determine the microstructure and properties of fabricated parts include laser power, scanning speed, hatch distance, and layer thickness. Their combined effect defines the volumetric energy density delivered to the material, which in turn governs the melting mode, cooling rate, microstructural evolution, and defect formation. Depending on the selected scanning strategy and para-

meter set, the resulting structure may consist of oriented grains with a preferred crystallographic orientation, more uniformly distributed equiaxed grains, or a combination of both [24]. A functionally graded component incorporating regions of fine-grained and highly oriented coarse-grained microstructures demonstrates the feasibility of producing materials with user-defined functional characteristics in different zones of a single part. At the same time, the anisotropy of mechanical properties is strongly influenced by the prevailing texture [25].

In the case of Inconel 718 fabricated by SLM, heat treatment preserves the as-built grain texture and morphology without signs of recrystallization. However, it promotes the formation of acicular δ -Ni₃Nb precipitates and untransformed Laves phases, which reduce ductility while improving yield strength by creating barriers to dislocation motion [26]. Even after hot isostatic pressing (HIP), a sharp microstructural boundary between fine- and coarse-grained regions is retained, along with a dominant (100) texture in the coarse columnar grain zones. Mechanical properties are markedly improved due to the dissolution of undesirable Laves and δ phases and the elimination of pores, strengthening the grain-size dependence of yield strength in accordance with the Hall–Petch relationship. The combined “HIP + heat treatment” approach provides superior mechanical performance compared with both cast and wrought Inconel 718 [28].

The developed technology for creating graded structures in nickel alloys also enables control over the propagation of fatigue cracks as they pass through

the interfacial zone between different microstructures, thereby slowing crack growth and delaying failure [26]. It has been shown that when a fatigue crack propagates across such an interfacial zone, its trajectory changes, which results in a reduced growth rate (Fig. 1).

Functionally graded materials with variable composition

Recent advances have enabled the fabrication of multi-material products with enhanced mechanical properties in a single production cycle by SLM [29]. However, this requires significant modifications to the printer design and the development of technologies for feeding and distributing two or more powder materials, as well as their subsequent separation [30]. In addition, the selected materials must be metallurgically compatible and capable of forming reliable, defect-free bonding [31]. Studies of the “heat-resistant bronze – heat-resistant nickel alloy VZh159 – BrKhZrTV” system produced by SLM have shown that a substantial increase in energy input markedly reduces porosity in the interfacial zones of multi-material samples (Fig. 2, *a*). Elemental distribution within the interfacial zone is characterized by Ni–Cu interdiffusion across the interface (Fig. 2, *b*), while microhardness gradually changes from alloy VZh159 to BrKhZrTV over a distance of about 300 μm (Fig. 2, *c*) [32–34].

Complete mixing of the alloys, in which both materials are detected in the X-ray patterns, continues

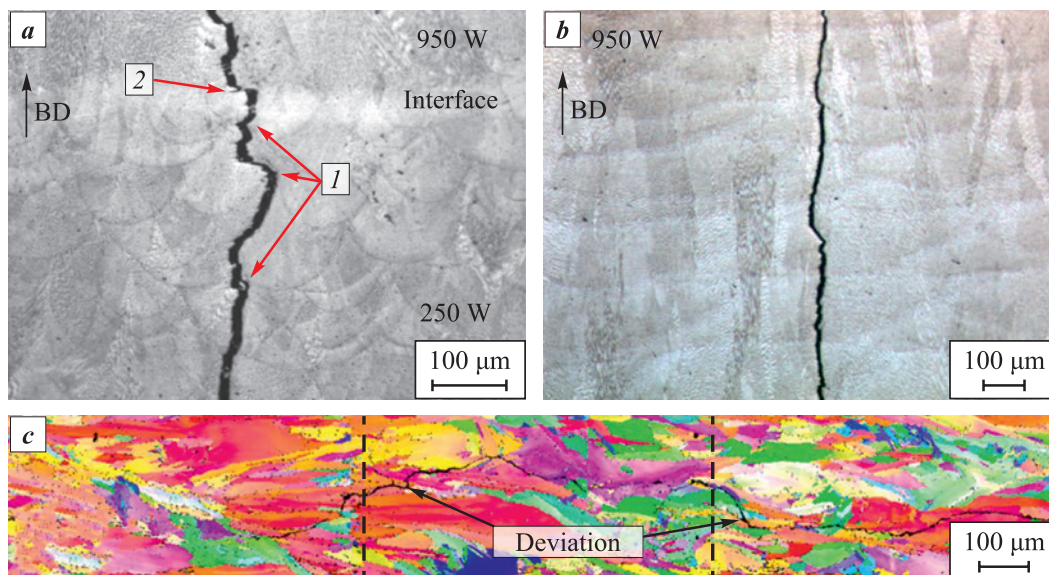


Fig. 1. Crack path deviation as a function of microstructural parameters [26], based on optical (*a*, *b*) and scanning electron (*c*) microscopy [27]

Рис. 1. Изменение траектории движения трещины в зависимости от параметров структуры [26], по результатам оптической (*a*, *b*) и сканирующей электронной (*c*) микроскопии [27]

up to the 6th layer of BrKhZrTV. At the 7th layer, a transition to pure BrKhZrTV is observed, which confirms an interfacial zone width of about 300 μm at a layer thickness of 50 μm (Fig. 2, *d*). Mechanical testing showed that the multi-material sample exhibits a tensile strength more than twice that of BrKhZrTV, although it does not reach the level of VZh159. To eliminate the lack-of-fusion defect during composition changes within a single layer, an overlap zone of approximately 350–400 μm must be ensured. Fig. 3 shows a prototype of a component that can be fabricated based on the VZh159/BrKhZrTV multi-material system.

The study of a multi-material AlSi10Mg/Al–Si–Mg–Cu sample fabricated by SLM revealed that the AlSi10Mg region contained only Al and Si without additional phases, whereas the Al–Si–Mg–Cu region also exhibited a small amount of the Al_2Cu phase, as confirmed by chemical composition analysis [35]. Microhardness measurements after heat treatment showed that the Al–Si–Mg–Cu zone had a hardness about 30 % higher than that of the AlSi10Mg zone.

Investigations of a titanium alloy multi-material system (VT6/VT1-0) produced by SLM demonstrated that in the interfacial zone, the contents of Al and V

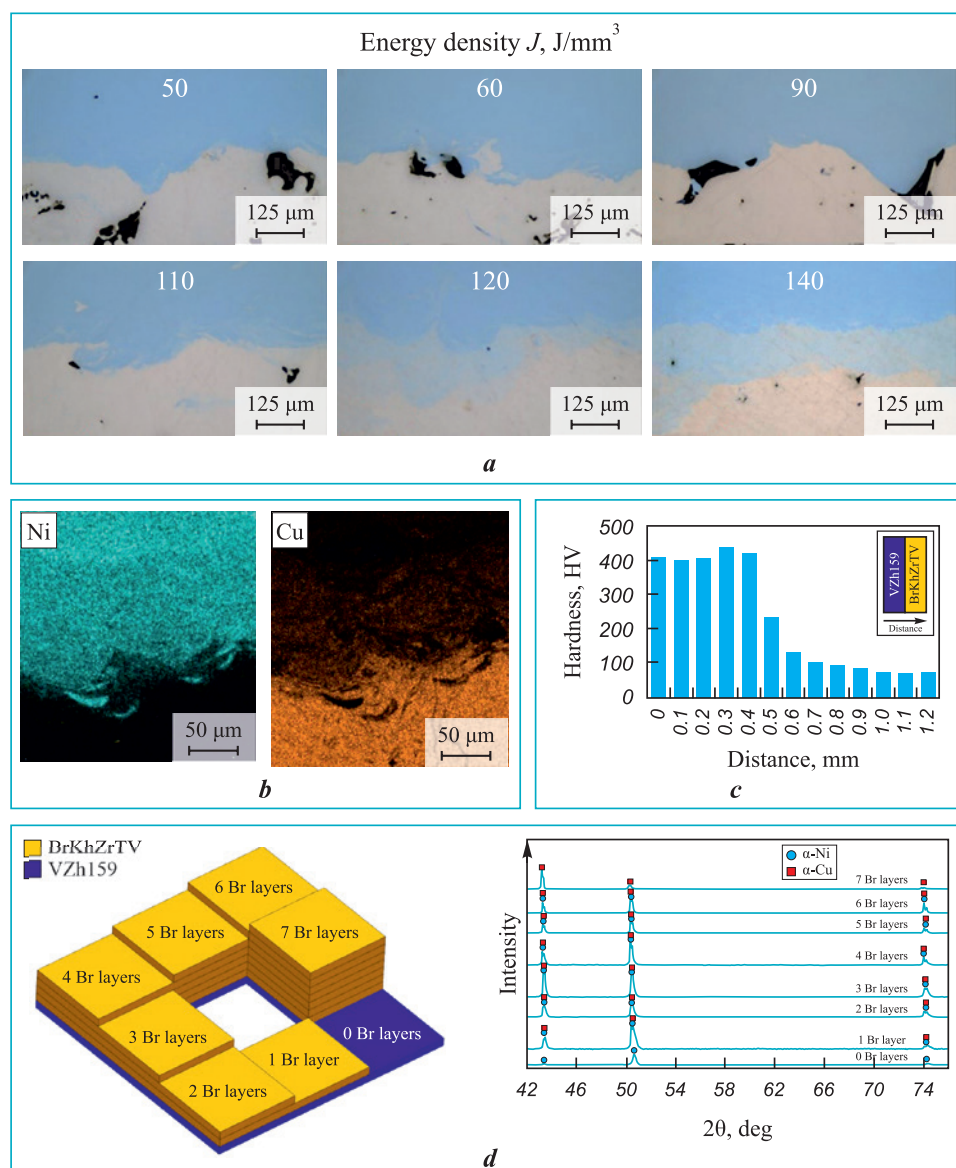


Fig. 2. Results of the investigation of the multi-material system VZh159/BrKhZrTV [32–34]

a – defect analysis in the interfacial zone; *b* – elemental distribution in the interfacial zone;
c – microhardness profile; *d* – measurement of interfacial zone width

Рис. 2. Результаты исследования мультиматериальной системы ВЖ159/БрХЦрТВ [32–34]

a – анализ дефектов в переходной зоне; *b* – распределение элементного состава в переходной зоне;
c – исследование твердости; *d* – оценка ширины переходной зоны



Fig. 3. Multi-material prototypes with lattice elements and tailored properties

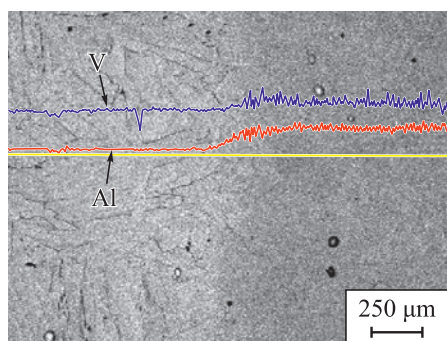
Рис. 3. Мультиматериальные модели с сетчатыми элементами и заданными свойствами

gradually increased from the VT1-0 side toward VT6 (Fig. 4, *a*), with the interfacial zone width being approximately 200 μm [36; 37]. The effect of the interfacial zone location on mechanical properties was examined, along with the influence of the multi-material archi-

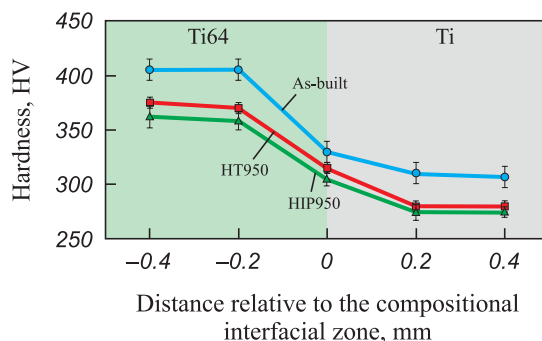
ture on fracture toughness, particularly the fatigue crack growth rate (Figs. 4, *b* and *c*).

The study of a unique 316L/FeNi36 multi-material system with a shape-change effect fabricated by SLM [38] identified three distinct compositional regions: an FeNi36 zone, an interfacial zone, and a 316L zone, with the interfacial zone measuring about 50 μm in width. Hardness values ranged from 163 HV in the FeNi36 region to approximately 200 HV in the interfacial zone and 214 HV in the 316L region. The most effective temperature range for achieving maximum displacement was found to be 25–215 $^{\circ}\text{C}$.

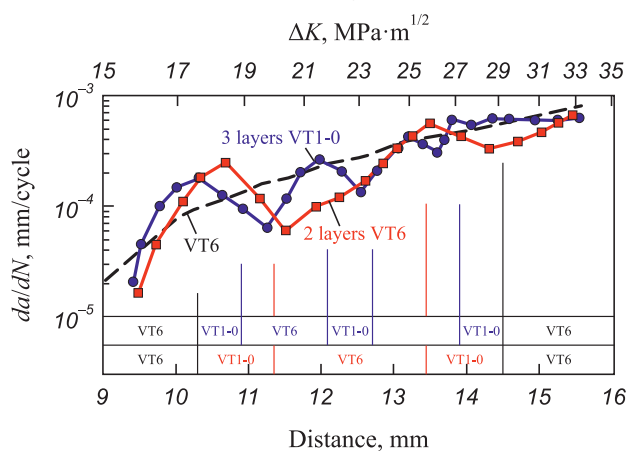
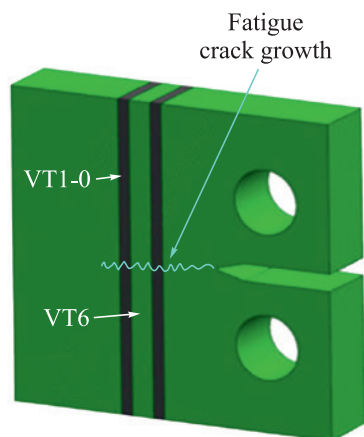
In the Ti6Al4V/Inconel 718 system of otherwise non-weldable alloys produced by SLM [39; 40], defect-free parts were successfully fabricated by introducing transitional layers of Cu and Cu + Nb. These layers showed no significant defects, although some alloy mixing was observed. Chemical composition analysis of multi-materials with a Cu transitional layer revealed that the interfacial zone between Cu and Ti6Al4V was wider than that between Cu and Inconel 718. When a Cu + Nb transitional layer was used, the Ti6Al4V/Nb



a



b



c

Fig. 4. Investigation of the VT6/VT1-0 multi-material system [36; 37]

a – distribution of V and Al in the interfacial zone; *b* – variation of Vickers hardness (HV) with depth; *c* – results of fatigue crack growth tests

Рис. 4. Исследование мультиматериальной системы VT6/VT1-0 [36; 37]

a – изменение содержания V и Al в переходной зоне; *b* – изменение твердости HV по глубине поверхности; *c* – результаты испытаний на рост усталостной трещины

and Inconel 718/Cu interfacial zones were relatively narrow, with a smooth compositional gradient between Nb and Cu. Mechanical testing further demonstrated that samples with Cu + Nb transitional layers achieved superior strength (ultimate tensile strength of 910 MPa) compared with those containing Cu alone (790 MPa). Although these values were lower than those of the base alloys, the fracture surfaces exhibited a stepwise morphology, with distinct fracture zones for each alloy reflecting their characteristic fracture mechanisms.

In the 316L/NiTi system incorporating a transitional layer of the high-entropy CoCrFeNiMn alloy [41], localized macrosegregation was observed in the interfacial zone, attributed to the Marangoni effect. Combined phase and chemical analyses, together with hardness measurements, suggested the formation of FeTi intermetallics in these macrosegregated regions, which, according to the authors, could promote crack initiation due to their embrittling influence.

Alternative strategies for producing multi-material products include methods that enable the design of composites with unique property combinations while retaining high functionality in the final product. Powder blending can be used to create systems with transitional layers, although some samples show limitations in dimensional accuracy [42]. For instance, Ti5Al2.5Sn and Ti6Al4V samples demonstrated defect-free interfacial zones suitable for critical applications, unlike the incompatible Ti6Al4V and IN718 alloys, unlike the non-weldable Ti6Al4V and IN718 alloys [43; 44]. The combination of SLM and powder metallurgy has produced nacre-like structures in titanium alloys with improved strain hardening [45], while multi-materials of Inconel 718 and 316L stainless steel achieved a tensile strength of 751.82 MPa with 25.14 % elongation [46]. Such systems have been applied in high-performance heat exchangers (316L/CuZr) for electronics and bio-inspired implants (Ti6Al4V/NiTi) for medical use [47; 48].

SLM processing of SS316L and CuSn10 alloys has been shown to significantly improve their functional performance [49], while the fabrication of bio-inspired structures from 18Ni300, CoCrMo, 316L, and CuSn alloys enables controlled anisotropy depending on the loading direction [50].

Functionally graded materials with shape memory effect

SLM technology is considered a highly promising method for the industrial production of products from shape memory alloys (SMAs) with tailored functional

characteristics. Its value lies in the flexibility to control not only geometric parameters during fabrication but also the functional behavior of the final component through process design. This approach is particularly valuable in high-tech fields that demand the manufacture of miniaturized parts with complex geometries, such as medical stents and implants [51], as well as aerospace actuators [52]. The possibility of achieving the desired structure and functional properties of NiTi (commonly referred to as nitinol) has been demonstrated by adjusting SLM process parameters [53; 54]. An increase in energy density or the use of a double-laser scanning strategy reduces the nickel content in the alloy and increases the phase transformation temperatures [53].

The formation of tailored structural parameters strongly influences the properties of nitinol. For instance, adjusting the hatch spacing makes it possible to control the development of a directional grain structure, dislocation density, the phase transformation temperature range, and the thermo-cyclic stability of NiTi alloys [55]. In the context of 4D printing of metallic materials, the phase transformation temperature range and the microstructure – closely linked to the thermo-mechanical response – are the two key factors that determine SMA performance. It has been shown that larger grain sizes lead to lower phase transformation temperatures [56]. Building on this effect, the creation of crystallographically oriented, directional structures in NiTi enables a substantial expansion of the superelastic region [57] and improves the stability of the shape memory effect by reducing irreversible plastic deformation (Fig. 5).

In a NiTi alloy with reduced nickel content (49.4 at. %) and a <001> texture produced by additive manufacturing, record superelasticity was achieved up to 453 K, with a broad transformation temperature range of 110 K. This behavior is attributed to high deformation resistance and improved phase compatibility between austenite and martensite. The developed approach simultaneously enhances superelasticity and stabilizes the shape memory effect by promoting the formation of textured martensite and suppressing dislocation motion through Ti_2NiO_x precipitates. Heat treatment primarily affects nanoscale precipitates and atomic defects, while having little influence on grain size or morphology. Direct aging after SLM facilitates the formation of Ti_2NiO_x within grains, whereas homogenization annealing dissolves metastable titanium in the NiTi matrix and reduces defect density. All heat treatment modes reinforce phase transformations by increasing the Ti/Ni atomic ratio and lowering defect density [58].

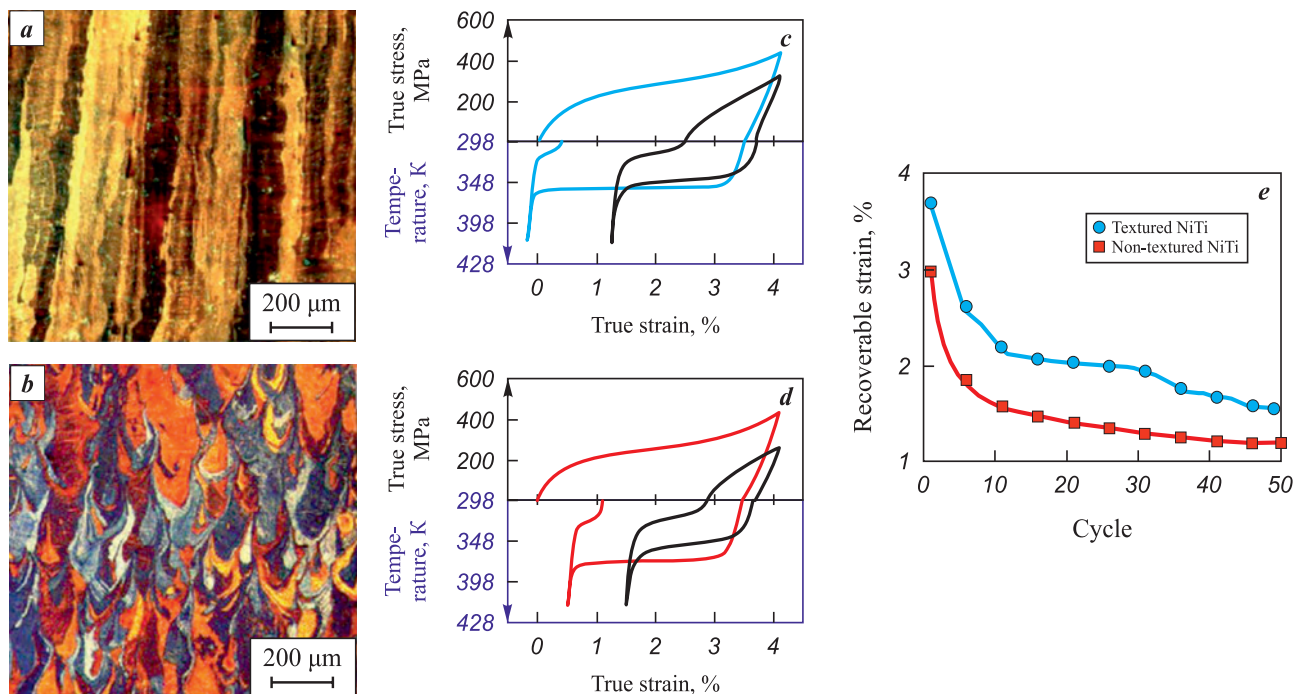


Fig. 5. Microstructure and strain curves of textured (*a, c*), and non-textured (*b, d*) NiTi alloys, and comparison of recoverable strain versus the number of cycles (*e*) [57]

Рис. 5. Структура и кривые деформаций текстурированного (*a, c*) и нетекстурированного (*b, d*) сплавов NiTi, а также сравнение восстановимой деформации в зависимости от количества циклов (*e*) [57]

Functionally graded metamaterials

Metamaterials are specially engineered materials with a unique internal architecture (geometry) that provides combinations of physical, mechanical, and functional properties distinct from those of the base material from which they are made. For example, auxetic meta-biomaterials with a negative Poisson's ratio and a low Young's modulus have been designed and modeled to closely replicate the properties of human trabecular bone [59], where the high stiffness of conventional materials often causes inflammation and implant rejection [60].

In energy absorption applications, metallic dampers with complex geometries frequently undergo permanent deformation due to local yielding. By contrast, nitinol (NiTi) provides recoverable deformation and effective energy dissipation through its unique superelasticity, offering new opportunities for the design and additive manufacturing of energy-absorbing architectural metamaterials [56]. Under uniaxial compression, lattice structures form superelastic hinges at their nodes, while the martensitic transformation gradually propagates from the nodes along the struts.

NiTi parts fabricated by SLM have also been shown to exhibit superelastic behavior under cyclic loading, with relatively low accumulation of irreversible strain (about 1.2 % after 11 cycles) [61], making them par-

ticularly suitable for applications requiring repeated shape recovery.

Modeling and design of functionally graded products

Digital design plays a crucial role in the development of functionally graded products. Because these products possess a heterogeneous internal structure, their design requires specially tailored methodologies. Traditional approaches have therefore been extended: today, not only the geometry of a single-material component is designed, but also its internal architecture, taking into account variable structures or the use of multiple materials. Finite element modeling has shown high accuracy in predicting the mechanical behavior of parts made from the heat-resistant alloy EI961, when combining SLM with direct laser deposition. Comparable results were obtained for the nickel alloy VZh159 in combination with the copper alloy CuCr1Zr. However, the authors [62; 63] highlighted the need for further refinement of models to more accurately account for the characteristics of interfacial zones in functionally graded materials. An innovative approach to predicting deformation and residual stresses in SLM-fabricated turbine blades was proposed in [64], showing how pre-deformed models can compensate for anticipated warping in the final parts. The inelastic behavior of func-

tionally graded products was investigated in [65] by calibrating modeling parameters against experimental samples, which produced good agreement between predicted and measured mechanical properties. In [66], a methodology for modeling the mechanical properties of endoprostheses was developed by varying the topology of lattice structures, identifying optimal configurations for replacing both cortical and trabecular bone tissue (Fig. 6).

To minimize defects in multi-materials fabricated by SLM and to predict their resulting properties, computer simulations of both manufacturing and service processes are employed [67–70]. This is particularly important for parts made of alloys prone to defect formation, such as NiTi [53]. In both cases, the decisive factor is the interaction between two dissimilar materials. For example, in [71], thermo-mechanical models were used to simulate residual stresses in parts made of Inconel 625. In [72], a cellular automata model was developed to predict microstructure evolution during SLM of materials exposed to large temperature gradients and high cooling rates.

Artificial intelligence technologies in additive manufacturing

Modern software solutions based on artificial intelligence (AI) are increasingly being applied to the digital design of multi-materials produced by additive manufacturing [73]. Traditional design tools can no longer handle tasks of this complexity, whereas new

approaches enable the full potential of multi-material products to be realized. For example, the company Leap 71 (United Arab Emirates) develops parts for SLM production using its proprietary AI-based software PicoGK (Fig. 7) [74].

Methods for designing smart multi-materials have also been proposed [75; 76]. In one study, an evolutionary algorithm was used for design [77]. This non-deterministic method relies on bio-inspired principles of natural selection and evolution, creating “more advanced individuals” across successive generations to represent candidate solutions. Alongside natural selection based on fitness – often referred to as “survival of the fittest” – concepts such as mutation, recombination, and populations containing “parents” and “children” are adapted to each design task. Using this digital design system, researchers demonstrated the feasibility of producing an active composite in the form of a simple cantilever beam with a multi-material structure that changed shape under thermal loading.

Machine learning methods can also be used to optimize processing parameters in the fabrication of multi-material products by SLM [78]. An algorithm based on a multidimensional Gaussian process was developed to predict part density and surface roughness as functions of parameters such as laser power, scan speed, and hatch spacing. Training data were collected using a high-throughput experimental approach. The resulting process maps provide clear visualization of the relationships between process parameters and the properties of interfacial zones in multi-material

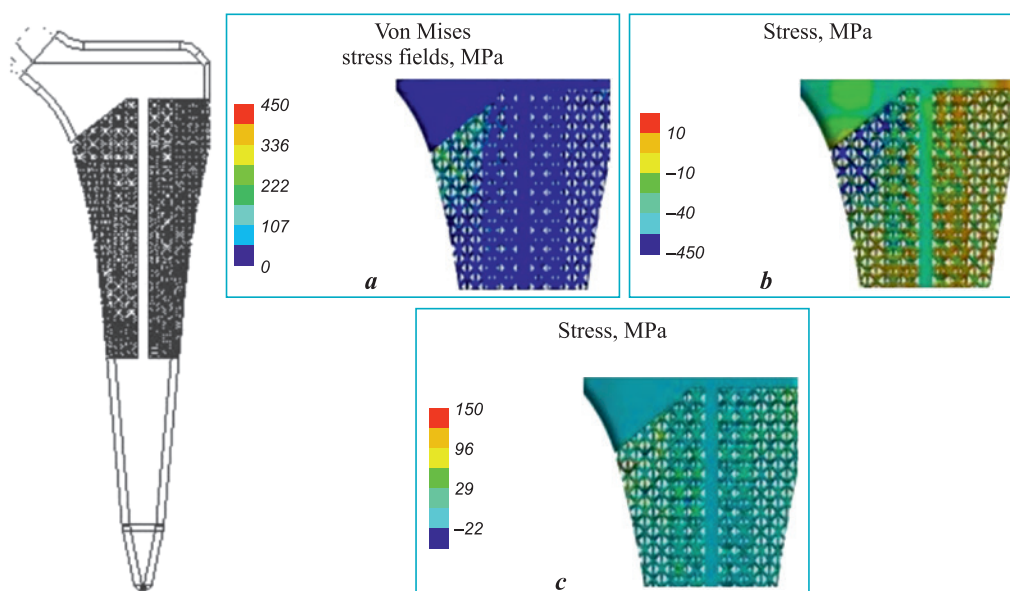


Fig. 6. Von Mises stress fields (a), maximum tensile stress fields (b), and maximum compressive stress fields (c) for an endoprosthesis with a graded structure under maximum load [67]

Рис. 6. Поля напряжений по фон Мизесу (a), поля максимальных растягивающих (b) и максимальных сжимающих (c) напряжений для эндопротеза с использованием градиентной структуры при наибольшей нагрузке [67]



Fig. 7. Examples of parts designed using the PicoGK software developed by Leap 71 [74]

a – heat exchanger, *b* – rocket engine parts, *c* – tubular heat exchanger

Рис. 7. Примеры изделий, спроектированных в программном продукте PicoGK фирмы Leap 71 [74]

a – теплообменник, *b* – компоненты ракетного двигателя, *c* – трубчатый теплообменник

parts. Notably, process parameters exhibit a nonlinear dependence on composition, meaning that settings suitable for alloy 1 or alloy 2 cannot be directly applied to the interfacial zones.

To further improve the quality of multi-materials produced by SLM, real-time process monitoring can be implemented, with printing parameters adjusted based on data analysis [79; 80]. Advanced techniques such as high-speed and infrared imaging allow the collection of critical information on melt bath size and characteristics, while machine learning provides powerful tools for analyzing these data. In one study, acoustic and optical emission signals associated with the laser wavelength were monitored during the fabrication of multi-material copper parts [81]. A specialized signal monitoring and classification system based on contrastive deep learning was applied. The results revealed clear differences in energy levels for powders of different compositions, indicating variations in melt dynamics. The study also confirmed the effectiveness of combining contrastive learning with multi-sensor monitoring strategies for SLM processes in multi-material production.

Conclusion

Functionally graded products produced by SLM represent a promising direction in modern materials science. Multi-material systems with compositional gradients show substantial improvements in mechanical performance compared with single-material counterparts. Interfacial zones between different alloys play a crucial role in ensuring reliable bonding, while optimizing energy density significantly reduces porosity

in these regions. The development of metamaterials with specially designed internal architectures imparts unique physical and mechanical properties, essential for applications such as biomechanically compatible implants and efficient energy-absorbing structures.

Functionally graded products with a shape memory effect, particularly NiTi alloys fabricated by SLM, exhibit enhanced functional performance. The formation of directional grain structures and textures extends the superelastic region and improves the stability of the shape memory effect. Advances in digital design and modeling now enable accurate prediction of properties and optimization of processing parameters, while the integration of artificial intelligence technologies opens new possibilities for design, real-time process monitoring, and process optimization.

Overall, functionally graded products produced by SLM hold great potential for aerospace, medicine, robotics, and other high-tech fields where unique combinations of properties are required.

References / Список литературы

1. Miyamoto Y., Kaysser W.A., Rabin B.H., Kawasaki A., Ford R.G. Functionally graded materials: Design, processing and applications. *Springer Science & Business Media*. 2013;5:1–478.
<https://doi.org/10.1007/978-1-4615-5301-4>
2. Koizumi M. FGM activities in Japan. *Composites Part B: Engineering*. 1997;28(1-2):1–4.
[https://doi.org/10.1016/S1359-8368\(96\)00016-9](https://doi.org/10.1016/S1359-8368(96)00016-9)
3. Mahamood R.M., Akinlabi E.T. Functionally graded materials. Cham: Springer. 2017;103:1–214.
<https://doi.org/10.1007/978-3-319-53756-6>

4. Yang J., Gu D., Lin K., Zhang Y., Guo M., Yuan L., Zhang H., Zhang H. Laser additive manufacturing of bio-inspired metallic structures. *Chinese Journal of Mechanical Engineering: Additive Manufacturing Frontiers*. 2022;1(1):100013.
<https://doi.org/10.1016/j.cmeaf.2022.100013>
5. Reichardt A., Shapiro A.A., Otis R., Dillon R.P., Borgogna J.P., McEnerney B.W., Hosemann P., Beese A.M. Advances in additive manufacturing of metal-based functionally graded materials. *International Materials Reviews*. 2021;66(1):1–29.
<https://doi.org/10.1080/09506608.2020.1747913>
6. Wang X., Xu S., Zhou S., Xu W., Leary M., Choong P., Qian M., Brandt M., Xie Y.M. Topological design and additive manufacturing of porous metals for bone scaffolds and orthopaedic implants: A review. *Biomaterials*. 2016;83:127–141.
<https://doi.org/10.1016/j.biomaterials.2016.01.012>
7. Kovalchuk M.V. The first Russian crystallographic congress. From convergence of sciences to nature-like technologies. *Crystallographiya*. 2018;(2):173–175. (In Russ.).
<https://doi.org/10.7868/S0023476118020017>
Ковальчук М.В. Первый российский кристаллографический конгресс. От конвергенции наук к природоподобным технологиям. *Кристаллография*. 2018;(2):173–175.
<https://doi.org/10.7868/S0023476118020017>
8. Yaraghi N.A., Kisailus D. Biomimetic structural materials: Inspiration from design and assembly. *Annual Review of Physical Chemistry*. 2018;69:23–57.
<https://doi.org/10.1146/annurev-physchem-040215-112621>
9. Su F.Y., Bushong E.A., Deerinck T.J., Seo K., Herrera S., Graeve O.A., Kisailus D., Lubarda A.V., McKittrick J. Spines of the porcupine fish: Structure, composition, and mechanical properties. *Journal of the Mechanical Behavior of Biomedical Materials*. 2017;73:38–49.
<https://doi.org/10.1016/j.jmbbm.2016.08.020>
10. Sullivan T.N., Pissarenko A., Herrera S.A., Kisailus D., Lubarda V.A., Meyers M.A. A lightweight, biological structure with tailored stiffness: The feather vane. *Acta Biomaterialia*. 2016;41:27–39.
<https://doi.org/10.1016/j.actbio.2016.05.022>
11. Salinas C.L., de Obaldia E.E., Jeong C., Hernández J.J., Zavattieri P., Kisailus D. Enhanced toughening of the crossed lamellar structure revealed by nanoindentation. *Journal of the Mechanical Behavior of Biomedical Materials*. 2017;76:58–68.
<https://doi.org/10.1016/j.jmbbm.2017.05.036>
12. Wegst U.G.K., Bai H., Saiz E., Tomsia A.P., Ritchie R.O. Bioinspired structural materials. *Nature Materials*. 2014;14(1):23–36. <https://doi.org/10.1038/nmat4089>
13. Rawat P., Zhu D., Rahman M. Z., Barthelat F. Structural and mechanical properties of fish scales for the bio-inspired design of flexible body armors: A review. *Acta Biomaterialia*. 2021;121:41–67.
<https://doi.org/10.1016/j.actbio.2020.11.040>
14. Yin S., Guo W., Wang H., Huang Y., Yang R., Hu Z., Chen D., Xu J., Ritchie R.O. Strong and tough bioinspired additive-manufactured dual-phase mechanical metamaterial composites. *Journal of the Mechanics and Physics of Solids*. 2021;149:104321.
<https://doi.org/10.1016/j.jmps.2021.104321>
15. Tee Y.L., Tran P. On bioinspired 4D printing: materials, design and potential applications. *Journal of the Institution of Engineers, Australia*. 2021;19(5):642–652.
<https://doi.org/10.1080/14484846.2021.1988434>
16. Yang Y., Song X., Li X., Chen Z., Zhou C., Zhou Q., Chen Y. Recent progress in biomimetic additive manufacturing technology: From materials to functional structures. *Advanced Materials*. 2018;30(36):1706539.
<https://doi.org/10.1002/adma.201706539>
17. Li W., Pei Y., Zhang C., Kottapalli A.G.P. Bioinspired designs and biomimetic applications of triboelectric nanogenerators. *Nano Energy*. 2021;84:105865.
<https://doi.org/10.1016/j.nanoen.2021.105865>
18. Brulé V., Rafsanjani A., Asgari M., Western T.L., Pasini D. Three-dimensional functional gradients direct stem curling in the resurrection plant *Selaginella lepidophylla*. *Journal of The Royal Society Interface*. 2019;16(159):20190454.
<https://doi.org/10.1098/rsif.2019.0454>
19. Du Plessis A., Broeckhoven C., Yadroitsava I., Yadroitsev I. Beautiful and functional: A review of biomimetic design in additive manufacturing. *Additive Manufacturing*. 2019;27:408–427.
<https://doi.org/10.1016/j.addma.2019.03.033>
20. Pathak S. Biomimicry: (Innovation Inspired by Nature). *International Journal of New Technology and Research*. 2019;5(6):1–8.
<https://doi.org/10.31871/IJNTR.5.6.17>
21. Nazari K., Tran P., Tan P., Ghazlan A., Ngo T.D., Xie Y.M. Advanced manufacturing methods for ceramic and bio-inspired ceramic composites: A review. *Open Ceramics*. 2023;15:100399.
<https://doi.org/10.1016/j.oceram.2023.100399>
22. Zhang B., Han Q., Zhang J., Han Z., Niu S., Ren L. Advanced bio-inspired structural materials: Local properties determine overall performance. *Materials Today*. 2020;41:177–199.
<https://doi.org/10.1016/j.mattod.2020.09.016>
23. Ahamed M.K., Wang H., Hazell P.J. From biology to biomimicry: Using nature to build better structures. A review. *Construction and Building Materials*. 2022;320:126252.
<https://doi.org/10.1016/j.conbuildmat.2021.126252>
24. Popovich V.A., Borisov E.V., Popovich A.A., Sufiarov V.S., Masaylo D.V., Alzina L. Functionally graded Inconel 718 processed by additive manufacturing: Crystallographic texture, anisotropy of microstructure and mechanical properties. *Materials & Design*. 2017;114:441–449.
<https://doi.org/10.1016/j.matdes.2016.10.075>
25. Popovich A.A., Sufiarov V.S., Borisov E.V., Polozov I.A., Masaylo D.V., Grigoriev A.V. Anisotropy of mechanical properties of products manufactured using selective laser melting of powdered materials. *Russian Journal of Non-Ferrous Metals*. 2017;58:389–395.
<https://doi.org/10.3103/S1067821217040149>
Попович А.А., Суфияров В.Ш., Борисов Е.В., Полозов И.А., Масайло Д.В., Григорьев А.В. Анизотропия механических свойств изделий, изготовленных методом селективного лазерного плавления порошковых материалов. *Известия вузов. Порошковая металлур-*

- гия и функциональные покрытия. 2016;(3):4–11.
<https://doi.org/10.17073/1997-308X-2016-3-4-11>
26. Popovich V.A., Borisov E.V., Popovich A.A., Sufiiarov V.S., Masaylo D.V., Alzina L. Impact of heat treatment on mechanical behaviour of Inconel 718 processed with tailored microstructure by selective laser melting. *Materials & Design*. 2017;131:12–22.
<https://doi.org/10.1016/j.matdes.2017.05.065>
 27. Ghorbanpour S., Sahu S., Deshmukh K., Borisov E., Riemsag T., Reinton E., Bertolo V., Jiang Q., Popovich A., Shamshurin A., Knezevic M., Popovich V. Effect of microstructure induced anisotropy on fatigue behaviour of functionally graded Inconel 718 fabricated by additive manufacturing. *Materials Characterization*. 2021;179:111350.
<https://doi.org/10.1016/j.matchar.2021.111350>
 28. Ghorbanpour S., Deshmukh K., Sahu S., Riemsag T., Reinton E., Borisov E., Popovich A., Bertolo V., Jiang Q., Sanchez M.T., Knezevic M., Popovich V. Additive manufacturing of functionally graded Inconel 718: Effect of heat treatment and building orientation on microstructure and fatigue behaviour. *Journal of Materials Processing Technology*. 2022;306:117573.
<https://doi.org/10.1016/j.jmatprotec.2022.117573>
 29. Bandyopadhyay A., Heer B. Additive manufacturing of multi-material structures. *Materials Science and Engineering: R: Reports*. 2018;129:1–16.
<https://doi.org/10.1016/j.mser.2018.04.001>
 30. Hasanov S., Alkunte S., Rajeshirke M., Gupta A., Huseynov O., Fidan I., Alifui-Segbaya F., Rennie A. Review on additive manufacturing of multi-material parts: Progress and challenges. *Journal of Manufacturing and Materials Processing*. 2021;6(1):4.
<https://doi.org/10.3390/jmmp6010004>
 31. Wang D., Liu L., Deng G., Deng C., Bai Y., Yang Y., Wu W., Chen J., Liu Y., Wang Y., Lin X., Han C. Recent progress on additive manufacturing of multi-material structures with laser powder bed fusion. *Virtual and Physical Prototyping*. 2022;17(2):329–365.
<https://doi.org/10.1080/17452759.2022.2051531>
 32. Reprin A.V., Borisov E.V., Popovich A.A., Shamshurin A.I. Creating multi-material samples of the system EI1319–BrCrCrTi by selective laser melting. *Global Energy*. 2023;29(2):175–188. (In Russ.).
<https://doi.org/10.18721/JEST.29212>
Репнин А.В., Борисов Е.В., Попович А.А., Шамшурин А.И. Создание мульти-материальных образцов системы ВЖ159–БрХЦрТ методом селективного лазерного плавления. *Глобальная энергия*. 2023;29(2):175–188. <https://doi.org/10.18721/JEST.29212>
 33. Reprin A.V., Borisov E.V., Popovich A.A., Golubkov N.A. Mechanical properties of the VZh159–CuCr1Zr alloy multi-material samples manufactured by selective laser melting. *Powder Metallurgy and Functional Coatings*. 2024;18(1):52–61.
<https://doi.org/10.17073/1997-308X-2024-1-52-61>
Репнин А.В., Борисов Е.В., Попович А.А., Голубков Н.А. Исследование механических свойств мультиматериальных образцов системы ВЖ159–БрХЦрТ, полученных методом селективного лазерного плавления. *Известия вузов. Порошковая металлургия и функциональные покрытия*. 2024;18(1):52–61.
<https://doi.org/10.17073/1997-308X-2024-1-52-61>
 34. Reprin A.V., Borisov E.V., Popovich A.A., Investigation of multi-material samples with three-dimensional composition change obtained by selective laser melting method. *Global Energy*. 2024;30(4):37–52. (In Russ.).
<https://doi.org/10.18721/JEST.30403>
Репнин А.В., Борисов Е.В., Попович А.А. Исследование мультиматериальных образцов с трехмерным изменением состава, полученных методом селективного лазерного плавления. *Глобальная энергия*. 2024;30(4):37–52.
<https://doi.org/10.18721/JEST.30403>
 35. Borisov E., Reprin A., Popovich A. Investigation of AlSi10Mg alloy composition modification by Cu addition in selective laser melting. In: *The International Conference “Advanced Mechanics: Structure, Materials, Tribology”* (Samarkand, 23–26 September 2024). AIP Conference Proceedings, 2025; 3562 (1):010001.
 36. Borisov E., Polozov I., Starikov K., Popovich A., Sufiiarov V. Structure and properties of Ti/Ti64 graded material manufactured by laser powder bed fusion. *Materials (Basel)*. 2021;14(20):6035.
<https://doi.org/10.3390/ma14206035>
 37. Reprin A., Borisov E., Popovich A., Shamshurin A. Fracture toughness of Ti6Al4V/Cp-Ti multi-material produced via selective laser melting. *Metals*. 2023;13(10):1738.
<https://doi.org/10.3390/met13101738>
 38. Reprin A., Borisov E., Maksimov A., Rozhkova D., Popovich A. Investigation of the 4D multi-material 316L/FeNi36 obtained by selective laser melting. *Micromachines*. 2024;15(11):1288.
<https://doi.org/10.3390/mi15111288>
 39. Reprin A., Borisov E., Popovich A. Investigation of Inconel 718/Ti6Al4V Multi-material obtained by selective laser melting with transition layer. In: *The International Conference “Advanced Mechanics: Structure, Materials, Tribology”* (Samarkand, 23–26 September 2024). AIP Conference Proceedings, 2025; 3562 (1):050005.
 40. Reprin A., Borisov E., Popovich A. Formation of the Cu + Nb interlayer in the inconel 718/Ti6Al4V multi-material obtained by selective laser melting. *Materials*. 2024;17(23):5801.
<https://doi.org/10.3390/ma17235801>
 41. Reprin A., Kim A., Popovich A. Interfacial characterization of selective laser melting of a SS316L/NiTi multi-material with a high-entropy alloy interlayer. *Crystals*. 2023;13(10):1486.
<https://doi.org/10.3390/cryst13101486>
 42. Demir A.G., Previtali B. Multi-material selective laser melting of Fe/Al–12Si components. *Manufacturing Letters*. 2017;11:8–11.
<https://doi.org/10.1016/j.mfglet.2017.01.002>
 43. Wei K., Zeng X., Li F., Liu M., Deng J. Microstructure and mechanical property of Ti–5Al–2.5Sn/Ti–6Al–4V dissimilar titanium alloys integrally fabricated by selective laser melting. *Journal of Metals*. 2020;72(3):1031–1038.
<https://doi.org/10.1007/s11837-020-04045-3>

44. Scaramuccia M.G., Demir A.G., Caprio L., Tassa O., Previtali B. Development of processing strategies for multigraded selective laser melting of Ti6Al4V and IN718. *Powder Technology*. 2020;367:376–389. <https://doi.org/10.1016/j.powtec.2020.04.010>
45. Liu X., Liu Z., Liu Y., Zafar Z., Lu Y., Wu X., Jiang Y., Xu Z., Guo Z., Li S. Achieving high strength and toughness by engineering 3D artificial nacre-like structures in Ti6Al4V-Ti metallic composite. *Composites Part B: Engineering*. 2022;230:109552. <https://doi.org/10.1016/j.compositesb.2021.109552>
46. Peng Y., Shi Y., Jin T., Ren J., Bian Y. Structural design, interfacial behavior and mechanical properties of bimetallic nacre-like structures by laser powder-bed fusion. *Journal of Alloys and Compounds*. 2024;990:174470. <https://doi.org/10.1016/j.jallcom.2023.174470>
47. Chueh Y.H., Hsieh B.Y., Shih A.J. Interfacial characteristics in multi-material laser powder bed fusion of CuZr/316L stainless steel. *CIRP Annals*. 2024;73(1):145–148. <https://doi.org/10.1016/j.cirp.2024.03.012>
48. Costa M.M., Lima R., Alves N., Silva N.A., Gasik M., Silva F.S., Bartolomeu F., Miranda G. Multi-material cellular structured orthopedic implants design: *In vitro* and bio-tribological performance. *Journal of the Mechanical Behavior of Biomedical Materials*. 2022;131:105246. <https://doi.org/10.1016/j.jmbbm.2022.105246>
49. Chen K., Wang C., Hong Q., Wen S., Zhou Y., Yan C., Shi Y. Selective laser melting 316L/CuSn10 multi-materials: Processing optimization, interfacial characterization and mechanical property. *Journal of Materials Processing Technology*. 2020;283:116711. <https://doi.org/10.1016/j.jmatprotec.2020.116711>
50. Zhang M., Yang Y., Xu M., Chen J., Wang D. Mechanical properties of multi-materials porous structures based on triply periodic minimal surface fabricated by additive manufacturing. *Rapid Prototyping Journal*. 2021;27(9):1681–1692. <https://doi.org/10.1108/RPJ-07-2020-0153>
51. Gracheva A., Polozov I., Popovich A. Additive manufacturing of biodegradable metallic implants by selective laser melting: Current research status and application perspectives. *Metals*. 2025;15(7):754. <https://doi.org/10.3390/MET15070754>
52. Tsaturyants M., Sheremetyev V., Dubinskiy S., Komarov V., Polyakova K., Korotitskiy A., Prokoshkin S., Borisov E., Starikov K., Kaledina D., Popovich A., Brailovskii V. Structure and properties of Ti–50.2Ni alloy processed by laser powder bed fusion and subjected to a combination of thermal cycling and heat treatments. *Shape Memory and Superelasticity*. 2022;8(1):16–32. <https://doi.org/10.1007/s40830-022-00362-5>
53. Zhu J.N., Borisov E., Liang X., Farber E., Hermans M.J.M., Popovich V.A. Predictive analytical modeling and experimental validation of processing maps in additive manufacturing of nitinol alloys. *Additive Manufacturing*. 2021;38:101802. <https://doi.org/10.1016/j.addma.2020.101802>
54. Borisov E., Starikov K., Popovich A., Tihonovskaya T. Investigation of the possibility of tailoring the chemical composition of the NiTi alloy by selective laser melting. *Metals*. 2021;11(9):1470. <https://doi.org/10.3390/met11091470>
55. Zhu J. N., Borisov E., Liang X., Huizenga R., Popovich A., Bliznuk V., Petrov R., Hermans M., Popovich V. Controlling microstructure evolution and phase transformation behavior in additive manufacturing of nitinol shape memory alloys by tuning hatch distance. *Journal of Materials Science*. 2022;57(10):6066–6084. <https://doi.org/10.1007/s10853-022-07043-9>
56. Yan Z., Zhu J.N., Borisov E., Riemsag T., Scott S.P., Hermans M., Jovanova J., Popovich V. Superelastic response and damping behavior of additively manufactured Nitinol architected materials. *Additive Manufacturing*. 2023;68:103505. <https://doi.org/10.1016/j.addma.2023.103505>
57. Zhu J.N., Liu K., Riemsag T., Tichelaar F.D., Borisov E., Yao X., Popovich A., Huizenga R., Hermans M., Popovich V. Achieving superelasticity in additively manufactured Ni-lean NiTi by crystallographic design. *Materials & Design*. 2023;230:111949. <https://doi.org/10.1016/j.matdes.2023.111949>
58. Zhu J.N., Zhu W., Borisov E., Yao X., Riemsag T., Goulas C., Popovich A., Yan Z., Tichelaar F.D., Mainali D.P., Hermans M., Popovich V. Effect of heat treatment on microstructure and functional properties of additively manufactured NiTi shape memory alloys. *Journal of Alloys and Compounds*. 2023;967:171740. <https://doi.org/10.1016/j.jallcom.2023.171740>
59. Farber E., Orlov A., Popovich A. Auxetic meta-biomaterials: Computer simulation and experimental results. *Metals*. 2025;15(3):241. <https://doi.org/10.3390/met15030241>
60. Farber E., Orlov A., Popovich A. Effect of lattice structures topology on the properties of the TiNi alloy: Computer simulation. *Prospects*. 2021;1:3.
61. Farber E., Orlov A., Borisov E., Repnin A., Kuzin S., Golubkov N., Popovich A. TiNi alloy lattice structures with negative Poisson's ratio: computer simulation and experimental results. *Metals*. 2022;12(9):1476. <https://doi.org/10.3390/met12091476>
62. Orlov A., Repnin A., Farber E., Borisov E., Popovich A. Fabrication of multi-material samples from nickel and copper alloys by selective laser melting: Computer simulation and experimental results. *AIP Conference Proceedings*. 2024;3154(1):020028. <https://doi.org/10.1063/5.0201286>
63. Orlov A., Masaylo D., Igoshin S., Razumov N., Popovich A. Mechanical properties prediction of the materials gained by combining additive technologies. *Materials Today: Proceedings*. 2020;30:752–755. <https://doi.org/10.1016/j.matpr.2020.01.563>
64. Orlov A., Borisov E., Popovich A.A. Numerical simulation of the selective laser melting process using the example of a turbine blade. *Materials Science Forum*. 2020;989:850–855. <https://doi.org/10.4028/www.scientific.net/MSF.989.850>
65. Orlov A.V., Sufiarov V.S., Borisov E.V., Polozov I.A., Masaylo D.V., Popovich A.A., Chukovenkova M.O., Soklakov A.V., Mikhaliuk, D.S. Numerical simulation of the inelastic behavior of a structurally graded material. *Letters on Materials*. 2019;9(1):97–102. <https://doi.org/10.22226/2410-3535-2019-1-97-102>
66. Sufiarov V.S., Orlov A.V., Borisov E.V., Sokolova V.V., Chukovenkova M.O., Soklakov A.V., Mikhaliuk A.A.,

- Popovich A.A. Modeling the mechanical properties of lattice structures made by selective laser melting. *Letters on Materials*. 2020;10(2):123–128.
<https://doi.org/10.22226/2410-3535-2020-2-123-128>
67. Sufiarov V.S., Orlov A.V., Borisov E.V., Sokolova V.V., Chukovenkova M.O., Soklakov A.V., Mikhaleuk D.S., Popovich A.A. Design and mechanical properties simulation of graded lattice structures for additive manufacturing endoprostheses. *Mechanics of Advanced Materials and Structures*. 2021;28(16):1656–1662.
<https://doi.org/10.1080/15376494.2019.1680701>
 68. Sorkin A., Tan J.L., Wong C.H. Multi-material modelling for selective laser melting. *Procedia Engineering*. 2017;216:51–57.
<https://doi.org/10.1016/j.proeng.2018.02.084>
 69. K ng V.E., Scherr R., Markl M., K rner C. Multi-material model for the simulation of powder bed fusion additive manufacturing. *Computational Materials Science*. 2021;194:110415.
<https://doi.org/10.1016/j.commatsci.2021.110415>
 70. Tang C., Yao L., Du H. Computational framework for the simulation of multi material laser powder bed fusion. *International Journal of Heat and Mass Transfer*. 2022;191:122855.
<https://doi.org/10.1016/j.ijheatmasstransfer.2022.122855>
 71. Wang Z., Denlinger E., Michaleris P., Stoica A.D., Ma D., Beese A.M. Residual stress mapping in Inconel 625 fabricated through additive manufacturing: Method for neutron diffraction measurements to validate thermo-mechanical model predictions. *Materials & Design*. 2017;113:169–177.
<https://doi.org/10.1016/j.matdes.2016.10.003>
 72. Ao X., Xia H., Liu J., He Q. Simulations of microstructure coupling with moving molten pool by selective laser melting using a cellular automaton. *Materials & Design*. 2020;185:108230.
<https://doi.org/10.1016/j.matdes.2019.108230>
 73. Miao H., Yusof F., Karim M.S.A., Badruddin I.A., Hussien M., Kamangar S., Zhang H. Process parameter optimisation for selective laser melting of AlSi10Mg-316L multi-materials using machine learning method. *The International Journal of Advanced Manufacturing Technology*, 2023;129(7): 3093–3108.
<https://doi.org/10.1007/s00170-023-12489-5>
 74. Gallery LEAP 71. URL: <https://leap71.com/gallery/> (Accessed: 01.10.2020).
 75. Athinarayanarao D., Prod'hon R., Chamoret D., Qi H.J., Bodaghi M., Andr  J.C., Demoly F. Computational design for 4D printing of topology optimized multi-material active composites. *Computational Materials*. 2023;9(1):1–9.
<https://doi.org/10.1038/s41524-023-00997-7>
 76. Benyahia K., Seriket H., Prod'hon R., Gomes S., Andr  J.C., Qi H.J., Demoly F. A computational design approach for multi-material 4D printing based on interlocking blocks assembly. *Additive Manufacturing*. 2022;58:102993.
<https://doi.org/10.1016/j.addma.2022.102993>
 77. Salonitis K., Chantzis D., Kappatos V. A hybrid finite element analysis and evolutionary computation method for the design of lightweight lattice components with optimized strut diameter. *The International Journal of Advanced Manufacturing Technology*. 2017;90(9–12):2689–2701.
<https://doi.org/10.1007/s00170-016-9528-x>
 78. Rankouhi B., Jahani S., Pfefferkorn F. E., Thoma D.J. Compositional grading of a 316L-Cu multi-material part using machine learning for the determination of selective laser melting process parameters. *Additive Manufacturing*. 2021;38:101836. <https://doi.org/10.1016/j.addma.2020.101836>
 79. Zhu Z., Ng D.W.H., Park H.S., McAlpine M.C. 3D-printed multifunctional materials enabled by artificial-intelligence-assisted fabrication technologies. *Nature Reviews Materials*. 2020;6(1):27–47.
<https://doi.org/10.1038/s41578-020-00235-2>
 80. Ibrahim Z.E., Linda I., Omer M., Kamran K., Andreas S.. Recent advancements in hybrid additive manufacturing of similar and dissimilar metals via laser powder bed fusion. *Materials Science and Engineering: A*. 2024;146833.
<https://doi.org/10.1016/j.msea.2024.146833>
 81. Pandiyan V., Baganis A., Axel Richter R., Wr bel R., Leinenbach C. Qualify-as-you-go: sensor fusion of optical and acoustic signatures with contrastive deep learning for multi-material composition monitoring in laser powder bed fusion process. *Virtual and Physical Prototyping*. 2024;19(1):e2356080.
<https://doi.org/10.1080/17452759.2024.2356080>


Information about the Authors

Evgenii V. Borisov – Cand. Sci. (Eng.), Leading Researcher of Laboratory “Synthesis of New Materials and Structures”, Peter the Great St. Petersburg Polytechnic University (SPbPU)

 **ORCID:** 0000-0003-2464-6706

 **E-mail:** evgenii.borisov@icloud.com

Arseniy V. Repnin – Engineer of Laboratory “Synthesis of New Materials and Structures”, SPbPU

 **ORCID:** 0009-0001-3157-3317

 **E-mail:** repnin_arseniy@mail.ru


Anatoliy A. Popovich – Dr. Sci. (Eng.), Professor, Director of the Institute of Machinery, Materials, and Transport, SPbPU

 **ORCID:** 0000-0002-5974-6654

 **E-mail:** popovicha@mail.ru

Сведения об авторах

Евгений Владиславович Борисов – к.т.н., вед. науч. сотрудник лаборатории «Синтез новых материалов и конструкций», Санкт-Петербургский политехнический университет Петра Великого (СПбПУ)

 **ORCID:** 0000-0003-2464-6706

 **E-mail:** evgenii.borisov@icloud.com

Арсений Вячеславович Репнин – инженер лаборатории «Синтез новых материалов и конструкций», СПбПУ

 **ORCID:** 0009-0001-3157-3317

 **E-mail:** repnin_arseniy@mail.ru

Анатолий Анатольевич Попович – д.т.н., профессор, директор Института машиностроения, материалов и транспорта, СПбПУ

 **ORCID:** 0000-0002-5974-6654

 **E-mail:** popovicha@mail.ru

Contribution of the Authors**Вклад авторов**

E. V. Borisov – manuscript writing, participation in the discussion of results.

A. V. Repnin – data processing, manuscript writing.

A. A. Popovich – conceptualization of the idea, definition of the study's aim and objectives, participation in the discussion of results.

Е. В. Борисов – написание статьи, участие в обсуждении результатов.

А. В. Репнин – обработка полученных результатов, написание статьи.

А. А. Попович – концептуализация идеи, определение цели работы и ее задачи, участие в обсуждении результатов.

Received 03.04.2025

Revised 19.05.2025

Accepted 22.05.2025

Статья поступила 03.04.2025 г.

Доработана 19.05.2025 г.

Принята к публикации 22.05.2025 г.



UDC 620.191.4

<https://doi.org/10.17073/1997-308X-2025-4-91-99>

Research article

Научная статья



Challenges in using powder feedstock for laser powder bed fusion

F. A. Baskov[✉], A. I. Logacheva, I. A. Logachev, A. N. Timofeev

JSC Kompozite

4 Pionerskaya Str., Korolev, Moscow region 141070, Russia

[✉ baskov_fa@mail.ru](mailto:baskov_fa@mail.ru)

Abstract. This paper reviews the main methods for producing and assessing the quality of powder feedstock intended for use in laser powder bed fusion (LPBF). The LPBF process involves the layer-by-layer laser fusion of powder feedstock on the surface of a build plate in accordance with a 3D model. The study examined powder feedstock produced domestically from industrial alloys based on nickel (Inconel 718, EP741NP, AZhK), titanium (VT6, VT6s, VT20), and iron (12Kh18N10T, Fe–Cr–Ni–Co–Mo system). The principal production methods considered are gas atomization, the Plasma Rotating Electrode Process (PREP), and plasma atomization in an inert gas atmosphere, with their respective advantages and limitations described. The most common defects in powder feedstock arising during production and use in LPBF are analyzed, including non-conforming particle size distribution, internal porosity, satellites, changes in bulk density and flowability, fine black particles, increased gaseous impurities, and non-conforming chemical composition. Measures for mitigating these defects and maintaining product quality are proposed. The findings show that achieving stable LPBF results requires regular quality control of powder feedstock to ensure compliance with the requirements specified in applicable standards, including particle size distribution (distribution quantiles d_{10} , d_{50} , and d_{90}), processing characteristics, particle morphology, chemical composition, and moisture content. For certain alloys, when defects occur systematically and cannot be effectively eliminated through process adjustments or post-processing, the most appropriate solution is to change the powder production method.

Keywords: additive manufacturing, powder feedstock, laser powder bed fusion (LPBF), heat-resistant alloys, powder defects, nickel-based alloys, titanium-based alloys, iron-based alloys

For citation: Baskov F.A., Logacheva A.I., Logachev I.A., Timofeev A.N. Challenges in using powder feedstock for laser powder bed fusion. *Powder Metallurgy and Functional Coatings*. 2025;19(4):91–99.
<https://doi.org/10.17073/1997-308X-2025-4-91-99>

О проблемах применения металлопорошковых композиций в технологии селективного лазерного сплавления

Ф. А. Басков[✉], А. И. Логачева, И. А. Логачев, А. Н. Тимофеев

АО «Композит»

Россия, 141070, Московская обл., г. Королёв, ул. Пионерская, 4

[✉ baskov_fa@mail.ru](mailto:baskov_fa@mail.ru)

Аннотация. В работе рассмотрены основные методы производства и контроля качества металлопорошковых композиций (МПК), предназначенных для применения в технологии селективного лазерного сплавления (СЛС). Метод СЛС представляет собой послойное лазерное сплавление МПК на поверхности металлической подложки в соответствии с 3D-моделью. В качестве объектов исследования использованы МПК из промышленных сплавов на основе никеля (Inconel 718, ЭП741НП, АЖК), титана (ВТ6, ВТ6с, ВТ20), железа (12Х18Н10Т, система Fe–Cr–Ni–Co–Mo) отечественного производства. Основными методами их изготовления являются газовая атомизация, плазменное центробежное распыление, плазменная атомизация в среде инертных газов. Приведены основные преимущества и недостатки

каждого из представленных способов производства МПК. Рассмотрены наиболее распространенные дефекты МПК, возникающие на этапе их получения и применения в процессе СЛС, такие как несоответствие гранулометрического состава, внутренняя пористость, сателлиты, изменение насыпной плотности и текучести, нагар, увеличение содержания газовых примесей и несоответствие химического состава. Предложены основные способы их устранения для сохранения качества выпускаемой продукции. Установлено, что для получения стабильных результатов в процессе послойного синтеза методом СЛС необходимо проводить регулярный контроль качества МПК на соответствие установленным в нормативной документации требованиям (гранулометрический состав – квантили распределения d_{10} , d_{50} и d_{90} , технологические свойства, форма частиц, химический состав, влажность). В случае возникновения на регулярной основе дефектов, которые затруднительно и/или невозможно устранить, наилучшим решением для некоторых сплавов является смена метода производства МПК.

Ключевые слова: аддитивные технологии, металлопорошковые композиции (МПК), селективное лазерное сплавление, жаропрочные сплавы, дефекты порошков, сплавы на основе никеля, сплавы на основе титана, сплавы на основе железа

Для цитирования: Басков Ф.А., Логачева А.И., Логачев И.А., Тимофеев А.Н. О проблемах применения металлопорошковых композиций в технологии селективного лазерного сплавления. *Известия вузов. Порошковая металлургия и функциональные покрытия*. 2025;19(4):91–99. <https://doi.org/10.17073/1997-308X-2025-4-91-99>

Introduction

The continuous development of powder metallurgy has led to the emergence of a modern method for producing components – additive manufacturing (AM). This technology encompasses techniques for the layer-by-layer fusion or deposition of powder or wire feedstock using high-energy sources such as lasers, electron beams, or electric arcs. The material is fused layer by layer in accordance with a 3D model [1].

The most widely employed AM process is laser powder bed fusion (LPBF), or selective laser melting (SLM), in which layers of powder are selectively fused by a laser on the surface of a build plate (also referred to as the substrate). The production of a component by LPBF typically involves the following stages:

- preparation of the 3D model (slicing, generation of support structures, positioning of the part on the build plate, and setting the LPBF process parameters);
- preparation of the equipment (cleaning, installation of the build plate, and uploading the prepared model file to the control unit);
- execution of the LPBF process;
- removal of the build plate with the fabricated part;
- post-processing of the part (mechanical processing, thermal treatment, and hot isostatic pressing).

Each stage of the process requires close control, as any deviation from the prescribed parameters may adversely affect the quality of the final component [2].

In addition to the stability of the equipment and software, the key factors influencing the quality of the end product include the properties of the powders, the LPBF process parameters, and the precision of the part geometry.

Powder feedstock – referred to in Russian standards as a metal powder composition (MPC) – is defined in GOST R 59035-2020 as a metallic powder formulated as a single composition for use in AM. At both the production stage of the MPC and during the use of powder feedstock in layer-by-layer synthesis, it is essential to control parameters such as particle morphology, particle size distribution, chemical composition, processing characteristics (apparent density and flowability), defects (internal – gas porosity; external – satellites), and moisture content. Any non-conformity of the powder feedstock with the specified requirements can result in diminished quality of the finished product [3–6].

A correctly selected LPBF mode – representing the combination of process parameters – is one of the key factors determining the final result, including the mechanical properties of the part and its compliance with the dimensions specified in the design documentation. For this reason, LPBF parameters are developed for each alloy, and dimensional optimization is carried out for each part. Both of these stages are labor-intensive and are implemented iteratively, with intermediate results followed by adjustments to the process parameters.

The final stage in producing the target component is comprehensive post-processing, involving the selection of the necessary mechanical and thermal operations. At this stage, the part is separated from the build plate, support structures and any residual powder feedstock are removed from its surface and internal channels, and machining is performed to achieve the dimensions specified in the design documentation. Thermal treatment and hot isostatic pressing are used to relieve residual thermal stresses, reduce and/or eliminate characteristic structural defects (such as pores and cracks), and form a microstructure that ensures optimal proper-

ties, for example through the precipitation of strengthening phases. The sequence of technological operations is determined individually for each alloy and part type [7–10].

According to the Order of the State Corporation Roscosmos dated 12 November 2021, No. 332, JSC “Kompozit” has been designated as the competence center for additive technologies in the rocket and space industry. In this capacity, it undertakes activities aimed at the development, design, analysis of new materials, as well as the refinement of technological approaches and the provision of services in the field of AM. To date, more than ten grades of industrial alloys have been adapted for LPBF, including EP741NP, AZhK, VZhL12U, VT6, VT6s, VT20, VNL-3, EI712, EP810, EI835, and others [11–13]. The results of this adaptation have shown that the nature of the alloy (chemical composition and processing characteristics) and the quality of the powder feedstock have a decisive influence on the final outcome. It should also be noted that alloys adapted for LPBF cannot always be used in other AM methods due to the specific nature of layer-by-layer synthesis in each process.

The aims of the present study were to:

- review the principal methods for producing and controlling the quality of powder feedstock used in LPBF;
- analyze the requirements for such feedstock;
- examine the characteristic defects in powder feedstock and the measures used to eliminate them.

Experimental procedure

The study examined powder feedstock produced by domestic manufacturers from industrial alloys based on nickel (Inconel 718, EP741NP, AZhK), titanium (VT6, VT6s, VT20), and iron (12Kh18N10T and alloys from the Fe–Cr–Ni–Co–Mo system).

The characteristics of the powder feedstock – both in the as-supplied state and after LPBF – were assessed using standardized methods:

- bulk density in accordance with GOST 19440-94 and GOST R 70907-2023;
- flowability, in accordance with GOST 20899-98 and GOST R 70910-2023;
- particle size distribution (granulometric composition), in accordance with GOST 18318-94 and GOST R 70909-2023;
- particle morphology, in accordance with GOST 25849-83 and GOST R 70908-2023;

– chemical composition, depending on the alloy grade;

– gaseous impurities, depending on the alloy grade.

The microstructure of the powder feedstock and of samples fabricated by LPBF was examined using optical microscopy (OM) with an AxioVert A1 microscope (Carl Zeiss, Germany) equipped with an E3IS PM digital camera (Touptek Photonics, China) for image capture, and by scanning electron microscopy (SEM) with an S-3400N microscope (Hitachi High-Technologies Corporation, Japan).

Results and discussion

Characteristics of powder feedstock: Structure and properties

In most cases, the powder feedstock used in LPBF must meet a standard set of requirements:

- particle size distribution in the range of 10–63 μm (the specification may indicate distribution quantiles d_{10} , d_{50} , and d_{90} , as well as the percentage of particles outside the target fraction);
- flowability of no more than 50 s;
- bulk density of at least 0.5 of the material’s density;
- spherical or near-spherical particle morphology;
- moisture content not exceeding 0.01 %;
- chemical composition in accordance with the alloy grade.

If no specific requirement for oxygen content is given, its allowable limit for the particular alloy should be established by collecting statistical data. This is important because, during repeated use (when powder not exposed to the laser is recycled), the oxygen content in the feedstock may increase, leading to degradation of the material’s mechanical properties.

Methods of powder feedstock production

The main methods for producing powder feedstock are gas atomization, plasma rotating electrode process (PREP), and plasma atomization in an inert gas atmosphere. The key advantages and disadvantages of each method for producing powder feedstock from nickel-, iron-, and titanium-based alloys are outlined below.

Gas atomization is one of the most widely used and high-throughput techniques for producing powder materials. In this process, the metal is melted in

an induction furnace and then atomized with an inert gas such as argon. The method is most often applied to the production of nickel- and iron-based powders.

Its advantages include low production cost, owing to the high process productivity and the straightforward melt preparation stage (heating system and charge material selection); capability to produce a broad range of materials; and narrow particle size distribution.

The disadvantages are: the presence of satellites on particle surfaces; internal gas (argon) porosity; oxidation of particles (in the case of open melting); and presence of a fine particle fraction, which impairs the processing characteristics of the feedstock and requires an additional separation step. Internal porosity forms during atomization when molten droplets entrap argon gas. Satellites occur because finer particles solidify more rapidly, are more easily entrained, and collide with larger particles under the influence of turbulent flows [14].

Plasma rotating electrode process (PREP) uses a cylindrical billet as the feedstock. While the billet rotates at high speed (up to 35,000 rpm), its end face is melted by a high-power direct-current plasma arc. This produces a thin molten film on the billet end, from which droplets detach and spheroidize under surface tension forces. Atomization takes place in an inert gas atmosphere (argon–helium mixture) under overpressure.

This technique is most frequently used to produce nickel- and iron-based powders. Its key advantages are: excellent processing characteristics of the resulting powder; uniform chemical composition; low levels of gaseous impurities; high productivity; and minimal internal and external defects. The latter results from the specifics of the centrifugal atomization process: the relatively low cooling rate allows each droplet to fully spheroidize before solidification, while the absence of turbulent flows reduces the formation of satellites [14].

The main drawbacks of PREP are: higher cost of powder feedstock, since the starting cylindrical billet requires several production stages (melting, machining) and must meet strict quality requirements (minimal run-out, uniform chemical composition, absence of defects such as cracks and cavities); low yield of the target particle size fraction; and a limited range of industrial alloys suitable for the method [15].

Plasma atomization in an inert gas atmosphere employs wire feedstock with a diameter of up to 5 mm. This technology is used primarily for titanium-based powders and selected nickel-based alloys. Its advantages

include homogeneous chemical composition; narrow particle size distribution; low levels of internal and external defects; and high processing performance.

Its disadvantages are: a restricted range of alloys (limited to those available in wire form); lower productivity compared with the methods described above; and relatively high production cost [16].

Plasma spheroidization also merits mention. In this process, powders are treated in a thermal plasma jet. While not an independent production method, it is used to spheroidize powders with angular or irregular particle shapes, rendering them suitable for LPBF. Plasma treatment also reduces the occurrence of satellites, thereby improving the processing properties of the feedstock. However, it may alter the particle size distribution and increase the proportion of fine particles, which adversely affects flowability. To remove the fine fraction, additional separation steps are performed, such as ultrasonic washing.

Defects in powder feedstock: Causes, formation mechanisms, and prevention measures

Non-conforming particle size distribution. Deviation in the particle size distribution of the powder feedstock from that originally used to establish LPBF process parameters changes the overall energy input and disrupts heat transfer. This can promote the formation of cracks and warping in the material (Fig. 1, *a*). Such deviations are cumulative, developing through repeated reuse of the same batch of powder [17]. A reduction in the proportion of fine particles impairs the deposition of powder feedstock onto the build plate, leading to a decrease in the density of the deposited layer. Laser exposure on a less densely packed layer leads to local overheating, increased thermal stresses, and the formation of defects such as cracks (Fig. 1, *b*). This effect is most pronounced when building parts of complex geometry and/or large size.

The issue can be addressed by adjusting LPBF parameters and/or blending in powder of a specific particle size to achieve the required particle size distribution with the target quantiles d_{10} , d_{50} , and d_{90} .

Internal porosity. This defect originates during powder production through entrapment of process gas, most commonly in gas atomization. Using feedstock with internal gas porosity in LPBF results in its transfer to the consolidated material and in uneven fusion, producing so-called fine black particles (Fig. 2). Porosity can be reduced by optimizing fusion parameters and/or

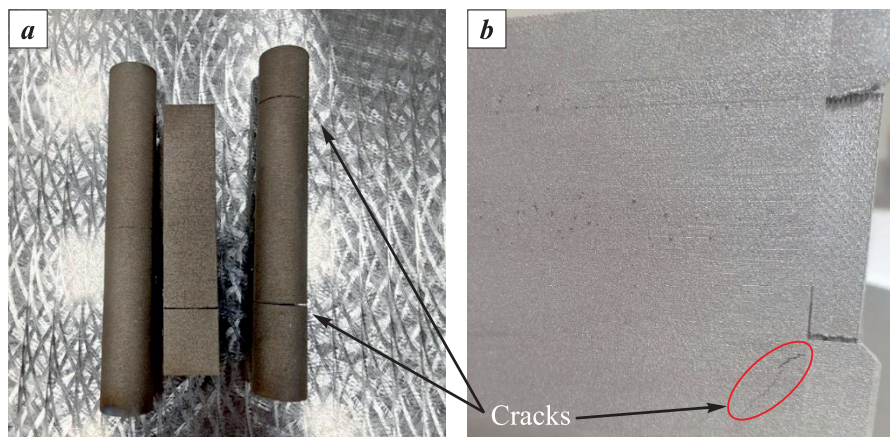


Fig. 1. Appearance of surface defects in a VT6 witness samples (a) and in a VT20 workpiece (b)

Рис. 1. Внешний вид поверхностных дефектов в образцах-свидетелях из сплава ВТ6 (a) и заготовке из сплава ВТ20 (b)

using powder with minimal gas porosity, for example by selecting an alternative production method.

Satellites. As noted earlier, satellites are characteristic of gas atomization. A high proportion of satellite-bearing particles reduces the processing performance of the powder and increases the formation of fine black particles during layer-by-layer fusion. The formation of these particles can be mitigated to some extent by optimizing fusion parameters. The satellite content can be lowered through additional sieving and thermal plasma treatment. However, these steps increase powder preparation complexity and the cost of the final product.

Bulk density. Bulk density should be carefully considered when selecting powder feedstock. It should be as close as possible to the theoretical maximum and comparable to that of powders from leading suppliers. Lower bulk density values are generally caused by higher internal porosity and/or changes in particle size distribution. Using powder with reduced bulk den-

sity in LPBF can lead to additional defects in the consolidated material and contribute to the formation of fine black particles.

This issue can be resolved by additional classification and/or blending powder of a specific particle size to restore the required particle size distribution with the target d_{10} , d_{50} , and d_{90} values. It is also advisable to verify the stability of the powder production process.

Flowability. Reduced powder flowability can result from changes in particle size distribution, an increased proportion of defective particles, or – in rare cases – elevated moisture content due to improper storage. Poor flowability increases equipment preparation time and can clog the powder recycling system, if present. Studies have also shown that powders with poor flowability spread less effectively across the build plate, affecting both the recoating process and layer uniformity [17–19].

Flowability can be improved by additional classification and/or adjusting the particle size distribution.

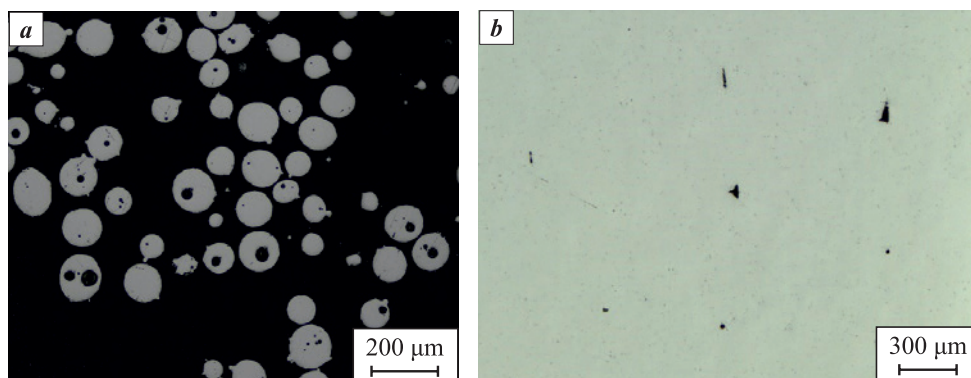


Fig. 2. Microstructure of powder (a) and LPBF-fabricated Inconel 718 material (b) with internal porosity

Рис. 2. Микроструктура МПК (a) и СЛС-материала из сплава Inconel 718 (b) с внутренней пористостью

If moisture is the cause, vacuum drying should be carried out.

Fine black particles. The term refers to fine, dark-colored particles generated during layer-by-layer fusion. Their accumulation clogs the filtration system and contaminates optical components, and when deposited on previously fused layers, they can cause defects or even halt the build (Fig. 3). Increasing the shielding gas flow can remove fine black particles from the melt pool area but also displaces fine powder particles into the filtration system. Reducing the fine fraction mitigates their formation but alters the feedstock particle size distribution. Observations indicate that powders with high internal porosity and a high proportion of satellites tend to generate more fine black particles. Adjusting LPBF parameters has not produced significant improvements. Further research is planned to investigate their formation mechanisms in powders from different alloys.

Gaseous impurities. The results of this study, together with literature data, indicate that under proper storage conditions, oxygen uptake by powder feedstock is negligible. In titanium-alloy powders, a slight increase in oxygen content during storage has been observed, but it remains within the permissible limits for the given alloy grade. Oxygen concentration increases when environmental conditions are not adequately controlled, as well as when operating equipment with a build chamber temperature above 500 °C. At present, most industrial LPBF systems do not have

this capability. Notably, adding fresh powder feedstock to recycled powder slows the rate of oxygen uptake – a feature typical of titanium-based alloys [18; 19].

The use of powder feedstock containing pre-oxidized particles results in the transfer of oxide phases into the LPBF-fabricated material, reducing its mechanical properties, particularly ductility [19]. The oxygen content does not decrease during the LPBF process. Fig. 4 shows a typical microstructure of powder feedstock particles from an Fe–Cr–Ni–Co–Mo alloy system containing oxide inclusions. Powders with such defects are not suitable for LPBF.

Scale factor. When optimizing LPBF parameters using small test samples – most often cubes measuring 10×10×10 mm – the geometry of larger workpieces must be considered. Due to the inherent characteristics of the LPBF process, thermal stresses accumulate during layer-by-layer fusion, which can lead to warping and cracking (Fig. 5). As a result, manufacturing a workpiece with complex geometry may require several iterations, each followed by adjustments to the 3D model and LPBF parameters. Currently, there are no software tools capable of fully minimizing this opti-

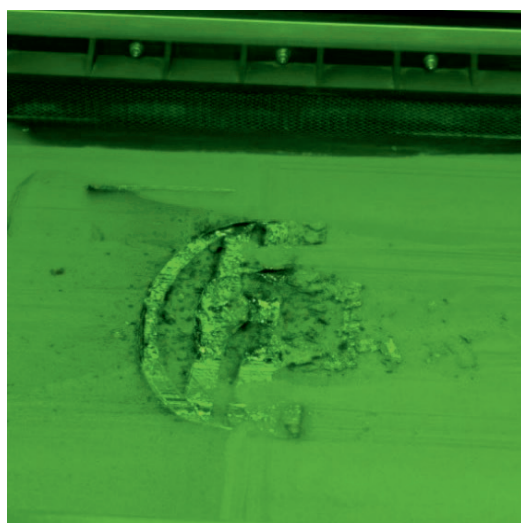


Fig. 3. Appearance of an Inconel 718 workpiece with accumulated fine black particles, which led to interruption of the LPBF process

Рис. 3. Внешний вид заготовки из сплава Inconel 718 с образовавшимся нагаром, что привело к остановке СЛС-процесса

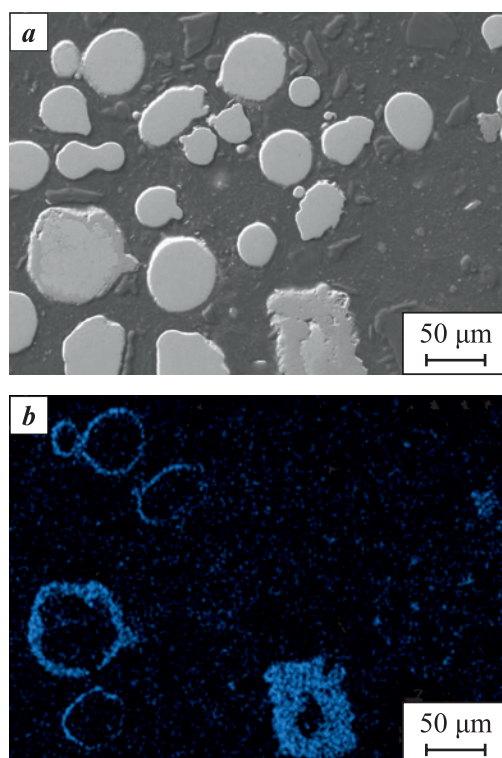


Fig. 4. Microstructure of oxidized powder feedstock particles from an Fe–Cr–Ni–Co–Mo alloy system (a) and oxygen distribution map (b)

Рис. 4. Микроструктура окисленных частиц МПК сплава системы Fe–Cr–Ni–Co–Mo (a) и карта распределения кислорода (b)

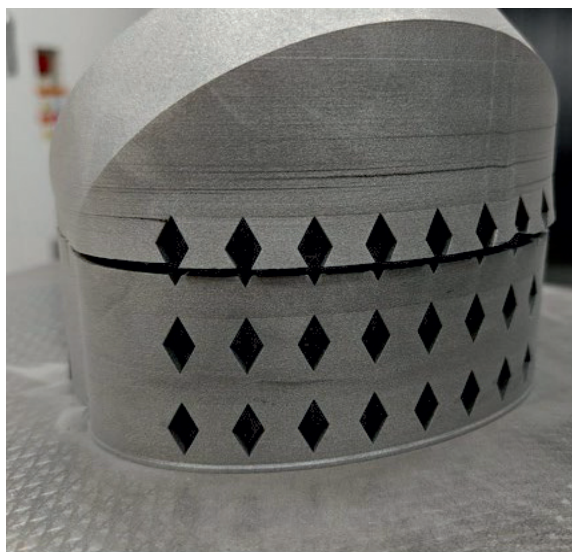


Fig. 5. Appearance of a VT6 workpiece showing delamination defects caused by high thermal stresses

Рис. 5. Внешний вид заготовки из сплава ВТ6 с дефектами в виде расслоения вследствие высоких термических напряжений

mization process, making operator expertise a critical factor.

Chemical composition. Analysis of the initial nickel-, titanium-, and iron-based powder feedstock and of the materials produced from them revealed no changes in the content of the principal alloying elements. Literature sources report that evaporation can occur when the process is carried out with excessive overall energy input. In this study, it was found that the elements most prone to evaporation are the low-melting constituents Mg, Zn, and Al [20]. For this reason, the overall chemical composition is monitored less frequently than gaseous impurities.

Conclusion

The present analysis has demonstrated that detecting all of the defect types considered – porosity, cracks, oxide inclusions, and others – requires regular quality control of powder feedstock to monitor for trends indicating degradation of its properties. This involves assessing particle size distribution, processing characteristics (bulk density and flowability), particle morphology, and chemical composition, both in the as-supplied state and after layer-by-layer fusion.

Consistently using high-quality powder feedstock ensures stable process outcomes. When defects such as porosity or fine black particles occur systematically, or when the feedstock exhibits poor processing

performance that cannot be effectively corrected through LPBF parameter adjustment or post-processing, the most appropriate solution for certain alloys is to change the powder production method.

There is also a growing trend towards adapting industrial alloys for additive manufacturing. However, not all materials are suitable for layer-by-layer fusion due to the specific features of their chemical composition. Since additive manufacturing is closely related to welding, alloys with limited weldability are generally unsuitable for layer-by-layer fusion.

References / Список литературы

1. Nandhakumar R., Venkatesan K. A process parameters review on selective laser melting-based additive manufacturing of single and multi-material: Microstructure, physical properties, tribological, and surface roughness. *Materials Today Communications*. 2023;35: 1–41. <https://doi.org/10.1016/j.mtcomm.2023.105538>.
2. Sefene E.M. State-of-the-art of selective laser melting process: A comprehensive review. *Journal of Manufacturing Systems*. 2022;63:250–274. <https://doi.org/10.1016/j.jmsy.2022.04.002>
3. Haferkamp L., Haudenschild L., Spierings A., Wegener K., Riener K., Ziegelmeier S., Gerhard J.L. The influence of particle shape, powder flowability, and powder layer density on part density in laser powder bed fusion. *Metals*. 2021;11(3):418. <https://doi.org/10.3390/met11030418>
4. Pleass C., Jothi S. Influence of powder characteristics and additive manufacturing process parameters on the microstructure and mechanical behaviour of Inconel 625 fabricated by selective laser melting. *Additive Manufacturing*. 2018;24:419–431. <https://doi.org/10.1016/j.addma.2018.09.023>
5. Haferkamp L., Spierings A., Rusch M., Jermann D., Spurek A.M., Wegener K. Effect of particle size of monomodal 316L powder on powder layer density in powder bed fusion. *Progress in Additive Manufacturing*. 2020;6(3):1–8. <https://doi.org/10.1007/s40964-020-00152-4>
6. Spierings A.B., Herres N., Levy G. Influence of the particle size distribution on surface quality and mechanical properties in AM steel parts. *Rapid Prototyping Journal*. 2011;17(3):195–202. <https://doi.org/10.1108/13552541111124770>
7. Wang G., Li B., Sun Y., Xia Y., Du J., Su G., Wang J., Han C. Characterization of microstructure and texture evolution of selective laser melting of nickel-based alloy subjected to machining. *Journal of Manufacturing Processes*. 2025; 140:63–77. <https://doi.org/10.1016/j.jmapro.2025.02.045>
8. Wang W., Wang S., Zhang X., Chen F., Xu Y., Tian Y. Process parameter optimization for selective laser melting of Inconel 718 superalloy and the effects of subsequent heat treatment on the microstructural evolution and mechanical properties. *Journal of Manufacturing Processes*. 2021;64:530–543. <https://doi.org/10.1016/j.jmapro.2021.02.004>

9. Korkmaz M.E., Gupta M. K., Waqar S., Kuntoglu M., Krolczyk G.M., Maruda R.W., Pimenov D.Y. A short review on thermal treatments of Titanium & Nickel based alloys processed by selective laser melting. *Journal of Materials Research and Technology*. 2022; 16:1090–1101.
<https://doi.org/10.1016/j.jmrt.2021.12.061>
10. Narasimharaju S.R., Zeng W., See T.L., Zhu Z., Scott P., Jiang (Jane) X., Lou S. A comprehensive review on laser powder bed fusion of steels: Processing, microstructure, defects and control methods, mechanical properties, current challenges and future trends. *Journal of Manufacturing Processes*. 2022;75:375–414.
<https://doi.org/10.1016/j.jmapro.2021.12.033>
11. Baskov F.A., Sentyurin Zh.A., Logachev I.A., Bychkova M.Ya., Logacheva A.I. Structure and properties of EP741NP heat-resistant nickel alloy produced by selective laser melting. *Russian Journal of Non-Ferrous Metals*. 2021;62(3):302–310.
<https://doi.org/10.3103/S1067821221030032>
12. Baskov F.A., Sentyurina Zh.A., Kaplanskii Yu.Yu., Logachev I.A., Semerich A.S., Levashov E.A. The influence of post heat treatments on the evolution of microstructure and mechanical properties of EP741NP nickel alloy produced by laser powder bed fusion. *Materials Science and Engineering: A*. 2021;817:141340.
<https://doi.org/10.1016/j.msea.2021.141340>
13. Baskov F.A., Sentyurina Z.A., Loginov P.A., Bychkova M.Y., Logachev I.A., Levashov E.A. Structure and properties evolution of AZhK superalloy prepared by laser powder bed fusion combined with hot isostatic pressing and heat treatment. *Metals*. 2023;13:1397.
<https://doi.org/10.3390/met13081397>
14. Nie Y., Tang J., Yang B., Lei Q., Yu S., Li Y. Comparison in characteristic and atomization behavior of metallic powders produced by plasma rotating electrode process. *Advanced Powder Technology*. 2020;31(5):2152–2160.
<https://doi.org/10.1016/j.appt.2020.03.006>
15. Zhang B., Huang Y., Dou Z., Wang J., Huang Z. Refractory high-entropy alloys fabricated by powder metallurgy: Progress, challenges and opportunities. *Advanced Materials and Devices*. 2024;9(2):100688.
<https://doi.org/10.1016/j.jsamd.2024.100688>
16. Hryha E., Riabov D. Metal powder production for additive manufacturing. *Encyclopedia of Materials: Metals and Alloys*. 2022;3:264–271.
<https://doi.org/10.1016/B978-0-12-819726-4.00089-2>
17. Emminghaus N., Bernhard R., Hermsdorf J., Kaierle S. Residual oxygen content and powder recycling: effects on microstructure and mechanical properties of additively manufactured Ti–6Al–4V parts. *The International Journal of Advanced Manufacturing Technology*. 2022; 121:3685–3701.
<https://doi.org/10.1007/s00170-022-09503-7>
18. Moghimian P., Poirie T., Habibnejad-Korayem M., Zavala J.A., Kroeger J., Marion F., Larouche F. Metal powders in additive manufacturing: A review on reusability and recyclability of common titanium, nickel and aluminum alloys. *Additive Manufacturing*. 2021;43:1–14.
<https://doi.org/10.1016/j.addma.2021.102017>
19. Zhuo Z., Ji R., Wang L., Mao J., Reusability of Ti–6Al–4V powder in laser powder bed fusion: Influence on powder morphology, oxygen uptake, and mechanical properties. *Journal of Materials Processing Technology*. 2025;335:1–7.
<https://doi.org/10.1016/j.jmatprotec.2024.118672>
20. Chowdhury S., Yadaiah N., Prakash C., Ramakrishna S., Dixit S., Gupta L.R., Buddhi D. Laser powder bed fusion: A state-of-the-art review of the technology, materials, properties & defects, and numerical modelling. *Journal of Materials Research and Technology*. 2022;20:2109–2172.
<https://doi.org/10.1016/j.jmrt.2022.07.121>

Information about the Authors

Fedor A. Baskov – Cand. Sci. (Eng.), Head of the Sector, JSC Kompozite

 **ORCID:** 0000-0001-6238-4378

 **E-mail:** baskov_fa@mail.ru

Alla I. Logacheva – Dr. Sci. (Eng.), Head of the Department of Metallic Materials and Metallurgical Technologies, JSC Kompozit

 **E-mail:** ailogacheva@yandex.ru

Ivan A. Logachev – Cand. Sci. (Eng.), Head of the Department, Deputy Head of the Department, JSC Kompozit

 **ORCID:** 0000-0002-8216-1451

 **E-mail:** ivan@logachev.biz

Anatoly N. Timofeev – Dr. Sci. (Eng.), Deputy General Director for Scientific Work of JSC Kompozit

 **E-mail:** info@kompozit-mv.ru

Сведения об авторах

Федор Алексеевич Басков – к.т.н., начальник сектора АО «Композит»


 **ORCID:** 0000-0001-6238-4378

 **E-mail:** baskov_fa@mail.ru

Алла Игоревна Логачева – д.т.н., начальник отделения металлических материалов и металлургических технологий АО «Композит»

 **E-mail:** ailogacheva@yandex.ru

Иван Александрович Логачев – к.т.н., начальник отдела, зам. начальника отделения АО «Композит»

 **ORCID:** 0000-0002-8216-1451

 **E-mail:** ivan@logachev.biz

Анатолий Николаевич Тимофеев – д.т.н., зам. генерального директора по научной работе АО «Композит»

 **E-mail:** info@kompozit-mv.ru

Contribution of the Authors**Вклад авторов**

F. A. Baskov – development of the main concept, formulation of the study aim and objectives, manuscript preparation, formulation of conclusions.

A. I. Logacheva – scientific supervision, manuscript revision, revision of conclusions.

I. A. Logachev – performing calculations, conducting sample tests, manuscript preparation.

A. N. Timofeev – scientific supervision, manuscript revision, revision of conclusions.

Ф. А. Басков – формирование основной концепции, постановка цели и задачи исследования, подготовка текста, формулировка выводов.

А. И. Логачева – научное руководство, корректировка текста, корректировка выводов.

И. А. Логачев – осуществление расчетов, проведение испытаний образцов, подготовка текста статьи.

А. Н. Тимофеев – научное руководство, корректировка текста, корректировка выводов.

Received 25.05.2025

Revised 02.07.2025

Accepted 04.07.2025

Статья поступила 25.05.2025 г.

Доработана 02.07.2025 г.

Принята к публикации 04.07.2025 г.

Олег Владиславович Роман

21 сентября 1925 – 16 марта 2013

Ученый в области порошковой металлургии
Академик НАН Беларуси,
первый директор Института порошковой металлургии
Доктор технических наук, профессор
Почетный профессор БНТУ



В 2018 г. Институту порошковой металлургии НАН Беларуси присвоено имя академика О. В. Романа

ул. Платонова, 41, 220005 Минск, Республика Беларусь

Зарегистрирован Федеральной службой по надзору
в сфере связи, информационных технологий
и массовых коммуникаций.

Свидетельство о регистрации ПИ № ФС77-79230

Журнал распространяется агентством «Урал-Пресс»
Подписной индекс: 80752 (печатная версия)
05108 (электронная версия)

ПЛАТОНОВА
улица
41

ИНСТИТУТ ПОРОШКОВОЙ МЕТАЛЛУРГИИ ИМЕНИ АКАДЕМИКА О.В. РОМАНА

